



<https://theses.gla.ac.uk/>

Theses Digitisation:

<https://www.gla.ac.uk/myglasgow/research/enlighten/theses/digitisation/>

This is a digitised version of the original print thesis.

Copyright and moral rights for this work are retained by the author

A copy can be downloaded for personal non-commercial research or study,
without prior permission or charge

This work cannot be reproduced or quoted extensively from without first
obtaining permission in writing from the author

The content must not be changed in any way or sold commercially in any
format or medium without the formal permission of the author

When referring to this work, full bibliographic details including the author,
title, awarding institution and date of the thesis must be given

Enlighten: Theses

<https://theses.gla.ac.uk/>
research-enlighten@glasgow.ac.uk

**Photonic Integration of InGaAs/InGaAsP
Quantum Well Lasers by Fluorine
Impurity Induced Disordering**

by

Stephen Alan Bradshaw
September 1994

Submitted to the faculty of Engineering of the University of
Glasgow for the degree of Doctor of Philosophy

© **Stephen Alan Bradshaw, 1994.**

ProQuest Number: 10992154

All rights reserved

INFORMATION TO ALL USERS

The quality of this reproduction is dependent upon the quality of the copy submitted.

In the unlikely event that the author did not send a complete manuscript and there are missing pages, these will be noted. Also, if material had to be removed, a note will indicate the deletion.



ProQuest 10992154

Published by ProQuest LLC (2018). Copyright of the Dissertation is held by the Author.

All rights reserved.

This work is protected against unauthorized copying under Title 17, United States Code
Microform Edition © ProQuest LLC.

ProQuest LLC.
789 East Eisenhower Parkway
P.O. Box 1346
Ann Arbor, MI 48106 – 1346

Thesis
10078
Copy 1



Acknowledgements

Firstly, it would not have been possible for me to carry out the following work without the financial support offered by the SERC and BNR Europe Ltd. (Formerly STC Ltd.), for this I am very grateful.

The technical support offered by the department throughout my work has been excellent, from the clean room to the electronics workshop, and the mechanical workshop. I would like to thank all the support staff for their hard work and dedication. On a more academic level it was a privilege to be part the optoelectronics research group and I acknowledge the special help that was given to me by Dr. Catrina Bryce who had the patience to introduce me to the RTP system, waveguide alignment procedures, and many other techniques that were central to my work. I also greatly appreciate the help from Dr. Rick Glew of BNR, my industrial supervisor, who offered his advice and supplied the wafers used throughout this thesis.

A great deal of moral support was also on hand in the department, and I would also like to thank the my many and varied friends who have so patiently awaited the arrival of this thesis!

My family have also shown me a great deal of support through out my years at University and I take this opportunity of thanking them for all their help.

The last note must go to Dr. John Marsh, my Ph.D. supervisor who has help me with this work in many ways too numerable to mention.

Table of Contents

Abstract	1
Publications	3
Chapter 1	5
Content of Thesis	5
Chapter 2	7
Review of Current Intermixing Processes	7
2.1 Introduction	7
2.2 GaAs Based Structures	7
2.2.1 AlAs/GaAs	8
2.2.2 GaAs/AlGaAs	9
2.2.3 InGaAlAs/GaAs	14
2.2.4 InGaAsP/GaAs	14
2.2.5 InGaAs/GaAs	14
2.2.6 Summary	16
2.3 InGaAs/InAlAs/InP	17
2.3.1 Thermal Stability	17
2.3.2 Impurity Induced Disorder	18
2.3.2a Zn IID Studies	18
2.3.2b Si IID Study	19
2.3.3 Impurity Free Intermixing	20
2.3.3a SiO ₂ and Rapid Thermal Annealing (RTA)	20
2.3.3b Si ₃ N ₄ and Repetitive Rapid Thermal Annealing (RRTA)	21
2.3.4 Summary	21
2.4 InGaAs/InP Intermixing	
2.4.1 Thermal Stability	23
2.4.2 Dopant IID	25
2.4.2a Zn Diffusion	25
2.4.2b Si Implantation and Diffusion	26
2.4.2c P Ion Implantation	26
2.4.2d Ga Implantation	26
2.4.2e Ge Implantation	27
2.4.2f S Diffusion	28

2.4.2g	O Implantation	28
2.4.2h	Ar Implantation	30
2.4.3	Impurity Free Disordering	30
2.4.4	Summary	32
2.5	InGaAsP & InGaAlAs Systems	33
2.5.1	Thermal Intermixing	33
2.5.2	IID	34
2.5.3	Dielectric Cap Disordering	35
2.5.4	Summary	35
2.6	The Disordering Mechanism	35
2.7	Conclusions	40
Chapter 3		55
Fluorine Impurity Induced Disordering		55
3.1	Introduction	55
3.1.1	The Structure Investigated	56
3.1.2	Energy Levels in Quantum Well Structures	57
3.1.3	Excitons	60
3.1.4	Effect of Well Composition on Energy	62
3.2	Ion Implantation - fluorine Incorporation Technique	64
3.2.1	Why Ion Implantation?	64
3.2.2	Why fluorine Impurity?	65
3.2.3	Implant Profiles (TRIM)	66
3.2.4	Calculation of Implant Concentration	66
3.3	Photoluminescence Measurements	68
3.3.1	Principles of Photoluminescence	68
3.3.2	Experimental Technique	69
3.4	Annealing Process	71
3.4.1	Conventional Furnace Annealing	71
3.4.2	Rapid Thermal Processing	72
3.5	Results	72
3.5.1	Concentration vs. Anneal Time	73
3.5.2	Conventional Annealing for 30 minutes	74
3.5.3	Rapid Thermal Processing (fixed time)	76
3.5.4	Rapid Thermal Processing (fixed temperature)	77
3.5.5	Summary	78
3.6	Theoretical Model of the Diffusion Process	79

3.6.1	Fick's Law of Diffusion	79
3.6.2	Hyperbolic Secant Profile	82
3.6.3	Diffusion Coefficients from Experimental Results	85
3.7	Summary	87
Chapter 4		91
Thermal Stability and Effects of Dielectric Caps		91
4.1	Introduction	91
4.2	Experiments	91
4.3.	Effect of SiO ₂	92
4.3.1	Wafer E791 Anneal Results	92
4.3.2	Wafer E799 Anneal Results	94
4.3.3	Wafer E795 Anneal Results	97
4.4.	Silicon Nitride Caps	98
4.5	Dielectric Cap Disordered Lasers	103
4.6.	Conclusions	105
Chapter 5		107
Design and Fabrication of Single-Mode Waveguides for Fabry-Perot Loss Measurements		107
5.1	Introduction	107
5.2	The Slab Waveguide	107
5.2.1	The Three Layered Slab	108
5.2.2	The Four Layered Slab	110
5.3	The Ridge Waveguide	111
5.3.1	The Effective Index Method	112
5.3.2	The Vector Finite Difference Method	113
5.4	Waveguide Design	113
5.4.1	The Starting Material	113
5.4.2	Fourlay Calculations	114
5.4.3	FWave Calculations	117
5.5	Fabrication Of The Waveguides	119
5.6	Conclusions	121
Chapter 6		124
Fabry-Perot Loss Measurements		124
6.1	Introduction	124
6.2	Theory	124
6.3	Experimental Technique	128

6.4	Results	130
6.5	Conclusions	136
Chapter 7		137
Oxide Stripe Laser Fabrication		137
7.1	Introduction	137
7.2	Oxide Stripe Laser Fabrication	137
7.2.1	Material Structure	137
7.2.2	Oxide Stripe Fabrication	138
7.3	Laser Characteristic Test	140
7.3.1	Test Procedure	140
7.3.2	Results	142
7.4	Fabrication of Oxide Stripe Extended Cavity Lasers	145
7.4.1	Implant Conditions	145
7.4.2	Fabrication	145
7.4.3	Test	149
7.4.4	Results	150
7.4	Conclusions	153
Chapter 8		154
Loss Measurement from Laser Characteristic		154
8.1	Introduction	154
8.2	Loss Measured by Luminescence	154
8.2.1	Measurement Technique	155
8.2.2	Experimental Technique	156
8.2.3	Results	157
8.3	Calculation of Loss From the Change in Threshold Current	160
8.3.1	Calculation of the Optical Confinement Factor (Γ_w)	161
8.3.2	Calculation of the Gain Parameter (G_o)	163
8.4	Conclusions	166
Chapter 9		168
Near- and Far-Field Patterns		168
9.1	Introduction	168
9.2	Near- and Far-Field Patterns	169
9.3	The Far Field Pattern	169
9.4	Theory of Field Patterns in Laser Arrays	170

9.4.1	The Equations	170
9.4.2	Theoretical Calculations	176
9.4.3	Theoretical Calculation Results	176
9.4.3a	Supermode $v=10$	178
9.4.3b	Supermode $v=9$	180
9.4.3c	Supermode $v=1$	183
9.4.3c	Supermode $v=2$	186
9.4.4	Summary	188
9.5	Measuring the Near-Field Pattern	189
9.6	Measuring the Far-Field Pattern	189
9.6.1	Rotary Stage Method	190
9.6.2	Camera Method	192
9.7	Results	193
9.7.1	No Extended Cavity	193
9.7.2	Oxide Stripes with Extended Cavity	196
Chapter 10		205
Summary and Conclusions		205
Appendix A		Ai
Wafer Structures		Ai
Appendix B		Bi
Computer Programme to Calculate the Near and Far-Field Patterns		Bi

Abstract

Impurity Induced Disorder (IID), using the neutral impurity fluorine, has been investigated in the InGaAs/InGaAsP quantum well (QW) system. The object of the thesis was to produce a method to intermix quantum well structures selectively in order to produce low loss optical waveguides suitable for the integration of photonic and optoelectronic devices.

The intermixing properties of fluorine have been investigated, and have proved successful in the fabrication of low loss waveguides. The intermixing process was modelled by using Fick's laws of diffusion, and the error function profile compared to a hyperbolic secant profile. It was found that the error function profile more closely models the disordering process, from this model the diffusion coefficient were calculated for thermal and F IID. A diffusion coefficient of $10^{15} \text{ cm}^2 \text{ s}^{-1}$ was calculated for the fluorine IID process, the thermal diffusion coefficient was found to be between $10^{16} \text{ cm}^2 \text{ s}^{-1}$ and $10^{17} \text{ cm}^2 \text{ s}^{-1}$.

A laser containing an extended cavity was fabricated and a loss of only 12.5 dB cm^{-1} was measured in the disordered section. The laser fabricated was a $75 \mu\text{m}$ oxide stripe extended cavity device; the result of adding the extended cavity was to produce a single lobed output in the far-field distribution pattern. By comparing the experimental results with theoretical calculations, it was determined that the effect of adding the extended cavity is to force the filaments observed in the near-field to lase in the first order supermode. Powers of 14 mW were observed in lobes with FWHM of around 2° .

The thermal stability of InGaAs/InGaAsP quantum wells proved to be an initial barrier to the fabrication of selectively disordered structures. This problem was overcome by using rapid thermal annealing (RTA), instead of using a conventional anneal furnace. The RTA process enables precisely controlled anneals for very short times (less than 30 s) to be carried out.

Intermixing effects using an alternative neutral impurity, boron, were also investigated. It was quickly established that boron enhanced intermixing, however red shifts were observed.

The desirable effect would have been the production of a blue shift, as is the case with fluorine implantation. It is thought that the red shift observed is due to preferential group III intermixing.

Impurity free disordering was also observed with silicon nitride caps, 30 - 40 meV blue shifts occur for very short anneal times (5 seconds) at 750°C in the RTA. Strontium fluoride and silica showed no effect on the intermixing process.

Publications

'(INVITED) -*Edge Emitting Laser Arrays with a well Controlled Transverse Mode Structure*' J.H. Marsh, K. McIlvaney, S.A. Bradshaw, F.R. Laughton, and J. Grey - to be presented at Circular-Grating Light-Emitting Sources (part of Photonics West'95), San Jose, CA, 4-10 February, 1995.

'*Extended Cavity Lasers Formed by Fluorine Induced Quantum Well Disorder*': S.A. Bradshaw, J.H. Marsh, and R.W. Glew, IEE Colloquium on Applications of Quantum Well Technologies, Savoy House, London, March 1993.

'*Very Low Loss Waveguides Formed by Fluorine Induced Disorder of GaInAs/GaInAsP*': S.A. Bradshaw, J.H. Marsh and R.W. Glew, IEEE/LEOS Proceedings Fourth International Conference on Indium Phosphide and Related Materials, Newport, Rhode Island, April 1992.

'*Dielectric Cap Disorder of InGaAs Quantum Well Structures on InP and GaAs*': S.A. Bradshaw, A.C. Bryce, E. Tozowonah, J.H. Marsh, R. Bradley, R. Niclin, R.W. Glew, IEEE/LEOS Proceedings Integrated Photonics Research, New Orleans, April 1992.

'*Neutral Impurity Induced Disorder of III-V Quantum Well Structures for Optoelectronic Integration*': J.H. Marsh, S.R. Andrew, S.G. Ayling, J. Beauvais, S.A. Bradshaw, R.M. De La Rue, and R.W. Glew, Mat. Res. Soc. Symp. Proc. Vol. 240, pp. 679-690, 1992.

'*Thermal Instability of InGaAs/InGaAsP*': R.W. Glew, J.P. Stagg, P.D. Greene, A.T.R. Briggs, S.A. Bradshaw, and J.H. Marsh, IEEE/LEOS Proceedings Third International Conference on Indium Phosphide and Related Materials, Cardiff, Wales, April 1991.

'*Impurity Induced Disorder of GaInAs Quantum Wells with Barriers of AlGaInAs or of GaInAsP*': J.H. Marsh, S.A. Bradshaw, A.C. Bryce, R.G. William, and R.W. Glew, J. Electron. Mat., 20, pp. 973-978, 1991.

'*Neutral Impurity Induced Disorder of III-V Quantum Well Structures for Optoelectronics*': J.H. Marsh, S.G. Ayling, A.C. Bryce, S.I. Hansen and S.A.

Bradshaw, Joint Soviet-American Workshop on the Physics of Semiconductor Lasers, Vol. 240 Ch. 240, pp. 111-129, 1992.

Chapter 1

Content of Thesis

The following work is concerned with the integration of photonic devices in the InGaAsP/InGaAs system lattice matched to InP. The system is important for producing semiconductor lasers in the 1.55 μm low loss window in modern single moded optical fibres. Integration of devices onto a single substrate is an important area of research in the optoelectronics industry due to the potential benefits in terms of cost reduction, increased functionality, and ease of use of optoelectronic devices. It is the objective of this thesis to develop an integration technique using the neutral impurity fluorine, to enhance the thermal intermixing of InGaAsP/InGaAs quantum wells (QWs). The optical losses of such disordered QWs will be measured, and a device produced and tested that uses the disordering process to produce a useful result.

The chapters are organised in the following way;

- Chapter 1:** Introduction to the thesis.
- Chapter 2:** A review of the current intermixing technology in various III-V semiconductor material systems.
- Chapter 3:** Fluorine Impurity Induced Disorder are investigated in InGaAsP/InGaAs Quantum Well structures. Annealing in a conventional anneal furnace and in a rapid thermal processor is investigated and the results compared.
- Chapter 4:** The thermal stability of InGaAsP/InGaAs Quantum Well structures, and the effects of silica and silicon nitride caps are investigated.
- Chapter 5:** Single moded waveguides are designed and fabricated for use in Fabry-Perot loss measurements.

- Chapter 6:** Loss measurements are taken of disordered waveguides using the Fabry-Perot technique.
- Chapter 7:** Oxide stripe lasers are fabricated with extended cavities using the disordering process developed here.
- Chapter 8:** Losses of the extended cavities are measured from the characteristics of the devices fabricated in Chapter 7.
- Chapter 9:** The effect of the extended cavity on the near- and far-field patterns is investigated. The far-field pattern is found to be improved with the addition of an extended cavity.
- Chapter 10:** Conclusions are drawn from the work carried out, and possible future work is discussed.

Chapter 2

Review of Current Intermixing Processes

2.1 Introduction

Intermixing of QW structures is becoming an important technique for the optoelectronic integration of III-V semiconductor optoelectronic devices. Because there are so many different material combinations available, many different processes have been developed for intermixing, some more successful than others.

This Chapter aims to introduce the disordering techniques used for the most common III-V material systems, and reference papers concerned with each process. Since intermixing began with the findings of Laidig et al¹ in the GaAs system. Section 2.2 begins with a review of intermixing processes in GaAs based structures. Section 2.2, is subdivided into sections relating to the different heterostructures used and includes AlAs/GaAs, InGaAs/GaAs, InGaAsP/GaAs, and InGaAs/GaAs.

The remaining sections are dedicated to the InP based materials generally used for long wavelength (1.3-1.55 μm range) optoelectronic devices, the subject of this work. Section 2.3 covers InGaAs/InAlAs, Section 2.4 InGaAs/InP, and Section 5 covers the two quaternary systems InGaAsP and InGaAlAs. The sections dealing with InP based systems are subdivided into the different disordering techniques that have been reported.

Finally, Section 2.5 introduces a model to describe the disordering process, taking into account the concentration of defects in the crystal lattice and the effect of the crystal's Fermi level on the rate of intermixing.

2.2 GaAs Based Structures

GaAs and its related alloys form the basis for the optoelectronics industry in the short wavelength ranges. Heterostructure semiconductor lasers were first developed in GaAs based systems in the 1970s, emitting in the 0.8-0.9 μm near infra-red region. This early

development resulted in the first generation of optical fibre communication systems. To take advantage of the low loss windows in silica fibres at 1.3 and 1.5 μm emphasis has shifted towards the development of long wavelength lasers. Long wavelength lasers require smaller band gap material than GaAs based systems can offer, thus InP based structures have become increasingly more important.

Still, many devices are manufactured in the GaAs system and much work has been carried out which is relevant to the InP based system. Importantly, enhanced QW intermixing was first observed in the AlAs/GaAs system by Laidig et al¹. They showed that by diffusing zinc into a MQW structure the temperature at which intermixing occurred was reduced by 300°C. This paper has led to many investigations aimed at understanding the mechanisms involved and finding optimum conditions for intermixing. Enhanced intermixing has been found to occur for many different conditions. Ion implantation or diffusion has been a popular approach with both neutral, donor and acceptor impurities being investigated. More recently it has been found that dielectric caps, often more than a micron from the QW structure, are capable of enhancing the intermixing rate.

The following section will outline and give reference to most of the processes investigated to date, this section is organised under material composition.

2.2.1 AlAs/GaAs

Zinc was the first impurity to be used to increase the inter-diffusion rate in the AlAs/GaAs system, with Laidig et al², as mentioned above, being the first group to report the phenomena. The work was repeated later by Kirchoefer et al³. Both papers show complete intermixing of superlattices when the sample was heated in an evacuated silica ampoule with a ZnAs₂ diffusion source at 575°C for four hours. Van Vechten⁴ almost immediately proposed a model for the process, where the coulombic interaction between Zn⁺ and the cation-on-anion-site divacancy complex enhances the rate of vacancy diffusion, which results in inter-diffusion on the group III lattice by providing spaces for the Ga and Al atoms to move into during the diffusion step.

Silicon implantation⁵ has also been used to intermix QW structures. Si is a donor in this system so the diffusion mechanism is suggested to be similar to that with Zn i.e. by an impurity-vacancy mechanism. The diffusion rate of Si into GaAs can be increased by oxidising a layer of SiGe on the surface⁶, reducing the time required for Si ion diffusion. A silicon diffusion depth of 200 nm was reported for an 800°C 30 min anneal using this technique.

Mitra et al⁷ examined the role of vacancies and the Si induced intermixing process. They were able to show that by growing Si into the structure (giving a small vacancy concentration), and by implanting Si (giving a high vacancy concentration), that vacancies play an important role in the diffusion of Si+, but not in the group III intermixing process. However when the gallium vacancy concentration is large enough, arsenic vacancies (positively charged) and gallium vacancies (negatively charged) can form pairs. These pairs enhance intermixing on the group III sublattice by lowering the activation barrier for the ring exchange mechanism, the currently most popular theory for the diffusion mechanism.

Sulphur diffusion has also been studied, Baba-Ali⁸ reported on the effects of incorporating S by annealing in a sealed ampoule at 1000°C. Although group III inter-diffusion was observed the technique is probably of little use due to the high temperatures required. S was examined because it is a good n-type dopant for GaAs, creating the high carrier mobilities crucial for integrating laser diodes with field effect transistors.

2.2.2 GaAs/AlGaAs

The GaAs/AlGaAs material structure has been the most commonly used system for optoelectronics, so it is not surprising that it has also received the most attention as far as QW intermixing is concerned. The main dopants used in the GaAs system are:

p-type: Zn, Be, Mg,

n-type: Si, Mg, C, Ge, S, Se, Sn, Mn,

all of which have undergone investigation to establish their positional stability within the crystal during annealing, and to observe their effect on intermixing SL and QW structures. The effect of implanting constituent elements such as Al⁹ has also been investigated as well as neutral impurities such as F and B. Finally the effect of introducing vacancies within the crystal by impurity free techniques has been investigated: in particular annealing with SiO₂ caps.

Implanting Si, the most commonly used n-type dopant, has been one of the most successful techniques and most commonly studied; however Si diffusion is also commonly used. Si implantation followed by an annealing step has been shown to cause layer intermixing by various groups^{10,11,12,13,14}, who generally come to the same conclusions: i.e. that Si diffusion aids the disordering process. Si implanted to concentrations as low as $3 \times 10^{16} \text{ cm}^{-3}$ can cause extensive layer disordering. At high Si doses ($5 \times 10^{13} \text{ cm}^{-2}$) and low anneal temperatures the Si forms interstitial loops which inhibit the formation of Si atoms that are free to diffuse and cause intermixing. A source of Ga vacancies¹⁵ can however free atomic Si from the interstitial loops and allow disordering to proceed. The introduction of Ga vacancies has been achieved by either capping the GaAs with SiO₂ or by providing an As overpressure. Annealing conditions used that produce significant intermixing¹⁶ are: 850°C for 30 mins to 3 hrs in a conventional furnace, and 1050°C for 10 s for anneals in a rapid thermal annealer.

Many devices have been reported which utilise Impurity Induced Layer Disorder (IILD) with Si implantation and annealing. Most of the devices reported concern the fabrication of a low-loss waveguide section with a view to integration: extended cavity lasers have been reported with cavity losses of 12-13 dB cm⁻¹ (17) and 11 cm⁻¹ (18). Birefringence has also been studied—Kapon et al¹⁹ reported an extinction ratio between TE and TM modes of 15 dB with a refractive index change of 2×10^{-3} at 1.15 μm. More complicated structures have also been studied: a DBR laser was fabricated by Hirata et al²⁰ who reported losses of 4.4 cm⁻¹ at the lasing wavelength and a linewidth of 840 kHz. Macda et al²¹ have taken this a stage further by integrating two DBR lasers with a

Y-branch coupler to generate beat signals. Finally Gavrilovic et al²² fabricated a buried stripe geometry laser using disordering to define the stripe.

Si diffusion has been achieved via two basic techniques depending on the diffusion source. The most common method is to evaporate a thin layer of Si (~100 Å) directly onto the surface and, on annealing at 850°C, Si diffuses into the QW or SL structure²³ causing intermixing. Holonyak et al²⁴ found that increasing the As₄ overpressure results in an increase in diffusion depth in the case of GaAs and a reduction for AlGaAs. The column III vacancy concentration determines Si diffusion and intermixing in GaAs, while column V vacancy concentration determines inter-diffusion in AlGaAs. They also found that the native defects, required for inter-diffusion are column III vacancies²⁵. The effects of doping on the inter-diffusion process were also studied by Holonyak et al²⁶; an n-type crystal enhances the inter-diffusion rate whereas a p-type crystal suppresses the inter-diffusion rate. The fabrication of disorder-defined buried-heterostructure lasers by the diffusion of Si has been investigated by a collaboration between the Xerox Palo Alto Research centre and the University of Illinois^{27,28,29,30,31,32,33} and more recently at Amaco³⁴, the latest paper reporting cw laser operation with an output from uncoated facets of 25 mW per facet with threshold currents as low as 7 mA at 812 nm. Other groups have fabricated devices by Si-diffusion, for example Zou et al³⁵ have reported a laterally injected laser. This is an interesting device as it provides a simple self-aligned planar process that would be easy to integrate with other planar devices on the same chip.

Diffusion has also been investigated from grown-in sources, with results consistent with diffusion from external sources^{36,37}. By using a grown-in source, Deppe et al³⁸ were able to show that the inter-diffusion rate of Al-Ga is dependent on the crystal Fermi-level, hence the Si concentration and crystal doping. The Fermi level of the crystal in this model controls the concentration of the column III vacancies and column III interstitials. The experimental data showed that, in n-type crystals, diffusion is enhanced by the increased solubility of the column III vacancy defect, and enhanced layer inter-diffusion in p-type superlattices is caused by enhanced solubility of column III interstitials. Guido et al have

fabricated two devices utilising Si IID from a grown-in source; an index guided QW laser capable of kink-free single-mode operation³⁹, and a coupled-stripe laser array capable of producing >100 mW.

A more novel method that has been investigated to produce Si for diffusion was reported by Guido et al⁴⁰. A film of SiO₂ deposited on an AlGaAs surface was reduced by the Al to form free Si and O, and Al₂O₃. The Si is then free to diffuse into the crystal and cause diffusion as described above, however O is also diffusing in this case. O is thought to compensate the Si donor leaving an area of high resistivity. A buried QW laser was fabricated to demonstrate the process.

The influence of Si has been studied extensively and there appears to be no outstanding difference between implantation and diffusion. However, implantation is usually considered as the most appropriate method, due to the ease with which it is possible to place an accurate predefined concentration of Si below the surface. It also appears that the creation of Ga vacancies plays an important role with this type of disordering as discussed above. Although much time has been spent on the development of procedures using Si implantation and diffusion, this is not an ideal solution since Si is electrically active and will therefore require to be co-doped to neutralise the implant if losses due to free carrier absorption are to be minimised. To complicate this further, not all of the implanted Si will be activated, therefore it makes the processes of neutralising the implant region much more complicated.

The other major n-type dopants to have been studied are Se⁴¹, S⁴², Ge⁴³ and Sn⁴⁴, the mechanism for the intermixing process in these dopants appearing to be similar to that of Si. S shows only limited intermixing⁴⁵ when diffused into QW structures from a layer of GaS at 825°C for 24 hours, the conclusion was that S is not very effective for IILD.

The p-type dopants Zn⁴⁶, Mn⁴⁷, Mg⁴⁸, and more recently C⁴⁹ have also been investigated.

High concentrations (10^{20} cm⁻³) of Mn can be diffused into GaAs from a MnAs source⁵⁰ at 800°C for 2 hours, resulting in a *p*-type layer. The mechanism for Mn diffusion and

intermixing is reported as being similar to that of Zn. Mg grown into the barriers of an MOCVD-grown structure have shown⁵¹ enhanced intermixing after anneals at 825°C for 2 hours. C doped structures may become important since it has been shown⁵² that the C is more stable than the sublattice itself against the effects of IID; this means greater control can be achieved over the doping profile of a structure. Inter-diffusion has been observed with all *p*-type dopants with a similar mechanism proposed for all.

Stripe geometry lasers had been fabricated using Zn diffusion (600°C) as early as 1984 by Meehan et al⁵³, further studies in the disordering process leading to papers being published on disorder delineated waveguides by Wolf et al⁵⁴, and Julien et al⁵⁵. The latter work was aimed at finding out more about the refractive index changes in the disordered material. It was found that the disordered regions show an increase in refractive index which is birefringent in nature, the TE mode seeing a higher refractive index step than the TM mode. Wolf et al comment that antiguiding is possible for TM polarized light that has a wavelength chosen to be 'sufficiently' below the bandgap of the material.

Dallesasse et al⁵⁶ have reported an interesting method for masking the diffusion of Si and Zn into their structures: a high Al-containing AlGaAs layer was oxidised in H₂O vapour at 400°C to produce a native oxide. This eliminates the requirement to grow a dielectric film onto the sample and therefore reduces the complexity and therefore cost of the disordering procedure.

An alternative impurity disordering technique is to implant neutral impurities: F and B have been implanted to produce blue shifts^{57,58,59}. Anneal temperatures of 890°C produced blue shifts of up to 100 meV, accompanied by refractive index changes >1%. Active dopants such as Si, used in IID, are ionized at room temperature leading to free carrier absorption in optical waveguides, neutral impurities by their nature will give rise to less absorption by this process.

It has been shown that Ga will out-diffuse in SiO₂ films^{60,61,62} during thermal annealing at 850°C. The out-diffusion of Ga causes column III vacancies to diffuse into the structure,

creating spaces for column III elements to diffuse, thus causing intermixing. The effect has been shown to be an order of magnitude less for the case of Si_3N_4 ⁶³ (this varies from paper to paper but demonstrates the general trend), with an even smaller shift for SrF_2 ⁶⁴ (strontium fluoride) capped samples. Vacancy diffusion using SiO_2 annealing caps has been used to fabricate birefringent waveguides⁶⁵, stripe geometry lasers⁶⁶, and reflection modulators⁶⁷

2.2.3 InGaAlAs/GaAs

The GaAs/InGaAlAs material system is important because it allows lasers to be fabricated that will operate at shorter wavelengths than GaAs/AlGaAs systems. Zn diffusion has been shown to disorder this material⁶⁸ for long anneals at 600°C-675°C, by increasing the diffusion rate on the group III sublattice. As-grown material was found to be thermally stable up to ~800°C.

2.2.4 InGaAsP/GaAs

Little work has been published to date concerning the disordering of InGaAsP on GaAs. Plano et al⁶⁹ have, however, shown that such structures can be disordered by Zn diffusion at 560°C (3 hrs), while the as-grown material remains thermally stable up to ~800°C. Their work was primarily concerned with showing that it is possible to grow ordered material containing As and P on the column V lattice site by MOCVD. Previously column V ordering had only been observed with GaAsSb and InGaAsP on InP.

2.2.5 InGaAs/GaAs

The strained layer InGaAs/GaAs QW system is becoming a popular material for optoelectronic structures because of the ability to produce strained layer lasers operating at 980 nm. It is natural therefore that it has also been studied with respect to its inter-diffusion characteristics. Si and Zn IID have been the most extensively studied processes, however Au⁷⁰, Be and impurity free techniques have also been investigated.

Si was diffused at 850°C from a 200 Å Si film to define a stripe geometry laser with a very low threshold current⁷¹. The optimum concentration of Si required for IID has been found to be around⁷² 10^{18} cm^{-3} . Major et al⁷³ used a layer of AlGaAs to reduce SiO₂ into Si, O, and Al₂O₃ at 825°C, and were then able to produce narrow stripe lasers with high differential quantum efficiencies, by disordering via Si-O diffusion.

Zn has been shown to significantly enhance the intermixing process⁷⁴, blue-shifting QW structures by ~30 meV for a 750°C diffusion for 15 mins. Be (a p-type dopant) at equivalent concentrations was found to have little effect on the inter-diffusion rate⁷⁵. Impurity free techniques have been reported such as thermal annealing⁷⁶ at temperatures greater than 850°C for times as short as 5 s, as well as the utilisation of SiO₂ caps⁷⁷, annealing at 900°C for 10s.

2.2.6 Summary

Figure 2.1 contains a summary of the IID techniques in the previous section for GaAs based QW structures.

Impurity/ Dielectric	Incorporation Technique	Direction of Energy Shift	Anneal Temp.	Material System	Doping	Ref.
Zn	Diffusion	BLUE	575°C 600°C 600-675°C 560°C 750°C	AlAs AlGaAs InGaAlAs InGaAsP InGaAs	p-type	1, 2, 3, 4, 46, 53, 54, 55
Mn	Diffusion		800°C	AlGaAs	p-type	47, 50
Mg	Diffusion		825°C	AlGaAs	p-type	48, 51
C	Diffusion	no effect	825°C	AlGaAs	p-type	49, 52
Be	Diffusion	little effect		InGaAs	p-type	75
Si	Diffusion	BLUE	800°C 850°C 850°C	AlAs AlGaAs InGaAs	n-type	6, 23, 24, 25, 26, 27, 28, 29, 30, 31, 32, 33, 34, 35, 36, 37, 38, 39, 40, 56
Si	Implantation		675°C 850°C (1050°C)	AlAs AlGaAs	n-type	5, 7, 10, 1, 12, 13, 14, 15, 16, 17, 18, 19, 20, 21, 22
S	Diffusion	little effect	1000°C 825°C	AlAs AlGaAs	n-type	8, 43, 45
Se	Diffusion		825°C	AlGaAs	n-type	41
Sn	Diffusion			AlGaAs	n-type	44

Ge	Diffusion			AlGaAs	n-type	43
F	Implantation	BLUE	890°C	AlGaAs	neutral	57, 58, 59
B	Implantation	BLUE	890°C	AlGaAs	neutral	57, 58, 59
Si-O	SiO ₂ reduced by AlGaAs		825°C	InGaAs		40
SiO ₂	Plasma Deposition	BLUE	850°C 900°C	AlGaAs InGaAs	column III vac	60, 61, 62, 65, 66, 67
Si ₃ N ₄	Plasma Deposition	BLUE	850°C	AlGaAs		63
SrF ₂	Plasma Deposition	No Shift	850°C	AlGaAs		64

Table 2.1. Summary of GaAs based IID techniques. Anneal temperatures given in parenthesis are for RTA processing, all other temperatures are for conventional anneal furnaces.

2.3 InGaAs/InAlAs/InP

The In_{0.53}Ga_{0.47}As/In_{0.52}Al_{0.48}As MQW system is important for the realisation of optoelectronic devices operating in the 1.3-1.5 μm spectral region.

2.3.1 Thermal Stability

The first studies on the properties of annealed InGaAs/InAlAs QW structures were carried out by Seo et al⁷⁸. A single, nominally undoped, 120Å thick, QW of In_{0.53}Ga_{0.47}As in In_{0.52}Al_{0.48}As was grown by MBE, and annealed with a halogen lamp with a protective GaAs cap under a flowing argon atmosphere. They used the results of photoluminescence and the assumption that only the Al and Ga were involved in the inter-diffusion process to calculate an effective diffusion coefficient. A blue shift was observed for 5 s anneals above 700°C. The effective group III diffusion coefficients were found to decrease from 3.2×10^{-16} to $1.3 \times 10^{-17} \text{ cm}^2 \text{ s}^{-1}$ for anneal times ranging from 5 s to 30 min. They offered three explanations for this result. Firstly, the annealing out of defects would reduce the

amount of diffusion by point defect assistance thereby reducing D . Secondly, D could be concentration dependent and, as diffusion progresses, the chemical potential across the well will decrease so reducing the rate at which diffusion can occur. Finally, the diffused well profile could be more complicated than the simple error function derived from Fick's laws of diffusion. In reality, a combination of the above is more likely. Later it was shown that their original assumption that only the Ga and Al were diffusing may be wrong⁷⁹.

Two years later Baird et al⁸⁰ showed that In was diffusing across the heterointerface between $\text{In}_{0.53}\text{Ga}_{0.47}\text{As}$ and $\text{In}_{0.52}\text{Al}_{0.48}\text{As}$. A single QW was grown by MBE, the sample was annealed with an over-pressure of As to prevent its out-diffusion during annealing at 1085 K, and the results were studied by Auger depth profiling. At first sight, the In diffusion seems surprising because of the almost constant In concentration across the structure, however the diffusion could be explained by examining the relative mobilities of the group III elements. If one assumes that the mobilities of these elements is inversely related to their bonding strengths in the lattice, the mobilities will have the order $\text{In} > \text{Ga} > \text{Al}$. In the above structure Ga diffusion will be driven by the Ga concentration profile, however the Al will not be able to diffuse quickly enough to compensate for the in-diffusion of Ga into the InAlAs layer, so to compensate for this, the more mobile In will diffuse into InGaAs to maintain stoichiometry.

2.3.2 Impurity Induced Disordering

The effect of charged impurities has also been studied in this system; the first to be covered here is the p-type impurity Zn followed by the n-type impurity Si.

2.3.2a Zn IID Studies

Kawamura et al⁸¹ diffused Zn into a superlattice consisting of sixty 75 Å InGaAs wells with 75 Å InAlAs barriers grown by MBE. PL spectroscopy and Auger profiling were used to monitor the Ga/Al inter-diffusion. They established that complete intermixing

occurred after a 1 hour Zn diffusion at 550°C, but offered no explanation as to why the dopant enhanced the intermixing rate. The material was thermally stable up to 700°C.

Baird et al⁸² also used an MBE grown structure, a 15 period superlattice consisting of 100 Å InGaAs and 100 Å InAlAs layers which was Zn diffused at 825 K (552°C). They used Auger profiling to monitor the In, Ga, and Al diffusion profile across the structure before and after Zn diffusion. They also found complete intermixing of the structure occurred. A Si₃N₄ mask was used to protect the waveguide section from the Zn diffusion, which was carried out at using a Zn₃As₂ source at 725 K for 1 hr. Optical loss measurements were taken by comparing the transmitted intensity of light from a colour centre laser as a function of waveguide cavity length (2.5 - 4 mm). A loss of 2.3 dB cm⁻¹ was reported for a single moded waveguide at 1.546 μm. This result appears at first sight to be very good, however the as-grown material had its PL peak at 1.2 μm which shifted to 0.94 μm after in-diffusion, so very little of the loss would be due to band edge absorption either before or after intermixing. A more interesting result would have been to see the effect in a structure grown to emit at 1.55 μm,. This would have more relevance to the integration of active and passive devices at the correct emission wavelength for optical communications. However, the experiment was principally designed to show the viability of producing waveguides by IID; the authors did indeed succeed in this aim.

2.3.2b Si IID Study

Baird et al⁸³ in the same paper as the Zn diffusion experiment described above reported results for Si⁺ implantation. Again using Auger profiling to monitor the In, Ga, and Al distribution profile they showed that Ga/Al intermixing occurred for Si concentrations above 2×10¹⁹ atoms cm⁻³, when annealed at 1075 K for one hour. For lower Si concentrations, In and Ga were the main diffusing species. These results confirmed the theory they developed earlier with the lamp annealed samples. The effect of Si was to increase the mobility of the group III elements, the mobility of Al increasing to such an extent that In diffusion is no longer required to maintain crystal stoichiometry. However

the material is intermixing thermally at the temperatures required to activate the Si, so making this process unattractive as a method of producing integrated structures.

2.3.3 Impurity Free Intermixing

The effects of both Si_3N_4 and SiO_2 capping layers on the thermal stability of InGaAs/InAlAs have been studied and are summarised below. The motivation behind this type of disordering is the elimination of the impurity which, in the case of a charged impurity leads inevitably to losses due to free carrier absorption.

2.3.3a SiO_2 and Rapid Thermal Annealing (RTA)

Spatially selective disordering using a patterned silica mask on an InGaAs/InAlAs structure was first reported by Chi et al⁸⁴. InGaAs single QW structures were grown by MBE and coated with 0.4 μm of RF sputtered silicon dioxide which was patterned to produce areas which would subsequently disorder and areas that would remain unaltered. The samples were annealed in a RTA with a nitrogen atmosphere for 15 s at between 700°C and 900°C. It was found that intermixing was inhibited in areas covered with SiO_2 with shifts of 80 meV being observed in the uncoated areas after annealing for 15 s at 800°C. A possible explanation for this is vacancy enhanced intermixing: indium evaporates rapidly from the surface causing indium vacancies to diffuse into the sample enhancing Ga and Al interdiffusion. In areas capped with SiO_2 , the indium evaporation is impaired and the vacancy enhanced process much reduced. No further evidence was given to support this theory.

The same group later reported a contrary set of results⁸⁵. A very similar experiment was carried out except that the samples were annealed with a GaAs proximity cap to produce an arsenic over-pressure, so protecting the surface from As or In desorption. The results of this were dramatically different to their previously reported data: instead of no shifts under the SiO_2 cap, blue shifts of up to 74 meV occurred for unspecified annealing conditions with 'minimal' shifting occurring in uncapped regions. It was ruled out as the diffusing species (as compared to furnace annealed samples) since they calculated that it

would only lead to red shifts. They therefore concluded that Ga and Al diffused. The mechanism for this was left unexplained, but suggestions were made that it could be due to Si diffusing in from the cap.

2.3.3b Si₃N₄ and Repetitive Rapid Thermal Annealing (RRTA)

A second impurity-free technique has been reported by Miyazawa et al⁸⁶. The sample used consisted of 145 InGaAs wells with a width of 67 Å and was grown by MBE. A 2000 Å film of Si₃N₄ was deposited onto the sample. Annealing was carried out in an RTA with 5 s anneals at 850°C repeated three times (RRTA), with a GaAs proximity cap. Partial intermixing was achieved selectively with a wavelength shift of 43 nm. A single anneal step with the same total anneal time as for RRTA was used and, a much smaller shift was then observed. A shift was also observed in the cap-less samples.

The difference in the intermixing due to the different anneal conditions is thought to arise from the difference in thermal expansion coefficient causing a stress field to build up at the dielectric semiconductor interface. The field would introduce vacancies into the MQW allowing diffusion to occur. The expansion coefficients are;

crystalline Si ₃ N ₄	2.8×10 ⁻⁶ K ⁻¹ ,
In _{0.53} Ga _{0.47} As	5.6×10 ⁻⁶ K ⁻¹ ,
In _{0.52} Al _{0.48} As	5.2×10 ⁻⁶ K ⁻¹ .

The thermal expansion coefficient for amorphous nitride is likely to be smaller than the crystalline value given above, thereby increasing the strain further. For SiO₂ the crystalline expansion coefficient is 6.8×10⁻⁶ K⁻¹ while that of the amorphous material is 5×10⁻⁶ K⁻¹.

2.3.4 Summary

Disordering has been demonstrated in the InGaAs/InAlAs QW system using both impurity-free techniques as well as charged impurities. Table 2.2 summarises the main points. Of the techniques reviewed here, Zn diffusion seems to be the most promising since it

is carried out at temperatures well below the temperature at which the system is thermally unstable. What could be a major draw-back with this technique is the electronic effect of adding Zn doping, it may not be possible to isolate devices electrically on the same wafer without adding another dopant (n-type) to compensate the Zn.

Impurity/ Dielectric	Incorporation Technique	Colour of Energy Shift	Anneal Temp.	Diffusion Species	Doping	Ref.
Thermal Stability	N/A	BLUE	700°C+	Ga/Al/In	N/A	78, 79, 80
Zn	Diffusion	BLUE	550°C	Ga/Al	p-type	81, 82
Si	Implantation	BLUE	800°C	Ga/Al	n-type	83
SiO ₂	RF sputtering electron beam	BLUE	RTP 750°C	Ga/Al	dopant free	84, 85
Si ₃ N ₄	plasma deposition	BLUE	RRTP 800°C	GaAl	dopant free	86

Table 2.2. Summary of InGaAs/InAlAs/InP Disorder. Anneal temperatures are for conventional annealing processes unless marked otherwise.

2.4 InGaAs/InP Intermixing

The InGaAs/InP system is important for QW structures required to emit between 1.3 μm and 1.55 μm . There have been a large number of studies of the intermixing properties of this system with the view to producing low-loss waveguides for optoelectronic and photonic integrated circuits (OEICs and PICs respectively). Following is a summary of the work carried out to date. It can be split into four major categories:

- Thermal Stability

- Dopant Impurity Induced Disorder (DIID): the impurities are expected to alter the Fermi level of the material since they are ionized at room temperature.
- Neutral Impurity Induced Disorder (NIID): the impurities are electrically neutral at room temperature.
- Impurity Free Disorder (IFD): intermixing is achieved without the need to introduce impurities into the structure under investigation.

2.4.1 Thermal Stability

Thermal interdiffusion of InGaAs/InP superlattice (SL) and quantum well (QW) structures has been investigated by both PL and Raman scattering.

Temkin et al⁸⁷(1987) investigated material grown by gas source molecular beam epitaxy (GSMBE) at 500°C. Samples were annealed between 600 and 850°C for 5 minutes in a carbon crucible with an InP cap and the resulting intermixing was monitored by low temperature PL. They found that the PL peaks remained remarkably narrow, indicating that diffusion above 700°C could not be occurring via Fick's law. Instead it was shown that, by taking into account the restricting forces that were trying to prevent the build up of strain, the diffusivity was varying as the second power of concentration.

Nakashima et al⁸⁸ (1987) used metal organic molecular beam epitaxy (MOMBE) to investigate the thermal stability between 500 and 700°C. They used absorption spectra, SIMS, and X-ray diffraction to characterise the process, concluding that intermixing only occurs above 700°C and is mainly due to group V atoms, especially phosphorous. This is contradictory to the assumption made by Temkin et al⁸⁷ who assumed that the material would resist the movement towards strain.

Fujii et al⁸⁹ used a first-order perturbation formula to analyse the dependence of the interdiffused energy shift on the quantum well width, diffusion time, and diffusion temperature. They used the results of this analysis to describe the macroscopic diffusion mechanism in undoped MQWs of various widths grown by MOVPE. After thermal

annealing, the photoluminescence energy shifted to higher energy as expected, this shift being inversely proportional to the well width and proportional to the anneal time. Using their model, they were able to conclude that group V species inter-diffuse easily inside both InP and InGaAs layers but inter-diffuse with difficulty through InGaAs/InP hetero-interfaces. The interdiffusion rate was determined by the diffusion rate at the hetero-interface and was postulated to be determined by the change in chemical potential of the diffusing species when crossing from InP to InGaAs. The lower limit for group V diffusion coefficient in the InGaAs well was reported as being $5 \times 10^{-15} \text{ cm}^2 \text{ s}^{-1}$, with an activation energy of 1.0 eV for the annealing temperatures in the range of 500°C and 640°C.

Finally Raman scattering was used by Jae et al⁹⁰ in 1991 to quantify the quantitative inter-diffusion rates of the constituent atoms. This was done by monitoring the InGaAs and InGaP-related optical phonon (LO) bands. Each band shows a two mode behaviour corresponding to InAs- and GaAs-like modes in InGaAs and, InP- and GaP-like modes in InGaP. Baker and Sievers⁹¹ showed that the mode strength of the LO phonon bands is proportional to the relative concentration of binary groups i.e. InP, GaAs etc, and it is therefore possible to monitor the behaviour of constituent atoms in the intermixed structure. Anneals were carried out between 700 and 850°C for between 5 and 60 minutes. The material was grown by GSMBE and capped with a Si₃N₄ film. It was concluded that the diffusion process occurred whilst maintaining lattice matched conditions, and that the diffusion coefficient is much greater in the wells than the barriers. Diffusion is thus limited by the diffusion coefficient in InP which was estimated from the Raman results to be $D_0 = 8.56 \times 10^{10} \text{ cm}^2 \text{ s}^{-1}$ with an activation energy of 5.82 eV, which compares closely with the diffusion coefficient of P in InP ($D_0 = 7.0 \times 10^{10} \text{ cm}^2 \text{ s}^{-1}$) with an activation energy of 5.65 eV. The diffusion coefficients in this report may well have been over-estimated as it has been shown that⁹² Si₃N₄ can be used to intermix this material system selectively.

To summarise this Section, it appears that the InGaAs/InP material system is thermally stable up to 700°C. Above this temperature intermixing occurs mainly on the group V lattice site and is limited by the diffusivity of P in InP. The question of strain build-up during intermixing has not been fully resolved, although it is possible that for long low temperature anneals strain can build-up, whilst for high temperature anneals the diffusivity of the group III sublattice increases sufficiently to compensate for the group V diffusion and maintain a lattice matched structure.

2.4.2 Dopant IID

The majority of disordering processes studied use an impurity that is thought to be electrically active at room temperature, with Zn diffusion being the most common. A brief summary of current research follows with a summary at the end of the section.

2.4.2a Zn Diffusion

Zinc diffusion into InGaAs/InP SLs and MQWs has been studied by various groups, who are all in agreement that Zn causes intermixing on the group III (cation) lattice site whilst the anion diffusion is negligible. Zinc is a p-type dopant. The effect of this diffusion is two fold—firstly the bandgap is decreased⁹³ continuously for diffusion temperatures above 410°C, and secondly strain is observed in the resultant structure^{94,95} with as much as 3.2% strain being predicted by Hwang et al⁹⁶.

Recently Micallef et al⁹⁷ showed that the confinement profile obtained after ‘significant’ diffusion can maintain its original abrupt nature with well widths equal to those of the as-grown quantum wells. This effect is due to the build-up of strain at the InGaAs/InP interface as Ga diffuses across the interface. The effect of strain together with the compositional profile produce ‘miniwells’ both inside the well and the barrier. The heavy hole band can support states within these wells and could therefore be of interest in future devices.

2.4.2b Si Implantation and Diffusion

Photoluminescence, transmission electron microscopy and optical absorption experiments have all been carried out on Si implanted QW structures⁹⁸. For a 25 period structure containing 50 Å InGaAs wells with 50 Å InP barriers and a cap of 0.1 μm InP, a 180 meV shift was observed. An implant dose of $5 \times 10^{14} \text{ cm}^{-2}$ at 200 keV was used followed by annealing at 650°C for 2 h in a H₂ atmosphere. Schwarz et al⁹⁹ used Si diffusion and showed, using SIMS and TEM, that diffusion is comparable on both the cation and anion lattice sites, resulting in an unstrained structure. Si is an n-type dopant and therefore will increase the number of free carriers in the implanted regions.

2.4.2c P Ion Implantation

Tell et al¹⁰⁰ implanted P with a dose of between $1 \times 10^{14} \text{ cm}^{-2}$ and $1 \times 10^{15} \text{ cm}^{-2}$ at 100 keV, and the samples were then annealed in either a conventional furnace at 650°C for 30 minutes or in a rapid thermal annealer (RTA) at 750°C for 5-40 secs. Since P is a matrix element this process is not really impurity induced disordering, and it is therefore ambiguous as to whether the effects observed are due to vacancies and interstitials caused by the implantation process or due to the excess P having an effect on the equilibrium concentration of the number of vacancies. Shifts of up to 200 meV for both types of anneal were reported. The same group have produced ridge waveguides using this technique¹⁰¹, and the resulting loss was found to be 3.5 cm^{-1} , however, these waveguides were fabricated using a regrowth step i.e. etching off the original p-type cladding layer and regrowing it. The regrowth step adds a complication to the manufacturing process and lessens the attractiveness of the technique. A measurement of the waveguide loss without the regrowth of the cladding region would be very informative.

2.4.2d Ga Implantation

Photoluminescence and Auger electron spectroscopy have been used by Sumida et al¹⁰² to study the effect of Ga implantation. The structure studied was grown by MOMBE and

contained six 50 Å QWs. The Ga was implanted to a projected range of 470 Å at room temperature with doses ranging from 3×10^{13} to 5×10^{14} cm⁻². Thermal annealing was carried out in a N₂ atmosphere and with a Si₃N₄ 'passivation' film on the samples. The annealing temperature was 640°C and annealing time between 30 and 180 min.

Large blue shifts of up 100 meV were reported and attributed to diffusion on both the column III and column V lattice sites. They also observed a decrease in diffusion close to the surface, which was due to the low concentration of implanted Ga at the surface.

Later in 1991, the same group reported the fabrication of quantum wires using a focused Ga ion beam¹⁰³. Ga was implanted into a single 50 Å InGaAs QW grown by MOMBE, using a 100 keV focused ion beam with doses of 1×10^{13} to 1×10^{14} cm⁻². The samples were annealed at 650-670°C for 60 min. Raman spectroscopy was used to find the Ga and As composition of the disordered material. They report that the compositional change takes place in such a way as to keep the resultant composition closely lattice matched to InP, except at the higher implant doses where the As concentration is in excess. It was clear from the data they presented that, at low implant doses, the resulting composition is also non-lattice matched, but with an excess of Ga.

Quantum wires appear to have been made successfully by the above technique; lateral potential barriers were created for electrons and holes.

2.4.2e Ge Implantation

Ge is an amphoteric atom so it can occupy both column III and V lattice sites, and is therefore similar to Si which can cause diffusion on both lattice sites. Bradley et al¹⁰⁴ implanted Ge⁺ at room temperature with an energy of 200 keV and dose of 2×10^{14} cm⁻² (calculated dose $\sim 2 \times 10^{19}$ cm⁻³). The material, grown by LP-MOCVD, consisted twenty 36 Å InGaAs QWs capped with 750 Å InP. An infrared RTA was used to anneal the samples to 650°C for 20 min in a stagnant N₂ atmosphere.

A peak shift of 50 meV corresponding to 60% intermixed was observed in a band of QWs having an implant dose greater than $1.8 \times 10^{19} \text{ cm}^{-3}$. SIMS measurements indicate that the As profile still showed inter-diffusion effects where the Ge level was well below that required for column III diffusion, which was postulated to be the result of rapidly diffusing implant defects.

2.4.2f S Diffusion

Pape et al¹⁰⁵ used SIMS, photoluminescence, and optical absorption to investigate the effect of S diffusion into two MQW structures. The structures investigated were grown by MBE the first containing sixty-five 61 Å QWs, and the second containing one hundred 20 Å QWs. Sulphur was incorporated into the structure by heating the sample to 600°C for 20 minutes in a graphite ampoule containing elemental S and InP pellets. Samples capped with SiN_x were then annealed at temperatures of between 600°C to 700°C for up to 6 h 40 min.

Large blue shifts were seen—a shift from $\sim 1.56 \mu\text{m}$ to $\sim 1.2 \mu\text{m}$ was observed for a 6 h 40 min anneal at 700°C. They attributed this to diffusion on both the column III and column V lattice sites. Sulphur exists as a donor impurity (S_{As}^+), which can substitute onto the column V sublattice by substitution and can cause intermixing on the III lattice as in GaAs/AlGaAs. Their technique is promising but there is no indication of the losses incurred in resultant waveguides, which could be high even for large bandgap shifts because of the excess carriers introduced due to S being ionised.

2.4.2g O Implantation

Oxygen can be used to create highly resistive areas in III-V semiconductors¹⁰⁶, a very useful process required in the fabrication of optoelectronic devices. Pappert et al¹⁰⁷ investigated the ability of implanted O to simultaneously intermix a SL and create areas of electrical isolation.

The structures investigated consisted of a SL containing fifty 20 Å QWs grown by LP-MOVPE, one structure being undoped and the being other *p*-type (Zn doped). Oxygen ions (O⁺) were implanted at 180 keV with doses between 5×10^{12} and 5×10^{14} cm⁻². The implants were carried out both at room temperature and at elevated temperatures of 200°C and 550°C. Post-implantation annealing was carried out at 550°C in the implantation assembly, and 650°C in a RTP with a forming gas of 15% H₂, 85% N₂. PL and rocking X-ray curves were used to measure the degree of disordering.

The best results were for the samples implanted at 550°C with a further 550°C anneal for 8 minutes with an implantation dose of 1×10^{13} cm⁻². For these conditions, the electrical resistance increased from 300 Ω to 794 kΩ with a wavelength shift from ~1.5 μm to ~1.25 μm.

Below some critical temperature (~185°C in this case), implantation disordering is relatively temperature independent. Subsequent annealing causes intermixing due to the stored defects introduced by implantation. More defects in the structure result in more intermixing, provided voids and clusters do not occur due to over implantation¹⁰⁸. More defects would be expected with decreasing implant temperature. The energy shift for 550°C implants followed by 550°C anneals was 175 meV, whilst for the RT implant and 550°C anneal it was 124 meV, a difference of 51 meV. For the 600°C implants the energy shift difference between the two samples shrank to only 8 meV. It is therefore difficult to assess the above theory since intermixing is seen to occur during the elevated implant. The real difference between the processes is shown up when comparing the resulting electrical isolation. The RT implanted and annealed samples showed a resistance of 6 kΩ compared to the sample implanted at 550°C and annealed which had a resistance of 794 kΩ. The authors are unclear as to whether this is due to the creation of damage induced traps or electronic compensation.

2.4.2h Ar Implantation

Implantation of Ar at an elevated temperature of $\sim 400^\circ\text{C}$ has been shown by Xia et al¹⁰⁹ to produce intermixing in $\text{In}_{0.5}\text{Ga}_{0.5}\text{As}/\text{InP}$ SL waveguides without the need for further high temperature annealing. Intermixing was carried out at 400°C with 190 keV Ar ions at a dose of $5 \times 10^{14} \text{ cm}^{-2}$ and $2 \times 10^{15} \text{ cm}^{-2}$. X-ray rocking curves and optical absorption were used to establish the diffusion effects on the SL. Intermixing occurred at up to 70% of the ion range, and residual damage was located near the end of the ion range as would be expected from TRIM calculations (Section 3.2.2). The technique was used to define a waveguide in the SL structure, which appeared to guide light despite high losses of 35 dB cm^{-1} . The authors do not attempt to explain the source of the loss but predict lower loss waveguides may be fabricated by optimising the implant conditions.

2.4.3 Impurity Free Disordering

Impurity free techniques involve the deposition of a dielectric onto the surface of the QW structure followed by an annealing stage. They potentially offer a method of producing higher bandgap material without the requirement for introducing impurities which cause losses due to free carrier absorption (with the exception of neutral impurity disordering), excess damage leading to non-radiative recombination etc.

Miyazawa et al¹¹⁰ used transmission spectroscopy to study the effect of repetitive rapid thermal annealing (RRTA) on a MQW structure coated with a Si_3N_4 film. The MQW, grown by MBE at 545°C , consisted of one hundred 84 \AA QWs, and a 200 \AA nitride film was then deposited using PECVD. Annealing was carried out in a H_2 atmosphere by ramping at 30°C s^{-1} up to 800°C , then allowing the sample to cool to 100°C before ramping again. The process was repeated 11 times.

For the repetitive anneal described above, significant blue shifts occurred in the capped samples (84 nm), however the uncapped samples also showed a smaller ($\sim 20 \text{ nm}$) but significant blue shift. Two samples annealed in a single step to 800°C for 15 s showed

evidence of disordering (~20 nm) in both cases. No explanation was given for the above result, however, it is likely that the effects of strain are important when the sample is heating up and cooling down. Later¹¹¹, the same group produced extended cavity lasers, blue shifting areas coated with Si₃N₄ as described above,. They were by then able to use a single anneal step since they had learnt the necessary conditions for depositing Si₃N₄ films to their samples that adhere properly,. No mention was given in the paper as to whether or not the film came off during the RRTP process. Although they have produced integrated cavities using their process, the active sections also show a blue shift which is an undesirable effect since it makes the process of growing a structure to lase at a predetermined wavelength much more difficult. No data was presented on the repeatability of the blue shifts.

The refractive index change of Si₃N₄ disordered samples was reported by the same group¹¹² in 1991. The film thickness used in the experiment was 1500 Å, the anneal temperature was given as 800°C for times of between 0 and 60 s, and no mention was made of RRTA. The structure used consisted of an MBE grown SL containing one-hundred-and-twenty-five 30 Å QWs, and a Bragg grating was fabricated on the SL surface to act as a band-stop wavelength filter. The effective index of the waveguide could be obtained from its wavelength response. Refractive index changes of $\pm 1.5 \times 10^{-3}$ were observed for 5 s anneals, and for 60 s anneals these rose to -1.5×10^{-2} for the TE-mode and $+6.7 \times 10^{-3}$ for the TM-mode at 1.5 μm in a waveguide, with the peak PL position detuned from 1.3 μm to 1.2 μm. Polarization mode selective waveguides have been fabricated¹¹³ by a single anneal process which can be used to guide TE or TM modes selectively: a single anneal step at 800°C was used to disorder a SL with an extinction ratio of about 13 dB.

2.4.4 Summary

Table 2.3 summarises the disordering processes that have been investigated for the InGaAs/InP QW system.

Impurity/ Dielectric	Incorporation Technique	Colour of Energy Shift	Anneal Temp.	Diffusion Species	Doping	Ref.
Zn	Diffusion	RED	410°C +	Group III	p-type	93, 94, 95, 96, 97
Si	Diffusion	BLUE	700°C	Group III Group V	n-type	98
Si	Implantation	BLUE	650°C	Group III Group V	n-type	99
P	Implantation	BLUE	650°C	Group III Group V	dopant free	100, 101
Ga	Implantation	BLUE	640°C	Group III Group V	dopant free	102, 103
Ge	Implantation	BLUE	650°C	Group III Group V	n-type	104
S	Diffusion	BLUE	700°C	Group III Group V	n-type	105
O	Implantation	BLUE	550°C	Group III Group V		106, 107, 108
Ar	Implantation		400°C		dopant free	109

Si_3N_4	plasma deposition	BLUE	RRTP 800°C	Group III Group V	dopant free	110, 111, 112, 113
-------------------------	----------------------	------	---------------	----------------------	----------------	-----------------------

Table 2.3 Summary of intermixing processes covered here in the InGaAs/InP QW system.

Techniques have been demonstrated by dopant free as well as charged impurity, and impurity free for enhancing intermixing in the above system.

2.5 InGaAsP & InGaAlAs Systems

Even though the InGaAsP and InGaAlAs systems lattice matched to InP have become increasingly important for the realisation of optoelectronic devices in the 1.3 μm to 1.55 μm regimes, there has been relatively little work carried out on intermixing of these layers. The following section outlines the main work to date and includes papers that have been published as a direct result of the work carried out in this thesis.

2.5.1 Thermal Intermixing

Thermal disordering occurs in the InGaAsP system at much lower temperatures than in the GaAs/AlGaAs system, Glew et al¹¹⁴ reported thermal disordering at temperatures as low as 550°C as reported in this thesis. This is important in the processing of devices since disordering occurs at the growth temperature (650°C) making it very difficult to produce sharp interfaces, especially for buried heterostructure and DFB structures which require a regrowth stage: for quantum well lasers this results in detuning of the operating wavelength.

Advantage can be taken of the poor thermal stability, however, as was demonstrated by McLean et al¹¹⁵ who used a laser to selectively disorder an InGaAs/InGaAsP QW structure by 132 meV using a CW Nd:YAG laser operating at 1064 nm to heat the sample. Devices are now being fabricated using this process with encouraging results.

2.5.2 IID

Little work has been carried out to date on impurity induced disordering; however, a few papers have been published. IID was first reported in InP/InGaAsP by Razeghi et al¹¹⁶ who studied thermal diffusion of Zn. This was reported to produce disordering on the group III sublattice only, which leads to a lattice mismatch of the resulting alloy. S diffusion was used by Pape et al¹¹⁷ who concluded that partial intermixing was occurring on both the group III and group V sublattices, and this was also observed using Si diffusion by Schwarz et al¹¹⁸. The advantage of inter-diffusion on both lattice sites is that it may be possible to disorder the QWs and leave the structure unstrained. Strain in QW structures has the effect of changing the bandgap and refractive index which may or may not be useful depending on the effects that are being sought. Many devices being investigated at the current time have strain built into them as part of the design.

This thesis is principally concerned with intermixing of the InGaAsP/InGaAs system using the neutral impurity F. Intermixing has been observed and results published, the reader is referred to Chapter 3 of this thesis for further information

2.5.3 Dielectric Cap Disordering

Dielectric cap disordering has also been investigated as part this thesis, and small shifts have been observed with Si₃N₄ caps. This is reported in more detail in Chapter 4 of this thesis.

2.5.4 Summary

Impurity/ Dielectric	Incorporation Technique	Colour of Energy Shift	Anneal Temp.	Diffusion Species	Doping	Ref.
Zn	Diffusion	Blue	750°C	Group III	n-type	116
S	Diffusion	Blue	700°C	Group III Group V	n-type	117
F	Implantation	Blue	550°C +	Group III Group V	Neutral	Chapter 3
B	Implantation	Red	550°C +	Group III Group V	Neutral	Chapter 3
Si ₃ N ₄	Plasma	Blue	750°C	Group III Group V	Impurity free	Chapter 4

Table 2.4 Summary of intermixing processes covered in the InGaAsP & InGaAlAs systems lattices matched to InP.

2.6 The Disordering Mechanism

The following section contains a review of a disordering mechanism that has been proposed for the AlGaAs/GaAs material system. The disordering process is not fully understood, and is further complicated in the InGaAsP/InGaAs/InP system by the addition of an extra element. Never the less, a similar type of behaviour is expected in both III-V systems and so it is of interest to review the AlGaAs/GaAs system here.

The model put forward here was developed by Deppe et al¹¹⁹.

In III–V crystals the self–diffusion of Column III lattice atoms must proceed through native point defects. These point defects occur on both lattice sites as well as interstitially, the concentration of these will have an effect on the inter-diffusion rate so by analysing the equilibrium equations involving the creation of these defects it is possible to get a feel of the conditions required for an increased self–diffusion rate.

The model reviewed here takes into account the effects of both the crystal surface condition during annealing (any over–pressure) and the crystal Fermi level. Native defects are considered as being neutral or only singly ionised.

Experimentally it has been observed that in the GaAs–AlGaAs system the inter-diffusion rate is increased during annealing if there is a large As₄ over–pressure, but it also increases for a small As₄ over–pressure i.e. there is an As₄ over–pressure at which inter-diffusion is at a minimum. This effect can be explained by self–diffusion of Column III lattice atoms being strongly dependent on native defects; for a high As₄ vapour pressure there is a large excess of As₄ at the crystal surface, so the stoichiometry of the crystal shifts towards As rich conditions. The **As–rich** point defects are,

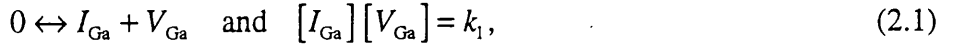
- As interstitial (As_I)–As atoms in the crystal not on a lattice site
- As antisite defects (As_{III})–As atoms on Column III lattice site
- Column III vacancies (V_{III})–missing Al or Ga atoms.

As the As₄ vapour pressure falls below that at which the inter-diffusion rate is minimum we have As–poor defects controlling the intermixing rate. The **As–poor** defects are,

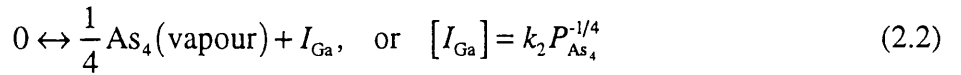
- Al or Ga Interstitials (Al_I or Ga_I)
- Al or Ga antisite defects (Al_{III} or Ga_{III})
- Column V vacancies (V_V).

The Column III self–diffusion is considered as being due to the Column III vacancies in As–rich conditions and Column III interstitials for As–poor conditions.

In the GaAs crystal Frenkel defects can occur on the Column III sublattice, i.e. a closely associated vacancy and interstitial, the equilibrium equation for the creation of these defects in the crystal is

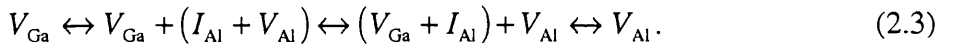


where k_1 is a constant that depends on temperature. Since the III–V semiconductors have a relatively large lattice structure the Ga interstitial is expected to have a high diffusion coefficient. In an As₄ rich environment Ga atoms reaching the surface will combine readily with free As causing an overall reduction in the Ga vacancies; from Equation 2.1 the Ga vacancy concentration will therefore increase. In other words, under As₄ rich conditions the surface acts as a sink for Ga interstitials. Under As poor conditions As will evaporate from the surface leaving a Ga–rich surface. The Ga atoms will then be free to diffuse into the crystal causing an increase in the Ga interstitial defect concentration. This can be expressed as,

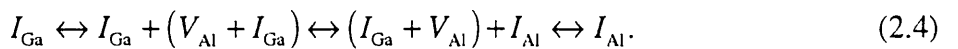


where $P_{\text{As}_4}^{-1/4}$ is the As₄ vapour pressure in the ampoule.

As mentioned above, Column III and Column V interstitials can lead to AlGa interdiffusion. Vacancy diffusion at a GaAs–AlAs interface can be represented by,



Equation 2.3 shows that a Ga vacancy interacts with an Al Frenkel pair at the interface to produce a Ga–Al Frenkel pair and an Al vacancy, a free Ga vacancy is replaced by a free Al vacancy which is now free to diffuse. A similar mechanism involving Frenkel pairs can also be used for the diffusion of Column III interstitials,



If a Ga interstitial either encounters or creates a Frenkel pair it can exchange places with the interstitial in the original Frenkel pair releasing, in this case, an Al interstitial which is

then free to diffuse, the rate of this diffusion being far greater than that of the vacancy created in Equation 2.3. Adding the effects of Column III vacancies and interstitials the following relationship is obtained,

$$D_{\text{III}} = f_1 D_{V_{\text{III}}} [V_{\text{III}}] + f_2 D_{I_{\text{III}}} [I_{\text{III}}] \quad (2.5)$$

substituting Equations 2.1 and 2.2, Equation 2.5 becomes,

$$D_{\text{III}} = f_1' D_{V_{\text{III}}} P_{\text{As}_4}^{1/4} + f_2' D_{I_{\text{III}}} P_{\text{As}_4}^{-1/4}. \quad (2.6)$$

This shows clearly that the Column III diffusion coefficient will be large for large As₄ over-pressure and for very small As₄ over-pressure, thus explaining the effects seen when varying GaAs-AlGaAs structures in practice. So far however the role of the crystal Fermi level has not been mentioned. If we now consider a GaAs crystal containing a fixed concentration of donor impurities we can model the effect of doping on the inter-diffusion rate. The defects present in the crystal can either act as donors or acceptor; in the GaAs/AlGaAs system the Column III vacancy and Column III antisite defects behave as acceptors, the other defects behaving as donors. The following analyses the effect of the Column III vacancy since this is what is most likely to play the major role in Column III self-diffusion.

For GaAs annealed in an As-rich atmosphere, the Gibb's free energy change on the creation of neutral Column III vacancies can be expressed as,

$$F(\text{crystal}) = F_o + N_v^x \Delta U_p - k_B T \ln \left[\frac{N_l!}{(N_l - N_v^x)! N_v^x!} \right] \quad (2.7)$$

where N_v^x is the number of neutral Column III vacancies in the crystal, N_l is the number of lattice sites, T is the anneal temperature, ΔU_p is the energy increase of the crystal upon creation of a vacancy, k_B is Boltzman's constant, and F_o is the part of the crystal free energy independent of the neutral impurities. If As₄ is taken as an ideal gas and the system is confined to an ampoule then the free energy of the gas is

$$F(\text{vapour}) = \frac{N_{\text{As}}}{4} k_B T \left\{ \ln \left[\frac{N_{\text{As}}}{4V} \cdot \left(\frac{2\pi \hbar^2}{Mk_B T} \right)^{3/2} \right] - 1 \right\}, \quad (2.8)$$

N_{As} is the number of As atoms in the vapour, V is the volume of the ampoule, \hbar is Planck's constant (divided by 2π), and M is the mass of the As_4 molecule. On the assumption that when one Column III vacancy is created an As atom is removed from the vapour, then when we minimise the total energy of the system (Equation 2.7 plus Equation 2.8) with respect to the Column III vacancies then we get,

$$[V_{\text{III}}^x] \approx C P_{\text{As}_4}^{1/4} (2 \times 10^{22}) \exp\left(\frac{-\Delta U_v}{k_B T}\right) \text{cm}^{-3}, \quad (2.9)$$

where C is a constant depending on temperature. Equation 2.9 gives the equilibrium concentration of neutral Column III vacancies. By taking into account the energy released by the crystal when the Column III vacancy, acting as an acceptor, becomes charged and minimising the crystal energy again with respect to the equilibrium concentration of ionised vacancies we get,

$$\begin{aligned} [V_{\text{III}}^-] &\approx C_1 P_{\text{As}_4}^{1/4} \exp\left\{ \frac{-[\Delta U_v - (E_F - E_A)]}{k_B T} \right\} \\ &= [V_{\text{III}}^x] \exp\left\{ \frac{E_F - E_A}{k_B T} \right\}, \end{aligned} \quad (2.10)$$

where E_F is the Fermi-level and E_A the acceptor energy level. Equation 2.10 shows that as the crystal Fermi level increases in the n -type structure, so the concentration of the singly charged acceptor like vacancies increases. A similar expression is obtained for the concentration of donor like defects in a p -type crystal. From Equation 2.6 we now get

$$\begin{aligned} D_{\text{III}} &= f_1'' P_{\text{As}_4}^{1/4} \left\{ D_{V_{\text{III}}^+} + D_{V_{\text{III}}^-} \exp\left[\frac{(E_F - E_A)}{k_B T} \right] \right\} \\ &+ f_2'' P_{\text{As}_4}^{-1/4} \left\{ D_{I_{\text{III}}^+} + D_{I_{\text{III}}^-} \exp\left[\frac{(E_D - E_A)}{k_B T} \right] \right\}, \end{aligned} \quad (2.11)$$

where E_D the energy level of the donor type interstitial. This relationship shows that the Column III self-diffusion will increase when the crystal is strongly n -type and annealed under As-rich conditions, or the crystal is strongly p -type and annealed under As-poor conditions.

It has been demonstrated that the vacancy concentrations are determined by the Fermi level in the crystal and the group V over-pressure.

2.7 Conclusions

Intermixing has been observed in many III-V semiconductor heterostructures. To date the main areas of research have been directed towards the effects of charged impurities such as Zn and Si; these impurities, because of their charged states will lead to free-carrier absorption in resulting optical waveguides. It is thought that the increase in the crystal's Fermi level, as a result of the charged impurity, leads to an increase in the intermixing process.

Impurity-free disordering has been observed in most of the material systems studied. Here the dielectric can act as a source of defects, and therefore increases the intermixing rate of the structure with the advantage of having no added impurities in the hetero-interface regions. Temperatures required for impurity free disordering do tend to be high however; this can cause problems with the InP based systems where the thermal stability of the hetro-interface is low.

Neutral impurity induced disordering promises to provide an alternative to the above two processes since relatively low temperatures can be used, and there will be no added losses in resulting waveguides due to free charges.

Finally, the actual intermixing process is very complicated and is very difficult to model, this is due the number of factors that are involved in the processes. The factors will include: temperature, impurity distribution, impurity mobility, defect density (interstitial as

well as vacancy), substrate defect concentration, capping layer effects, position of hetero-interface with respect to the surface, and strain (this list is not exhaustive).

References

¹'Disorder of an AlAs-GaAs Superlattice by Impurity Diffusion', W.D. Laidig, N. Holonyak Jr., M.D. Camras, K. Hess, J.J. Coleman, P.D. Dapkus, and J. Bardee, Appl. Phys. Lett. **38** (10), pp. 776-778, 1981.

²'Disorder of an AlAs-GaAs Superlattice by Impurity Diffusion', W.D. Laidig, N. Holonyak Jr., M.D. Camras, K. Hess, J.J. Coleman, P.D. Dapkus, and J. Bardee, Appl. Phys. Lett. **38** (10), pp. 776-778, 1981.

³'Zn Diffusion and Disorder of an AlAs-GaAs Superlattice along its Layers', S.W. Kirchoefer, N. Holonyak Jr., J.J. Coleman, and P.D. Dapkus, J. Appl. Phys. **53** (1), pp. 766-768, 1982.

⁴'Intermixing of an AlAs-GaAs Superlattice by Zn Diffusion', J.A. Van Vechten, J. Appl. Phys., **53** (10), pp 7082-7084, 1982.

⁵'Disorder of an AlAs-GaAs Super-Lattice By Silicon Implantation', J.J. Coleman, P.D. Dapkus, C.G. Kirkpatrick, M.D. Camras, N. Holonyak, Appl. Phys. Lett. **40** (10), pp. 904-906, 1982.

⁶'Interdiffusion Between GaAs and AlAs', L.L. Chang and A. Koma, Appl. Phys. Lett. **29** (3), pp. 138-141, 1976.

⁷'Role of Vacancies and Implantation Defects in GaAs/AlAs Superlattice Intermixing', S. Mitra and J.P. Stark, J. Mat. Sci. **26**, pp. 6650-6654, 1991.

⁸'Sulphur Diffusion in GaAs-AlAs Superlattices', N. Baba-Ali, I. Harrison, B. Tuck, H.P. Ho, and M. Henini, Opt. and Quant. Elect. **23**, S813-S821, 1991.

⁹'Aluminium Implantation-Induced Disorder of AlGaAs/GaAs Quantum Well Structures', I.V. Bradley, B.L. Weiss, and J.S. Roberts, Opt. and Quant. Elect. **23**, S823-S828, 1991.

¹⁰'Implantation Disorder of $\text{Al}_x\text{Ga}_{1-x}\text{As}$ Superlattices', P. Gavrilovic, D.G. Deppe, K. Meehan, N. Holonyak Jr., J.J. Coleman, R.D. Burnham, Appl. Phys. Lett. **47** (2), pp. 130-132, 1985.

¹¹'Impurity Induced Layer Disordering of Si Implanted $\text{Al}_x\text{Ga}_{1-x}\text{As}$ -GaAs Quantum-Well Heterostructures: Layer Disordering via Diffusion from Extrinsic Dislocation Loops', L.J. Guido, K.C. Hsieh, N. Holonyak Jr., R.W. Kaliski, V. Eu, M. Feng, and R.D. Burnham, *J. Appl. Phys.* **61** (4), pp. 1329-1334, 1987.

¹²'Si Diffusion in Compositional Disordering of Si-Implanted GaAs/AlGaAs Superlattices Induced by Rapid Thermal Annealing', M. Uematsu and F. Yanagawa, *Japan. J. of Appl. Phys.* **27** (9), pp. L1734-L1735, 1988.

¹³'Layer Intermixing in 1 MeV Implanted GaAs/AlGaAs Superlattices', S.T. Lee, S. Chen, G. Rajeswaran, G. Braunstein, P. Fellingner, and J. Madathil, *Appl. Phys. Lett.* **54** (12), pp. 1145-1147, 1988.

¹⁴'Si Impurity-Induced Layer Disordering of $\text{Al}_x\text{Ga}_{1-x}$ -GaAs Quantum-Well Heterostructures by As-Free Open-Tube Rapid Thermal Annealing', J.S. Major, F.A. Kish, T.A. Richard, A.R. Sugg, J.E. Baker, and N. Holonyak Jr., pp. 6199-6206, 1990.

¹⁵'Impurity Induced Layer Disordering of Si Implanted $\text{Al}_x\text{Ga}_{1-x}\text{As}$ -GaAs Quantum-Well Heterostructures: Layer Disordering via Diffusion from Extrinsic Dislocation Loops', L.J. Guido, K.C. Hsieh, N. Holonyak Jr., R.W. Kaliski, V. Eu, M. Feng, and R.D. Burnham, *J. Appl. Phys.* **61** (4), pp. 1329-1334, 1987.

¹⁶'Layer Intermixing in 1 MeV Implanted GaAs/AlGaAs Superlattices', S.T. Lee, S. Chen, G. Rajeswaran, G. Braunstein, P. Fellingner, and J. Madathil, *Appl. Phys. Lett.* **54** (12), pp. 1145-1147, 1988.

¹⁷'A Novel GRIN-SCH-SQW Laser Diode Monolithically Integrated with Low Loss Passive Waveguides', T. Hirata, M. Maeda, and H. Hosomatsu, *Japan. J. Appl. Phys.* **28** (8), pp. L1429-1432, 1989.

¹⁸'Integrated External Cavity GaAs/AlGaAs Lasers Using Selective Quantum Well Disordering', J. Werner, E. Kapon, N.G. Stoffel, E. Colas, S.A. Schwarz, C.L. Schwarz, and N. Andreadakis, *Appl. Phys. Lett.* **55** (6), pp. 540-542, 1989.

¹⁹'Birefringent Channel Waveguides Defined by Impurity-Induced Superlattice Disordering', E. Kapon, N.G. Stoffel, E.A. Dobisz, and R. Bhat, *Appl. Phys. Lett.* **52** (5), pp. 351-353, 1988.

²⁰'GaAs/AlGaAs GRIN-SCH-SQW DBR Laser Diodes with Passive Waveguide Integrated by Compositional Disordering of the Quantum Well Using Ion Implantation', T. Hirata, M. Maeda, M. Suehiro, and H. Hosomatsu, Japan. J. Appl. Phys. **29** (6), pp. L961-L963, 1990.

²¹'Photonic Integrated Circuit Combining Two GaAs Distributed Bragg Reflector Laser Diodes for Generation of the Beat Signal', M. Maeda, T. Hirata, M. Suehiro, M. Hihara, A. Yamaguchi, and H. Hosomatsu, Jpn. J. Appl. Phys. Vol. 31 (1992) pp. L 183-L 185, Part 2, No. 2B, 1992.

²²'Si-Implanted and Disordered Stripe-Geometry Al_xGa_{1-x}As-GaAs Quantum Well Lasers', P. Gavrilovic, K. Meehan, L.J. Guido, N. Holonyak, V. Eu, M. Feng, Burnham, Appl. Phys. Lett. **47** (9), pp. 903-905, 1985.

²³'Disorder of an Al_xGa_{1-x}As-GaAs Superlattice by Donor Diffusion', K. Meehan, N. Holonyak Jr., J.M. Brown, M.A. Nixon, P. Gavrilovic, R.D. Burnham, Appl. Phys. Lett. **45** (5), pp. 549-551, 1984.

²⁴'Effect of Surface Encapsulation and As₄ Overpressure on Si Diffusion and Impurity-Induced Layer Disordering in GaAs, Al_xGa_{1-x}As, and Al_xGa_{1-x}As-GaAs Quantum Well Heterostructures', L.J. Guido, W.E. Plano, D.W. Nam, N. Holonyak Jr., J.E. Baker, R.D. Burnham, P. Gavrilovic, J. of Elect. Mat. **17** (1), pp. 53-56, 1988.

²⁵'Comparison of Si^{III}-Si^V and Si^{III}-V^{III} Diffusion-Models in III-V Heterostructures Lattice Matched to GaAs, D.G. Deppe, W.E. Plano, J.E. Baker, N. Holonyak Jr., M.J. Ludowise, C.P. Kuo, R.M. Fletcher, T.D. Osentowski, M.G. Craford, Appl. Phys. Lett. **53** (22), pp. 2211-2213, 1988.

²⁶'Si Impurity-Induced Layer Disordering of Al_xGa_{1-x}-GaAs Quantum-Well Heterostructures by As-Free Open-Tube Rapid Thermal Annealing', J.S. Major, F.A. Kish, T.A. Richard, A.R. Sugg, J.E. Baker, and N. Holonyak Jr., pp. 6199-6206, 1990.

²⁷'Highly Efficient, Long Lived AlGaAs Lasers Fabricated by Silicon Impurity Induced Disordering', R.L. Thornton, R.D. Burnham, T.L. Paoli, N. Holonyak Jr., D.G. Deppe, Appl. Phys. Lett. **49** (3), pp. 133-134, 1986.

- 28[']Low Threshold Planar Buried Heterostructure Lasers Fabricated by Impurity-Induced Disorder R.L. Thornton, R.D. Burnham, T.L. Paoli, N. Holonyak Jr., D.G. Deppe, *Appl. Phys. Lett.* **47** (12), pp. 1239-1241, 1985.
- 29[']Monolithic Waveguide Coupled Cavity Lasers and Modulators Fabricated by Impurity Induced Disorder', R.L. Thornton, W.J. Mosby, T.L. Paoli, *J. Lightwave Technol.* **6** (6), pp. 786-792, 1988.
- 30[']Low-Threshold Disorder Defined Buried-Heterostructure $\text{Al}_x\text{Ga}_{1-x}\text{As-GaAs}$ Quantum Well Lasers', D.G. Deppe, K.C. Hsieh, N. Holonyak Jr., R.D. Burnham, and R.L. Thornton, *J. Appl. Phys.* **58** (12), pp. 4515-4520, 1985.
- 31[']Donor-Induced Disorder-Defined Buried-Heterostructure $\text{Al}_x\text{Ga}_{1-x}\text{As-GaAs}$ Quantum-Well Lasers', K. Meehan, P. Gavrilovic, J.E. Epler, K.C. Hsieh, N. Holonyak Jr., R.D. Burnham, R.L. Thornton, and W. Streifer, *J. Appl. Phys.* **57** (12), pp. 5345-5348, 1985.
- 32[']Impurity-Induced Layer-Disordered Buried Heterostructure $\text{Al}_x\text{Ga}_{1-x}\text{As-GaAs}$ Quantum Well Edge-Injection Laser Array', D.G. Deppe, G.S. Jackson, N. Holonyak Jr., D.C. Hall, R.D. Burnham, R.L. Thornton, J.E. Epler, T.L. Paoli, *Appl. Phys. Lett.* **50** (7), pp. 392-394, 1987.
- 33[']Coupled Stripe $\text{Al}_x\text{Ga}_{1-x}\text{As-GaAs}$ Quantum Well Lasers Defined by Impurity-Induced (Si) Layer Disorder', D.G. Deppe, G.S. Jackson, N. Holonyak Jr., R.D. Burnham, R.L. Thornton, *Appl. Phys. Lett.* **50** (11), pp. 632-634, 1987.
- 34[']Low-Threshold Disorder-Defined Buried-Heterostructure $\text{Al}_x\text{Ga}_{1-x}\text{As-GaAs}$ Quantum-Well Lasers By Open-Tube Rapid Thermal Annealing', T.A. Richard, J.S. Major, F.A. Kish, N. Holonyak Jr., S.C. Smith, R.D. Burnham, *Appl. Phys. Lett.* **57** (27), pp. 2904-2906, 1990.
- 35[']Laterally Injected Low-Threshold Lasers by Impurity-Induced Disorder', W.X. Zou, K.-K. Law, J.L. Merz, R.J. Fu, and C.S. Hong, *Appl. Phys. Lett.* **59** (26), pp. 3375-3377, 1991.
- 36[']Impurity Diffusion and Layer Interdiffusion in $\text{Al}_x\text{Ga}_{1-x}\text{As-GaAs}$ Heterostructures', D.G. Deppe, N. Holonyak Jr., W.E. Plano, V.M. Robbins, J.M. Dallesasse, K.C. Hsieh, and J.E. Baker, *J. Appl. Phys.*, **64** (4), pp. 1838-1844, 1988.

- ³⁷'Dopant Induced Disorder of Annealed AlGaAs Heterostructures', C.L. Reynolds Jr., and M. Geva, *Appl. Phys. Lett.* **61** (2), pp 165-167, 1992.
- ³⁸'Impurity Diffusion and Layer Interdiffusion in Al_xGa_{1-x}As-GaAs Heterostructures', D.G. Deppe, N. Holonyak Jr., W.E. Plano, V.M. Robbins, J.M. Dallesasse, K.C. Hsieh, and J.E. Baker, *J. Appl. Phys.*, **64** (4), pp 1838-1844, 1988.
- ³⁹'Index-Guided Al_xGa_{1-x}As-GaAs Quantum Well Heterostructure Lasers Fabricated by Vacancy-Enhanced Impurity-Induced Layer Disorder From an Internal (Si₂)_y(GaAs)_{1-y} Source', L.J. Guido, G.S. Jackson, W.E. Plano, K.C. Hsieh, N. Holonyak Jr., R.D. Burnham, J.E. Epler, R.L. Thornton, T.L. Paoli, *Appl. Phys. Lett.* **50** (10), pp. 609-611, 1987.
- ⁴⁰'Disorder-Defined Buried-Heterostructure Al_xGa_{1-x}As-GaAs Quantum Well Lasers by Diffusion of Silicon and Oxygen from Al-Reduced SiO₂', L.J. Guido, J.S. Major, J.E. Baker, N. Holonyak Jr., R.D. Burnham, *Appl. Phys. Lett.* **54** (13), pp. 1265-1267, 1989.
- ⁴¹'Layer Interdiffusion in Se-Doped Al_xGa_{1-x}As-GaAs Superlattices', D.G. Deppe, N. Holonyak Jr., K.C. Hsieh, P. Gavrilovic, W. Stutius, J. Williams, *Appl. Phys. Lett.* **51** (8), pp. 581-583, 1987.
- ⁴²'Layer Disorder of n-Type (Se) and p-Type (C) Al_xGa_{1-x}As-GaAs Superlattices By S-Diffusion', J.S. Major, J.M. Dallesasse, L.J. Guido, J.E. Baker, W.E. Plano, A.R. Sugg, E.J. Vesely, T.A. Richard, N. Holonyak Jr., *Appl. Phys. Lett.* **56** (18), pp. 1720-1722, 1990.
- ⁴³R.W. Kaliski, P. Gavriolvic, K. Meehan, J. Gavriolvic, K.C. Hsieh, G.S. Jackson, N. Holonyak, Jr., J.J. Coleman, R.D. Burnham, R.L. Thirnton, and T.L. Paoli, *J. Appl. Phys.* **58**, pp. 867, 1985.
- ⁴⁴E.V.K. Rao, P.Ossart, F. Alexandre, and H.Thibierge, *Appl. Phys. Lett.* **50**, pp. 588, 1987.
- ⁴⁵'Layer Disorder of n-Type (Se) and p-Type (C) Al_xGa_{1-x}As-GaAs Superlattices By S-Diffusion', J.S. Major, J.M. Dallesasse, L.J. Guido, J.E. Baker, W.E. Plano, A.R. Sugg, E.J. Vesely, T.A. Richard. N. Holonyak Jr., *Appl. Phys. Lett.* **56** (18), pp. 1720-1722, 1990.

- 46'Impurity-Induced Disorder of Single Well $\text{Al}_x\text{Ga}_{1-x}\text{As-GaAs}$ Quantum Well Heterostructures', K. Meehan, J.M. Brown, M.D. Camras, N. Holonyak, R.D. Burnham, T.L. Paoli, W. Streifer, *Appl. Phys. Lett.*, **44** (4), pp. 428-430, 1984.
- 47'Diffusion of Manganese in GaAs and its Effect on Layer Disorder in $\text{Al}_x\text{Ga}_{1-x}\text{As-GaAs}$ Superlattices', C.H. Wu, K.C. Hsieh, G.E. Hofler, N. Elzein, N. Holonyak Jr., *Appl. Phys. Lett.* **59** (10), pp. 1224-1226, 1991.
- 48'Thermal Annealing and Photoluminescence on $\text{Al}_x\text{Ga}_{1-x}\text{As-GaAs}$ Quantum-Well Heterostructures with Se and Mg Sheet Doping', R.W. Kaliski, D.W. Nam, D.G. Deppe, N. Holonyak Jr., K.C. Hsieh, and R.D. Burnham, *J. Appl. Phys.* **62** (3), pp. 998-1005, 1987.
- 49'Column-III Column-V Sublattice Interaction via Zn and Si Impurity-Induced Layer Disorder of ^{13}C -Doped $\text{Al}_x\text{Ga}_{1-x}\text{As GaAs}$ Superlattices', L.J. Guido, J.S. Major, J.E. Baker, N. Holonyak Jr., B.T. Cunningham, G.E. Stillman, *Appl. Phys. Lett.* **56** (6), pp. 572-574, 1990.
- 50'Diffusion of Manganese in GaAs and its Effect on Layer Disorder in $\text{Al}_x\text{Ga}_{1-x}\text{As-GaAs}$ Superlattices', C.H. Wu, K.C. Hsieh, G.E. Hofler, N. Elzein, N. Holonyak Jr., *Appl. Phys. Lett.* **59** (10), pp. 1224-1226, 1991.
- 51'Thermal Annealing and Photoluminescence on $\text{Al}_x\text{Ga}_{1-x}\text{As-GaAs}$ Quantum-Well Heterostructures with Se and Mg Sheet Doping', R.W. Kaliski, D.W. Nam, D.G. Deppe, N. Holonyak Jr., K.C. Hsieh, and R.D. Burnham, *J. Appl. Phys.* **62** (3), pp. 998-1005, 1987.
- 52'Column-III Column-V Sublattice Interaction via Zn and Si Impurity-Induced Layer Disorder of ^{13}C -Doped $\text{Al}_x\text{Ga}_{1-x}\text{As GaAs}$ Superlattices', L.J. Guido, J.S. Major, J.E. Baker, N. Holonyak Jr., B.T. Cunningham, G.E. Stillman, *Appl. Phys. Lett.* **56** (6), pp. 572-574, 1990.
- 53'Stripe-Geometry AlGaAs-GaAs Quantum-Well Heterostructure Lasers Defined by Impurity-Induced Layer Disorder', K. Meehan, J.M. Brown, N. Holonyak, R.D. Burnham, T.L. Paoli, W. Streifer, *Appl. Phys. Lett.*, **44** (7), pp. 700-702, 1984.

- 54'Lateral refractive Index Step in GaAs/AlGaAs Multiple Quantum Well Waveguides Fabricated by Impurity-Induced Disorder', T. Wolf, C.L. Shieh, R. Engelmann, K. Alavi, and J. Mantz, *Appl. Phys. Lett.* **55** (14), pp. 1412-1414, 1989.
- 55'Impurity-Induced Disorder-Delineated Optical Wave-Guides in GaAs-AlGaAs Superlattices', F. Julien, P.D. Swanson, M.A. Emanuel, D.G. Deppe, T.A. Detemple, J.J. Coleman, N. Holonyak, *Appl. Phys. Lett.* **50** (14), pp. 866-868, 1987.
- 56'Native-Oxide Masked Impurity-Induced Layer Disorder of $\text{Al}_x\text{Ga}_{1-x}\text{As}$ Quantum Well Heterostructures', J.M. Dallesasse, N. Holonyak Jr., N. El-Zein, T.A. Richard, F.A. Kish, A.R. Sugg, R.D. Burnham, and S.C. Smith, *Appl. Phys. Lett.* **58** (9), pp 974-976, 1991.
- 57'Multiple Quantum Well Optical Waveguides with Large Absorption Edge Blue Shift Produced by Boron and Fluorine Impurity-Induced Disorder', M. O'Neil, A.C. Bryce, J.H. Marsh, R.M. De La Rue, J.S. Roberts, and C. Jeynes, *Appl. Phys. Lett.* **55** (14), pp 1373-1375, 1989.
- 58'Reduction of the Propagation Losses in Impurity Induced Disordered Quantum Well Waveguides', M. O'Neil, J.H. Marsh, and R.M. De La Rue, *Electron. Lett.* Vol. 26, No. 19, pp 1613-1614, 1990.
- 59'Refractive Index Changes in a GaAs Multiple Quantum Well Structure Produced by Impurity-Induced Disorder Using Boron and Fluorine', S.I. Hansen, J.H. Marsh, J.S. Roberts, and R. Gwilliam, *Appl. Phys. Lett.* **58** (13), pp 1398-1400, 1991.
- 60'Characterization of Ga Out-Diffusion from GaAs into SiO_xN_y films during thermal annealing', M. Kuzuhara, T. Nozaki, T. Kamejima, *J. Appl. Phys.* **66** (12), pp. 5833-5836, 1989.
- 61'Column III Vacancy- and Impurity-Induced Layer Disorder of $\text{Al}_x\text{Ga}_{1-x}\text{As}$ -GaAs Heterostructures with SiO_2 and Si_3N_4 Diffusion Sources', L.J. Guido, J.S. Major Jr., J.E. Baker, W.E. Plano, N. Holonyak Jr., and K.C. Hsieh, *J. Appl. Phys.* **67** (11), pp 6813-6818, 1990.
- 62'Effects of Dielectric Encapsulation and As pressure on Al-Ga Interdiffusion in $\text{Al}_x\text{Ga}_{1-x}\text{As}$ -GaAs Quantum Well Heterostructures', L.J. Guido, N. Holonyak Jr., K.C. Hsieh,

W.E. Plano, R.D. Burnham, R.L. Thornton, J.E. Epler, and T.L. Paoli, *J. Appl. Phys.* **61** (4), pp. 1372-1379, 1987.

⁶³'Column III Vacancy- and Impurity-Induced Layer Disordering of $\text{Al}_x\text{Ga}_{1-x}\text{As}$ -GaAs Heterostructures with SiO_2 and Si_3N_4 Diffusion Sources', L.J. Guido, J.S. Major Jr., J.E. Baker, W.E. Plano, N. Holonyak

⁶⁴'Suppression of Bandgap Shifts in GaAs/AlGaAs Quantum Wells Using Strontium Fluoride Caps', J. Beauvais, J.H. Marsh, A.H. Kean, A.C. Bryce, and C. Button, *Electron. Lett.* **28** (17), pp. 1670-1672, 1992.

⁶⁵'TE/TM Mode Selective Channel Waveguides in GaAs/AlAs Superlattice Fabricated by SiO_2 Cap Disordering', Y. Suzuki, H. Iwamura, O. Mikami, *Appl. Phys. Lett.* **56** (1), pp. 19-20, 1990.

⁶⁶'Stripe-Geometry Quantum Well Heterostructure $\text{Al}_x\text{Ga}_{1-x}\text{As}$ -GaAs Lasers Defined by Defect Diffusion', D.G. Deppe, L.J. Guido, N. Holonyak Jr., K.C. Hsieh, R.D. Burnham, Thornton_rl, T.L. Paoli, *Appl. Phys. Lett.* **49** (9), pp. 510-512, 1986.

⁶⁷'Post Growth Fabrication of GaAs/AlGaAs Reflection Modulators via Impurity Free disordering', M. Ghisoni, G. Parry, M. Pate, G. Hill, and J. Roberts, *Jpn. J. Appl. Phys.* Vol. 30, No. 6A, pp. L 1018-L 1020, 1991.

⁶⁸'Impurity-Induced Layer Disordering of High Gap $\text{In}_y(\text{Al}_x\text{Ga}_{1-x})_{1-y}\text{P}$ Heterostructures', D.G. Deppe, D.W. Nam, N. Holonyak Jr., K.C. Hsieh, J.E. Baker, C.P. Kuo, R.M. Fletcher, T.D. Osentowski, and M.G. Craford, *Appl. Phys. Lett.* **52** (17), pp 1413-1415, 1988.

⁶⁹'Column III and V Ordering in InGaAsP and GaAsP Grown on GaAs by Metalorganic Chemical Vapor-Deposition', W.E. Plano, D.W. Nam, J.S. Major, K.C. Hsieh, N. Holonyak Jr., *Appl. Phys. Lett.* **53** (25), pp. 2537-2539, 1988.

⁷⁰'Compositional Disordering of Strained InGaAs/GaAs Quantum Wells by Au Implantation: Channeling Effects', T.E. Jackman, S. Charbonneau, L.B. Allard, R.L. Williams, I.M. Templeton, M. Buchanan, M. Vos, I.V. Mitchell, and J.A. Jackman, *Appl. Phys. Lett.* **59** (21), pp 2733-2735, 1991.

- 71'Ultralow Threshold Strained InGaAs-GaAs Quantum Well Lasers by Impurity Induced Disorder', W.X. Zou, J.L. Merz, R.J. Fu, and C.S. Hong, *Electron. Lett.*, Vol. 27, No. 14, pp1241-1243, 1991.
- 72'Thermal Interdiffusion in InGaAs/GaAs and GaAsSb Strained Quantum Wells as a Function of Doping Density', W.P. Gillin, B.J. Seally, and K.P. Homewood, *Optical and Quant. Electron.* **23**, pp. S975-S980, 1991.
- 73'High Performance $\text{Al}_y\text{Ga}_{1-y}\text{As}/\text{GaAs}/\text{In}_x\text{Ga}_{1-x}\text{As}$ Quantum Well Lasers Defined by Silicon-Oxygen Impurity-Induced Layer Disorder', J.S. Major, L.J. Guido, N. Holonyak Jr., K.C. Hsieh, E.J. Vesely, D.W. Nam, D.C. Hall, J.E. Baker, P. Gavrilovic, K. Meehan, W. Stutius, and J.E. Williams, *J. Elect. Mat.* Vol. 19, No. 1, 1990.
- 74'Enhancement of Compositional Disorder in Strained $\text{In}_x\text{Ga}_{1-x}\text{As}/\text{GaAs}$ Quantum Wells by Zn Diffusion', M.T. Furtado, E.A. Sato, and M.A. Sacilotti, *Superlattices and Microstructures*, **10** (2), pp. 225-230, 1991.
- 75'Thermal Interdiffusion in InGaAs/GaAs and GaAsSb Strained Quantum Wells as a Function of Doping Density', W.P. Gillin, B.J. Seally, and K.P. Homewood, *Optical and Quant. Electron.* **23**, pp. S975-S980, 1991.
- 76'Optical-Properties And Stokes Shifts In Lamp-Annealed InGaAs/GaAs Strained Layer Superlattice', G.P. Kothiyal, P. Bhattacharya, *J. Appl. Phys.*, **63** (8), pp. 2760-2764, 1988.
- 77'"Strained InGaAs/GaAs single quantum well lasers with saturable absorbers fabricated by quantum well intermixing', N. Yamanda and J.S. Harris, Jr., *Appl. Phys. Lett.* **60** (20), pp2463-2465, 1992.
- 78'Interdiffusion and Wavelength Modification in $\text{In}_{0.53}\text{Ga}_{0.47}\text{As}/\text{In}_{0.52}\text{Al}_{0.48}\text{As}$ Quantum Wells by Lamp Annealing', K.S. Seo, P.K. Bhattacharya, G.P. Kothiyal, and S. Hong, *Appl. Phys. Lett.* **49** (16), pp 966-968, 1986.
- 79'Indium Diffusion in the Chemical-Potential Gradient at an $\text{In}_{0.53}\text{Ga}_{0.47}\text{As}/\text{In}_{0.52}\text{Al}_{0.48}\text{As}$ Interface', R.J. Baird, T.J. Potter, G.P. Kothiyal, P.K. Bhattacharya, *Appl. Phys. Lett.* **52** (24), pp. 2055-2057, 1988.
- 80'Indium Diffusion in the Chemical-Potential Gradient at an $\text{In}_{0.53}\text{Ga}_{0.47}\text{As}/\text{In}_{0.52}\text{Al}_{0.48}\text{As}$ Interface', R.J. Baird, T.J. Potter, G.P. Kothiyal, P.K. Bhattacharya, *Appl. Phys. Lett.* **52** (24), pp. 2055-2057, 1988.

- 81'Disordering by Zn-Diffusion of InGaAs/InAlAs MQW Superlattice Structure Grown by MBE', Y. Kawamura, H. Asahi, A. Kohzen, and K. Wakita, *Electron. Lett.* Vol. 21, No. 6, pp 218-219, 1985.
- 82'Impurity-Induced Layer Disordering of In_{0.53}Ga_{0.47}As/In_{0.52}Al_{0.48}As Heterostructures', R.J. Baird, T.J. Potter, R. Lai, G.P. Kothiyal, and P.K. Bhattacharya, *Appl. Phys. Lett.* **53** (23), pp 2302-2304, 1988.
- 83'Impurity-Induced Layer Disordering of In_{0.53}Ga_{0.47}As/In_{0.52}Al_{0.48}As Heterostructures', R.J. Baird, T.J. Potter, R. Lai, G.P. Kothiyal, and P.K. Bhattacharya, *Appl. Phys. Lett.* **53** (23), pp 2302-2304, 1988.
- 84'Modification of Exciton Emission in InGaAs/AlInAs Quantum Wells by Rapid Thermal Annealing', J.Y. Chi, E.S. Koteles, and R.P. Holmstrom, *Appl. Phys. Lett.* **53** (22), pp 2185-2187, 1988.
- 85'Effects of Rapid Thermal Annealing and SiO₂ Encapsulation on GaInAs/AlInAs Heterostructures', S. O'Brian, J.R. Shealy, D.P. Bour, L. Elbaum, J.Y. Chi, *Appl. Phys. Lett.* **56** (14), pp 1365-1367, 1990.
- 86'Compositional Disordering of In_{0.53}Ga_{0.47}As/In_{0.52}Al_{0.48}As Multiple Well Structures by Repetitive Rapid Thermal Annealing', T. Miyazawa, Y. Suzuki, Y. Kawamura, H. Asai, and O. Mikami, *Japan. J. Appl. Phys.*, Vol. 28, No. 5, pp L1030-L1041, 1989.
- 87'Thermal Stability of InGaAs/InP Quantum well Structures Grown by Gas Source Molecular Beam Epitaxy', H. Temkin, S.N.G. Chu, M.B. Panish, and R.A. Logan, *Appl. Phys. Lett.* **50** (15), pp 956-958, 1987.
- 88'Intermixing Process of InGaAs/InP MQW Grown by Metalorganic Molecular Beam Epitaxy at Thermal Annealing', K. Nakashima, Y. Kawaguchi, Y. Kawamura, H. Asahi, and Y. Imamura, *J. Jour. Appl. Phys.*, Vol. 26, No. 10, pp L1620-L1622, 1987.
- 89'Macroscopic Mechanism of Group V Interdiffusion in Undoped InGaAs/InP Quantum Wells Grown by MOVPE', T. Fujii, M. Sugawara, S. Yamazaki, and K. Nakajima, *J. Crystal Growth* **105**, pp. 348-352, 1990.

- ⁹⁰'Raman Scattering Study of Thermal Interdiffusion in InGaAs/InP Superlattice Structures', S.J. Yu, H. Asahi, S. Emura, S. Gonda, and K. Nakashima, *J. Appl. Phys.*, **70** (1), pp 204-208, 1991.
- ⁹¹A.S. Barker, Jr., and G.L. Sievers, *Rev. Mod. Phys.* **47**, Suppl. No.1, p. S1, 1966.
- ⁹²'Dielectric Cap Disorder of InGaAs Quantum Well Structures on InP and GaAs', S.A. Bradshaw, A.C. Bryce, E. Tozowonah, J.H. Marsh, R. Bradley, R. Niclin, R.W. Glew, *IEEE/LEOS Proceedings Integrated Photonics Research*, New Orleans, April 1992.
- ⁹³'Diffusion-Induced Disorder of Ga_{0.47}In_{0.53}As/InP Multiple Quantum Wells with Zinc', L.J. Pape, P. Li Kam Wa, J.P.R. David, P.A. Claxton, and P.N. Robson, *Electron. Lett.* **24** (15), pp. 910-911, 1988.
- ⁹⁴'Zn-Diffusion-Induced Intermixing of InGaAs/InP Multiple Quantum Well Structures', K. Nakashima, Y. Kawaguchi, Y. Kawamura, Y. Imamura, and H. Asahi, *Appl. Phys. Lett.* **52** (17), pp. 1383-1385, 1988.
- ⁹⁵'InGaAs/InP Superlattice Mixing by Zn or Si Diffusion', S.A. Schwarz, P. Mei, T. Venkatesan, R. Bhat, D.M. Hwang, C.L. Schwartz, M. Koza, L. Nazar, and B.J. Skromme, *Appl. Phys. Lett.* **53** (12), pp. 1051-1053, 1988.
- ⁹⁶'Cation Diffusion in InP/In_{0.53}Ga_{0.47}As Superlattices: Strain Build-Up and Relaxation', D.M. Hwang, S.A. Schwarz, R. Bhat, C.Y. Chen, and T.S. Ravi, *Opt. and Quant. Elec.* **23**, S829-S846, 1991.
- ⁹⁷'Confinement and Strain Profiles Produced by Cation Interdiffusion in In_{0.53}Ga_{0.47}As/InP Quantum Wells', J. Micallef, E. Herbert. Li, and B. Weiss, *Appl. Phys. Lett.* **61** (4), pp. 435-437, 1992.
- ⁹⁸'Disordering of InGaAs-InP Quantum Wells by Si Implantation', B. Tell, J.L. Zyskind, J.M. Brown, J.W. Sulhoff, K.F. Brown-Goebeler, B.I. Miller, and U. Koren, *Appl. Phys. Lett.* **52** (17), pp 1428-1430, 1988.
- ⁹⁹'InGaAs/InP Superlattice Mixing by Zn or Si Diffusion', S.A. Schwarz, P. Mei, T. Venkatesan, R. Bhat, D.M. Hwang, C.L. Schwartz, M. Koza, L. Nazar, and B.J. Skromme, *Appl. Phys. Lett.* **53** (12), pp. 1051-1053, 1988.

- 100'Phosphorous Ion Implantation Induced Intermixing of InGaAs-InP Well Structures', B. Tell, J. Shah, P.M. Thomas, K.F. Brown-Goebeler, A. DiGiovanni, B.I. Miller, and U. Koren, *Appl. Phys. Lett.* **54** (16), pp 1570-1572, 1989.
- 101'Large Blueshifting of InGaAs/InP Quantum-Well Band Gaps by Ion Implantation', J.E. Zucker, B. Tell, K.L. Jones, M.D. Divino, K.F. Brown-Goebeler, C.H. Joyner, B.I. Miller, and M.G. Young, *Appl. Phys. Lett.* **60** (24). pp. 3036-3038, 1992.
- 102'Intermixing of InGaAs/InP Multiple Quantum Well Structures by Ga Implantation', H. Sumida, H. Asahi, S.J. Yu, K. Asami, and S. Gonda, *Appl. Phys. Lett.* **54** (6), pp 520-522, 1989.
- 103'Disordering of InGaAs/InP Superlattice and Fabrication of Quantum Wires by Focused Ga Ion Beam', S.J. Yu, H. Asahi, J. Takizawa, K. Asami, S. Emura, S. Gonda, H. Kubo, C. Hamaguchi, and Y. Hirayama, *J. Vac. Sci. Technol. B9* (5), pp 2683-2686, 1991.
- 104'Interdiffusion of InGaAs/InP Quantum Wells by Germanium Ion Implantation', M.A. Bradley, F.H. Julien, J.P. Gilles, Y. Gao, E.V.K. Rao, M. Razeghi, and F. Omnes, *Electron. Lett.* **26** (3), pp. 208-210, 1990.
- 105'Disorder of Ga_{0.47}In_{0.53}As/InP Multiple Quantum Well Layers by Sulphur Diffusion', *Elect. Lett.* **24** (19), L.J. Pape, P. Li Kam Wa, J.P.R. David, P.A. Claxton, P.N. Robson, pp. 1217-1218, 1988.
- 106S.J. Pearton, *Mater. Sci. Rep.* **4**, p. 313 (1990).
- 107'Simultaneous Disordering and Isolation Induced by Ion Mixing in InGaAs/InP Superlattice Structures', S.A. Pappert, W. Xia, B. Zhu, A.R. Clawson, Z.F. Guan, P.K.L. Yu, and S.S. Lau, *J. Appl. Phys.* **72** (4), pp 1306-1311.
- 108S. Chen, S-Tong Lee, G. Braunstein, K.Y. Ko, and T.Y. Tan, *J. Appl. Phys.* **70**, 25 (1991).
- 109'InGaAs/InP Superlattice Waveguides by elevated temperature Ion Mixing', W. Xia, S.C. Lin, S.A. Pappert, C.A. Hewett, M. Fernandes, T.T. Vu, P.K.L. Yu, and S.S. Lau, *Appl. Phys. Lett.* **55** (19), pp. 2020-2022, 1989.

- ¹¹⁰'Compositional Disordering of In_{0.53}Ga_{0.47}As/InP Multiquantum Well Structures by Repetitive Rapid Thermal Annealing', T. Miyazawa, H. Iwamura, O. Mikami, and M. Naganuma, *Japan. J. Appl. Phys.* **28** (6), pp. L1039-L1041, 1989.
- ¹¹¹'Integrated External-Cavity InGaAs/InP Lasers Using Cap-Annealing Disordering', T. Miyazawa, H. Iwamura, and M. Naganuma, *IEEE Photon. Technol. Lett.* **3** (5), pp. 421-423, 1991.
- ¹¹²'Refractive Index Change of GaInAs/InP Disordered Superlattice Waveguide', A. Wakatsuki, H. Iwamura, Y. Suzuki, T. Miyazawa, and O. Mikami, *IEEE Photon. Technol. Lett.* **3** (10), pp. 905-907, 1991.
- ¹¹³'Polarization Mode Selective Channel Waveguides in An InGaAs/InP Disordered Superlattice', Y. Suzuki, H. Iwamura, T. Miyazawa, and O. Mikami, *Appl. Phys. Lett.* **57** (26), pp. 2745-2747, 1990.
- ¹¹⁴'Thermal Instability of InGaAs/InGaAsP Quantum Wells', R.W. Glew, J.P. Stagg, A.T.R. Briggs, S.A. Bradshaw, and J.H. Marsh, *Proc, Third Int. Conf. InP and Related Materials, Cardiff 1991*.
- ¹¹⁵'Layer Selective Disordering by Photoabsorption-Induced Thermal Diffusion in InGaAs/InP Based Multiquantum Well structures', C.J. McLean, J.H. Marsh, R.M. DeLaRue, A.C. Bryce, B. Garret, R.W. Glew, *Electron. Lett.* Vol. 28, No. 12, pp.1117-1119, 1992.
- ¹¹⁶'Disorder of Ga_xIn_{1-x}As_yP_{1-y} / InP Quantum Wells by Zn Diffusion', M. Razeghi, O. Acher, and F. Launay, *Semicond. Sci. Technol.* Vol 12, No. 2, pp. 793-796, 1987.
- ¹¹⁷'Diffusion Induced Disordering of Ga_{0.43}In_{0.57}As MQWs with Zn', I.J. Pape, P. Li Kam Wa, J.P.R. David, P.A. Claxton, and P.N. Robson, *Electron. Lett.* Vol. 24, No. 15, pp.910-911, 1988.
- ¹¹⁸S.A. Schwarz, P. Mei, P. Mei, T. Venkatesan, R. Bhat, D.M. Hwang, C.L. Schwartz, M. Koza, L. Nazar, and B.J. Skromme

¹¹⁹'Atom diffusion and impurity induced layer disordering in quantum well III-V semiconductor heterostructures', D.G. Deppe, and N. Holonyak Jr., J. Appl. Phys., **64**, pp. R93-R113, 1988.

Chapter 3

Fluorine Impurity Induced Disorder

3.1 Introduction

The following Chapter discusses the process central to the work carried out in this thesis: Fluorine Impurity Induced Disorder (FIID). The technique described in this Chapter for controlling the bandgap of InGaAs/InGaAsP based multiple quantum well (MQW) structures is built on extensively in subsequent chapters to produce laser devices with special characteristics, and to produce waveguides suitable for low-loss photonic integration.

FIID is a technique whereby InGaAs/InGaAsP based QWs can be disordered selectively; areas containing the fluorine implant will disorder (intermix), leaving the surrounding, unimplanted regions unaltered. Fluorine is introduced into the sample through a mask by ion implantation and subsequently annealed. The implantation followed by anneal process is a relatively straight forward technique for the fabrication of photonic integrated circuits (PICs) and has the advantage that it can be carried out at low temperatures; alternative techniques for producing PICs often require the wafer to be processed at elevated temperatures causing thermal intermixing of unimplanted regions of the wafer.

This Chapter begins by describing the material structure used to investigate the disordering process, and briefly discusses the factors which influence the bandgap of QW structures to show how, by disordering them, an increase in bandgap is possible. Ion implantation is then introduced, and the relative advantages of this technique for incorporating fluorine into the well structure are discussed. Finally, photoluminescence is introduced as a technique for measuring the change in bandgap of the semiconductor devices.

Results are presented for various fluorine implant concentrations, and various post implant thermal treatments.

3.1.1 The Structure Investigated

Two basic structures have been used to investigate the effects of disordering. Figure 3.1 is a schematic of the typical structure, the main difference between the two types of structure used are with the upper cladding and contact regions.

The first set of wafers have an undoped upper cladding region which is approximately $1\ \mu\text{m}$ in depth, and does not have the upper InGaAs contact layer. This structure is used to investigate the disordering process initially since the thin upper cladding region means that low implant energies can be used for introducing the impurity and, since the dopant is not present the effects of F on the disordering process can be more clearly seen.

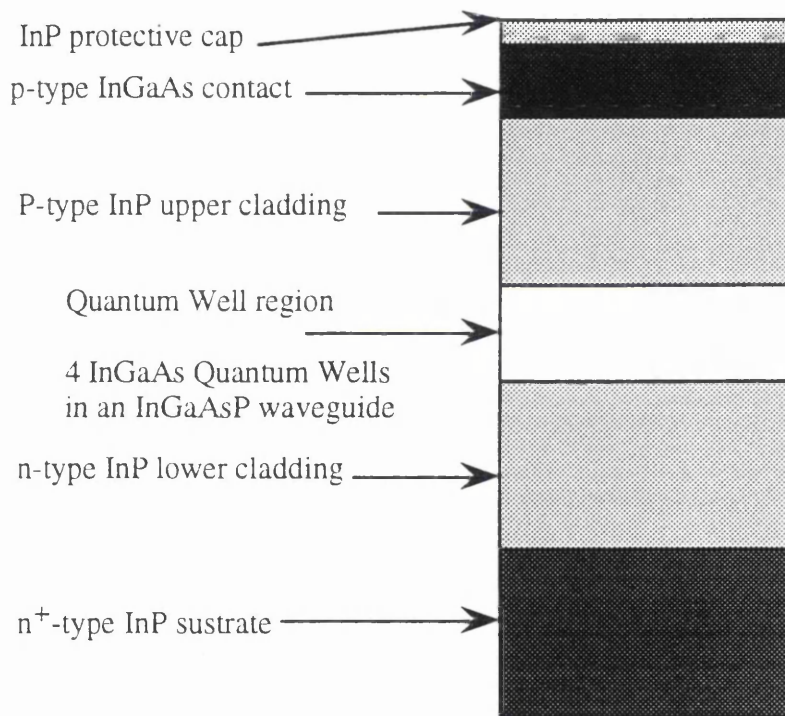


Figure 3.1. Typical waveguide structure used for F IID testing.

The second set of wafers used, more closely resemble the diagram in Figure 3.1, the upper cladding and contact layers are present, and it forms a laser structure¹. Extended cavity lasers using F IID are fabricated from these wafers in Chapter 7.

Both structures contain quantum wells consisting of approximately 100\AA of $\text{In}_{0.53}\text{Ga}_{0.47}\text{As}$ (lattice matched to InP) and 120\AA barriers of $\text{In}_{0.79}\text{Ga}_{0.21}\text{As}_{0.45}\text{P}_{0.55}$

(lattice matched to InP). Appendix A gives a detailed list of the wafers used in the following experiments.

3.1.2 Energy Levels in Quantum Well Structures

The wavelength at which a laser operates in a Multiple Quantum Well structures depends on several factors, the most important of these being the width of the individual quantum wells and the composition of the well and barrier.

Figure 3.2 shows two quantum well structures side by side. The energy level within the well (E_g) is modified from the bulk value of the well (E_0) due to the confinement imposed by the barrier material. The confinement causes quantisation of the electrons within the wells, this is easiest explained by means of the effective mass approximation². The basic assumption in the effective mass approximation is that any variations in the potential of the material band structure are slow compared to the unit cell size, with the exception of the underlying periodic potential of the unit cell. A further assumption is that the particle has an effective mass associated with it, which is dependent on the material that it is in, and is determined by the diffraction of the particle through the lattice.

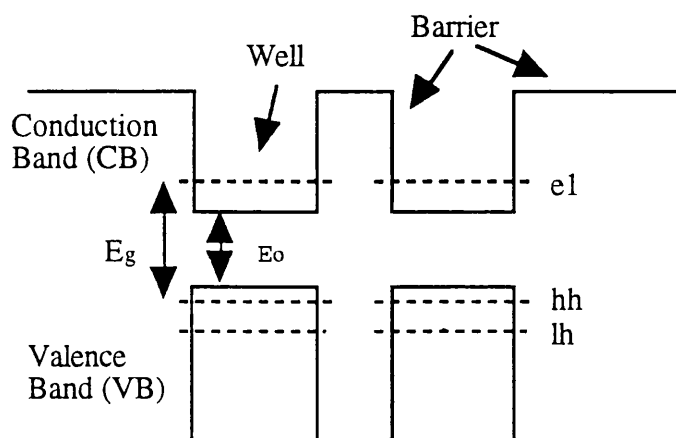


Figure 3.2. Energy levels in a QW that is not disordered.

In the plane of the layers making up the quantum well, the electrons and holes can move freely and their energies are governed by the same dispersion law as for the 3-dimensional

bulk crystal. The conduction and valence band energies, E_c and E_v respectively, are given by

$$E_c(k) = E_o + \frac{\hbar^2}{2m_e}(k_x^2 + k_y^2), \text{ and} \quad (3.1)$$

$$E_v(k) = -\frac{\hbar^2}{2m_h}(k_x^2 + k_y^2), \quad (3.2)$$

where E_o is the bandgap of the well material, m_e is the effective mass of the electron, and m_h is the effective mass of the holes, $k_{x,y}$ is the de Broglie wavenumbers in the x and y directions.

In the z -direction the Schrödinger waveequation is used to model an electron in a potential barrier. The one dimensional time independent Schrödinger equation is given by equation 3.3,

$$\frac{-\hbar^2}{2m} \frac{d^2u(z)}{dz^2} + V_o u(z) = Eu(z). \quad (3.3)$$

Using the boundary conditions that the wavefunction is continuous at the boundaries and the gradient of the wavefunction in the z -direction is also continuous, leads to a solution of the Schrödinger equation that is sinusoidal in the well and decays exponentially outside the well, giving a penetration depth of L_p into the barrier. The boundary conditions give rise to the quantisation of allowable energies, or states, of carriers within the well.

The energies of the confined states are found³ by the solution of equations 3.4 and 3.5,

$$\alpha \cot(\alpha a) = -\beta \quad (3.4)$$

and,

$$\alpha \tan(\alpha a) = \beta, \quad (3.5)$$

where

$$\alpha = \sqrt{\frac{2mE}{\hbar^2}}$$

$$\beta = \sqrt{\frac{2m(V_o - E)}{\hbar^2}}$$
(3.6)

The first two energy levels in the valence band of a QW structure are shown in Figure 3.2; these energy levels are denoted as the light and heavy holes, lh and hh respectively. The heavy and light holes are a consequence of the very complicated band structure observed in the valence band of III-V materials⁴. A simplification in the analysis of the bands is often made however. This simplification is that the band is only considered around the Γ -point since direct transitions occur at this point which is required for laser operation⁵; here the bands are considered parabolic.

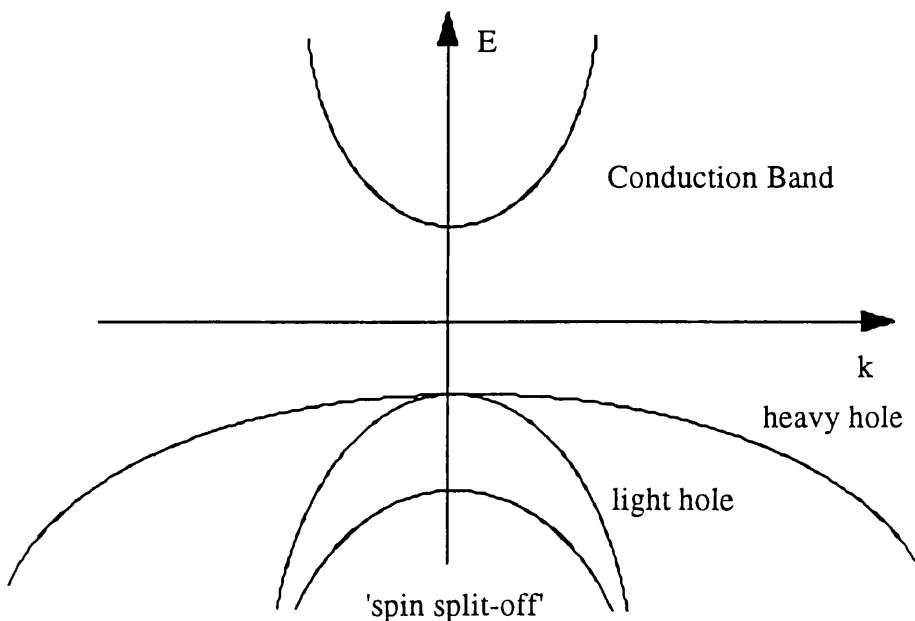


Figure 3.3. Band structure of a direct gap III-V semiconductor in the vicinity of the Γ point.

Figure 3.3 shows the first energy levels in the conduction and valence bands around the Γ -point. The valence band consists of three levels: the light and heavy holes (degenerate at $k=0$) and the spin split-off band⁶.

3.1.3 Excitons

An exciton is by definition⁷ a non-conducting excited electronic state in a perfect insulator, normally a non-magnetic insulator. The concept can be extended to include semiconductors, and in particular to the bound state of an electron and hole, which act as a composite particle.

Composite particles, or excitons, can be modelled in a similar way to the hydrogen atom; the exciton is assigned a specific radius corresponding to the binding energy of the electron-hole pair, known as the Bohr radius.

In bulk semiconductors the exciton is three dimensional and has a radius given by a_{3d} , as in Equation 3.7,

$$a_{3d} = \frac{\epsilon \hbar^2}{e^2 m^*} \quad (3.7)$$

where m^* is the reduced effective mass of the electron-hole state. The other symbols have their usual meanings. The binding energy E_n of the electron-hole state is expressed in terms of the Rydberg constant R_y as,

$$E_{3d} = -\frac{R_y}{n^2} \quad (3.8)$$

where

$$R_y = \frac{e^4 m^*}{2\epsilon^2 \hbar^2} \quad (3.9)$$

where n denotes the quantum level. Typical values of the Rydberg energy are between 4 and 5 meV, and a radius of around 150 Å.

In a quantum well system the exciton binding energy is greatly dependent on the well size. For well widths of the order of the exciton diameter, nearly three dimensional effects are expected; as the well width decreases, the exciton increasingly takes on a two dimensional nature. The binding energy in the two dimensional limit⁸ is given by,

$$E_n = -\frac{R_y}{\left(n - \frac{1}{2}\right)^2}. \quad (3.10)$$

From Equation 3.10 a binding energy of $4R_y$ is therefore expected for the $n=1$ level in the quantum well, a fourfold increase from the case of bulk semiconductor. A binding energy of 16 to 20 meV would therefore be expected for an exciton confined to two dimensions, at 273 K, kT (the thermal energy) is 23 meV and the exciton would be ionised; the electron and hole would not be coupled at room temperature.

In the quantum well situation there will be a non-negligible depth of the wavefunctions into the larger bandgap material, this penetration increases with decreasing well width. The effect of the wavefunction penetration is to create a maximum binding energy of the exciton, typically in the range $\frac{1}{2}a_{3d} \leq L_z < a_{3d}$.

The energy corresponding to the absorption line of the exciton is given by the energy of the conduction to valence band transition less the binding energy of the exciton.

As a consequence of p-orbitals, the hh-e1, and lh-e1 excitons are excited selectively by polarised light. The heavy and light holes can be expressed quantum mechanically as⁹,

$$\text{hh:} \left| \begin{matrix} 3 & 3 \\ 2 & 2 \end{matrix} \right\rangle = \sqrt{\frac{1}{2}} |x \uparrow\rangle + j\sqrt{\frac{1}{2}} |y \downarrow\rangle \quad (3.11)$$

$$\text{lh:} \left| \begin{matrix} 3 & 1 \\ 2 & 2 \end{matrix} \right\rangle = \sqrt{\frac{1}{6}} |x \downarrow\rangle + j\sqrt{\frac{1}{6}} |y \downarrow\rangle + \sqrt{\frac{2}{3}} |z \uparrow\rangle \quad (3.12)$$

If light is polarised along z then there will only be coupling via the light holes (Equation 3.12), since the expression for heavy holes (Equation 3.11) contains no terms in z . If the incident radiation is polarised in x , or y then both the heavy and light holes will be excited. In other words, TE radiation will excite both the hh-e1 and lh-e1 excitons, whereas TM radiation will only excite the lh-e1 excitons.

3.1.4 Effect of Well Composition on Energy

The phosphorous quaternary system is used extensively in long wavelength semiconductor devices, due to the range of bandgaps available when the material remains lattice matched to InP. Figure 3.4 shows how the bandgap of $\text{In}_{1-x}\text{Ga}_x\text{As}_y\text{P}_{1-y}$ varies with composition. The solid line on the surface of the curve represents the compositions of $\text{In}_{1-x}\text{Ga}_x\text{As}_y\text{P}_{1-y}$ that are lattice matched to InP. The relationship between the Ga(x), and As(y) components for the material to remain lattice matched follows the rule,

$$x = 0.47y \quad (3.13)$$

which is found by the quaternary interpolation scheme¹⁰.

The composition of the well layer determines the absolute minimum bandgap of the quantum well, the well's barrier composition determines the height of the potential barrier in the QW and will affect the confinement of the wavefunction. The higher the barrier of the QW, the more confined the wavefunction will become and ultimately the greater the bandgap of the structure.

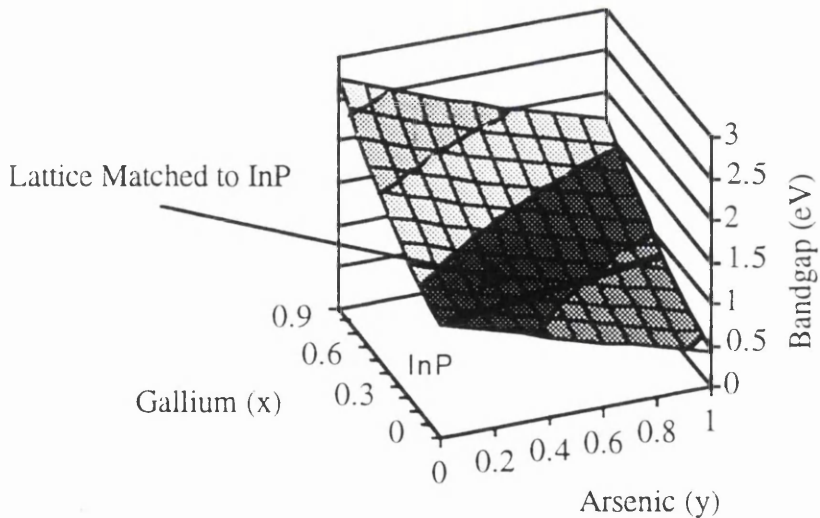


Figure 3.4. Bandgap of $\text{In}_{1-x}\text{Ga}_x\text{As}_y\text{P}_{1-y}$ versus the composition, as the Gallium (x) and Arsenic (y) proportions are varied.

3.1.5 Effect of Intermixing on Bandgap

Figure 3.5 shows two QWs that have intermixed, the as-grown wells are shown in Figure 3.2. The effect of intermixing on the bandgap of the QW is two fold;

1. The well shape flattens out which reduces the barrier height of the quantum well and allows the wavefunction to extend into the barrier material; the result of this is a drop in energy due to loss of confinement.
2. The composition of the well and barrier material will average out by the diffusion process. The effect of averaging is to increase the energy levels of the conduction and valence bands in the well region.

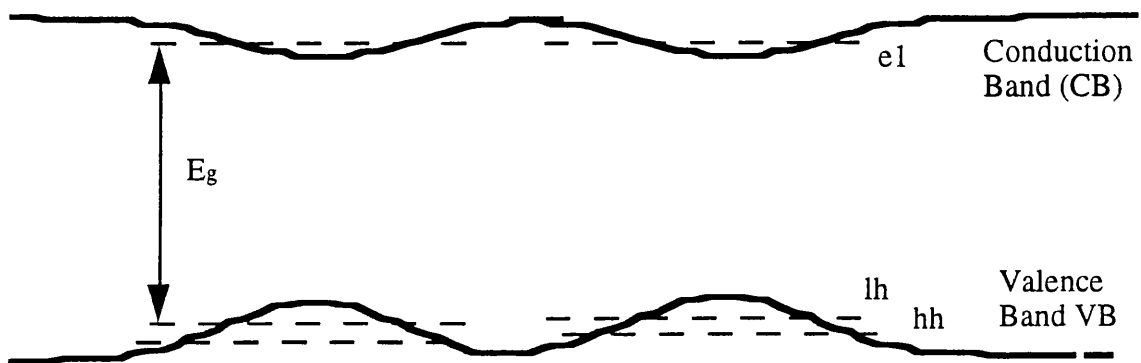
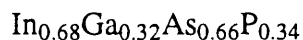


Figure 3.5 Bandgap increase due to intermixing of quantum wells.

After full intermixing the resultant material composition is expected to be



which has a bandgap of 976 meV (at 15 K). The as-grown bandgap of the QW system is 850 meV (at 15 K), so a maximum energy shift of 130 meV can be expected for a totally intermixed region.

It is interesting to note here that if group III atoms were to diffuse in preference to group V then the well material would have a reduced bandgap and strain would be introduced into the system¹¹, the well becoming compressively strained. Strain in III-V semiconductors

has become of greater interest due to the added possibilities of bandgap engineering. Some possible topics of interest to strained devices include; high mobility transistors, lasers, and devices with a negative differential resistance.

3.2 Ion Implantation - fluorine Incorporation Technique

Ion implantation is the technique chosen for introducing fluorine into the MQW structures used in this thesis. The following section outlines how and why this process was used.

3.2.1 Why Ion Implantation?

The reasons for choosing ion implantation as opposed to diffusion are,

1. Fluorine is a very volatile gas and would be difficult to diffuse into the wafer structures.
2. High concentration of the impurity ($\sim 10^{18} \text{ cm}^{-3}$) can be introduced into the MQW region with a relatively low dose of ions ($\sim 10^{14} \text{ cm}^{-2}$) when compared to the concentrations achievable with techniques such as impurity diffusion, where due to the flatter impurity profile a significantly greater dose would be required.
3. The concentration profile of ions incorporated via ion implantation is very narrow, with a vertical straggle at FWHM of typically 500 nm at a depth of 1,500 nm, it is therefore possible to produce a relatively high concentration of ions at a given depth below the surface of a structure with a negligible concentration of ions 500 nm from the surface. Defined areas of impurity can be easily produced. Techniques such as growing in an impurity would typically require regrowth and masking, an added complication in the already delicate growth process.
4. Techniques involving the diffusion of atoms into semiconductors require elevated temperatures. Usually these temperatures will be close to or above the temperature where the MQW will intermix thermally ($>550^\circ\text{C}$), this is especially important for the InGaAsP/InGaAs system because of its low thermal stability.

Ion implantation does however have several problems;

1. Implantation to a depth of 1.5 μm in InP requires energies of approximately 1.5 MeV. This has implications concerning the commercial viability of the process due to the required investment in a high energy ion accelerator.
2. Ion implantation damage is caused in a layer at around 90 % above the peak ion concentration, this however may prove advantageous for the disordering process because the creation of excess interstitial atoms and vacancies leading to an increase in the intermixing rate. The ion implantation damage complicates the process of modelling the diffusion process.

3.2.2 Why fluorine Impurity?

Fluorine was chosen as the impurity to use in the InP/InGaAsP system since initial results¹² showed that fluorine disordering produces blue shifts in the QW material when annealed in a conventional furnace at temperatures over 550°C. The work reported in this thesis builds on these initial results and finds the conditions necessary to reduce the thermal disordering in non-implanted regions.

Other impurities have shown similar effect in the InP/InGaAs QW system (Section 2.3), but many of these impurities do however have inherent problems. Disordering using the silicon and zinc impurities has been demonstrated¹³, but waveguide losses in excess of 71 dB cm⁻¹ are obtained. The high loss observed with the silicon and zinc impurity is expected since they are known to exist in an ionised state at room temperature leading to free carrier absorption.

Since fluorine is expected to exist in a non-ionised state at room temperature losses due to free-carrier absorption will be much smaller than with charged impurities. Propagation losses are measured in Chapters 6 & 8.

Some results are included for boron implantation, but a red shift is initially observed with this implant and it is therefore not suitable for the production of low loss waveguides, as a

red shift indicates a reduction in bandgap and therefore an increase in the absorption of light emitted from the as-grown material.

3.2.3 Implant Profiles (TRIM)

The implant conditions required to produce a given impurity concentration profile were calculated with a computer program called TRIM (TRansport of Ions in Matter). TRIM is a Monte-Carlo simulation which calculates the slowing down and scattering of energetic ions in amorphous targets. It has advantages over analytical techniques because it allows a more rigorous treatment of elastic scattering and an explicit treatment of surfaces and interfaces as well as allowing easy determination of energy and angular distributions. Analytic solutions can produce predictions much faster than the Monte-Carlo modelling, however the detail available with Monte-Carlo simulation is lost. The reader is referred to ref.¹⁴ for a detailed discussion on ion implantation and TRIM.

TRIM was designed for use with amorphous materials so there is a limitation to the accuracy of the predicted ranges in crystal structures such as those used here. The main reason for this is an effect called channelling. Channelling occurs in crystalline material due to the extremely ordered nature of the atoms within the crystal which create planes containing high densities of atoms. As a result of the ordering, ions entering the crystal in the same direction as a plane will experience only relatively weak electronic forces to slow them down. This channelling results in a deeper penetration of the implanted ion than that predicted by TRIM (an error of 10% being a generally accepted figure).

3.2.4. Calculation of Implant Concentration

The following example shows how an implant concentration is calculated using TRIM, for a given implant energy and dose.

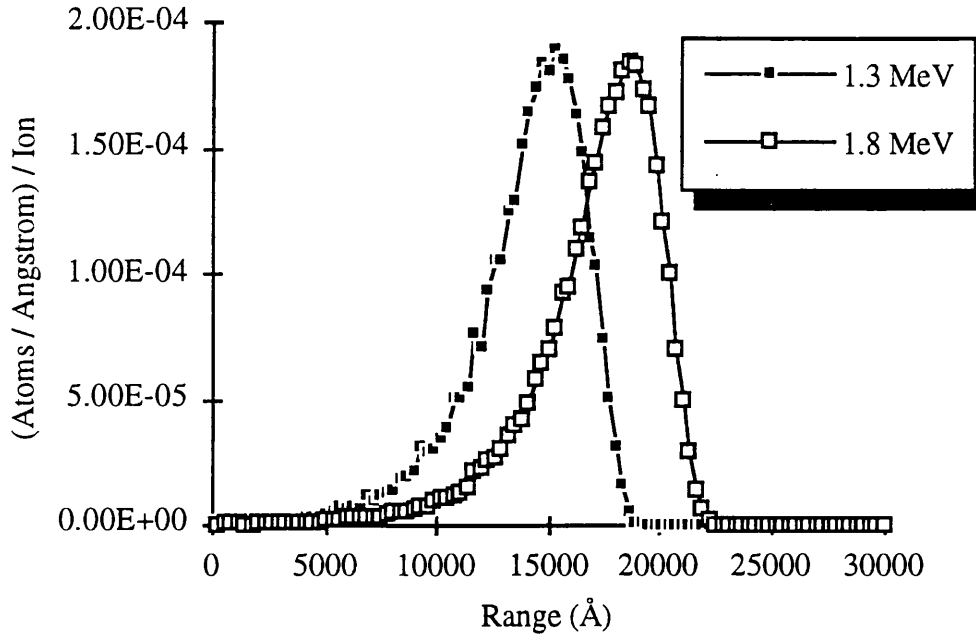


Figure 3.6. Predicted implant profiles for fluorine implanted into InP at 1.3 MeV and 1.8 MeV.

Figure 3.6 shows the distribution of fluorine atoms in InP (density 4.79 g cm^{-3}) at implant energies of 1.3 MeV and 1.8 MeV. The vertical axis represents the number of fluorine atoms found per Ångstrom per fluorine ion implanted into the InP, and multiplying this by the dose (atoms per unit area) gives the concentration at a particular depth. The range of fluorine into the wafer is simply defined as the position of the peak of one of the curves of Figure 3.6. The vertical straggle at the FWHM point can be seen to be 500 nm, for the profiles shown in Figure 3.6, at implant depths around $1.5 \text{ }\mu\text{m}$.

Due to the time taken to produce the curves in Figure 3.6 by the Monte Carlo technique and the inherent inaccuracy in the model used by TRIM, implantation conditions were calculated for pure InP and not for the exact laser structure. In this way a graph can be constructed of implant energy versus range, (Figure 3.7). Figure 3.7 was used to select the required implant energy to give a peak in the concentration profile at a particular depth.

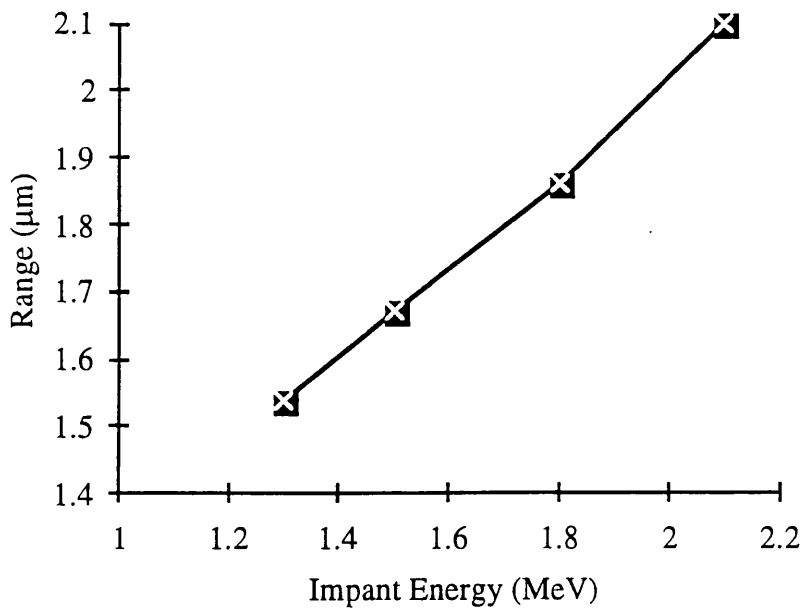


Figure 3.7. Range predicted using TRIM, as a function of the implant energy for fluorine in InP.

The actual implant doses and energies used will be given with each set of results in the following sections and chapters of this thesis.

3.3 Photoluminescence Measurements

Photoluminescence measurements provide a simple and quick method to monitor the bandgap of the materials. The basics of the technique are introduced here, and the experimental apparatus used to take the measurements is outlined.

3.3.1 Principles of Photoluminescence

Photoluminescence is the emission of optical radiation as a result of excitation of a sample by optical radiation. For an in-depth discussion on this topic the reader is referred to ref.¹⁵.

Incident optical radiation with an energy greater than the bandgap (E_g) will cause some electrons to jump from the valence to the conduction band forming hot carriers. These carriers relax by emitting phonons and then recombine to produce a photon of energy equal to one of the allowed states within the quantum well.

3.3.2 Experimental Technique

The majority of the photoluminescence measurements taken during this work were carried out at liquid nitrogen temperatures. The experiments were carried out at low temperature to reduce the thermal broadening of the photoluminescence peaks, and to therefore increase the accuracy of the technique. The equipment used is outlined in Figure 3.8. The sample under investigation is stuck onto the end of an optical fibre with a weak adhesive solution and placed into a polystyrene beaker containing enough liquid nitrogen to completely submerge the sample and the end of the fibre. The other end of the fibre is held in a device manipulator and the light from an Argon-Ion laser is coupled into the fibre at this point.

Photoluminescence emitted from the sample is coupled back into the fibre and extracted using a directional coupler. The luminescence from the sample is then passed through a monochromator which is controlled via an IEEE interface by a computer. At each step of the monochromator, the luminescence is measured by monitoring the signal produced by a cooled Ge detector, the detector being cooled to liquid nitrogen temperatures to improve its noise performance¹⁶. The computer is used to set the required scan, control a lock-in amplifier, step the monochromator, and record the results. A programme was written in LabVIEW to carry out the experiment, and to produce a user friendly interface.

A typical PL spectra, taken at 77K is shown in Figure 3.9. The spectra is for an arbitrary sample that has been annealed for between 10 and 40 seconds in the RTA. The PL spectra have been normalised so that the overlap between the spectra can be easily seen. The FWHM for the spectra are approximately 30 meV, and it remains relatively constant as the intermixing progresses. The FWHM is dependant on, amongst other factors, the interface roughness of the QWs. If the intermixing process is uniform across the wafer, and is not depth dependant we would expect that the FWHM remains constant during intermixing.

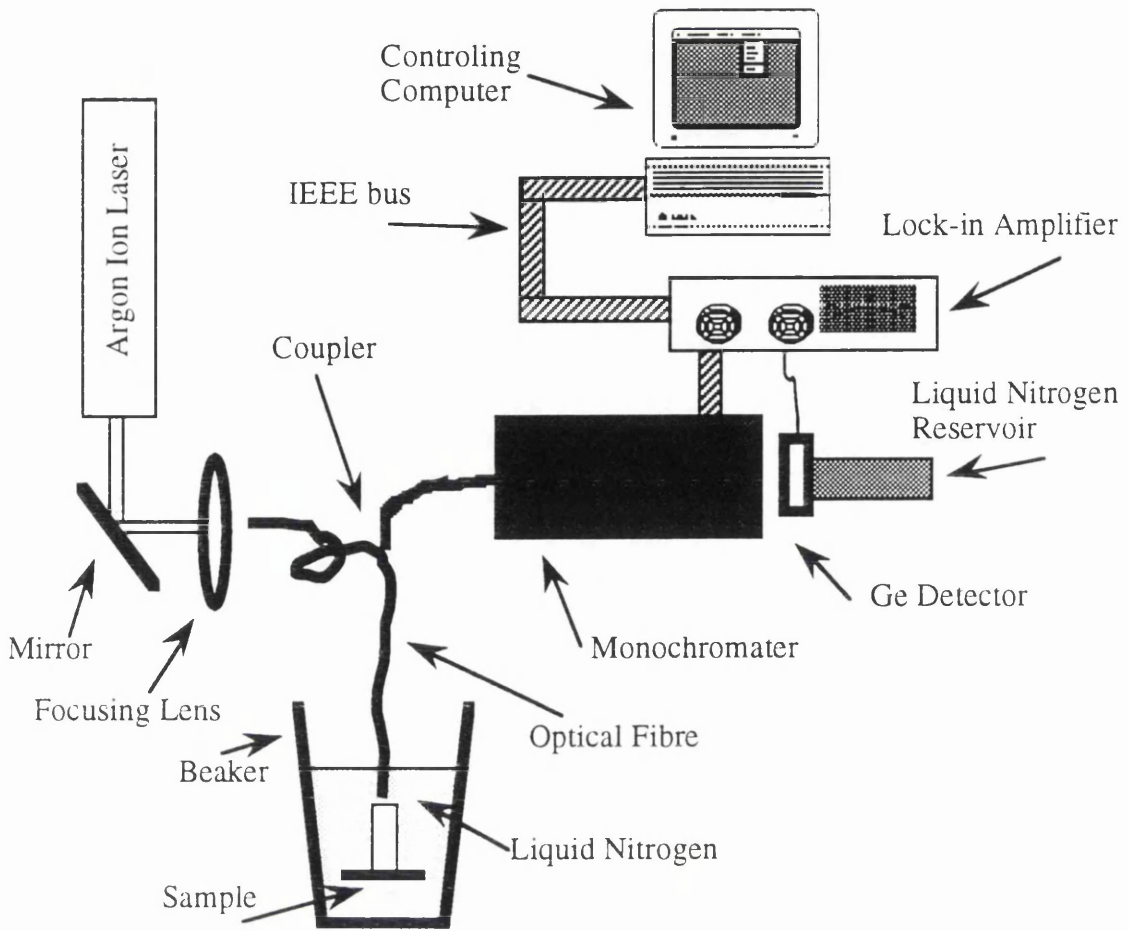


Figure 3.8. Experimental set-up used to perform photoluminescence measurements on samples at liquid nitrogen temperature.

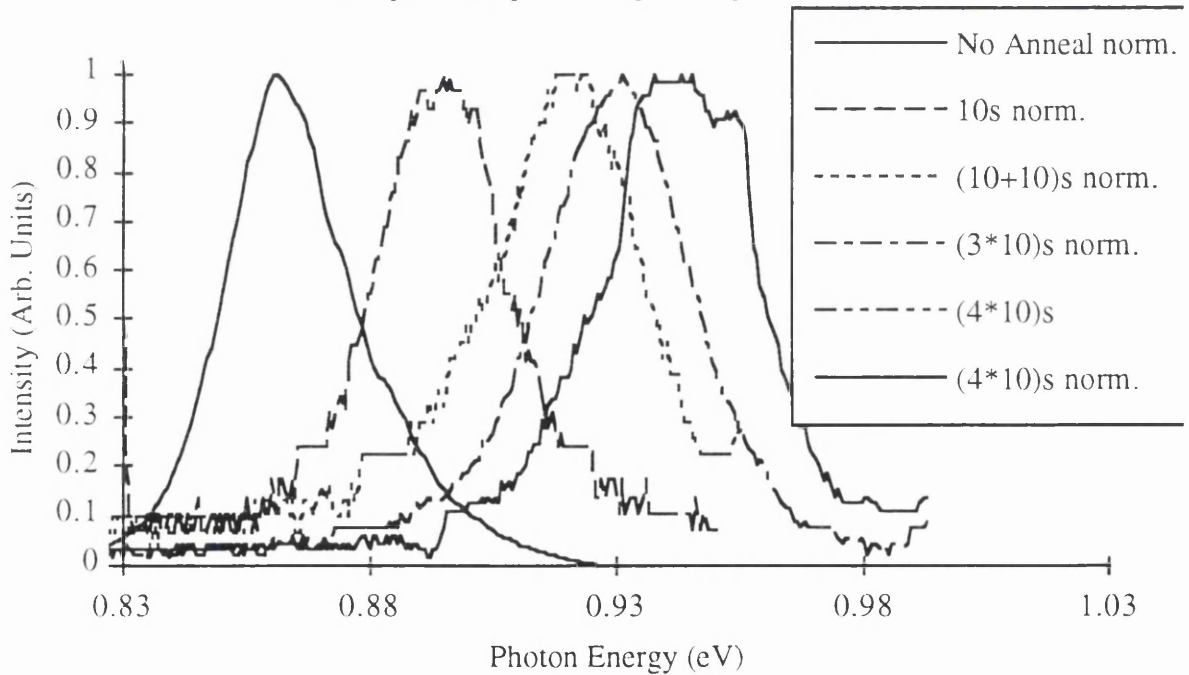


Figure 3.9 Typical PL spectra (77K) obtained using the above measurement technique.

The energy shift between the as grown sample and one annealed for 40 seconds is 80 meV, it is important to note here that the overlap between the two PL spectra is very small, therefore PL emitted from the as grown sample can only be very weakly absorbed into the intermixed sample. This condition is required in order to produce a low loss waveguide by IID.

3.4 Annealing Process

Two annealing processes have been used in this thesis: conventional furnace annealing used for long anneal times, and rapid thermal processing used for anneals that last for less than 3 minutes.

3.4.1 Conventional Furnace Annealing

The first technique, conventional annealing, was used extensively in previous work¹⁷, and uses the simplest equipment. A sample is placed in a graphite boat, which, in turn, is placed in a silica tube. A thermocouple is embedded in the graphite boat to record the temperature. An electric furnace is used which is run up to the required annealing temperature whilst the sample is well away from the heat source. Zero grade nitrogen is passed through the apparatus at all times.

Once the oven has settled at the required temperature, the graphite boat containing the required samples is placed in the centre of the oven, still with zero grade nitrogen flowing over the sample, and the temperature of the boat is monitored with the thermocouple. Typically the boat requires 15 minutes to reach its equilibrium temperature. Once the sample has reached the target temperature the anneal time starts.

The major problem with this technique is that because of the relatively slow heating cycle, large errors in the anneal time are introduced for anneals shorter than 10 minutes.

3.4.2 Rapid Thermal Processing

Rapid Thermal Processing is a technique suitable for annealing samples for typically less than 3 minutes. A Jipelec FAV 4 system was used.

The FAV 4 system contains a water cooled chamber where the samples to be processed are placed. The samples are placed on a graphite susceptor. The chamber is heated via 12 tungsten lamps that are controlled via a dedicated computer; control signals for the temperature are taken from either a thermocouple in the range 100–400°C, or a pyrometer in the range 400–1000°C.

The great advantage of this system over the conventional annealing furnace is the rate at which a selected temperature can be achieved; the ramp-up rate is 700°C s⁻¹, whilst the ramp-down rate is 350°C s⁻¹. The disadvantage is that long anneals are not possible, due to excessive wear on the heating elements.

The heating and cooling process as mentioned above are controlled by a dedicated on-board computer which allows a programme of several heating and cooling cycles to be carried out. A typical single heating and cooling cycle used is:

1. Purge the chamber for 2 minutes.
2. Ramp up to 700°C in 15 seconds with 20 sccm of zero grade nitrogen flowing through the chamber.
3. Hold at 700°C for 30 seconds (20 sccm of zero grade nitrogen)
4. Cool to room temperature in 15 seconds (20 sccm of zero grade nitrogen)
5. Purge the chamber before opening to the atmosphere.

3.5 Results

The following sections contain the results of a series of experiments that were carried out to investigate the disordering by F IID, of InGaAsP/InGaAs MWQ structures.

Section 3.5.1 shows the effect of varying the fluorine concentration on the bandgap shift, at a fixed temperature, for anneals in the RTP for up to 60 seconds.

Section 3.5.2 show the result of annealing in a conventional anneal furnace for 30 minutes for temperatures between 500°C and 750°C.

Section 3.5.3 shows results of rapid thermal processing for 30 seconds at temperatures ranging from 650°C to 750°C.

Section 3.5.4 shows the results of annealing wafers in the RTP at 700°C and 750°C for between 20 and 50 seconds.

Section 3.5.5 provides a summary of the intermixing process so far.

A detailed description of the wafers used is given in Appendix A. Unless otherwise stated, after implantation the samples were coated with a 1000 Å layer of SiO₂ to protect the surface of the wafer.

3.5.1 Concentration vs. Anneal Time

The following experiment was carried out using a wafer with four 100 Å QWs and an undoped upper cladding region of 1 μm (E242). The aim of the experiment was to identify the optimum implant concentration for disordering. Samples were implanted with different doses of fluorine into the QW region with doses ranging from 10¹³ cm⁻² to 10¹⁵ cm⁻², and annealed at 700°C for 10 to 60 seconds. One sample was implanted at a reduced energy (0.5 MeV) so that the impurity did not enter the well layers but damage is caused in the upper cladding regions of the wafer.

As can be seen from Figure 3.10 the implant concentration for maximum energy shift¹⁸ is around 10¹⁸ cm⁻³, corresponding to an implant dose of 10¹⁴ cm⁻² at an implant energy of 0.9 MeV. A higher concentration of implant inhibits the disordering process as shown by the open diamonds of Figure 3.10. Implanting so that the fluorine does not enter the QWs results in a red shift, or at best a small blue shift under the annealing conditions studied

here.

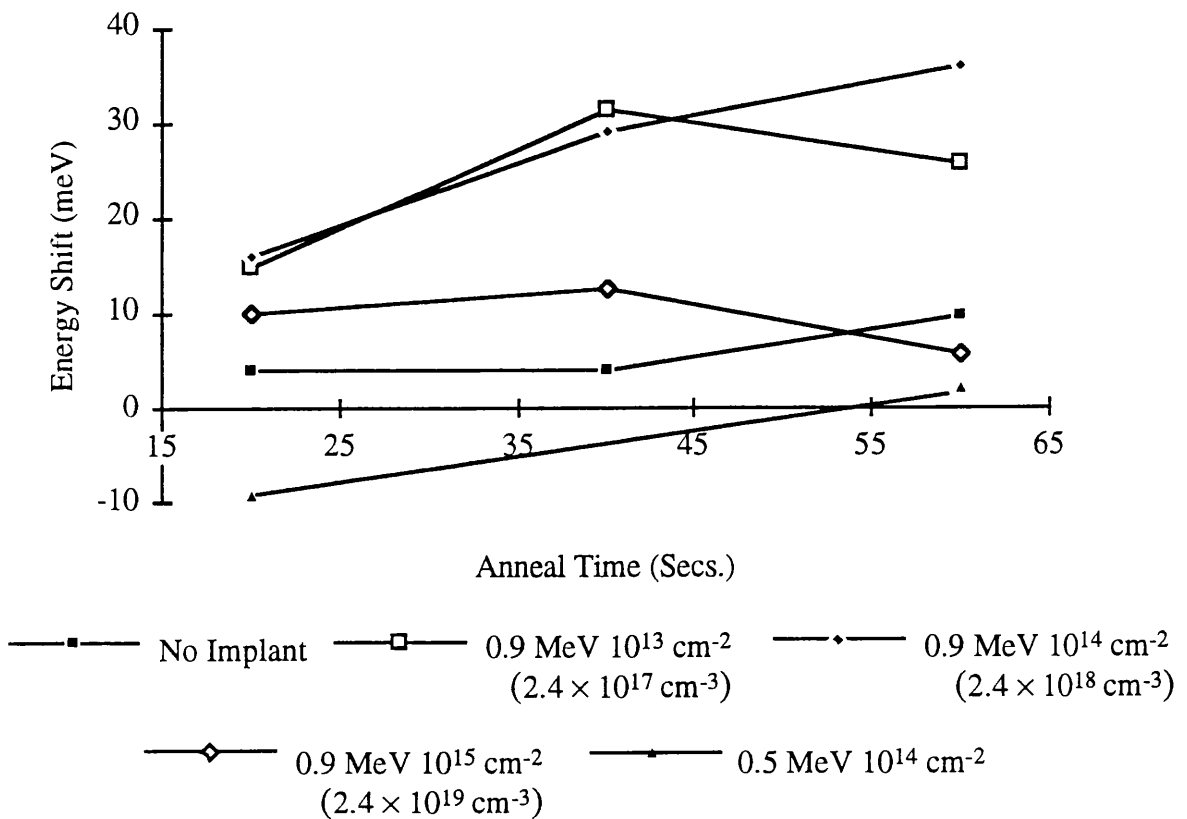


Figure 3.10 Sample E242 annealed with different concentrations of fluorine for anneal times of 20 to 60 seconds at a temperature of 700°C.

3.5.2 Conventional Annealing for 30 minutes

The effects of F IID were investigated in the conventional anneal furnace using a sample containing four 100 Å InGaAs QWs with an undoped InP upper cladding region (A2261). The wafer was implanted to obtain an implant concentration of $5 \times 10^{17} \text{ cm}^{-3}$ and annealed for 30 minutes in the conventional annealing furnace at temperatures of between 550°C and 750°C.

Boron was also investigated as a possible impurity for IID at this stage; boron is also expected to be a neutral impurity at room temperature.

The fluorine implanted samples show a significant blue shift, as observed in Figure 3.11, with a maximum recorded shift of nearly 100 meV at 750°C. Boron implanted samples show a significant red shift for all but the lowest temperature anneals. The control samples

highlight a significant problem with this technique: large blue shifts are observed in all annealed samples, this being due to the poor thermal stability of this material system.

As a result of these measurements, work was carried out at BNR Europe Ltd. in order to explain the thermal instability and to try to improve it. A paper has been published on their initial findings¹⁹. Rather unexpectedly it was found that substrates containing a high etch pit density (indicating defects in the crystal structure) would inhibit intermixing and thus provide a more stable QW structure. The explanation put forward was that dislocations on the substrate extend during growth of the epilayers, so that the dislocation density of the epilayers is similar to the substrate. On annealing these dislocations provide a sink for the point defects at the surface of the wafer that provide the means for interdiffusion. The positive effect seen by the high etch pit density is rather controversial since defects in a crystal are generally unwanted since they produce undesirable effects in semiconductors such as dark spots in QW lasers, and catastrophic damage of a device.

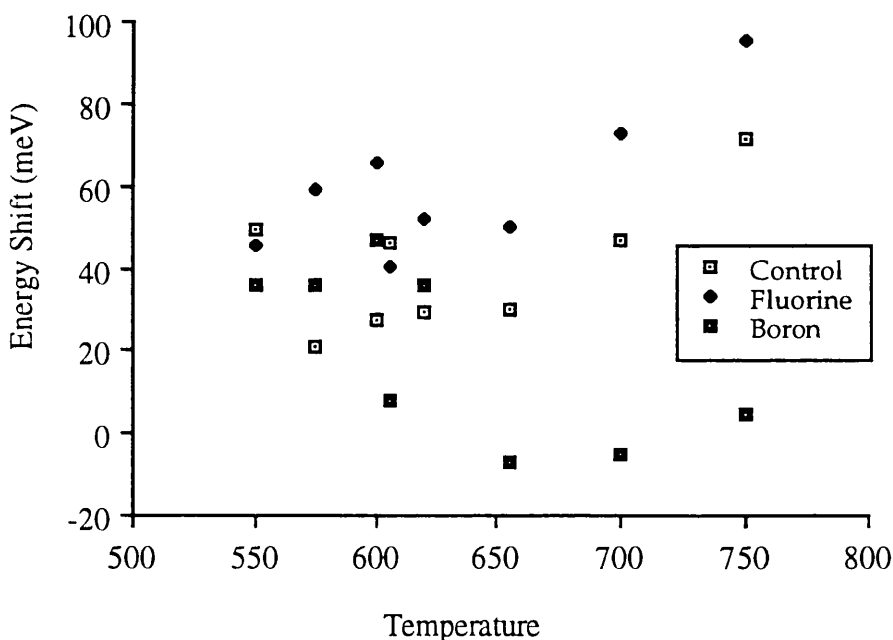


Figure 3.11. Sample A2261 annealed in the conventional furnace for 30 minutes, between 550°C and 750°C.

3.5.3 Rapid Thermal Processing (fixed time)

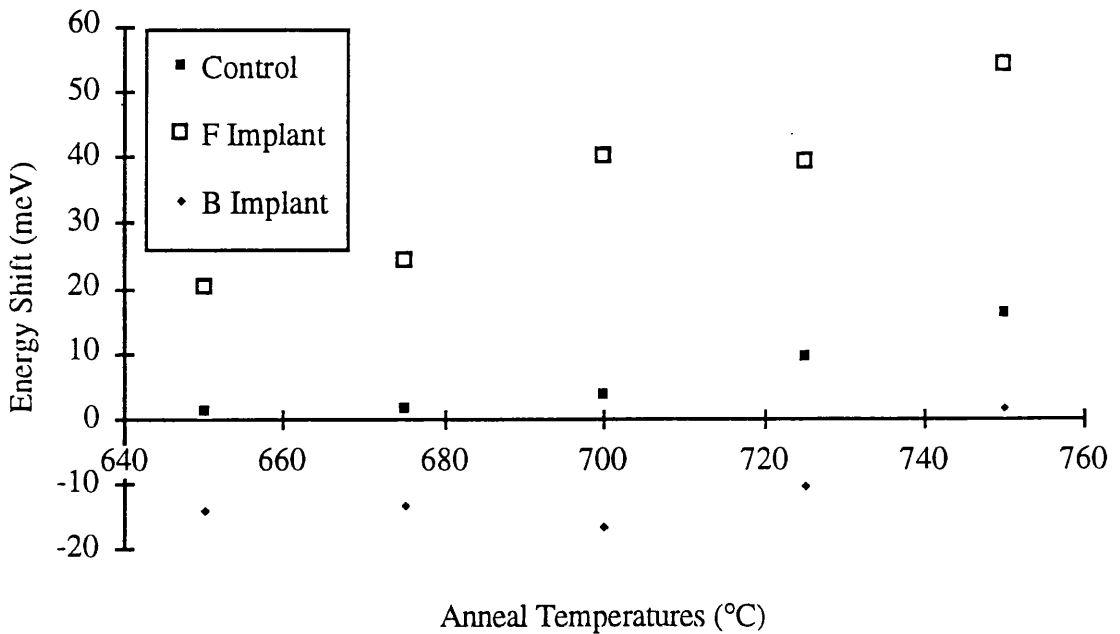


Figure 3.12. A2409 annealed in by rapid thermal processing with B and F at a concentration of 10^{18}cm^{-3} for 30 seconds.

In order to try to minimise the effects of thermal instability in unimplanted regions, a rapid thermal treatment was investigated.

Figure 3.12 shows the results of annealing samples of a four 100 \AA MQW structure, with a $1\text{ }\mu\text{m}$ upper cladding (A2409), in the RTA for 30 s at temperatures between 650°C and 7650°C . At 700°C , a shift of 40 meV is obtained with very little shift in the control, or unimplanted material. Annealing above this temperature causes significant blue shifts in the control material. The boron implanted samples again show a red shift, as was observed in Section 3.5.2.

3.5.4 Rapid Thermal Processing (fixed temperature)

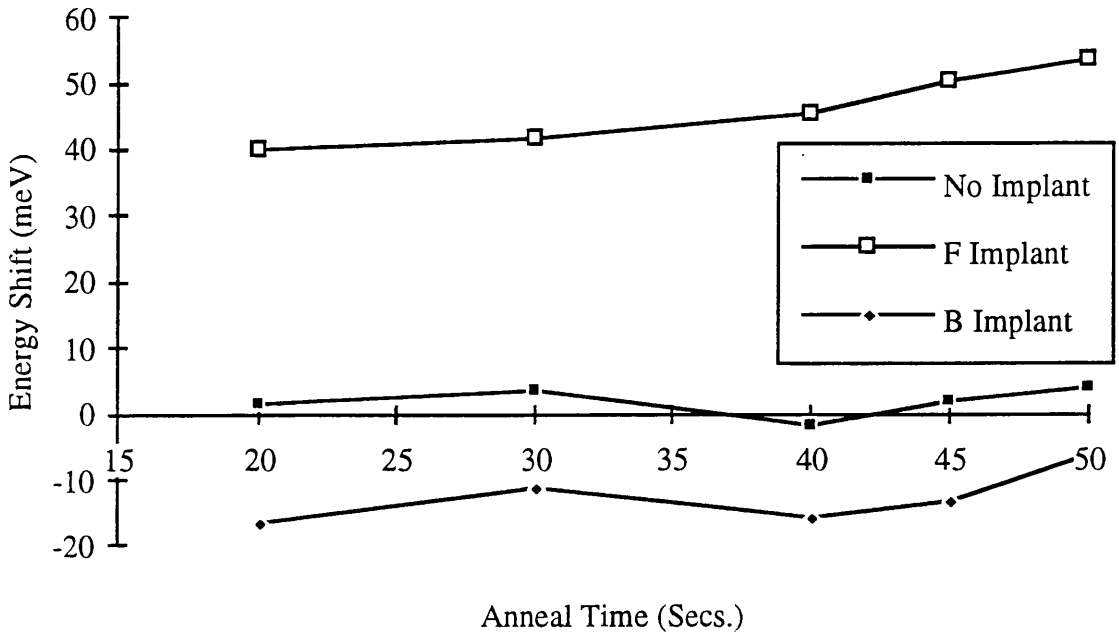


Figure 3.13. Sample A2409 implanted with B and F to a concentration of 10^{18}cm^{-3} and annealed at 700°C for 20 to 50 seconds.

Figure 3.13 shows a set of results for the same QW structure as in Section 3.5.3, A2409, with anneals carried out at 700°C for between 20 and 50 seconds. A gentle increase in bandgap is observed for fluorine implanted samples with an almost constant 40 meV bandgap difference between samples implanted with fluorine and the control samples.

Figure 3.14 shows the result of annealing a similar wafer to that of the previous results, A2262, at 750°C . Although a larger blue shift is obtained in the fluorine implanted samples, than with anneals at 700°C , a large blue shift is now present in the control samples.

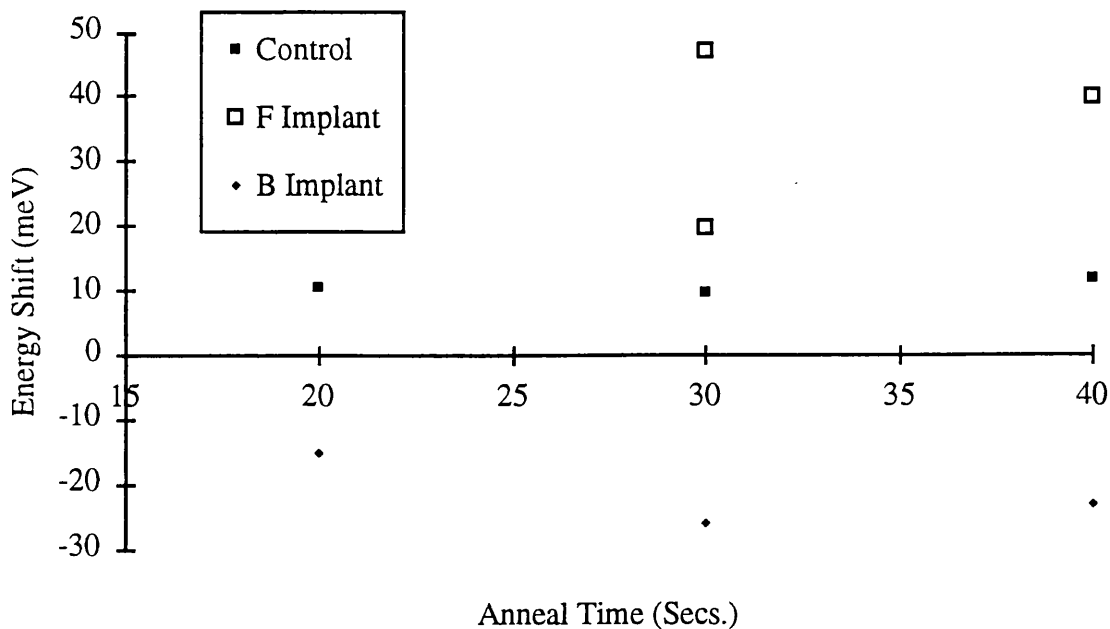


Figure 3.14 Sample A2262 implanted with fluorine and Boron and annealed at 750°C 20 to 40 seconds.

The red shift observed for the shallow implant is similar to that observed with boron implantation. In the case of boron implantation it was suggested that the disordering was due to the creation of damage in the structure, not the presence of the B implant, this suggests further that the two processes producing the red shift are caused by damage and the increase in group III diffusion over that of group V.

3.5.5 Summary

The desired effect is to anneal a sample containing fluorine and have a resulting blue shift in the PL emission, and at the same time to be able to anneal a sample that is as grown, under the same conditions as the implanted one, with no change in the wavelength of the PL emission. This is almost achieved when annealing at 700°C for 30 seconds in the rapid thermal processor. Certain wafers do have a reduced thermal stability, which results in a greater shift of the control samples, but this is nominally less than 5 meV. In Chapter 4, the effects on the thermal stability with different dielectric caps is investigated. It was hoped that a dielectric cap would increase the thermal stability of the wafer, enabling the anneal

temperature for fluorine implanted samples to be increased, and to therefore increase the amount of disordering in the wafer.

3.6 Theoretical Model of the Diffusion Process

The diffusion model used here to predict the diffusion coefficient of the disordering process makes the following assumptions,

1. The diffusion coefficients of the constituent atoms are the same,
2. Any lattice mismatch is ignored during diffusion so the effects of strain can be ignored,
3. The diffusion coefficients are taken to be concentration independent.

3.6.1 Fick's Law of Diffusion

Fick's laws of diffusion are based on the hypothesis that the rate of transfer of diffusant across a unit area is proportional to the concentration gradient in the direction of diffusion. The first law is simply a mathematical representation of the above statement,

$$F = -D \frac{\partial C}{\partial x} \quad (3.14)$$

where F is the amount of diffusant crossing unit area in the x -direction per unit time, D is the diffusion coefficient, and C is the concentration of diffusant at x . By considering diffusion through a unit volume and using Equation 3.14, Fick's second law can be derived,

$$\frac{\partial C}{\partial t} = D \frac{\partial^2 C}{\partial x^2} \quad (3.15)$$

where t is time. Equation 3.15 is for diffusion in the x -direction only, but because we are considering diffusion across a quantum well this equation can be used; diffusion in the plane parallel to the quantum wells has no effect on the effective bandgap of a MQW structure. A solution to equation 3.15 is,

$$C = \frac{A}{\sqrt{t}} \exp\left(\frac{-x^2}{4Dt}\right) \quad (3.16)$$

where A is an arbitrary constant. Equation 3.16 represents diffusion from an infinite source at $x=0$, the diffusion profile being symmetric about $x=0$. The total amount of diffusant in a cylinder of infinite length and unit cross section is given by the integral,

$$\begin{aligned} M &= \int_{-\infty}^{\infty} C \cdot dx \\ &= 2A\sqrt{\pi D} \end{aligned} \quad (3.17)$$

M being the total amount of diffusant which, as expected, is constant and equal to the total amount of diffusant deposited at $t=0$ and $x=0$. Substituting Equation 3.17 back into Equation 3.16 we obtain,

$$C = \frac{M}{2\sqrt{\pi Dt}} \exp\left(\frac{-x^2}{4Dt}\right) \quad (3.18)$$

which now represents the solution to the diffusion equation of a total amount of substance M deposited at a surface at $t=0$ and $x=0$.

In the case of QW structures (and in most practical situations), we are dealing with extended sources, but we can model this as an infinite number of line sources as in Figure 3.15.

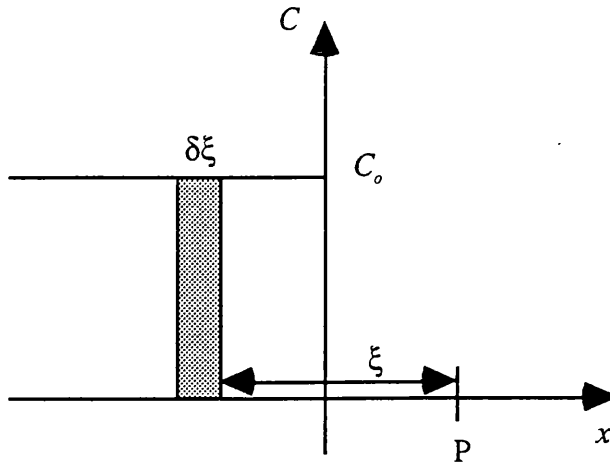


Figure 3.15. An infinite number of line sources of thickness $\delta\xi$ concentration C_0 .

Figure 3.15 shows an infinite number of line sources of thickness $\delta\xi$ for $x < 0$, the amount of diffusant per unit area in each strip being given by $C_0\delta\xi$. The concentration of diffusant at point P from the highlighted strip is given by,

$$C = \frac{C_0\delta\xi}{2\sqrt{\pi Dt}} \exp\left(\frac{-\xi^2}{4Dt}\right). \quad (3.19)$$

The total concentration at point P from the line source in the region $-\infty < x < 0$ is calculated by integrating Equation 3.19 over this region. The result of the integration can be expressed in terms of the complementary error function (erfc),

$$C(x,t) = \frac{C_0}{2} \operatorname{erfc} \frac{x}{2\sqrt{Dt}} \quad (3.20)$$

Using the same procedure, the diffusion of a finite source into an infinite sink can be found, which is a good approximation to the diffusion of QW structures,

$$C(x,t) = \frac{C_0}{2} \left(\operatorname{erfc} \frac{x-h}{2\sqrt{Dt}} + \operatorname{erfc} \frac{x+h}{2\sqrt{Dt}} \right) \quad (3.21)$$

where the source is confined to the area $-h < x < h$. The effect of barriers and multiple sources can also be taken into account by using superposition. For the case of a diffusion

barrier at a distance l and an infinite number of reflections off of this barrier the concentration profile is given by,

$$C(x,t) = \frac{C_0}{2} \sum \left\{ \operatorname{erf} \frac{h+2nl-x}{2\sqrt{Dt}} + \operatorname{erf} \frac{h-2nl+x}{2\sqrt{Dt}} \right\} \quad (3.22)$$

Equation 3.22 can be used to model a series of wells a distance of $2l$ apart.

The concentration profile calculated using Equation 3.22 is used to calculate the potential profile across the diffused well in the following way;

1. The concentration profile of one of the constituent elements is calculated using Equation 3.22.
2. Using the relationship between bandgap and composition in Ref. 10, an energy gap profile is calculated from the result of step 1, above.
3. The conduction and valence band discontinuities are used to convert the energy gap profile into a valence and conduction band profile. From this profile the energy level of the diffused well can be calculated with different values of Dt .

3.6.2 Hyperbolic Secant Profile

An alternative diffusion profile, the hyperbolic secant profile²⁰, has been considered when modelling the disordering process. This profile has the advantage over the error function profile in that it produces an analytical solution to Schrödinger equation and it is therefore much simpler to calculate the energy levels in partially disordered quantum wells. For the conduction and valence bands respectively, the hyperbolic secant profile is expressed as

$$V_c(z) = V_{oc} [1 - \operatorname{sech}^2(\beta z)] + E_g(z) \quad (3.23)$$

$$V_v(z) = V_{ov} [\operatorname{sech}^2(\beta z) - 1] \quad (3.24)$$

where,

$$\beta = \frac{2}{L_z} \cdot \frac{\Delta E_{gd}}{\Delta E_{gs}} \quad (3.25)$$

and V_{ov} and V_{oc} are the steps in the valence and conduction bands respectively. Equation 3.25 is obtained by setting the total number of diffusant atoms in the error function and hyperbolic secant profiles to be the same, as well as setting the height of the hyperbolic secant profile in the centre of the well to equal that of the error function profile at the same position. In this way, the hyperbolic secant can be made to approximate closely the error function profile for long diffusion times.

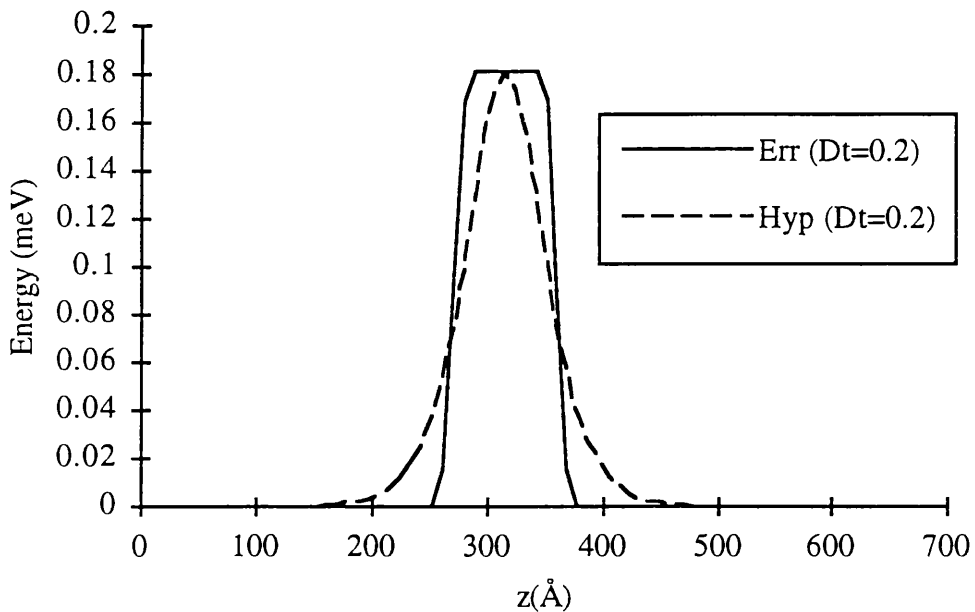


Figure 3.16. Comparison of the hyperbolic secant profile (Hyp) and the Error Function Profile (Err) for small Dt. The two profiles are significantly different, even though the two wells have the same depth.

The formulation of these equations is discussed in greater depth in ref.²¹.

The hyperbolic secant profile and the error function profile converge for large diffusion times but, for small times, the hyperbolic secant estimates larger shifts than with the error function profiles²². Figure 3.16 shows an error function profile (solid line) and the hyperbolic secant profile (dashed line) for the same values of Dt . It can be clearly seen for the small value of Dt used (0.2), there is a large discrepancy between the curves.

Figure 3.17 shows the same two curves as in Figure 3.16, except Dt , is now one hundred times larger ($Dt=20$), and the curves are now starting to converge.

Finally, the effect of the difference in well shape for the error function and hyperbolic secant profiles on the bandgap can be clearly seen in Figure 3.18. For large Dt , the bandgap converges for the two profiles, however, for small Dt , i.e. <5 , there is a large difference. In practice the energy shifts due to disordering, as seen in Section 3.5, are expected to be in the order of 40 meV; from Figure 3.18 it is clear that the error function profile will be most appropriate for modelling the diffusion process, even though the calculations will be numerical as discussed above.

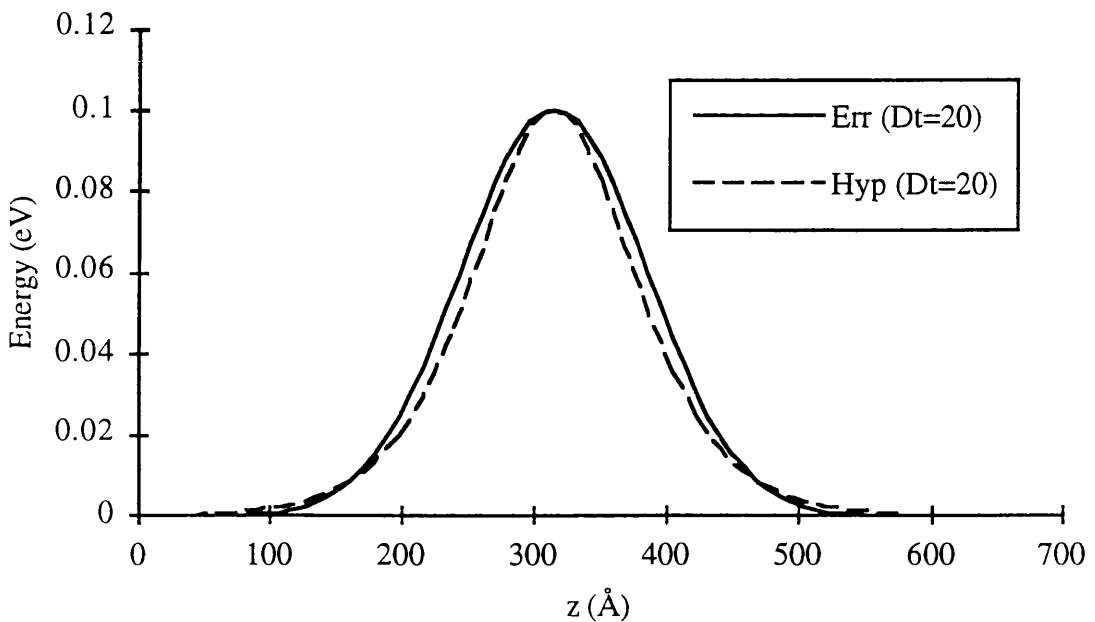


Figure 3.17 Comparison of the hyperbolic secant profile (Hyp) and the Error Function Profile (Err) for large Dt . The two curves are approximately equal.

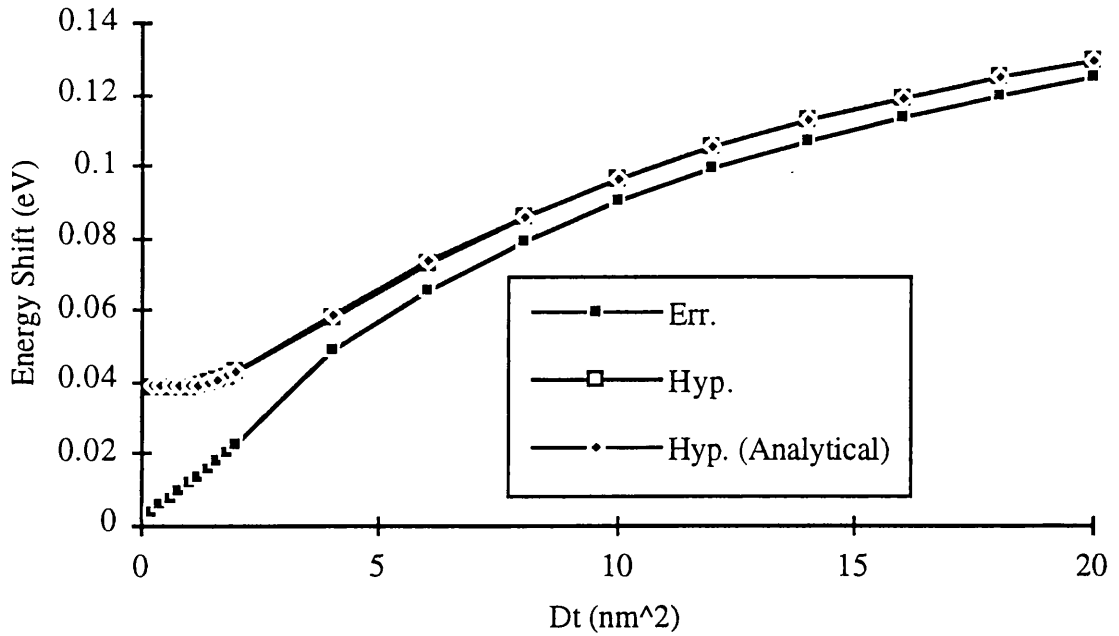


Figure 3.18. Energy shift vs. Dt for the error function profile and hyperbolic secant profile.

In Figure 3.18 the curve marked 'Err' is the error function calculated numerically, 'Hyp' is the hyperbolic profile calculated with the same numerical method as the 'Err' profile, and 'Hyp. (Analytical)', is the hyperbolic profile calculated by an analytical process.

3.6.3 Diffusion Coefficients from Experimental Results

The curve calculated in Figure 3.18 for the error function profile, can be used to find the diffusion coefficients for a given energy shift at different temperatures and times. A curve was calculated for each wafer investigated and was used as a look-up table.

Figure 3.19 shows the diffusion coefficient of samples containing 100 Å InGaAs QWs (A2409) implanted with fluorine at a concentration of 10^{18} cm^{-3} and annealed at 700°C for between 20 and 50 seconds (Section 3.5.3). The model in the previous section does not predict a red shift for any part of the diffusion process. This is because the system is assumed to remain lattice matched to InP. As observed in Figure 3.4 a red shift can only occur if the group III interdiffusion is taking place quicker than group V diffusion.

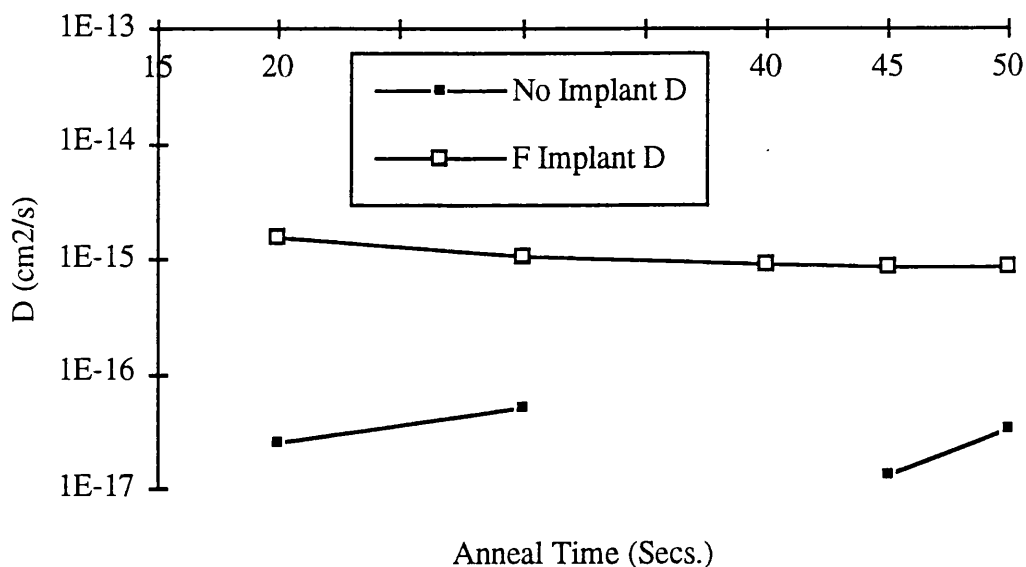


Figure 3.19. A2409 diffusion coefficient calculated assuming diffusion produces a well that has an error function profile.

Figure 3.20 is an Arrhenius plot of diffusion coefficients calculated by the above technique for wafer A2409 annealed at various temperatures (650°C to 750°C) for 30 seconds. The Arrhenius plot gives information concerning the activation energy for the diffusion process²³ and is equal to the gradient of the curve multiplied by -1. D_c is the diffusion coefficient for the control sample, D_f the diffusion coefficient for the fluorine implanted sample.

The activation energies are therefore 79 meV for the fluorine implanted samples, and 206 meV for the high temperature control samples, and 87 meV for the lower temperature control samples. A straight line indicates a linear process is involved with the disordering.

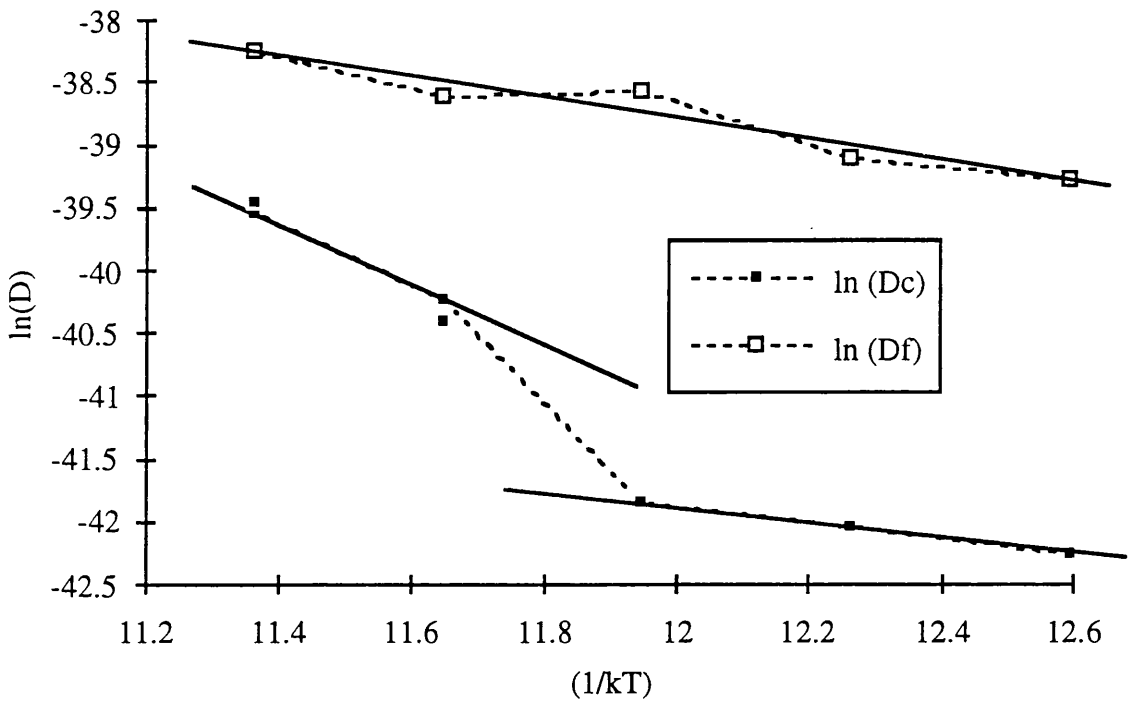


Figure 3.20 An Arrhenius plot for sample A2409 annealed for 30 seconds

3.7 Summary

Rapid thermal processing, as opposed to annealing in a conventional furnace, has been shown to significantly improve the disordering properties of InGaAs/InGaAsP with the neutral impurity, fluorine. The diffusion coefficient of the material has increased typically from $10^{17} \text{ cm}^2 \text{ s}^{-1}$ to $10^{15} \text{ cm}^2 \text{ s}^{-1}$, for anneals at 700°C resulting in energy shifts of 50 meV in the implanted samples with very little alteration to the as-grown bandgap in unimplanted samples heated by the same process. Larger blue shifts of up to 100 meV are observed in fluorine implanted samples; however, the higher temperatures required cause thermal intermixing in unimplanted material, which is an undesirable effect.

Boron implants have been shown to cause red bandgap shifts, due to intermixing on the group three lattice site only, compared to diffusion on the group III and V lattice sites with the fluorine impurity induced disordering process. The subsequent blue shifts observed in Figure 3.11 can be explained by the thermal diffusion effects becoming greater than the effect of boron on the interdiffusion process.

A proportion of the change in bandgap observed in fluorine implanted samples is likely to be due to damage caused in the crystal by the ion implantation process. In Figure 3.11, the change in energy of the fluorine implanted samples is increasing at the same rate as the change in energy in the unimplanted samples, for 30 minute anneals. This observation suggests that an initial energy shift is caused by a combination of ion damage and impurity induced disordering but, at temperatures over 650°C the effect observed is probably thermal. A high diffusion rate of the fluorine impurity in the wafer would explain this, since as the temperature of the anneal increases the diffusion of fluorine out of the well region will increase and the effect of fluorine on the III-V interdiffusion rate will decrease. The results shown in Figure 3.10 also support this argument since the anneals shown here are for between 20 and 50 seconds only; fluorine has less chance to diffuse out of the QW region, and there is a greater rate of change in energy shift with time for the shorter anneals than with the longer times.

From the estimations of the diffusion coefficients made in Section 3.6.3 a linear process is seen for Fluorine implanted materials (Figure 3.20) suggesting a linear process is involved in the disordering technique. The thermal diffusion process does however appear to be a two stage mechanism, since the Arrhenius plot has two straight line segments. An explanation for this is that the group III species have a higher activation energy than the group V species.

References

- ¹'Long-Wavelength Semiconductor Lasers', G.P. Agrawal, N.K. Dutta, Van Nostrand Reinhold Electrical/Computer Science and Engineering Series, 1986.
- ²'Room Temperature Excitonic Nonlinear-Optical Effects in Semiconductor Quantum-Well Structures', D.S. Chemla, and D.A.B. Miller, J. Opt. Soc. Am. B, **2** (7), pp.1155-1173, 1985.
- ³'Quantum Mechanics', R. Eisberg, and R. Resnick, John Wiley and Sons.
- ⁴'Physical Properties of Semiconductors', C.M. Wolfe, N. Holonyak Jr., and G.E. Stillman, Prentice Hall, 1989.

- ⁵'Quantum Mechanics', L.I. Schiff, Third Edition, McGraw-Hill.
- ⁶'Wave Mechanics Applied to Semiconductor Heterostructures', G. Bastard, Halsted Press, p.42, 1988.
- ⁷'Quantum Theory of Solids', C. Kittel, John Wiley & Sons, New York, p.298, 1987.
- ⁸'Energy-gap discontinuities and effective masses for GaAs-AlGaAs Quantum Wells', R.C. Miller, D.A. Keinman, and A.C. Gossard, Phys., Rev. B29, pp. 7085-7087, 1984.
- ⁹lecture notes, Dr. J.H. Davies, Dept. of Electronics and Electrical Engineering, The University of Glasgow. June 1990.
- ¹⁰'Material Parameters of InGaAsP and Related Binaries', S. Adachi, J. of Appl. Phys. Lett., **54**(14), p.1353, 1989.
- ¹¹'Strained Layer Structures: Principles and Applications', S. Adachi, J. of Appl. Physics, **53** (12). p. 8775, 1982.
- ¹²'Impurity Induced Disorder for Long Wavelength Narrow Linewidth Multiple Quantum Well Lasers', M.Sc. Thesis, Stephen Bradshaw, The University of Glasgow, 1990.
- ¹³'Semiconductors', R.A. Smith, Second Edition, Cambridge University Press.
- ¹⁴'The Stopping Range of Ions in Solids', J.F. Ziegler, J.P. Biersack, and U. Littmar, Pergamon Press, New York, 1985.
- ¹⁵"Photoluminescence Theory", H. Barry, E.W. Williams.
- ¹⁶'Optical Electronics', Fourth Edition, Amon Yariv, pp. 411, Saunders College Publishing, 1991.
- ¹⁷'Impurity Induced Disorder for Long Wavelength Narrow Linewidth MQW Lasers', M.Sc. Thesis submitted to the Faculty of Engineering, The University of Glasgow, by S.A. Bradshaw, September 1990.
- ¹⁸'Very Low Loss Waveguides Formed by Fluorine Disorder of GaInAs/GaInAsP Quantum Wells', S.A. Bradshaw, J.H. Marsh, and R.W. Glew, IEEE/LEOS Proceedings,

Fourth International Conference on Indium Phosphide and Related Materials, Newport, Rhode Island, April 1992.

¹⁹'The Influence of the Substrate on the Thermal Stability of InGaAs/InGaAsP Qws', R.W. Glew, A.T.R. Briggs, P.D. Greene, and E.M. Allan. Proceedings 4th International Conference on InP and Related Materials, pp.234-237, 21-24 April 1992.

²⁰'The Optical Properties of AlGaAs/GaAs Hyperbolic Quantum Well Structures', E.H. Li, B.L. Weiss, J. Appl. Phys., **70**, pp 1054-1056, 1991.

²¹Chapter 3 of the Ph.D. thesis submitted by C.Keladis of the Department of Electronic and Electrical Engineering, The University of Glasgow, 1994.

²²'Comparison of Impurity Induced Disorder Potential Profiles', C. Kelaidis, and J.M. Arnold.

²³'Point Defects and Diffusion', C.P. Flynn, Clarendon Press, Oxford, 1972.

Chapter 4

Thermal Stability and Effects of Dielectric Caps

4.1 Introduction

In Chapter 3 fluorine was shown to increase the overall diffusion coefficient of the InGaAs/InGaAsP based QW structures, leading to a widening of the material's bandgap in fluorine implanted regions. The major problem of the thermal instability of the QW structures observed in unimplanted regions was reduced by using Rapid Thermal Processing (RTP) as opposed to long anneal times in a conventional annealing furnace; however disordering is still observed in unimplanted regions at temperatures over 700°C.

In this Chapter the effects of different dielectric caps on the thermal stability of the QW structure are investigated. The aim was to try to find a cap that would reduce the bandgap shift of unimplanted QWs. Silica caps have previously been shown to enhance the intermixing process in the GaAs/AlGaAs system as described in Chapter 2, with silicon nitride and strontium fluoride acting as inhibitors to the diffusion process. It was therefore decided to investigate the properties of the above mentioned dielectric on the InGaAs/InGaAsP based QW structure.

Photoluminescence was used to monitor the bandgap shift of the samples as reported in Chapter 3. The analysis technique reported in Chapter 3 was again used to estimate the diffusion coefficients.

4.2 Experiments

Three types of dielectric cap have been used in this Chapter: silica, strontium fluoride, and silicon nitride. The following sections are arranged as;

Section 4.3: The effect of silica caps is investigated on three wafer structures, with different QW configurations.

Section 4.4: Tensile silicon nitride and nominally unstrained silicon nitride are investigated along with the effects of repetitive thermal processing. Samples coated with strontium fluoride are also processed.

4.3. Effect of SiO₂

A set of experiments was designed to investigate the effect of silica caps on InGaAsP/InGaAs QW structures. The silica was deposited by plasma deposition. Three material structures were used to see the effect of varying the width of quantum wells, and strain in the quantum wells on the intermixing process. For each wafer five samples were used with different configurations;

1. Both sides of the samples were coated with 1000 Å of silica.
2. The top of the sample was coated with 1000 Å of silica.
3. Both sides of the sample were coated in 1000 Å silica and annealed in a Si box.
4. The top of the sample was coated with 1000 Å of silica and annealed in a Si box.
5. No silica and no Si box.

The three wafers used were;

E791 with 90Å unstained QWs with a RT PL peak of 1.45 μm,

E795 with 30 Å strained QWs with a RT PL peak of 1.46 μm, and

E799 with unstained QWs with a RT PL peak of 1.3 μm. For a detailed description of the materials used see Appendix A

4.3.1 Wafer E791 Anneal Results

Material E791 is a laser structure as indicated in Appendix A that contains unstrained 90 Å quantum wells. This structure is typical of many used for the fabrication of semiconductor lasers emitting in the 1.55 μm regime.

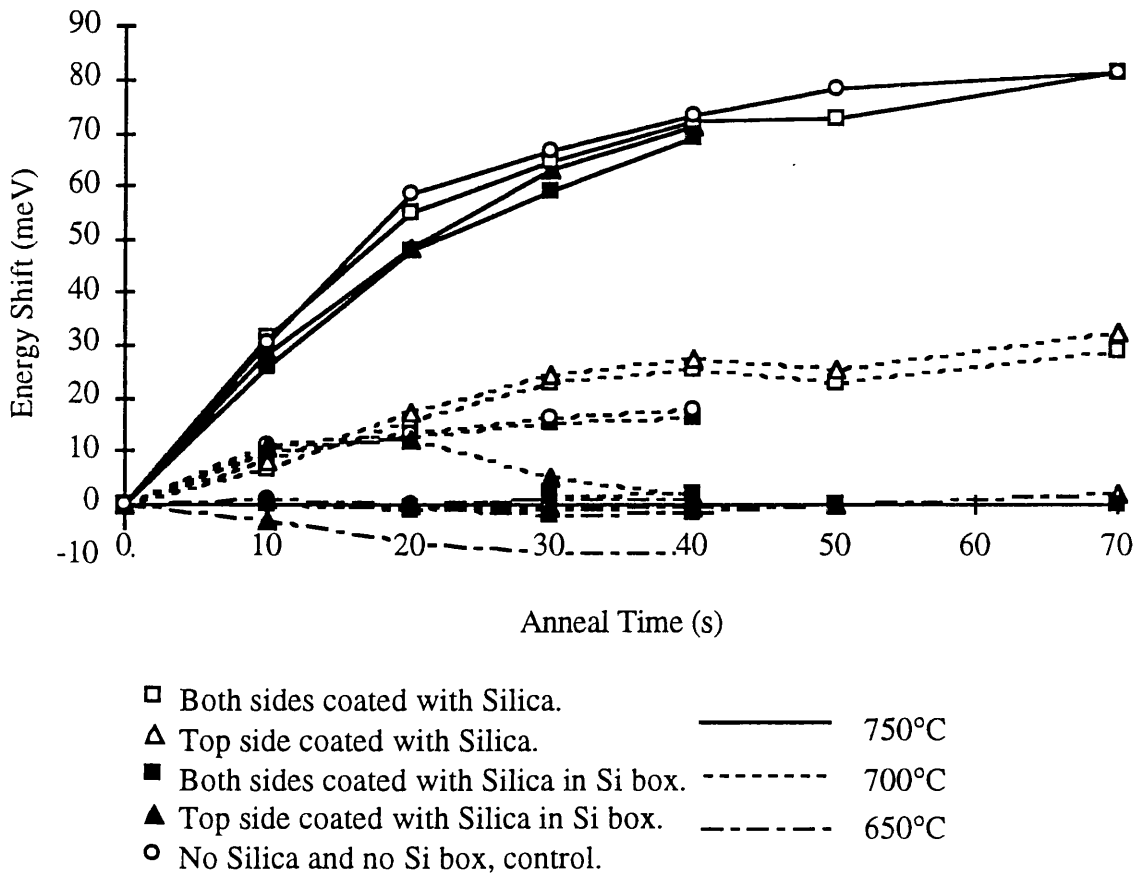


Figure 4.1. E791 thermal stability tests at 750°C, 700°C and 650°C with various silica cap configurations and Si encapsulation.

Figure 4.1 shows the energy shift obtained when annealing the samples at 750°C, 700°C, and 650°C in the RTP. No difference in the energy shift is observed in structures coated with or without silica, therefore encapsulation does not seem to affect the disordering process. Samples which were annealed with silica on the surface did, however, retain a good morphology, especially for the higher temperature anneals whereas samples without a protected surface would often be damaged by the thermal processing.

Figure 4.2 shows the corresponding diffusion coefficients for the thermal processing. The slight red shifting observed in the samples that were annealed at 650°C cannot be explained with the simple diffusion model used in Chapter 3. For these samples a diffusion coefficient cannot therefore be calculated.

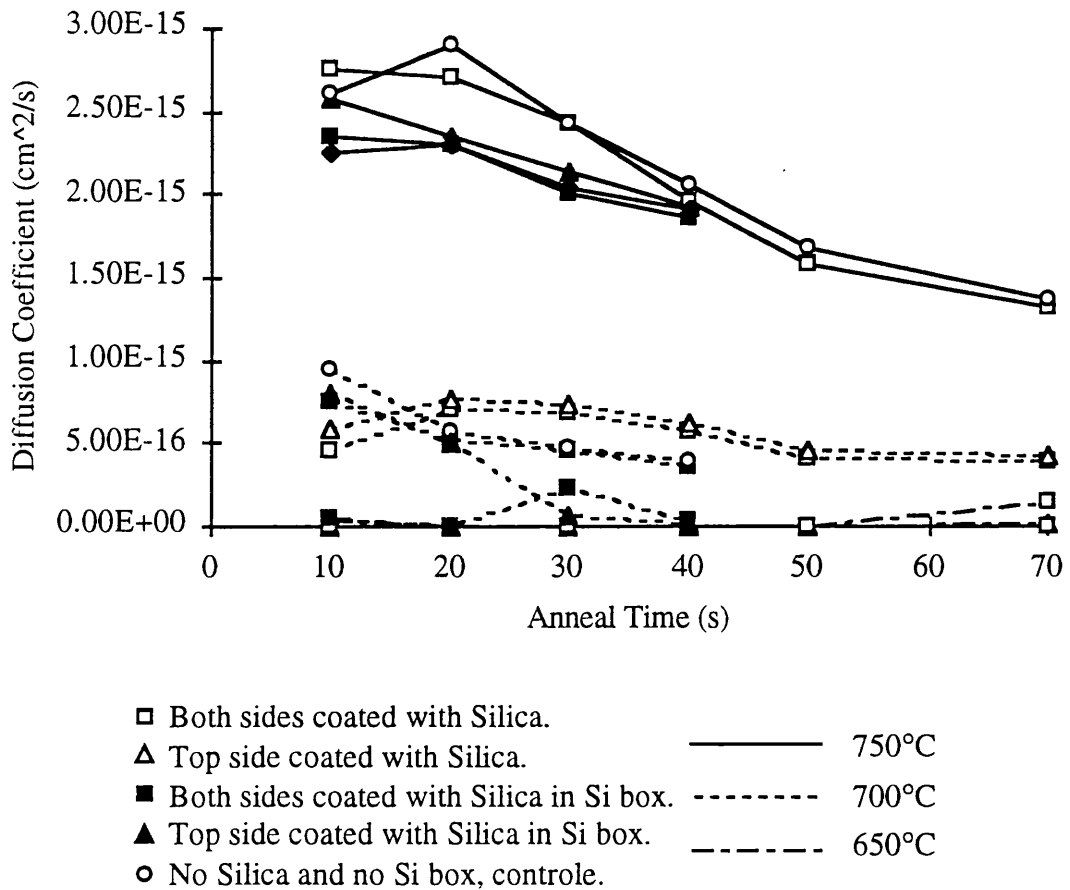


Figure 4.2 Diffusion coefficients calculated from experimental results and the theoretical calculation.

4.3.2 Wafer E799 Anneal Results

The material structure E799 has a room temperature photoluminescence peak of around 1.3 μm , with unstrained 30 \AA quantum wells. This structure was grown so that the same well size as samples E795 could be investigated, with the same material composition as structure E791.

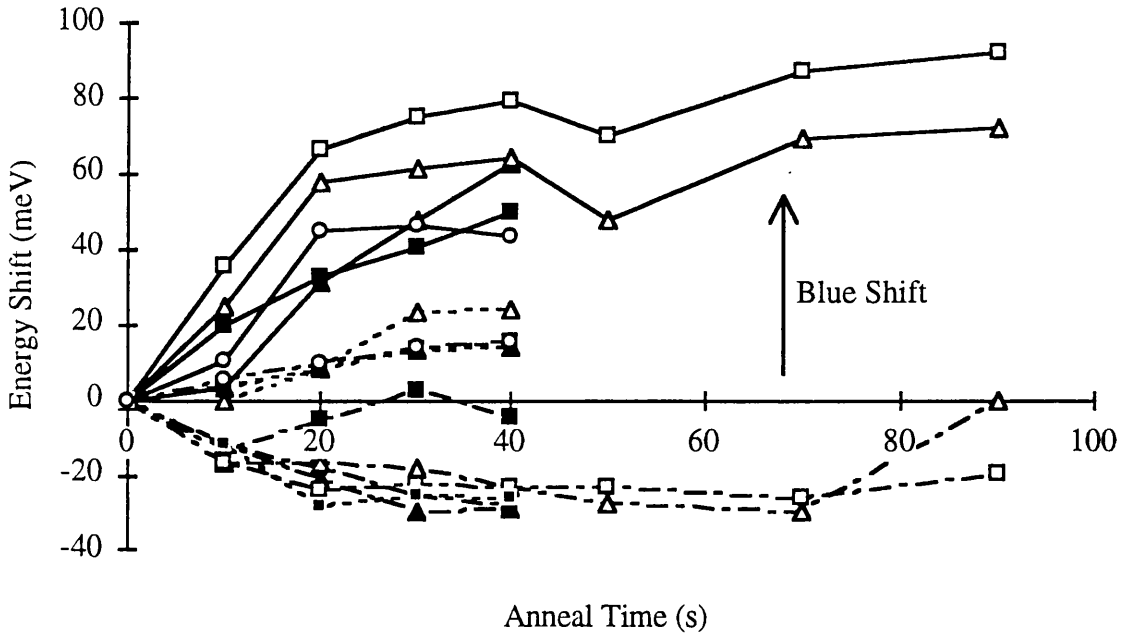


Figure 4.3 . E799 thermal stability tests at 750°C, 700°C and 650°C with various silica cap configurations and Si encapsulation.

Figure 4.3 shows the thermal diffusion of sample E799 with the same conditions as the results shown in Figure 4.1. Although the maximum shifts appear to be very similar in size there are two differences with this set of results.

1. The spread of results at higher temperatures indicates that with, smaller quantum wells, the diffusion process is more sensitive to temperature. The sample enclosed in a silicon box would presumably reach equilibrium temperature more slowly than the other samples: in the results the samples in the silica box show a lower energy shift.
2. At the lower temperature anneals, the red shift is much more prominent. A red shift is most likely to be due to preferential diffusion of group III elements i.e. indium diffusing into the wells and gallium out of the wells. This is interesting since it

indicates that the Group III species are the first to start disordering, but at higher temperatures disordering of the Group V elements begins, and a blue shift results. Due to the composition of the structure the photoluminescence peak is bound to show an overall blue shift after complete intermixing (approximately 130 meV).

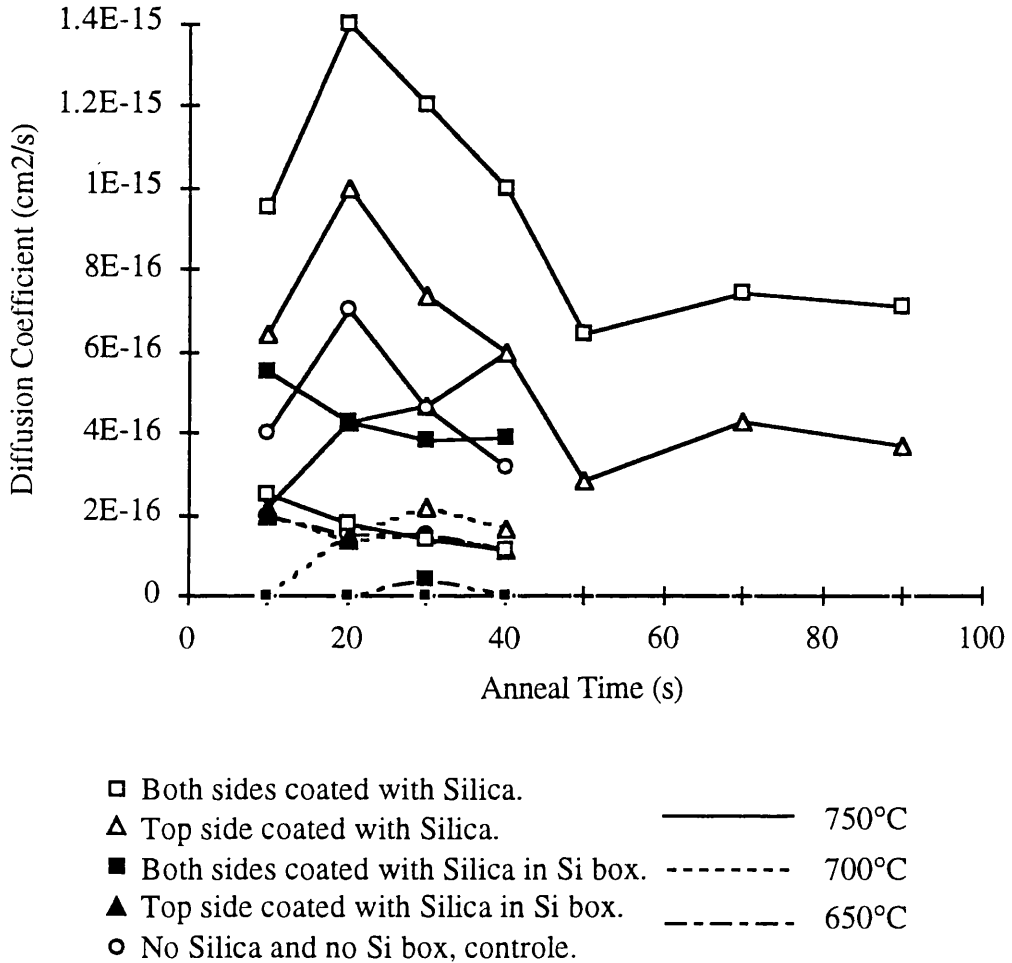


Figure 4.4 Energy shift vs. anneal time for E799 samples with and without coatings of SiO₂ at 600°C, 700°C and 750°C. E799 contains 30 Å InGaAs quantum wells.

Figure 4.4 shows the diffusion coefficients calculated using the method described in Chapter 3. Again the red shift was not explained with the model so a diffusion coefficient could not be calculated for anneals resulting in a red shift.

Figure 4.5 shows the set of photoluminescence curves measured from samples of wafer E799 annealed at 650°C for up-to 90 seconds. The 20 to 30 meV red shift observed was an

unexpected result, even though smaller red shifts had been observed in wafer E791 (90 Å QWs). The increased red shift can be explained by the fact that the QWs in wafer E799 are 30 Å instead of 90 Å as in wafer E791. The reduced thickness of the well material would mean that less group III diffusion would be required to reduce the bandgap of the well section, observed as a reduction in the PL emission energy.

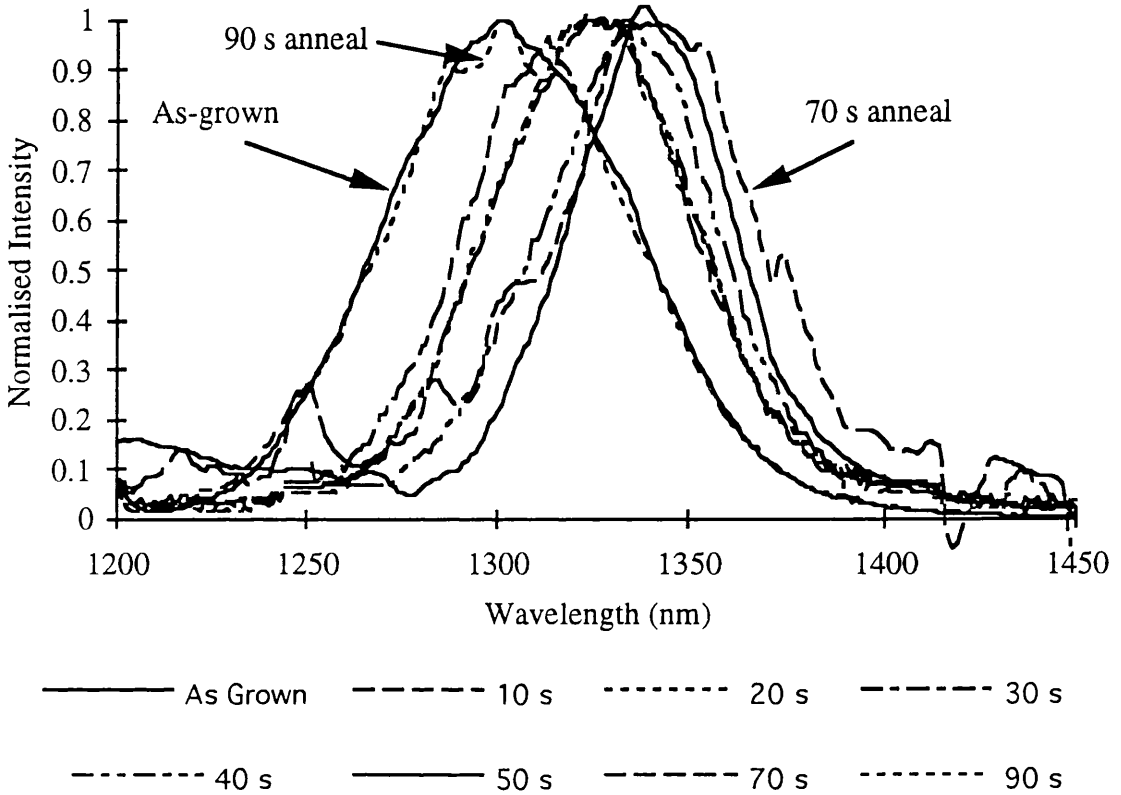


Figure 4.5 PL curves showing the red shift indicated in Figure 4.3.

4.3.3 Wafer E795 Anneal Results

Figure 4.6 shows the effect of annealing a sample with the same well thickness as wafer E799, but with the same well composition as wafer E791. A relatively large red shift is also observed in this wafer when it is annealed at 650°C, although the shift in energy is smaller than that observed in wafer E799. This result suggests that the strain in the structure is slowing down the group III intermixing process since there is a larger chemical potential across the well barrier heterointerface in wafer E795 than in wafer E799; a larger potential difference would suggest that a greater change in energy is possible in the well material.

The diffusion coefficient has not been calculated for structure E795, the effects of strain on the energy level in the disordered structure have not been taken into account. In order to take these effects into account the diffusion properties of each atomic species in the structure would have to be known.

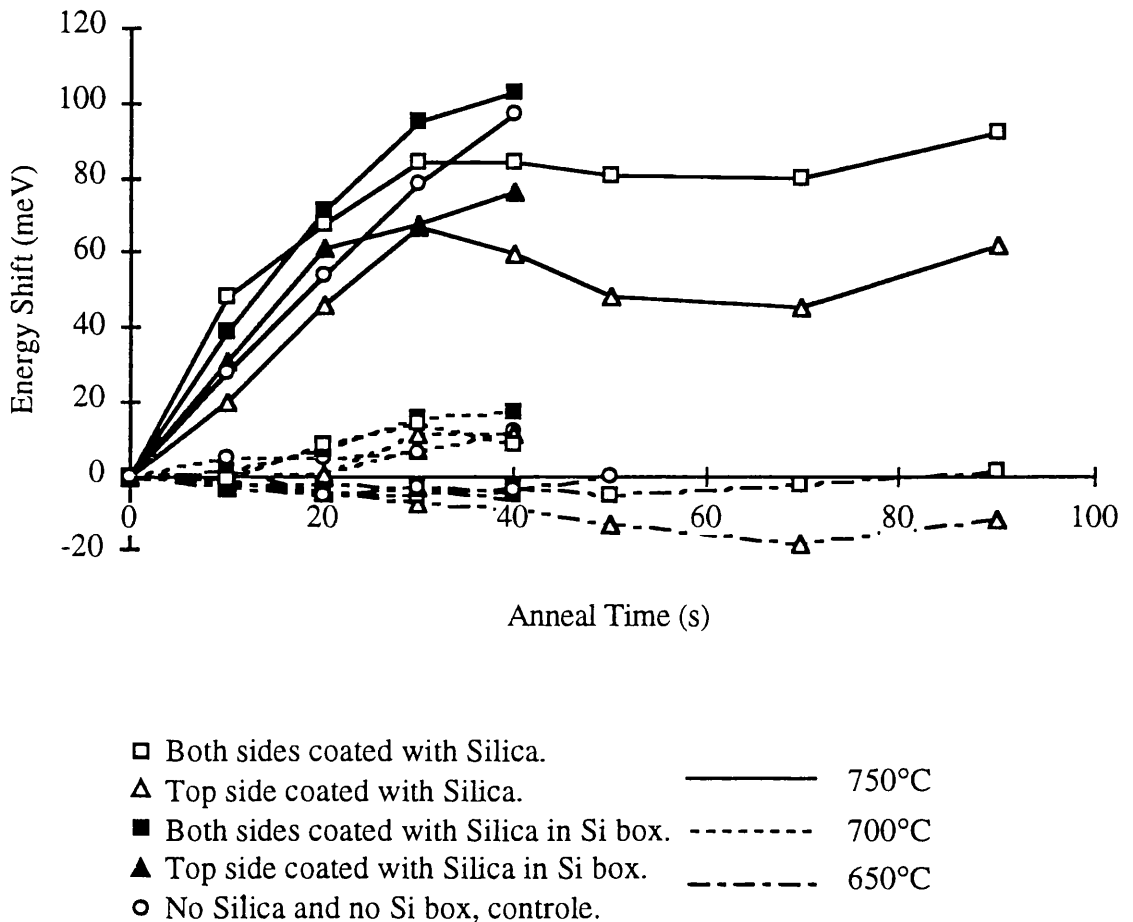


Figure 4.6 E795 A Strained Structure.

4.4. Silicon Nitride Caps

The following set of results compare the effects of silicon nitride caps with silica and strontium fluoride, on various QW laser structures. The diffusion effects are investigated when annealed by RTP, and a simple oxide stripe laser is tested that has been bandgap shifted using a silicon nitride cap.

Silicon nitride has been shown to intermix InGaAs/InP QW structures previously by Miyazawa et al¹. A 55 nm wavelength shift of the QW structure was observed between a sample coated with silicon nitride and one that was uncoated but otherwise processed in the same way, however, the uncoated sample also bandgap shifted by approximately 40 meV. The extra 40 meV shift is undesirable, for most situations.

The effects of strontium fluoride on the intermixing rate are also investigated in this section. Strontium fluoride has been shown by Beauvais et al² to increase the thermal stability in GaAs/AlGaAs; this would be a desirable effect in the InP based quaternaries since it would allow for larger bandgap shifting in unprotected areas.

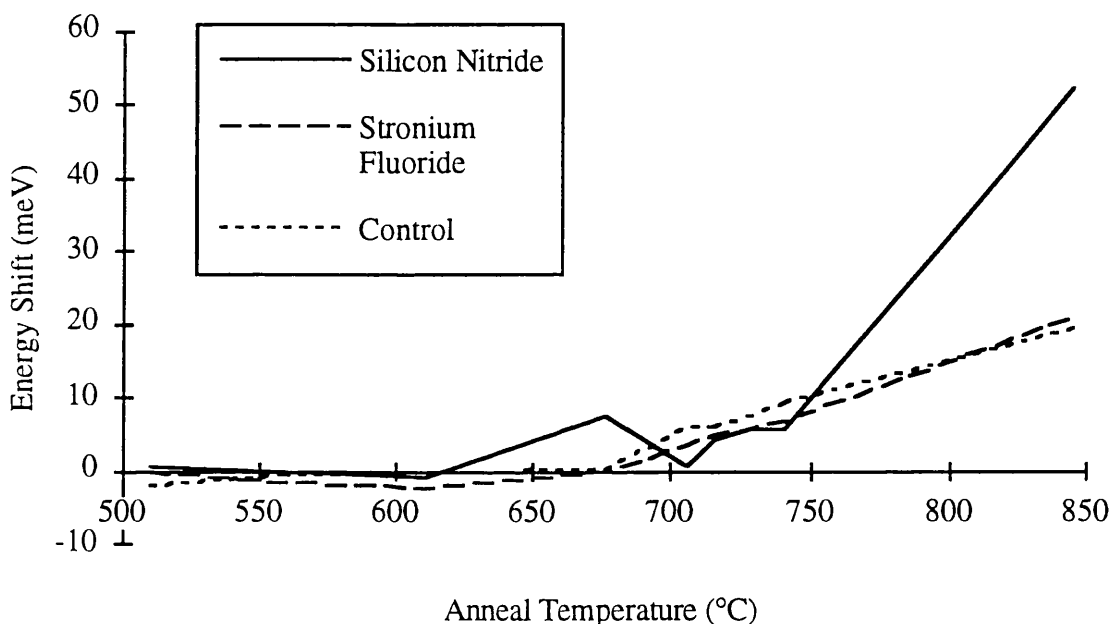


Figure 4.7 E269 30 second anneals with different 1000 Å of dielectric capping layers. The control sample had no dielectric cap.

Figure 4.7 shows a comparison between samples of E269, containing 4 100Å InGaAs QWs, coated with either silicon nitride, strontium fluoride, or with no cap. Up to around 750°C there is no significant difference in the behaviour of the three dielectric caps. Above 750°C, however, it is clear that silicon nitride is causing an increase in the diffusion coefficient in the QW structure. Although it was shown by Beauvais et al that strontium

fluoride can increase the thermal stability of GaAs/AlGaAs structures, unfortunately this is not the case in the InGaAsP/InGaAs system.

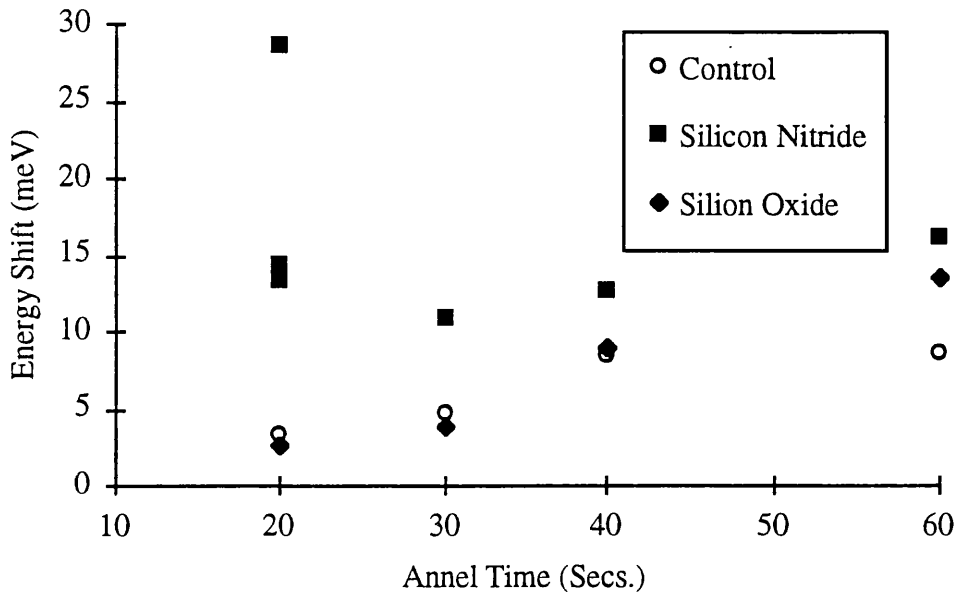


Figure 4.8. Wafer E288 annealed at 700°C for between 20 and 60 seconds with a 1000 Å dielectric caps of either silicon nitride or silicon oxide.

To take advantage of the large shifts produce by the silicon nitride caps conditions must be found where disordering can be confined to specific areas. Figure 4.8 shows that for short anneals, it is possible to produce a modestly large shift of 15 meV in the PL peak for silicon nitride capped structures with only a relatively small shift in silica or uncapped structures of around 2-3 meV, i.e. a difference in bandgap of around 12 meV. Figure 4.9 shows the diffusion coefficients for the experimental results shown in Figure 4.8, calculated in the same manner as described in Chapter 3.

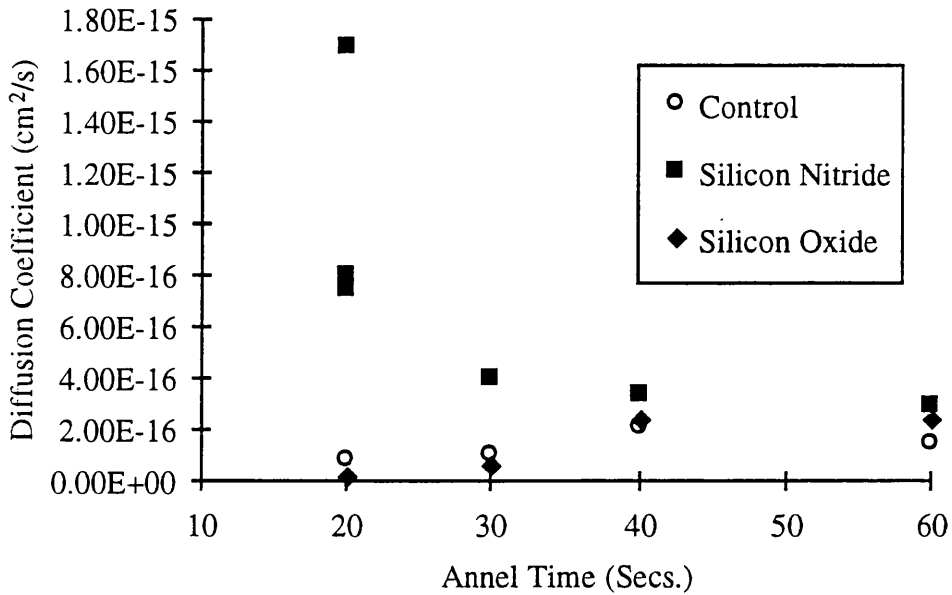


Figure 4.10. Diffusion coefficients of wafer E288 annealed at 700°C for between 20 and 60 seconds with a 1000 Å dielectric caps of either silicon nitride or silicon oxide.

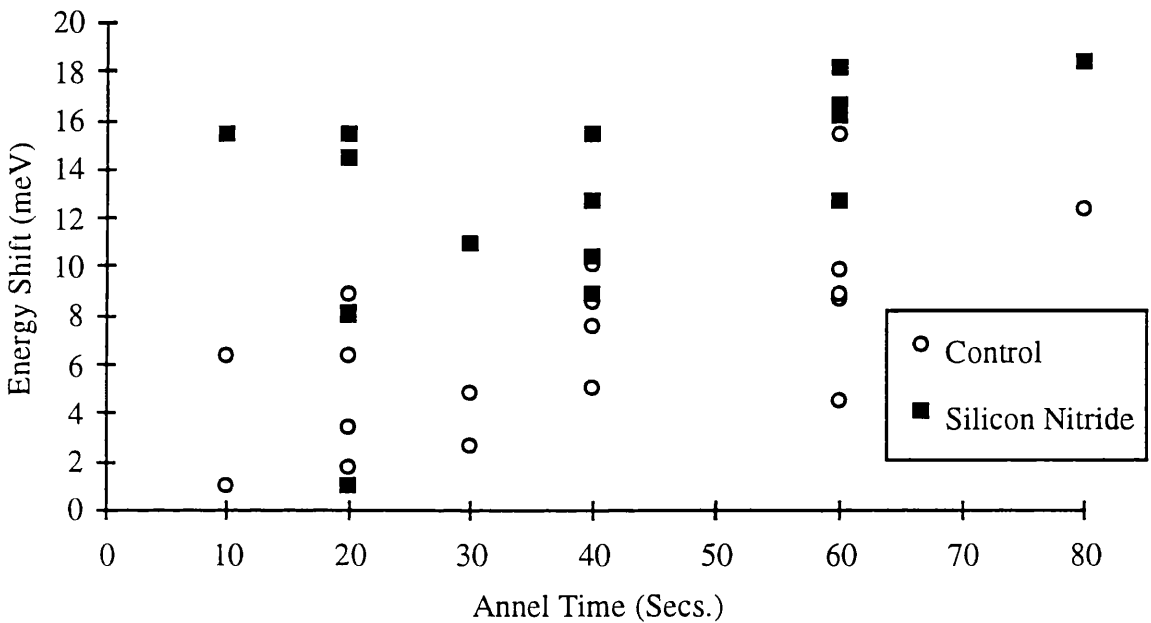


Figure 4.10. Combine Nitride Results at 700°C.

The main problem with this type of disordering is the spread of results which, for small overall shifts can be a serious problem. Figure 4.10 and 4.11 show a summary of several experiments run to find the reproducibility of the energy shifts. From these results it is clear that nitride causes an increase in the disordering process for short anneal times, whilst oxide has little effect, but the spread is typically between 5 and 10 meV.

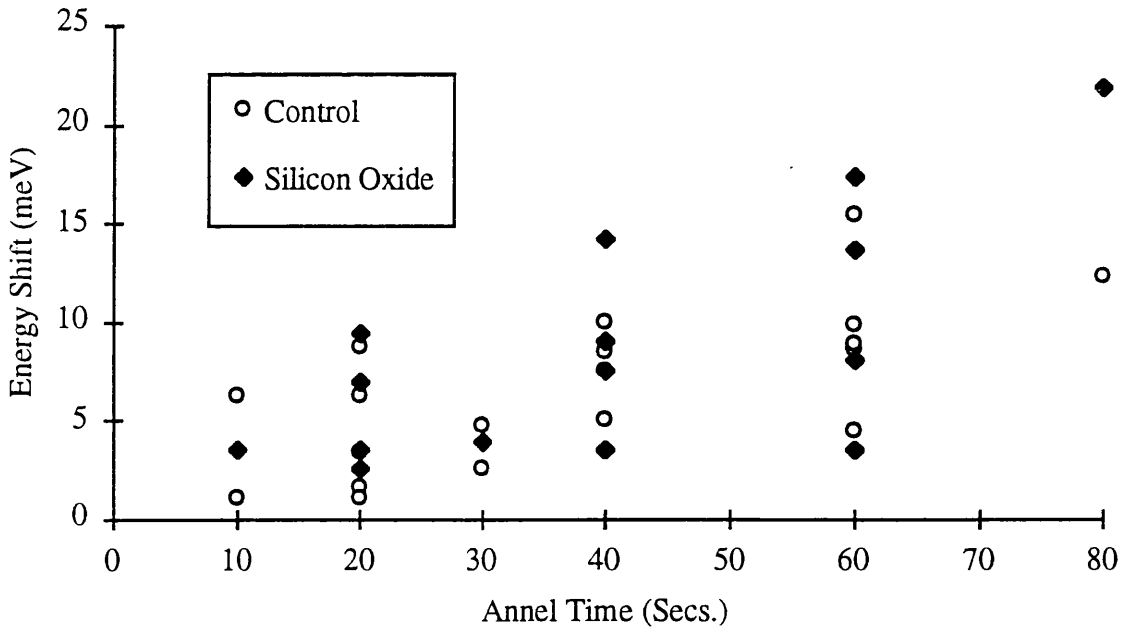


Figure 4.11 Combined Oxide and Control results at 700°C.

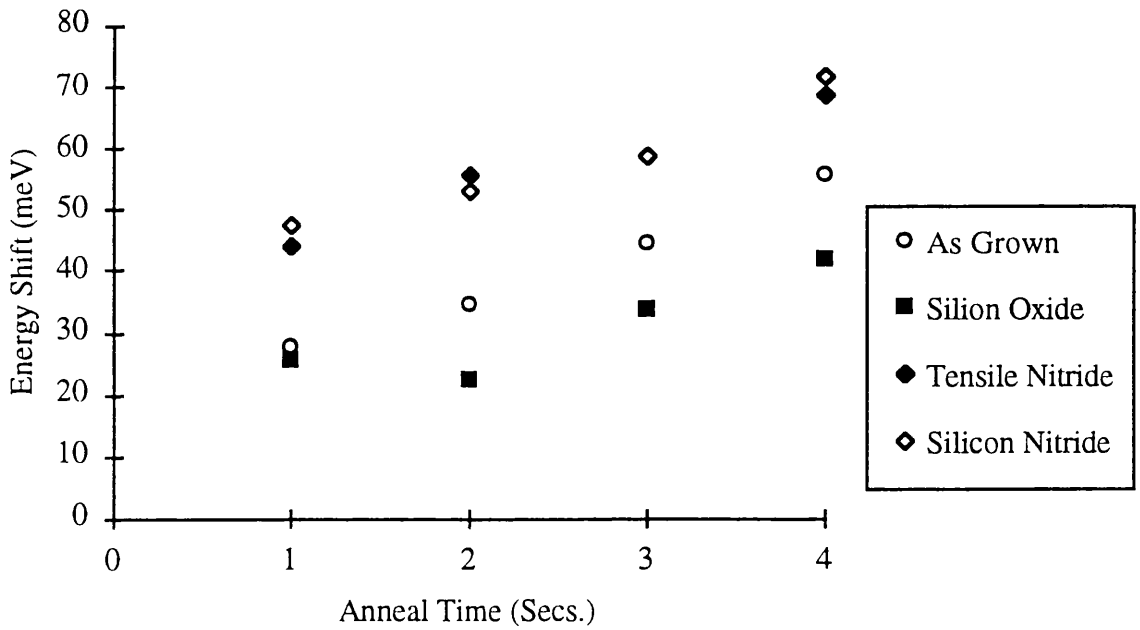


Figure 4.12. Room Temperature PL E795 @ 800°C.

Figure 4.12 shows room temperature PL results for anneals on the strained narrow well structure E795. The energy shifts observed here are larger than those seen in previous experiments; this is due to the thin wells and the elevated anneal temperature of 800°C. It

can be seen that silicon oxide appears to be suppressing the intermixing process compared to uncapped samples. Also on this sample two alternative nitride layers were investigated, the first being a conventional structure which produces only a nominal strain on the surface of the sample at room temperature, the second deposited in such a manner as to produce tensile strain (1%) on the sample surface at room temperature. The different strained dielectrics were used to see if strain caused by the nitride layer is responsible for the intermixing process.

Figure 4.13 show the results of samples annealed at 750°C with the same dielectric caps as in the previous Figure. These results again demonstrate that the nitride strain appears to have little effect on the disordering process, and that the oxide layer appears to have the effect of reducing the disordering especially for very short diffusion times.

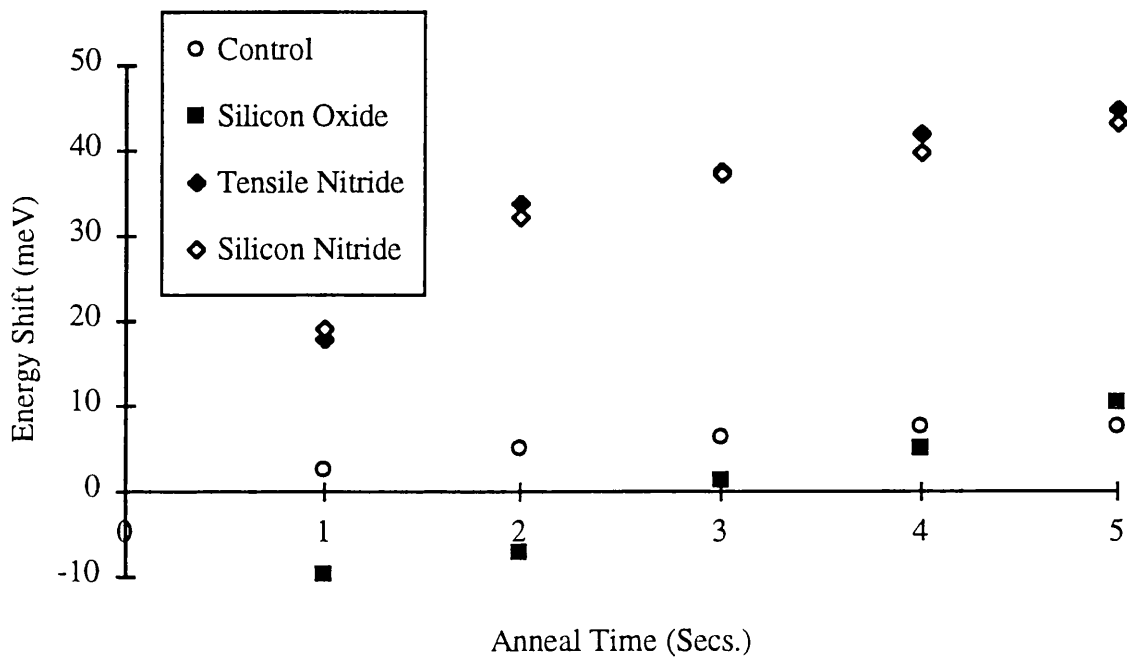


Figure 4.13. Room Temperature PL E795 @ 750°C.

4.5 Dielectric Cap Disordered Lasers

A sample of wafer E795 was disordered using a silicon nitride cap and annealed for 5 seconds at 750°C. A 75µm oxide stripe laser was fabricated out of the disordered material as well as the as-grown material to see how the characteristics of a laser that had been

bandgap shifted altered from the as-grown case. The fabrication technique used for oxide stripe extended cavity lasers is covered in Chapter 7.

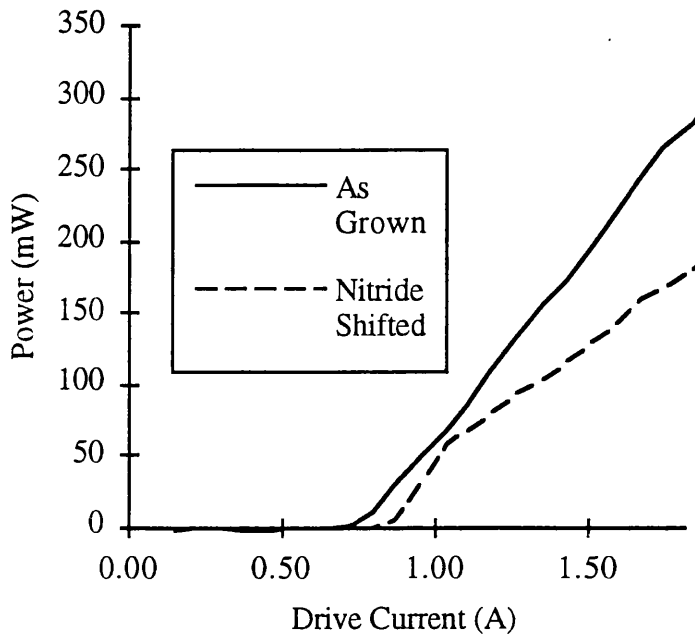


Figure 4.14. Laser characteristic of disordered and non disordered device.

The graph in Figure 4.14 shows that a remarkably low difference in threshold current is achievable with a disordered laser structure. The as-grown sample has a threshold current of 0.75 A whereas the disordered laser has a threshold current of 0.85 A. The measurements were taken as in Chapter 8.

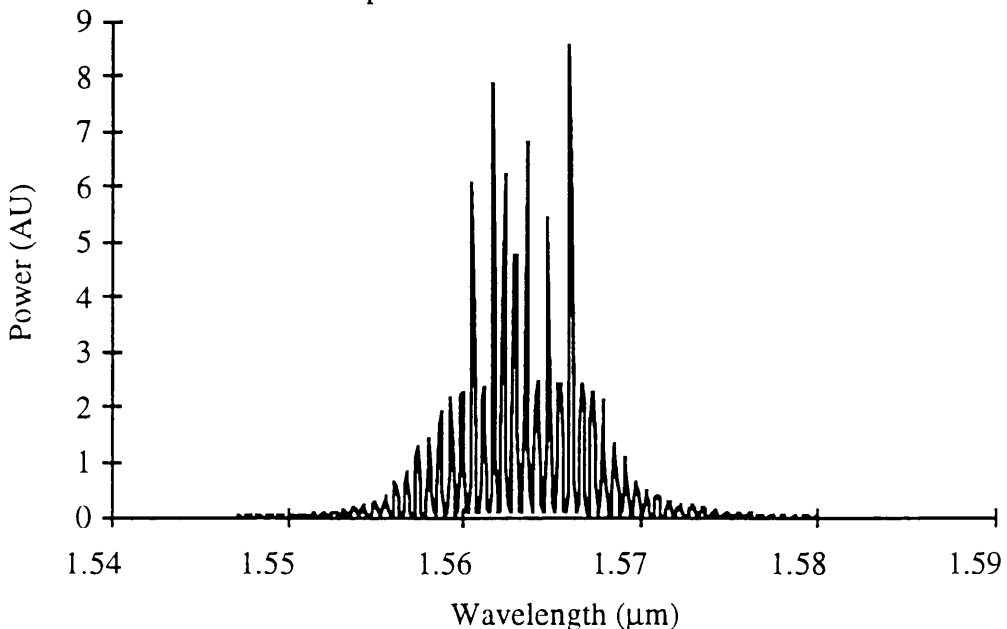


Figure 4.15. Spectrum of as-grown sample 75µm oxide stripe laser at 1.5 A/

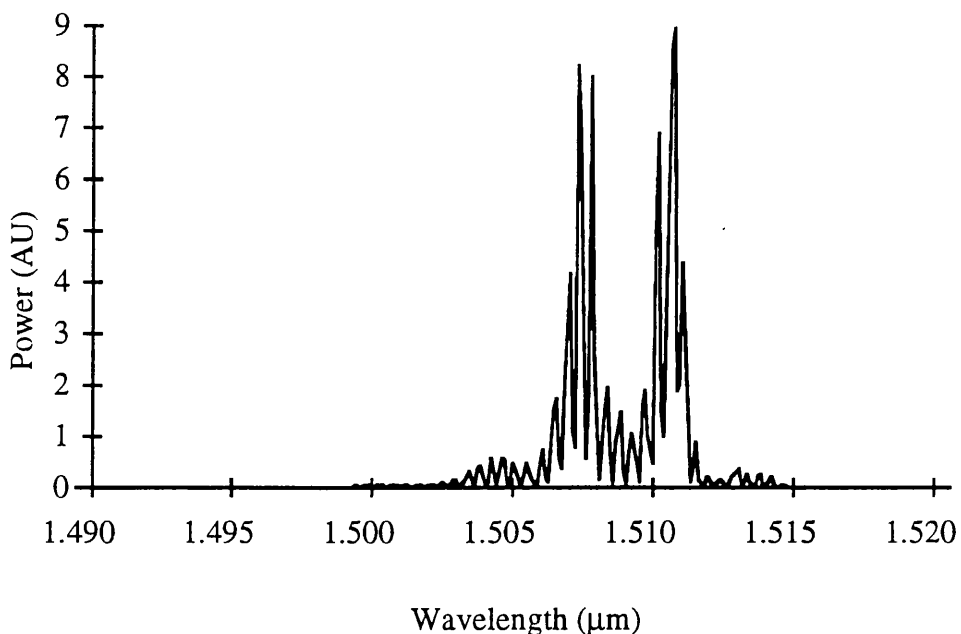


Figure 4.16. Spectra of laser disordered with Silicon Nitride. 1.5 A drive current.

Even though the wavelength of operation has been shifted by approximately, 56 nm (30 meV) from 1.565 μm to 1.509 μm , the threshold current has only increased by 100 mA (12%).

This technique for widening the bandgap of QW structures will not be a good technique to produce passive waveguides because the structure remains electrically active, however this does appear to be a good method for changing the wavelength of operation after growth, also for applications where electrical activation is required but not lasing action e.g. modulators.

4.6. Conclusions

- Silicon nitride can be used to disorder QW structures. Selective disordering occurs for anneal time less than 5 seconds at 750°C. Annealing above this temperature will cause the silica capped structures to thermally disorder, as will annealing for longer times at 750°C. Oxide stripe lasers have been fabricated from material that has been disordered by thermal treatment with a silicon nitride cap, as shown above.
- The dielectric disordering process appears to be a relatively weak process. It is most effectively employed on laser structures containing thin quantum wells, with or without strain.

- The strain in the silicon nitride caps, at room temperature, used in this section appears to have little effect on the intermixing process.
- Structures disordered using silicon nitride caps followed by thermal processing maintain good optical and electrical characteristics as evidenced by the characteristics of bandgap shifted lasers.
- Unlike the GaAs and related systems, a silica cap does not enhance intermixing in the InGaAsP material system. Little effect has been observed with the silica caps except for an improved surface morphology after annealing at temperatures over 700°C, when compared to the surface of samples annealed with no cap.

References

¹'Integrated External-Cavity InGaAs/InP Lasers Using Cap-Annealing Disordering', T. Miyazawa, H. Iwamura, and M. Naganuma, IEEE Photonics Tech. Lett., **3**(5), pp. 421-423, 1991.

²Suppression of Bandgap Shifts in GaAs/AlGaAs Quantum Wells Using Strontium Fluoride Caps', J. Beauvais, J.H. Marsh, A.H. Kean, A.C. Bryce, and C. Button, Electron. Lett. **28** (17), pp. 1670-1672, 1992.

Chapter 5

Design and Fabrication of Single-Mode Waveguides for Fabry-Perot Loss Measurements

5.1 Introduction

The design and fabrication of a single-moded waveguide structure is described in this Chapter. Although the aim of this part of the work was to produce a single mode ridge waveguide suitable for Fabry-Perot loss measurements (Chapter 6), the principles could equally well be applied if the structure was to be a single transverse mode laser.

In this Chapter an introduction to waveguide theory will be given, followed by a brief description of the two programs used to design the waveguides. The two computer programs used are called Fourlay and FWave. Fourlay is a program written by B.Bhumbra of this Department, and adapted by the author, which calculates the mode depth and slab refractive index in a structure containing up to four layers. Fourlay can also be used to model two dimensional confinement using the effective index method. FWave, written by M.R.S. Taylor also of this Department, uses a finite difference model to solve the vector EM equations of ridge structures containing multiple layers. Results are presented from both programs and an explanation of the fabrication process is given.

5.2 The Slab Waveguide

This section gives a brief introduction to waveguide theory for slab waveguides. For a more detailed treatment, the reader should refer to the references included in the following section. The slab structure is very important in the realisation of optoelectronic devices: it is from a slab that many different devices are fabricated. First the three layered slab is introduced due to the simple nature of the analysis, this is followed by the extension to a four layered structure which is of more general interest.

5.2.1 The Three Layered Slab

Figure 5.1 illustrates a slab waveguide. It consists of three layers of a dielectric where

$$n_1 < n_2 > n_3, \tag{5.1}$$

n_l is the refractive index of layer l .

In Figure 5.1 a slab waveguide mode exists when the secondary plane wave i.e. the wave after two reflections, is in phase with the primary wave. The condition required for this is easily found and will be briefly outlined.

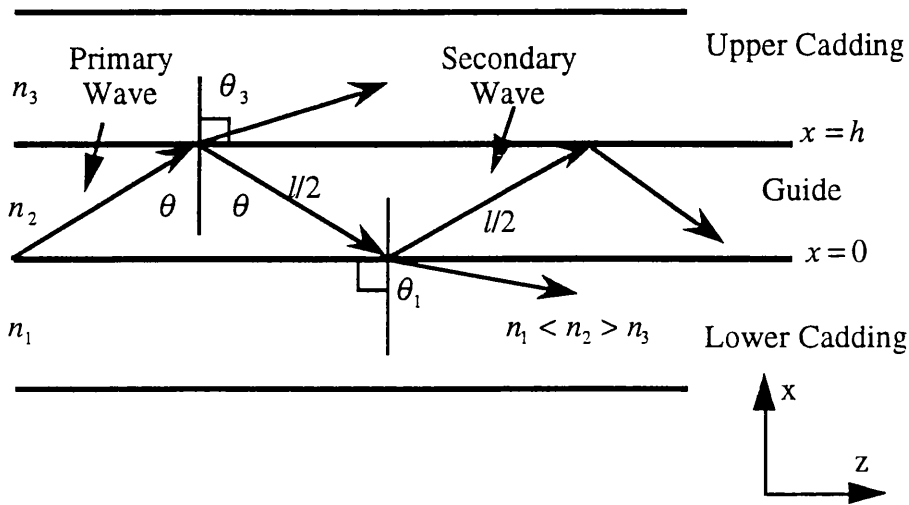


Figure 5.1. A three layered slab waveguide used to model light propagation.

At the n_2/n_1 and the n_2/n_3 interfaces the plane wave is totally internally reflected. This leads to a purely phasor Fresnel reflection coefficient¹ with a phase change denoted by ϕ_1 and ϕ_2 respectively. As well as the phase change due to total internal reflection, there is a phase change of n_2kl which is due to the propagation of the plane wave a distance l ; this can be related to the waveguide thickness (h) by simple geometry,

$$l = 2h \cos(\theta), \tag{5.2}$$

where θ is the angle between the waveguide normal and the direction of propagation of the plane wave, and k is equal to $2\pi/\lambda_o$, where λ_o is the free space wavelength of the light. If the total phase shift after two reflections is equal to a multiple of 2π , then the primary wave and secondary wave will add in-phase which results in the propagation of a guided wave. This is expressed in Equation 5.3,

$$2n_2kh \cos(\theta) + \phi_1 + \phi_2 = 2q\pi \quad (5.3)$$

where $q = 0, 1, 2, 3, \dots$. This is commonly referred to as the *Characteristic Equation* of the waveguide. The solution of Equation 5.3 leads to the modal refractive index and propagation constant^{2,3} of the guided modes. Substituting the Fresnel reflection coefficients in Equation 5.3 yields,

$$n_2kh \cos(\theta) - \tan^{-1} \left[j \frac{n_3 \cos(\theta_3)}{n_2 \cos(\theta)} \right] - \tan^{-1} \left[j \frac{n_1 \cos(\theta_1)}{n_2 \cos(\theta)} \right] = q\pi, \quad (5.4)$$

where the phase changes ϕ_1 and ϕ_2 have been written out in full for the TE mode. The Fresnel reflection coefficients of the TE and TM modes are derived in ref⁴. For the TM modes Equation 5.4 becomes

$$n_2kh \cos(\theta) - \tan^{-1} \left[j \frac{n_2 \cos(\theta_3)}{n_3 \cos(\theta)} \right] - \tan^{-1} \left[j \frac{n_2 \cos(\theta_1)}{n_1 \cos(\theta)} \right] = q\pi. \quad (5.5)$$

A recap of Snell's law shows that $\cos(\theta_3)$ is negative and imaginary since total internal reflection is assumed to be taking place. Snell's law is

$$n_2 \sin(\theta) = n_3 \sin(\theta_3). \quad (5.6)$$

The largest real value of $\sin(\theta_1)$ is 1; the largest angle of incidence before total internal reflection occurs is therefore,

$$\sin(\theta) = \frac{n_1}{n_2} = \sin(\theta_c) \quad (5.7)$$

where θ_c is the critical angle. If θ is greater than the critical angle, Snell's law implies that $\sin(\theta_1)$ must be greater than 1, which can only happen if θ_1 is complex i.e. the field

does not propagate into the cladding. Instead it is said to be evanescent, decaying exponentially. So using the relation,

$$\cos(\alpha) = (1 - \sin^2(\alpha))^{1/2} \quad (5.8)$$

and for $\sin(\theta_1) > 1$,

$$\cos(\theta_1) = \cos(\theta_3) = -\text{Imaginary}. \quad (5.9)$$

For small differences in the refractive indices of the slab layers $n_1/n_2 \approx n_2/n_1$ and $n_3/n_2 \approx n_2/n_3$, Equations 5.4 and 5.5 are approximately equal which means that we can use either equation to find the effective index of TE and TM modes. This is the *Scalar Approximation*.

5.2.2 The Four Layered Slab

A more useful structure than the three layered waveguide is the four layered waveguide. This is the general type of structure used in this thesis: the bottom layer is the lower cladding, the second layer the active region (itself being made up of many layers), the third the upper cladding layer and finally the air. We have to take into account the air layer here because, when a ridge waveguide is fabricated, we can no longer assume that the field in the upper cladding layer decays to zero, especially in the regions on either side of the ridge where the upper cladding is sometimes completely removed. Hewark et al⁵ have analysed four layered structures, the characteristic equation becoming,

$$\begin{aligned} k_2 h = & \tan^{-1} \left[\frac{\eta_1 k_1}{\eta_2 k_2} \right] \\ & + \tan^{-1} \left[\frac{\eta_3 k_3}{\eta_2 k_2} \cdot \frac{e^{k_3 d_3} (\eta_3 k_3 + \eta_4 k_4) - e^{k_3 d_3} (\eta_3 k_3 - \eta_4 k_4)}{e^{k_3 d_3} (\eta_3 k_3 + \eta_4 k_4) + e^{k_3 d_3} (\eta_3 k_3 - \eta_4 k_4)} \right] \\ & + q\pi \end{aligned} \quad (5.10)$$

where η_i is a term which enables the same equation to be used for TE and TM modes (not the scalar approximation)

$$\begin{aligned}
\eta_i = 1 & \quad : \text{ TE modes} \\
\eta_i = \frac{1}{n_i^2} & \quad : \text{ TM modes}
\end{aligned}
\tag{5.11}$$

and $\cos(\theta_i)$ is replaced by $k_i = \frac{2\pi}{\lambda_o} \cos(\theta_i)$.

The roots of the above equation will thus yield the refractive index of any TE or TM mode of propagation for a symmetric or nonsymmetric waveguide. This is the equation solved in Fourlay.

Equation 5.10 is derived by applying the boundary conditions for the electric and magnetic fields i.e. the tangential components of \mathbf{E} and \mathbf{H} must be continuous at the interfaces.

5.3 The Ridge Waveguide

The theory of the previous section is exact. It is used to calculate the number of modes in a slab structure for pure TE and TM modes. Unfortunately we are not interested in the slab waveguide in most devices, instead we want to calculate the number of modes in a ridge type structure where there is both vertical and lateral light confinement. We are no longer dealing with purely TE or TM mode propagation: from the ray model it can be seen that \mathbf{E} is no longer perpendicular to the direction of propagation (in the x direction) but will have components in the y and z directions also, the size of which depends on the exact trajectory of the ray. These components are generally much smaller than the component along the x direction, so the modes are referred to as being *quasi-TE* and *quasi-TM* modes and can be approximated as TE and TM modes. There is no exact solution to the ridge waveguide problem as there is with the slab waveguide. There are, however, numerical calculations which can be performed to analyse ridge waveguide structures. The following two sections introduce the two techniques used to analyse ridge waveguides in this thesis; these are the effective index method and the finite difference method.

5.3.1 The Effective Index Method

The effective index method (EIM)^{6,7} provides a quick and simple way of analysing a ridge waveguide or similar. The procedure is as listed below;

1. The ridge is split into three sections as illustrated in Figure 5.2: a central section, Region 2, containing the ridge, and two sections one either side of the ridge, Region 1 and Region 3.
2. Each section is taken to be a slab waveguide with upper cladding regions of thickness a in Region 2 and of thickness b in Region 3 and Region 1. Using the above theory, the waveguide index of each slab section can be calculated. If the quasi-TE mode is to be analysed the TE equations are used at this stage (an exact result is obtained here for the true TE mode of the slab).
3. The structure is now considered to be equivalent to a symmetric slab waveguide with refractive indices equal to the slab indices calculated in the previous step. This is where the approximation is introduced into the calculation. The TM mode equations are used at this point since we are looking at the waveguide in an orthogonal direction to that of step 2. The resulting effective index calculated here is that of the guided quasi-TE mode.

The approximation is very good for modes far from cut-off, but predicts that the mode will be cut-off under slightly weaker guiding conditions than that predicted by more accurate numerical solutions⁸. Either TE or TM calculations may be performed in steps 2 and 3 if the scalar approximation is being used. This is often a good approximation in semiconductor devices since the refractive index difference between layers is generally small.

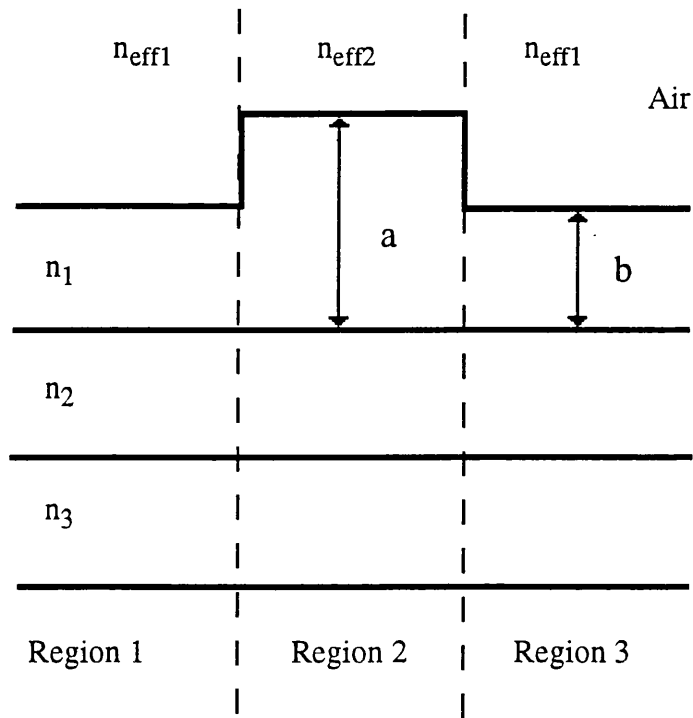


Figure 5.2 Ridge waveguide showing areas used in the effective index approximation.

5.3.2 The Vector Finite Difference Method

The finite difference method is a technique where the vector electromagnetic wave equation is solved by splitting the structure into a fine mesh. The calculation is very intensive of computational power and, although it produces more accurate results than the effective index method, it does take some time to run. The smaller the mesh size used, the greater the accuracy of the results, but the greater the computational power required! A good review of the design of waveguides can be found in reference⁹.

5.4 Waveguide Design

The following Section outlines the actual waveguide design procedure, using the programs Fourlay and FWave.

5.4.1 The Starting Material

The basic slab structure in which the ridge waveguide is to be designed has been described previously in Section 5.2.1. A problem with the techniques discussed above for analysing

the waveguide is that neither of them can cope with QW structures because they cannot deal with the quantisation effects on the refractive index. To overcome this problem, the QWs are replaced with an averaged layer. Figure 5.3 shows the simplification of the actual structure. Due to averaging of the material in the guiding region, removing the quantum well structure, we have introduced an approximation which must be kept in mind when analysing the results.

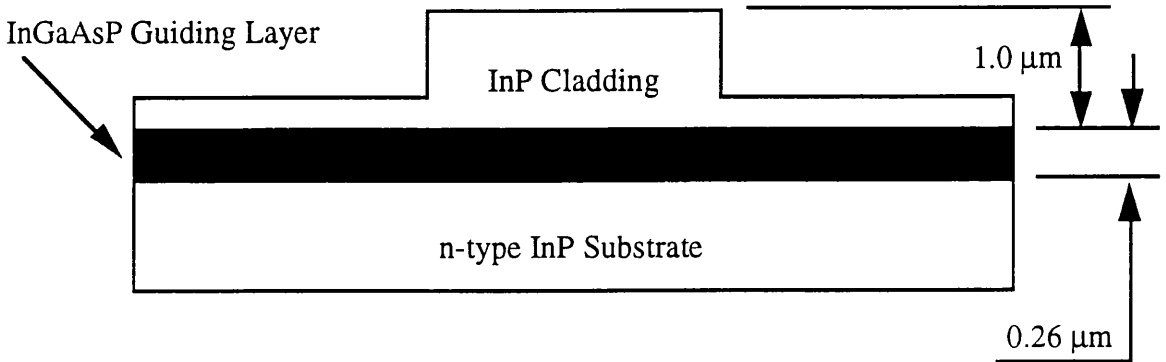


Figure 5.3 The simplified structure used to model a MQW waveguide.

The model used to average the refractive index of the active layer is the weighted rms model¹⁰, for TE modes this is

$$n_{TE} = \sqrt{\frac{n_w^2 L_w + n_b^2 L_b}{L_w + L_b}}, \quad (5.12)$$

whilst for TM modes it is,

$$n_{TM} = \sqrt{\frac{(L_w + L_b)n_w^2 n_b^2}{n_w^2 L_w + n_b^2 L_b}}. \quad (5.13)$$

5.4.2 Fourlay Calculations

Fourlay calculates the effective index and mode depth of a four layered structure using slab waveguide mode theory. The program can be used to calculate the mode propagation coefficients in a ridge structure by using the effective index method described in Section 5.3.1. To get a clearer picture of the behaviour of ridge waveguides, the program was

modified to calculate the mode depth and refractive index as a function of ridge width and etch depth. The resulting data is readily converted to graphical form as can be seen below.

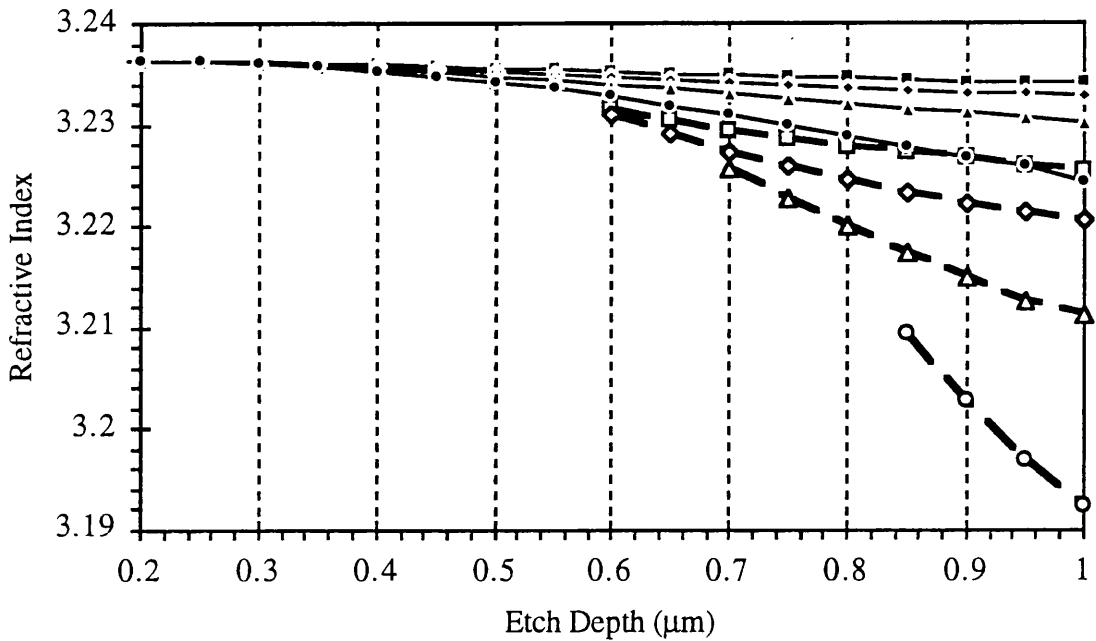


Figure 5.4 Results from Fourlay showing the variation in effective index of the SCH material structure with etch depth. The key to the graph is as follows

The broken lines correspond to the first order modes (TE_{01}), the solid lines to the zeroth-order modes (TE_{00})-

The symbols correspond to different ridge widths as follows,

▪ or □	5μm ridge
◆ or ◇	4μm ridge
▲ or △	3μm ridge
• or ○	2μm ridge

Figure 5.4 shows the effect of varying the etch depth for various ridge widths for an InP upper cladding layer depth of 1.0 μm and an averaged active layer thickness of 0.26 μm. The Refractive index of InP was taken to be 3.16886 and the index of the averaged

InGaAsP was taken to be 3.4067. From Figure 5.4, it can be seen that the etch depth at which the first order mode (TE_{01}) becomes cut-off for a 3 μm ridge width will lie somewhere between 0.575 μm and 6.0 μm . This is only approximate because; firstly, the effective index approximation has been used, secondly, the scalar approximation has been used, and finally, the analysis has only been carried out for etch steps of 0.05 μm . The result is still useful, however, since it gives a good indication of the mode characteristics as the ridge width and etch depth are varied. A more accurate analysis is performed later using FWave.

Figure 5.5 shows the variation of mode width with the etch depth for various ridge widths. The graphs in Figure 5.4 and 5.5 can be used simultaneously to find the conditions for the ridge to be single-moded and to have reasonable confinement. It is important to have strong confinement in low loss guides to reduce scattering due to discrete defects¹¹.

For example, a 3 μm ridge structure would be single-moded for etch depths up to 0.65 μm giving a minimum mode width of approximately 6 μm . A greater etch depth would cause stronger confinement of the zeroth-order mode, but the guide would also support the first-order mode. For a 2 μm ridge the guide would be single-moded up to an etch depth of 0.8 μm and have a mode width of approximately 3 μm , and again any further etching would increase the strength of the guide enabling it support two modes. So a compromise has to be struck between mode confinement and ridge width: in practice the narrower the ridge the more difficult it becomes to fabricate. Ridges of around 3 μm are relatively easy to make, but below this limit the task becomes much more difficult because problems start to occur due to the difficulty in producing a photolithographic etch mask.

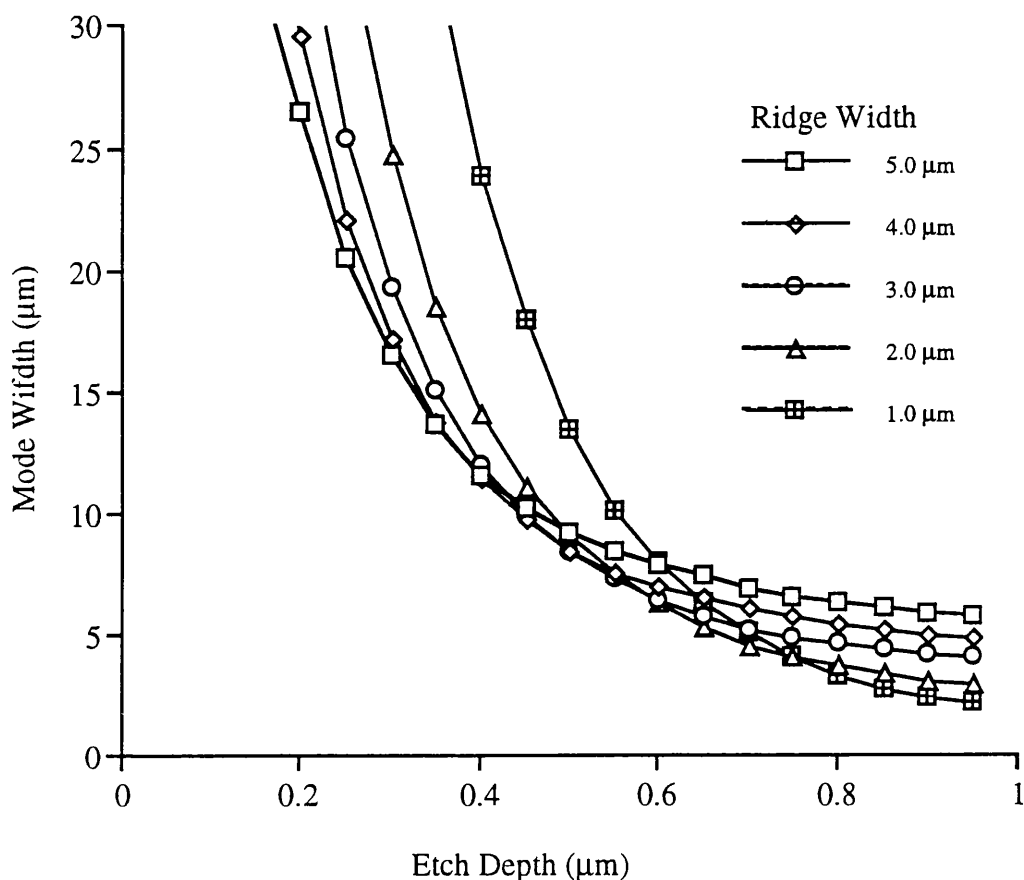


Figure 5.5 Results from Fourlay showing the variation in mode thickness of the zero order modes of the SCH material structure with etch depth.

5.4.3 FWave Calculations

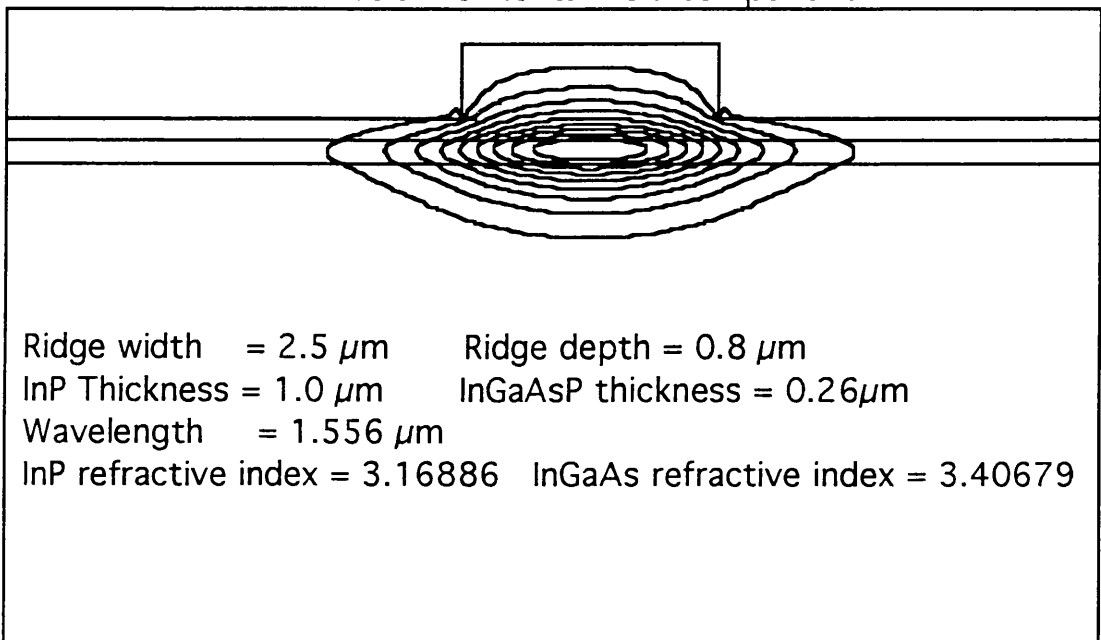
FWave, written by MRS Taylor, uses a numerical finite difference technique to solve the vector EM equation. The program is limited because it is unable to handle thin layers and will therefore suffer from some of the same problems as Fourlay, however it will produce more accurate results for a given structure than the EIM. It is possible to develop the finite difference method by varying the mesh size across the structure allowing thin layers to be considered. however the effects of quantum confinement on the refractive index are still not being taken into account because it is not known exactly what these are. If the effect of quantum confinement on refractive index were known more accurately then this could be used in the program and the calculation would be improved.

Figures 5.6 and 5.7 show two contour plots of the electric field calculated by the program for a guide of the same structure as Figure 5.3. Figure 5.6 shows the zeroth-order TE

mode, and Figure 5.7 the first-order TE mode. The zeroth-order mode has a modal refractive index of 3.23306 according to FWave, but 3.23091 with Fourlay, the difference being due to the approximations inherent in the EIM. A similar discrepancy is seen for the first order mode, FWave giving a waveguide index of 3.2202 whilst Fourlay gives 3.21739.

Due to the length of time required to run FWave, it has been found that the best way to use the program is to find approximately the design of waveguide from Fourlay and then, if further accuracy is required, use FWave.

Plot of horizontal field component.

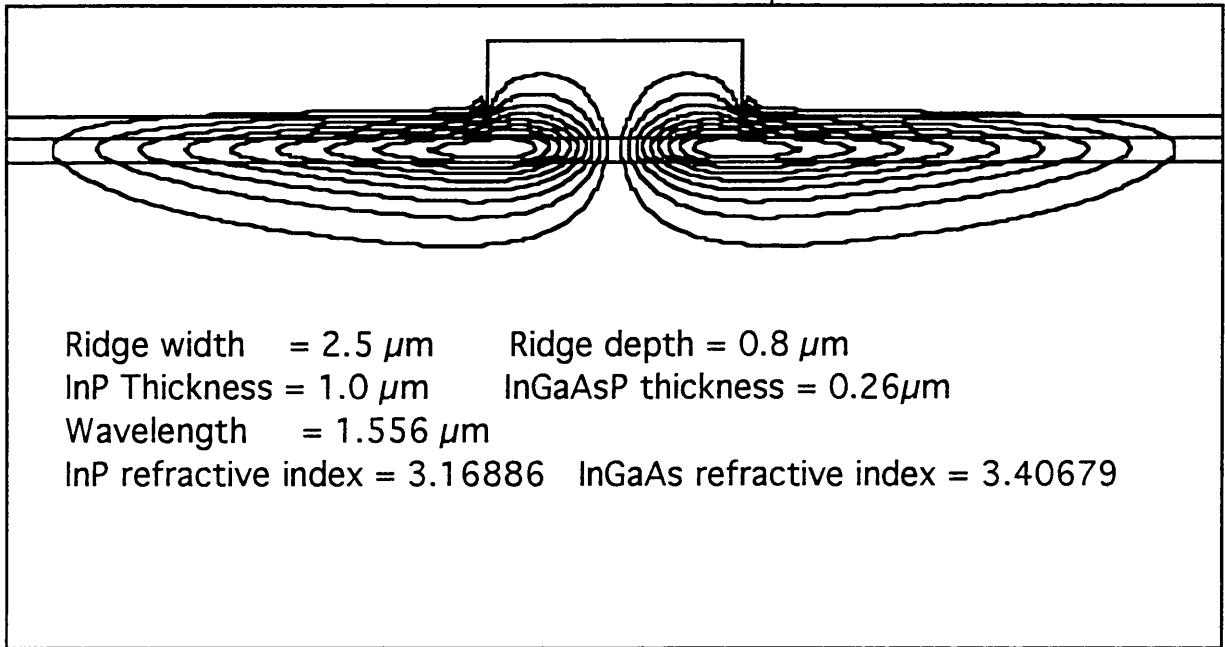


Effective index = 3.23306

Peak field = 1.00826

Figure 5.6 Output from FWave showing the first TE mode for the guide indicated.

Plot of horizontal field component.



Effective index = 3.22002

Peak field = 0.77643

Figure 5.7 Output from FWave showing the second TE mode for the guide indicated.

5.5 Fabrication Of The Waveguides

The mask used to fabricate the waveguides contained stripes with various widths ranging from $1 \mu\text{m}$ to $10 \mu\text{m}$, the reason for this being that if the dry etching process under- or over-etched the sample then there would still be a reasonable possibility of finding a single-moded waveguide.

The waveguides are fabricated by the following procedure:

ION IMPLANTATION - fluorine and boron were implanted at Surrey as described Appendix A. Distribution energies and doses are calculated using TRIM¹².

HEAT TREATMENT - the samples are heat treated by the chosen method

CLEANING - before depositing the etching mask the samples are cleaned as follows :

- i five minutes in the ultrasonic bath with trichloroethane
- ii five minutes in the ultrasonic bath with methanol

- iii five minutes in the ultrasonic bath with acetone
- iv the samples are rinsed in RO water, and inspected to see if clean under an optical microscope.

MASK - a photoresist mask is deposited onto the dry samples as follows :

- i primer is spun on at 4,000 rpm for 10 seconds
- ii The primer is Hexadimethylsilylane which is a water soluble adhesion promoter.
- iii S1400-17 resist (Shipley) is spun on at 4,000 rpm for 20 seconds
- iv the sample is baked at 90°C for 30 minutes the samples are left to cool to room temperature.

PATTERNING - the resist mask is exposed to UV. radiation using the mask aligner for 4.5 seconds.

DEVELOPING - the exposed mask is developed for 1 minute in the appropriate developer.

DRY ETCHING - methane hydrogen is used to etch the InP. The etching conditions are as follows:

- i methane to hydrogen ratio, 1 : 5
- ii pressure 14 mTorr
- iii forward power 80 W
- iv DC bias -750 V
- v Temperature 30°C

The resulting etch rate is approximately 480 nm/min.

THINNING - a 3 µm alumina grit on a flat glass plate is used to thin the samples which results in thinning at a rate of approx. 15 µm/min

CLEAVING - the samples are now ready to be cleaved.

The above method has been chosen for simplicity and good results. However the more conventional approach is to:

- i lay down a thin layer of SiO_2 ($\approx 1000 \text{ \AA}$) after step 3.
- ii follow steps 4 to 6 to lay down a photoresist mask.
- iii etch the SiO_2 in Freon-14 (C_2F_6) so producing a mask of SiO_2 instead of photoresist. The etching conditions used for Freon-14 are:

actual gas flow 20 sccm
pressure 16 mTorr
forward power 100 W
reverse power 0 W
bias 410V
temperature 20°C

with the resulting etch rate of $500 \text{ \AA}/\text{min}$.

- iv clean the samples as in step then continue as before.

This more lengthy procedure is commonly used when the material may need to be re-etched, due to under-etching. The photoresist mask must be removed to find the methane hydrogen etch depth whereas the silica mask can be left on whilst the etch depth is being measured.

Care must be taken in the stage prior to spinning the photoresist to ensure that the surface is dry: if the surface is not dry the resist does not adhere properly, and thin lines may come off or become wavy due to resist sliding across the surface.

5.6 Conclusions

Single-moded waveguides have been designed using Fourlay with the effective index method and the scalar approximation, and with FWave using a more accurate but, much slower, finite difference technique for solving the vector EM equations. Although Fourlay used with the effective index method and the scalar approximation contains many approximations, the results are still useful in the design process enabling a feeling of mode

behaviour to be assessed quickly. The modal refractive indices calculated using the two techniques are the same to two decimal places.

References

¹'Electromagnetic Principles of Integrated Optics', D.L. Lee, p. 63, John Wiley & Sons, New York, 1986

²'Light Waves in Thin Films and Integrated Optics', P.K. Tien, Appl. Opt. **10** (11), 2395 (1971)

³'Scaling Rules for Thin-Film Optical Waveguides', H. Kogelink and V. Ramaswamy, Appl. Opt. **13** (8), 1857 (1974)

⁴ as Ref. 1.

⁵'Generalised Dispersion Properties of a FourLayer ThinFilm Waveguide', D.W.Hewark, J.W.Y. Lit, Appl. Opt., **26**(5), pp.833841, 1984.

⁶'Correction to Refractive Index Method for Rectangular Dielectric Waveguides', J.J.G.M. Van Der Tol, N.H.G. Baken, Electron. Lett, **24** (4), 208 (1988)

⁷'Electromagnetic Principles of Integrated Optics', D.L. Lee, p. 128, John Wiley and Sons Inc., New York, (1986).

⁸ as Ref. 7.

⁹'Design and Modelling of Passive and Active Optical Waveguide Devices', R.Baets, P.Kaczmariski, and P.Vankwikelberge, Waveguide Optoelectronics, NATO ASI Series E: Applied Science Vol. 226, pp. 2172, 1992.

¹⁰'Optical Waveguides Using GaAs-AlGaAs Multiple Quantum Wells', S. Ohke, T. Umeda, and Y. Cho, Optics Commun. **56**, p. 235, 1985.

¹¹'Low-Loss Multiple Quantum Well GaInAs/InP Optical Waveguides', R.J. Deri, E. Kapon, M. Seto and K. Kash, Appl. Phys. Lett, **54** (18), 1737 (1989)

¹²'The Stopping Range of Ions in Solids', J.F. Ziegler, J.P. Biersack and U. Littmar, Pergamon Press, New York, 1985.

Chapter 6

Fabry–Perot Loss Measurements

6.1 Introduction

The Fabry–Perot loss measurement technique described in this Chapter was used to find the optical loss of waveguides disordered using fluorine IID. The structure used to investigate the waveguide losses is not a full laser structure, the upper cladding layer being undoped (this would be p-type doped in a full laser structure). The lack of p-type doping will give rise to a smaller loss than would be expected in a passive laser because of the reduced losses associated with free–carrier absorption of the optical field overlapping the doped area; the effects of free carrier absorption can be calculated if required. Although the loss figure measured here is smaller than we would expect in an unpumped laser, the actual measurement will give a lower estimate of the waveguide loss.

Walker¹ first used the Fabry–Perot technique in his work on the losses of ring lasers. The measurement technique exploits the ability to determine the ratio of the resonant and anti–resonant transmissions of a waveguide. The following gives a brief explanation of how the transmission states occur, followed by the experimental technique used in this thesis and some results. The technique is only valid for single moded waveguides, the waveguides being fabricated as described in Chapter 5.

6.2 Theory

The system used to establish the transmission of an optical waveguide is shown in Figure 6.1. The waveguide consists of a medium with a facet at either end. The facets act as reflectors due to the abrupt change of refractive index from the guiding medium within the cavity to air outside the cavity. Starting on the left hand side of the diagram, a normally incident optical wave with amplitude E_i arrives at *Facet 1*. The amount of light entering the structure is equal to $t_1 E_i$ where t_1 is the electric field transmission coefficient of *Facet 1*. By the time the wave has reach *Facet 2* it has been attenuated by a factor $e^{-\alpha l}$ and has

undergone a phase shift of e^{-ikl} . The light then gets split into two components: a fraction t_2 is transmitted through the facet and a fraction r_2 is reflected back into the cavity. The reflected light then travels down the cavity once more until it reaches *Facet 1* when it is partially reflected back towards *Facet 2*. This process carries on indefinitely. What is important to mention here is that optical intensity can be lost at the facets: it is either reflected or transmitted, as there are assumed to be no scattering losses. The relation ($T = 1 - R$) can therefore be used to simplify the following expressions, where $T^2 = t^2$, and $R^2 = r^2$.

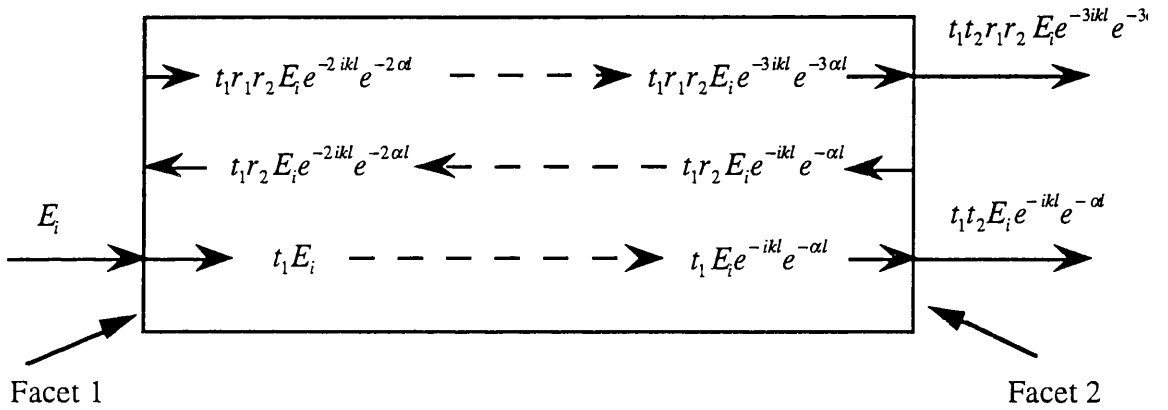


Figure 6.1. Schematic of an optical waveguide with partially reflecting facets, Facet 1 and Facet 2, used to derive the transmission coefficient of the Fabry-Perot structure.

By following the ray, as indicated in Figure 6.1 it is easy to show that the transmitted wave will have an amplitude given by the following summation,

$$E_t = E_i t_1 t_2 e^{-ikl} e^{-\alpha l} \left[1 + r_1 r_2 e^{-2ikl} e^{-2\alpha l} + r_1^2 r_2^2 e^{-4ikl} e^{-4\alpha l} + \dots \right]. \quad (6.1)$$

If we simplify Equation 6.1 by substituting $T = t_1 t_2$ and $R = r_1 r_2$ and note that the term in the bracket is a geometric progression, we obtain the following ,

$$\frac{E_t}{E_i} = \left[\frac{T e^{-ikl} e^{-\alpha l}}{1 - R e^{-2ikl} e^{-2\alpha l}} \right]. \quad (6.2)$$

The ratio of the incident to transmitted intensities is given by:

$$\left| \frac{E_t}{E_i} \right|^2 = \frac{E_t E_t^*}{E_i E_i^*} = \frac{T^2 e^{-2\alpha l}}{\left[(1 - R e^{-2\alpha l} \cos(2kl)) + i R e^{-2\alpha l} \sin(2kl) \right] \cdot \left[(1 - R e^{-2\alpha l} \cos(2kl)) - i R e^{-2\alpha l} \sin(2kl) \right]} \quad (6.3)$$

where A^* is the complex conjugate of A . Expanding the denominator and using the relation $\cos^2 \theta + \sin^2 \theta = 1$, Equation 6.3 simplifies to Equation 6.4.

$$\left| \frac{E_t}{E_i} \right|^2 = \frac{T^2 e^{-2\alpha l}}{1 - 2R e^{-2\alpha l} \cos(2kl) + R^2 e^{-4\alpha l}} \quad (6.4)$$

Substituting $\gamma = e^{-\alpha l}$ and $T = (1 - R)$,

$$\left| \frac{E_t}{E_i} \right|^2 = \frac{(1 - R)^2 \gamma^2}{1 - 2R\gamma^2 \cos(2kl) + R^2 \gamma^4} \quad (6.5)$$

γ now represents the fractional single pass loss of the waveguide.

A plot of this function is shown in Figure 6.2. Here the length of the waveguide is kept constant but the propagation coefficient k is varied.

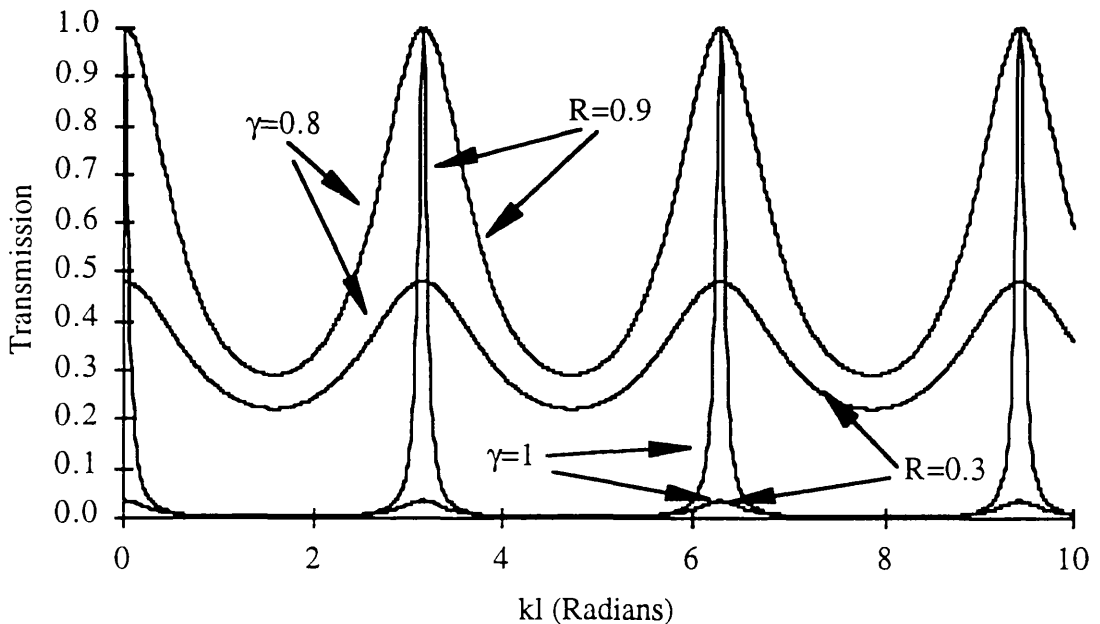


Figure 6.2 Shows the curves for two systems, one with a reflection coefficient $R = 0.9$, the other with a coefficient equal to 0.3, with the loss parameter $\gamma = 1.0$ and 0.8.

Maximum transmission will occur when the denominator of Equation 6.6 is at its smallest value. If we vary k only, then this will occur when $\cos(2kl)=1$ i.e. when $kl=m\pi/2$, and m is an integer. In this case the Fabry–Perot transmission is said to be in the resonant state and is given by,

$$T_R = \left[\frac{(1-R)\gamma}{1-R\gamma^2} \right]^2. \quad (6.6)$$

On the other hand when $\cos(2kl)=-1$, i.e. when $kl=m\pi$ and again m is an integer, the resonator is said to be in the anti-resonant state. The transmission is at its lowest value and is given by,

$$T_A = \left[\frac{(1-R)\gamma}{1+R\gamma^2} \right]^2. \quad (6.7)$$

By comparing these two expressions it is now possible to obtain the loss of the waveguide i.e. γ in terms of the transmission coefficients. Simplifying the expressions by defining K as

$$K = \frac{I_i T_R}{I_i T_A} = \frac{T_R}{T_A}, \quad (6.8)$$

then using Equations 6.6 and 6.7 the single pass loss can be shown to be equal to

$$\Gamma = -20 \log_{10} \gamma = -10 \log_{10} \left[\frac{\sqrt{K}-1}{R(\sqrt{K}+1)} \right]. \quad (6.9)$$

Finally to solve Equation 6.9 we need to know one of the parameters on the right hand side of the equation, since we are to measure the Fabry–Perot resonances we must calculate the reflectance R . The reflection coefficient at a dielectric interface is:

$$R = \left(\frac{n_{dielct} - n_{air}}{n_{dielct} + n_{air}} \right)^2 \quad (6.10)$$

where n_{dielct} is the refractive index of the dielectric waveguide and n_{air} the refractive index of air i.e. unity.

The above equation is used in the following experiment to calculate the loss of an optical waveguide from the ratio of the resonant and anti-resonant transmissions. Fabry-Perot fringes are observed by varying kl (Equation 6.6) and probing the waveguide with a narrow linewidth source at the wavelength of interest. kl is varied by heating the waveguide: heating has the effect of increasing the refractive index of the waveguide which changes the optical length of the waveguide. In order that the fringes are visible, the linewidth of the laser used to probe the waveguide must be very much less than the free spectral range of the etalon. The free spectral range is the frequency difference between two adjacent maxima in transmission as is given by,

$$\Delta\nu = \frac{c}{2nL} \quad (6.11)$$

where c is the speed of light in a vacuum, L the length of the waveguide and n the refractive index of the waveguide. For a waveguide approximately 1 mm long this value is therefore around 1×10^{10} Hz: this is the absolute maximum linewidth of a laser that can be used to observe the Fabry-Perot fringes, though obviously the narrower the linewidth of the source the greater the clarity of the fringes will be. A DFB laser is used in this experiment, which will have a linewidth in the order of 10^6 Hz; due to the finite line-width of the laser source, the technique will always give an over estimate of the loss.

6.3 Experimental Technique

The apparatus used to measure loss by the Fabry-Perot technique is shown in Figure 6.3. The sample, which should be more than approximately 3 mm long in order to remove leaky modes, was placed on a device manipulator. A thin metal stand was made to hold the waveguide above the device manipulator so that the objective lenses could be brought close up to the facets. On the input side a DFB laser at $1.546 \mu\text{m}$ is first approximately collimated using a $\times 20$ objective lens and then focused into the waveguide. The output from the other side of the waveguide was collected with another $\times 20$ objective which approximately collimates the output beam. The output is then monitored with a lock-in amplifier, the reference frequency for which is provided by inserting a chopper into the beam

and sending a signal directly from the chopper to the lock-in amplifier with a frequency equal to that of the chopped light. A Ge detector was used to convert the optical pulses into an electrical signal. The output of the lock-in amplifier was monitored with a chart recorder. From the oscillations recorded on the chart recorder, the loss of the waveguide was calculated.

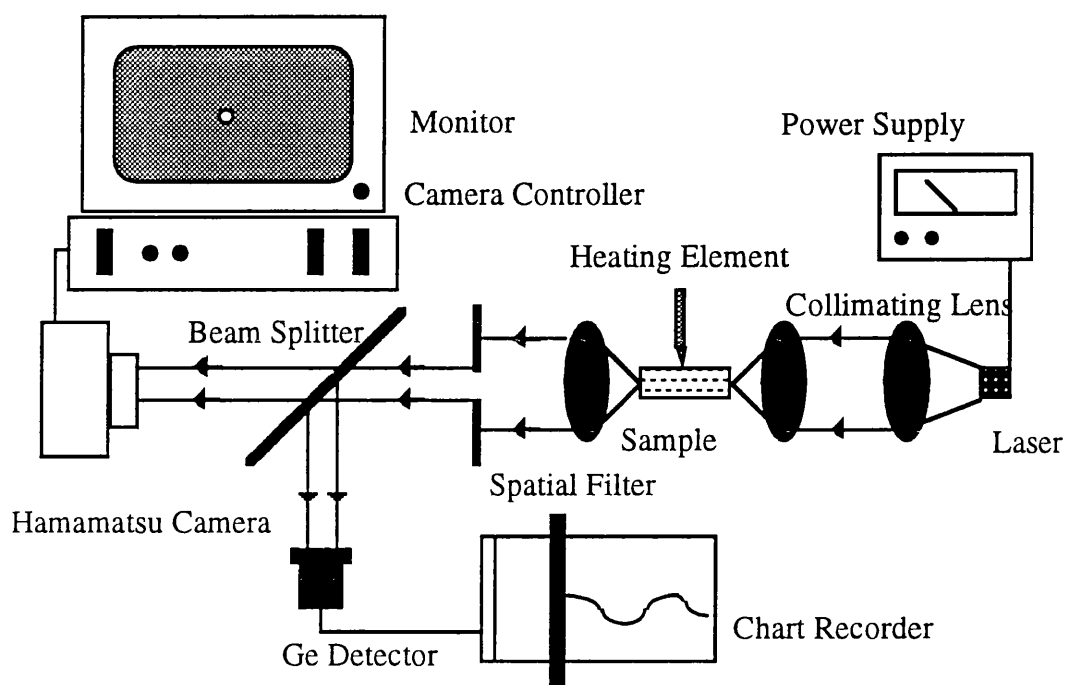


Figure 6.3. Experimental set-up used to determine the Fabry-Perot oscillations of the waveguides.

It is important to make sure that the optics are properly aligned. It is possible to launch light into the waveguide if the optics are not aligned properly, but this leads to difficulty when trying to vary the light path along a single plane. The easiest technique for aligning the apparatus was found to be as follows;

- Remove the waveguide and the objective lenses, except for the one at the DFB laser.
- Collimate the beam using the camera and monitor making sure the beam goes through the centre of the objective mounts at the device manipulator, and align the laser collimating lens properly. When the collimating lens is in the correct

place, the laser spot will stay in the same position on the monitor when the focus is moved in and out. If it is not in the right place the beam will wonder around the monitor's screen as the focus is changed.

- Replace the objectives, and align the beam through them. Again, when these are in the correct place, the focus can be changed and the spot will stay in the same place on the screen.
- The sample can now be replaced. In order to approximately focus the output lens, a corner of the sample is used, which has more features than the upper edge where it is difficult to focus.
- Once the output objective is focused the input focus can be changed and the device can be carefully moved up or down until either a slab or a ridge waveguide is observed. The key point to look out for when doing this, is interference fringes between light reflected off the surface of the structure and light passing straight over the surface. When these are seen, guiding is not far away. The fringes become distorted when there is a feature on the surface of the waveguide. By looking for this effect it is often possible to find the ridges of the waveguides. Of course sometimes the source of the disturbance is not a ridge but a piece of dust!

6.4 Results

It is important to remember that any error in the measurements will be such that an over-estimate is calculated for the actual waveguide loss: the optical feedback in the cavity for a waveguide with a certain loss will never be bigger than that measured by this technique; if it were it would mean that there must be some amplification of the light fed back from the facets.

The lowest losses were observed in a fluorine implanted waveguide, followed by annealing in the RTP. The structure, as described in Appendix A, was coded A2262, the room

temperature PL peak of this wafer was 1.53 μm . The sample was annealed at 700°C for 30 seconds and had an implant dose of 10^{14} cm^{-2} at 700 keV, giving an estimated concentration of $8 \times 10^{17} \text{ cm}^{-3}$ fluorine ions in the QW region. The resulting energy shift was estimated to be over 90 meV, though it was not possible to measure this shift due to the loss of photoluminescence after annealing. White light transmission experiments were also unable to resolve the band edge after annealing. Figure 6.4 shows a section of the Fabry–Perot oscillations recorded from the device. The zero was obtained by blocking the path of the probe during the heating cycle.

From the Fabry–Perot fringes $K = 3.286$, and, assuming a reflectance R of 29.8%, this gives a loss figure of,

$$\Gamma = -10 \log \left[\frac{\sqrt{3.286} - 1}{\sqrt{3.286} + 1} \cdot \frac{1}{R} \right] (\text{dB}) = 0.13 \text{ dB}.$$

The cavity length of this device was 2.3 mm giving a loss of,

$$\Gamma = \frac{0.13}{0.23} = 0.57 \text{ dB cm}^{-1}.$$

The resonances are not very uniform, as seen in Figure 6.4, which is probably due to the heating of the surrounding optics, resulting in a calculated loss of between 0.57 dB cm^{-1} and 4.35 dB cm^{-1} . The lower value should be the most accurate.

Unfortunately only one guide from the sample was found to have such a low propagation loss. A more typical measurement is illustrated in Figure 6.5. Here K ranges from 2.39 to 2.07 giving a loss of between 6 dB cm^{-1} and 10 dB cm^{-1} .

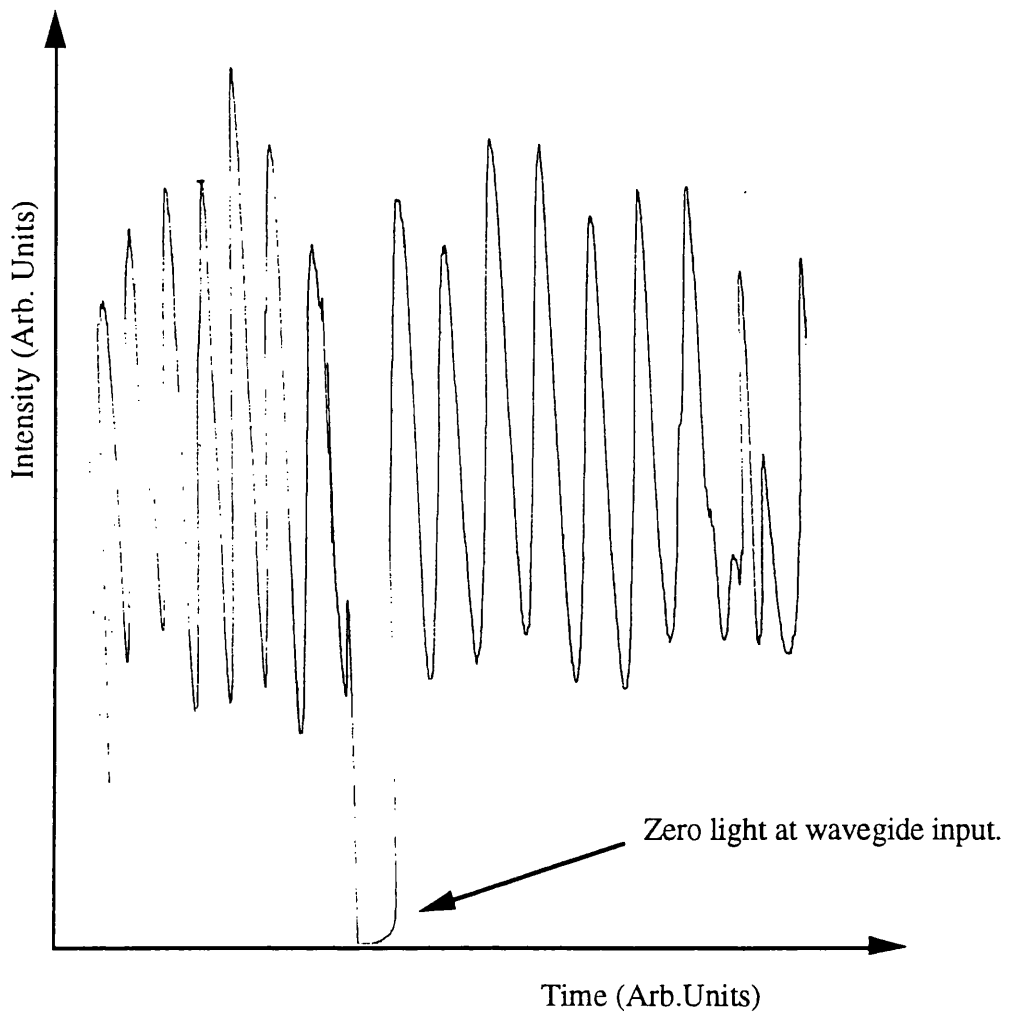


Figure 6.4. Fabry-Perot Resonances for a F IID waveguide.

Figures 6.6 and 6.7 highlight some of the problems encountered with this measurement technique. In Figure 6.6 the waveguide shows multi-mode characteristics, in this case two modes exist in the waveguide. As can be seen, this gives rise to an oscillation pattern containing several peaks. The loss cannot be measured with this sample because of the overlapping resonances.

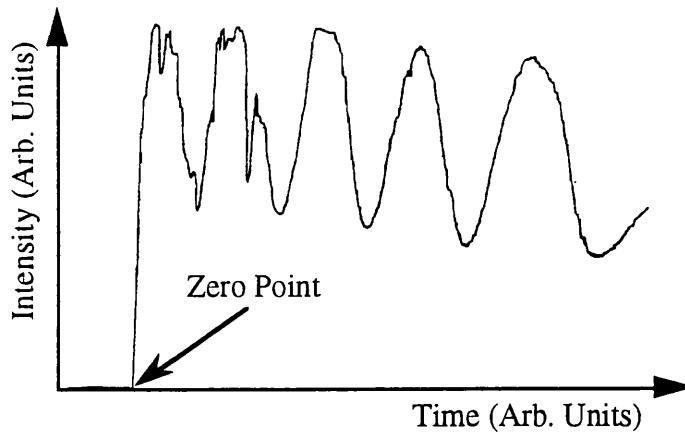


Figure 6.5. Fabry-Perot Resonances for a sample processed identically to the one in Figure 6.4 .

Figure 6.7 shows a Fabry-Perot scan highlighting the problem of heating the optics. The resonance peaks should be parallel but in this case they are strongly rising and falling. This is probably due to the optics moving, due to thermal expansion, out of optimum alignment. It can be seen that during the cooling phase the optics contract putting them back into their original position.

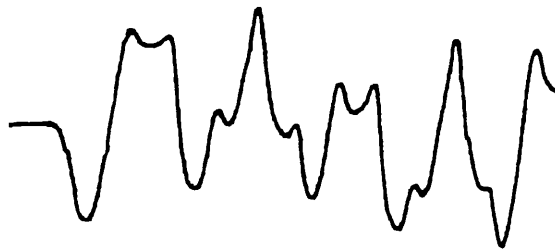


Figure 6.6. A multi-moded waveguide produces a superposition of individual Fabry-Perot fringes, this is useless as far as loss measurements are concerned.

A plot of waveguide loss against energy shift is shown in Figure 6.8 for waveguides disordered by fluorine IID and by thermal effects only. As can be seen there appears to be little difference between the loss of waveguides disordered by similar amounts, whether the guide has been disordered thermally or by fluorine. This shows that F doesn't add any

additional loss to the guide i.e. no increased free carrier absorption that would occur if F was ionised.

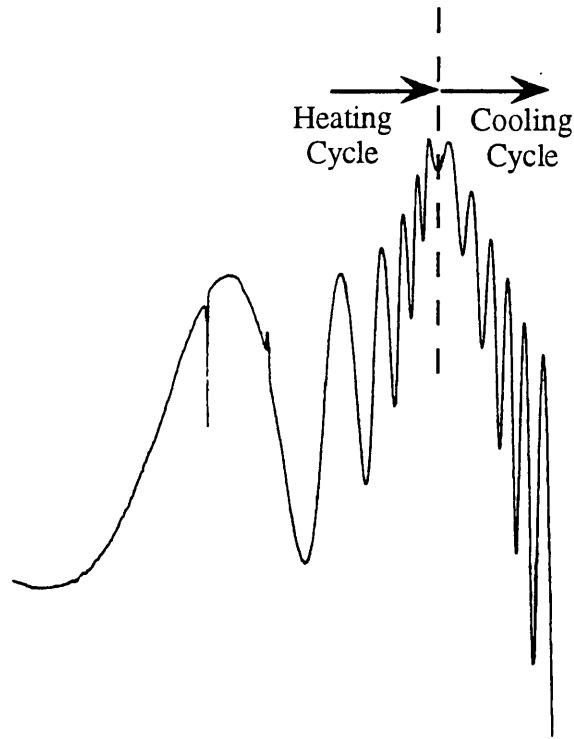


Figure 6.7. A Fabry–Perot scan highlighting one of the problems with this technique for calculating loss measurements. The resonance peaks should be parallel for a useful result.

No results exist for waveguides with small energy shifts (<50 meV) produced by IID because, in this situation no photoluminescence was observed, possibly due to damage related effects. For complete intermixing it would be expected that the loss will not drop to zero but will reach a limiting value imposed by scattering losses.

Figure 6.8 shows the losses measured in several samples by the Fabry Perot technique against the shift in energy from the as-grown condition. Results are shown for samples intermixed by thermal processing alone (Thermally Disordered) as well as samples intermixed using fluorine impurity induced disordering). A key point to this result is that for the same shift in bandgap there is no difference between samples containing fluorine and those which do not contain the impurity. This is a very desirable effect since no extra losses are being added to the cavity using F IID.

There are two possible causes for the effect described above;

1. Fluorine diffuses so rapidly within the QW region that there is only a very small concentration left in the wells which does not affect the absorption of the probe signal.
2. Fluorine exists as a neutral impurity in the QW region and therefore does not contribute to absorption of the probe signal via free carrier effects².

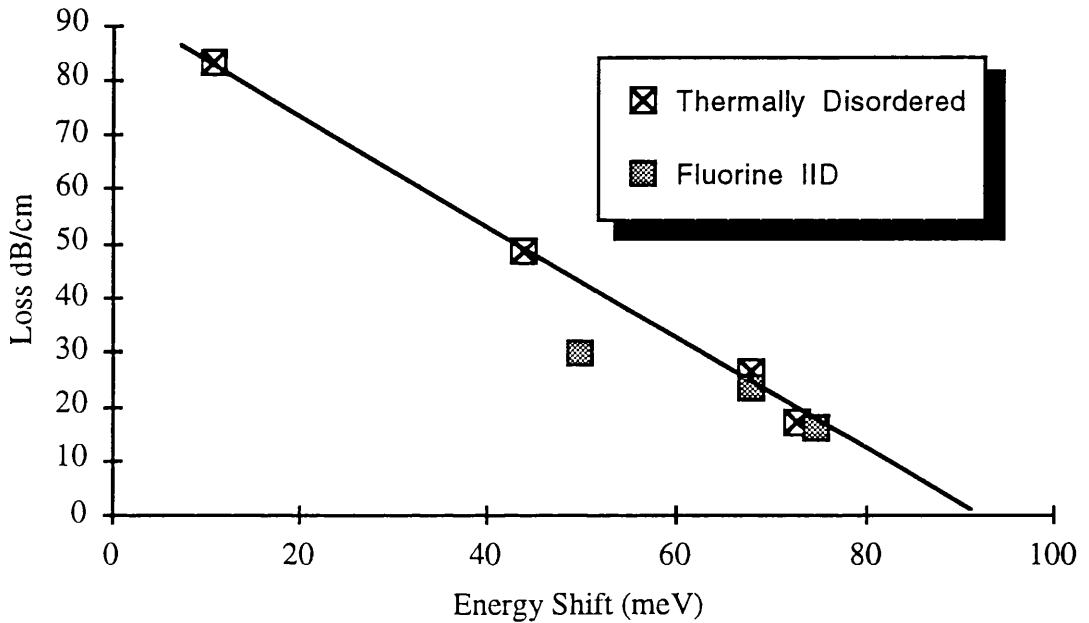


Figure 6.8. Graph of Energy Shift vs. Waveguide loss for samples either implanted with fluorine followed by annealing by RTA, or with sample disordered by thermal effects only.

The graph in Figure 6.8 can be extrapolated back to the band edge;

Wavelength of probe laser = $1.546\mu\text{m}$ (803 meV)

RT PL of as-grown sample $\approx 1.53\mu\text{m}$ (811 meV)

Energy difference for as-grown samples is = 8 meV

In other words the loss measurements recorded above are for total energy of the energy shift plus 8 meV, from the probe DFB.

6.5 Conclusions

The Fabry–Perot loss measurement technique has been used to find the propagation losses of disordered waveguides.

Waveguide losses down to 0.57 dB cm^{-1} have been measured in fluorine IID structures. This is an excellent result and should therefore open the way for producing integrated devices using the process developed in this thesis. Further, it has been observed that the losses of FIID fabricated waveguides are equivalent to the losses measured in thermally disordered material with an equivalent degree of intermixing. Chapters 8 and 9 use F IID to produce a simple integrated device. In these Chapters device characteristics are reported and further loss measurements are taken.

References

- ¹'Simple and Accurate Loss Measurement Technique for Semiconductor Optical Waveguides', R.G. Walker, *Electron. Lett.*, **21**, 581 (1985)
- ²'Physical Properties of Semiconductors', C.M. Wolfe, N. Holonyak, and G. Stillman, Prentice Hall, 1989.

Chapter 7

Oxide Stripe Laser Fabrication

7.1 Introduction

An oxide stripe extended cavity laser was fabricated to show one application of fluorine Impurity Induced Disorder and to provide an alternative method to find the waveguide losses in band-gap shifted waveguides. The oxide stripe laser was chosen for this purpose because of its ease of fabrication; there is no need to etch into the laser structure.

The use of external cavities to narrow the linewidth of semiconductor lasers is commonplace but they are bulky and require careful alignment with good mechanical stability. An internal extended cavity promises to be appreciably more stable and would require a cavity a factor of four¹ shorter than the equivalent air cavity. Recently Tanbun-Ek et al² have reported an InGaAsP/InP MQW-DFB laser integrated with a passive waveguide section fabricated by a selective area MOVPE technique. A linewidth reduction factor of 3.5 for a waveguide with losses of 35 cm⁻¹ was reported, a reduction factor of 10 was predicted for a waveguide with lower losses.

Before fabrication of the oxide stripe extended cavity laser, a laser without the extended cavity was made to check the quality of the material and to compare the characteristics of the laser.

7.2 Oxide Stripe Laser Fabrication

This Section briefly outlines the material structure used to fabricate the lasers and outlines the technique used to prepare a wafer containing a laser structure for the addition of contacts necessary for the device.

7.2.1 Material Structure

The laser structures were grown by Low Pressure Metal-Organic Vapour Phase Epitaxy (LPMOVPE). The wafers used were not identical the individual structures are presented in

Appendix A, but the following is a general description of the wafer design. From the substrate (n-type InP) upwards; 1 μm n-type InP, four 100 \AA $\text{In}_{0.53}\text{Ga}_{0.47}\text{As}$ quantum wells centred in a 0.2 μm $\text{In}_{0.79}\text{Ga}_{0.21}\text{As}_{0.45}\text{P}_{0.55}$ waveguide, a 1.5 μm p-type InP upper cladding layer and a 0.2 μm p-type $\text{In}_{0.53}\text{Ga}_{0.47}\text{As}$ contact layer. A 300 \AA InP layer was grown onto the surface as a protection layer.

7.2.2 Oxide Stripe Fabrication

The laser samples of area approximately 1 cm^2 were processed in the following way;

1. The samples were first cleaned thoroughly in order to remove any dirt which, if left, could cause poor adhesion of the silica layer and cause problems with the following patterning and etching steps.
2. 1000 \AA of silica was sputtered onto the surface to form an electrical isolation layer over the entire surface. The normal method of silica deposition used in the department is plasma enhanced chemical vapour deposition (PECVD). At the time of fabrication the system was unoperational so the sputtering technique was used instead. The silica film was inspected for defects with an optical microscope. If pin holes were observed in the silica, it would be stripped off and redeposited until a good layer was formed.
3. Positive photoresist (Shipley S1400-31) was spun onto the oxide and baked in the usual manner³. A 75 μm stripe was opened in the resist.
4. The sample was post-baked at 120°C for ten minutes to harden the resist against the subsequent etches. The silica was etched from the stripe in 4:1 HF:H₂O etch for 30 seconds. An optical microscope was used to inspect the etched regions—any areas where the silica had not been completely removed could be easily seen due to interference patterns. The samples were etched for a further 10 s after the last of the interference patterns had vanished, to make sure that the surface was entirely silica-free. $\text{In}_{0.53}\text{Ga}_{0.47}\text{As}$ etches at a very slow rate in the etch solution allowing the over etching procedure to be carried out. The remaining photoresist was removed in acetone and the sample cleaned in the usual manner.

5 Alumina grit (3 μm) was used to lap the samples to 180 nm. This was followed by a 20 minute etch in 1:3 HCl:H₃PO₄, thinning the sample to approximately 160 nm. During this etching stage the top surface of the device was protected by sticking it onto a glass slide with photoresist. Thinning is required to ensure that the sample cleaves easily and a good optical facet is produced.

6 The protective InP layer was removed by etching in 1:1 HCl:H₂O for 60 seconds to expose the contact layer.

7 The sample was then stuck with photoresist p-side down on a glass slide and baked, this step being necessary to mount the device before contact evaporation. The n-type contact was evaporated with the following layers,

250 Å Gold,
400 Å Germanium,
250 Å Gold,
250 Å Nickel,
2000 Å Gold.

The contact was annealed for 1 minute at 400°C in the RTP in order to alloy the metals.

8 The sample was cleaned and stuck n-type down onto a glass slide, as in step 9 above, to prepare it for the p-type contact. The p-type contact was evaporated with the following layers:

700 Å Titanium
1700 Å Gold

The p-contact was then annealed at 300°C for 1 minute.

9 The samples were then cleaved and tested.

7.3 Laser Characteristic Test

The output characteristics of lasers produced using the above technique are presented in the following Section, along with an outline of the experimental technique used. The procedure described for measuring the laser output characteristics forms an important technique that is integral to experiments later on in this thesis.

7.3.1 Test Procedure

Figure 7.1 shows the equipment used to measure the laser characteristics of the devices made in this and subsequent chapters. The test facility evolved during the course of this thesis to the level that is presented here. Initially all tests were performed manually, i.e. as the power supply to the laser was increased, by turning a knob on the input power amplifier, the drive current and the resulting optical intensities had to be written down. The results were then transferred to a spreadsheet or similar application for further processing and recording. This was found to be extremely time consuming and extremely tedious.

The next stage was to automate of the procedure, a computer was available with LabVIEW and, a GPIB card on board. A LabVIEW virtual instrument was written to control the equipment via the IEEE 488 GPIB, this was found to be much quicker than carrying out the measurements manually. The data was loaded straight into the computer and the power supply to the laser under test controlled from the front panel of the LabVIEW program. Unfortunately the results were still noisy—this was due to the method by which the optical power and drive currents were being measured: a digital oscilloscope was being used to measure the peak values of current and power, and since only instantaneous values could be recorded, the data tended to contain a lot of noise. In an attempt to reduce the noise, several readings of each parameter were taken and averaged, however this tended to slow down the experiment considerably for very little reduction in noise (many samples would be needed to reduce the noise). Eventually a Boxcar Averager was obtained. This piece of equipment can take an averaged reading of a portion of a pulse and produced a significant reduction in noise as compared to the pervious use of the oscilloscope. The Boxcar Averager takes a sample of

a periodic pulse stream and integrates over the sample taken then an average is taken over a set number of pulses. Using LabVIEW to control the experiment also enabled the voltage across the diode to be recorded with very little increase in experiment time.

Figure 7.1 shows the experimental set-up used to characterise the lasers in its final state. The laser sits in a gold plated clip on top of a heat sink, and the power to the laser is supplied from an Avtech pulse generator through a $50\ \Omega$ to $12\ \Omega$ load transformer. The power supply to the laser was pulsed at typically 1 kHz, with pulse widths of approximately 100 ns. The current being supplied to the device was monitored by measuring the voltage across a $1\ \Omega$ resistor and measured with the Boxcar Averager, the voltage across the laser was also being measured. A reverse biased Ge photodiode was used to monitor the laser output, the voltage from this was measured with the Boxcar Averager. The Boxcar was set up to measure the value of drive current and optical intensity at a steady position during the pulse cycle.

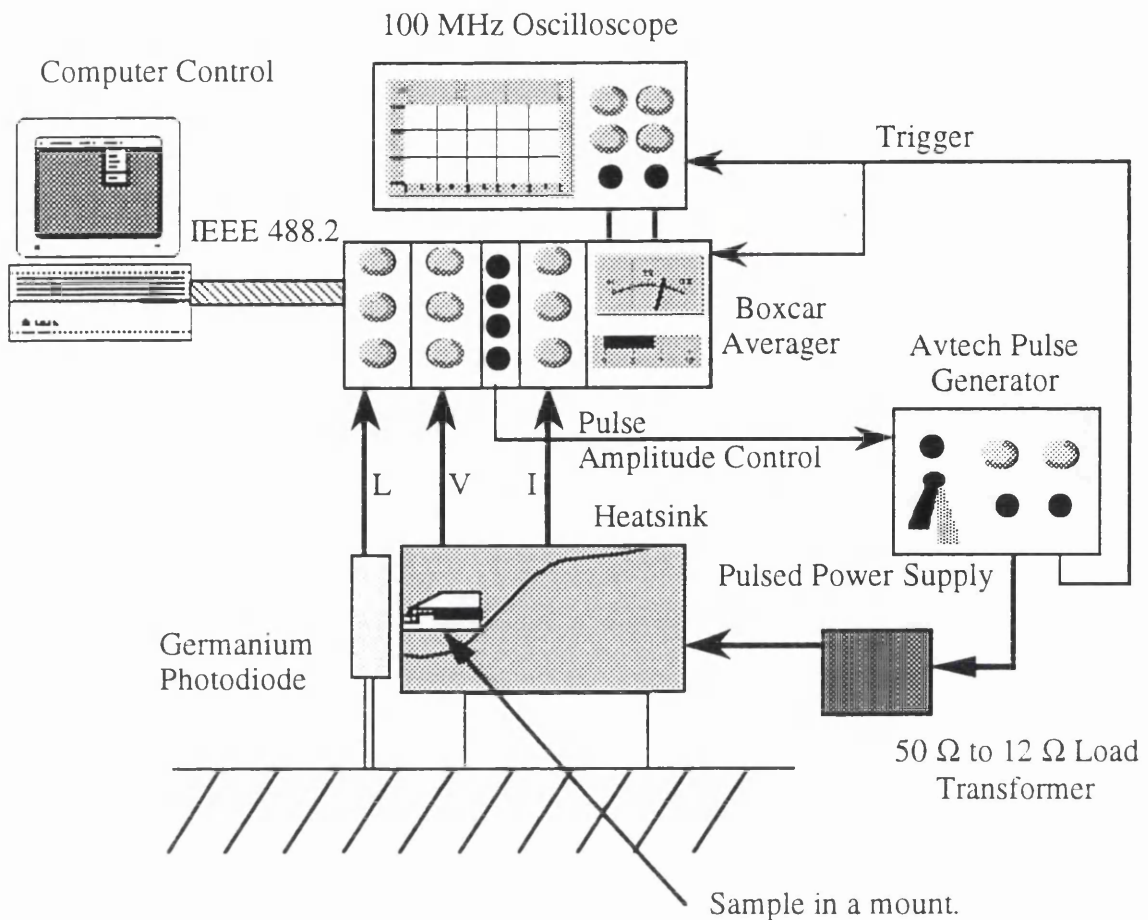


Figure 7.1. Apparatus used to measure laser characteristics.

7.3.2 Results

The following threshold currents and threshold current densities have been measured for 80 ns pulses at 1 kHz repetition frequency, with wafer E288, Appendix A contains a listing of the wafer composition.

Cavity Length (μm)	Threshold Current (A)	Threshold Current Density (kA cm^{-2})
1047	1.1	1.40
720	0.75	1.38
1051	1.0	1.27
725	0.73	1.34

Table 7.1. Threshold currents from wafer E288.

A similar set of lasers fabricated from another wafer had the following threshold currents,

Cavity Length (μm)	Threshold Current (A)	Threshold Current Density (kA cm^{-2})
780	1.05	1.69
780	0.9	1.54
600	0.95	1.97
600	0.6	1.25

Table 7.2. Threshold currents from wafer E795.

Figure 7.2 shows typical output characteristics of the oxide stripe lasers fabricated. The output power indicated is calculated by multiplying the pulsed power by the duty cycle. The cavity length of the lasers was $500 \mu\text{m}$ giving an average threshold current density in this case of 1.86 kA cm^{-2} .

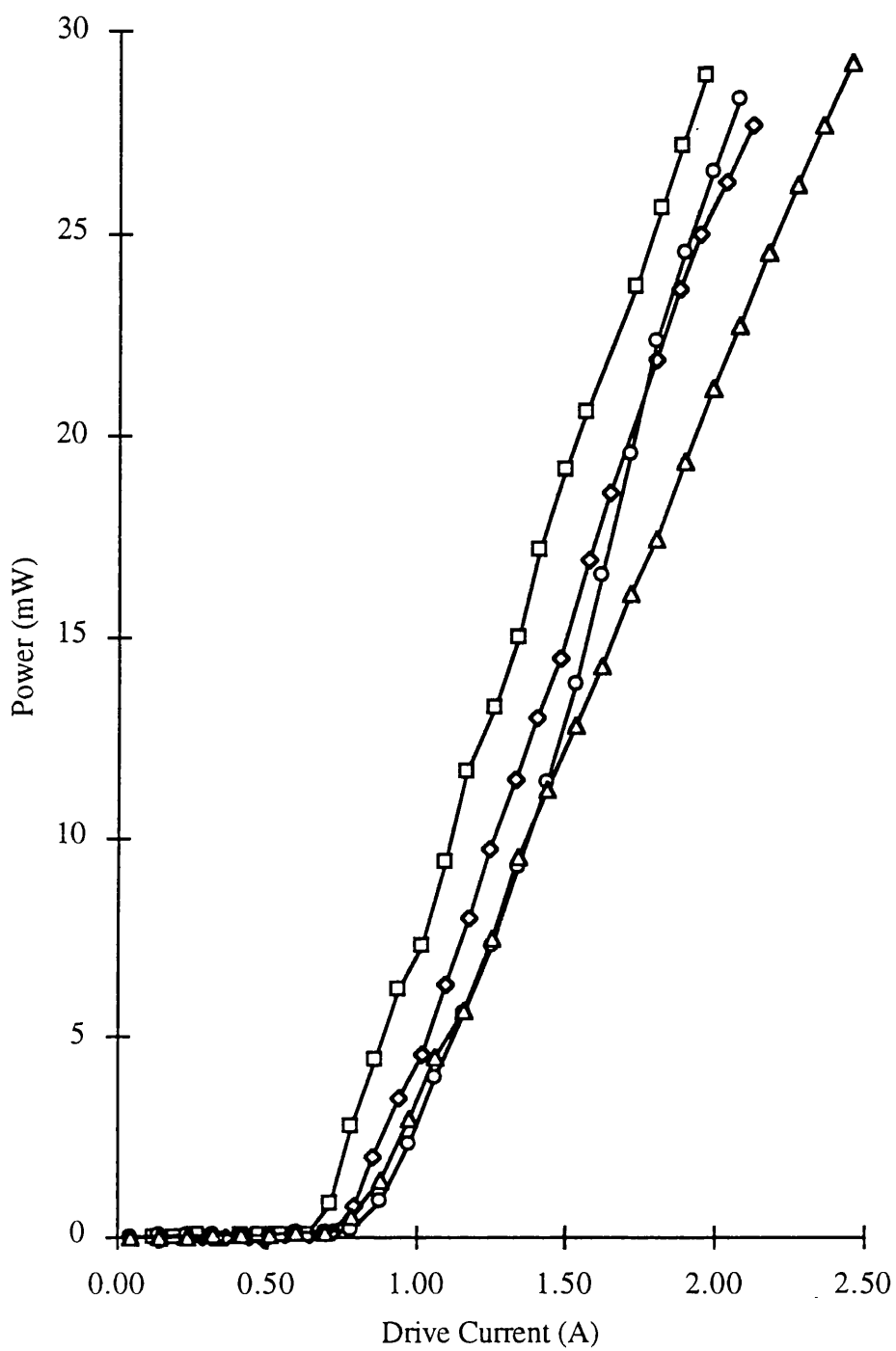


Figure 7.2. E795 75 μm Oxide stripe lasers pulsed at 470 ns with a 1 kHz repetition rate.

7.4 Fabrication of Oxide Stripe Extended Cavity Lasers

The fabrication of devices with extended cavities requires a significant amount of processing on top of that required to produce normal lasers, however, compared to all the other techniques used for integrating extended cavities onto semiconductor lasers the process is simple and relatively straight forward. The extra step involved in producing the extended cavity lasers is to mask off a region that will form the active area of the device, implant fluorine into the areas to be disordered, apply the thermal processing and then continue as before.

7.4.1 Implant Conditions

In Section 3.5.1 it was shown that there is an optimum implant concentration for intermixing the quantum wells of around 10^{18} cm^{-3} . The concentration of fluorine in the wells was calculated by using TRIM. Using the concentration of fluorine for maximum intermixing, the implant energy and dose required for the deeper implant were calculated. A deeper implant is required since the laser structure contains a $1.5 \mu\text{m}$ upper cladding and a contact layer (Appendix A), in Section 3.5.1 the wafer had a $1.0 \mu\text{m}$ upper cladding with no contact layer. Two implants were carried out the first 1.5 MeV with a dose of $1.4 \times 10^{13} \text{ nuclei cm}^{-2}$, the second with the same implant energy but a lower dose of $1.4 \times 10^{13} \text{ nuclei cm}^{-2}$.

7.4.2 Fabrication

The extended cavity lasers were fabricated by the following process:

1. A $3 \mu\text{m}$ silica and $0.2 \mu\text{m}$ gold implant mask was deposited on top of the $\text{In}_{0.53}\text{Ga}_{0.47}\text{As}$ contact layer. The silica was deposited by plasma deposition, the gold was evaporated on top of the silica. The depth of silica required for the implant mask was calculated using TRIM (Section 3.2.2). Figure 7.3 shows the TRIM plot for a 1.5 MeV fluorine implant into $3 \mu\text{m}$ silica and $0.2 \mu\text{m}$ gold. The mask was designed so that the majority of the fluorine ions stopped $0.5 \mu\text{m}$ from the InGaAs contact layer.

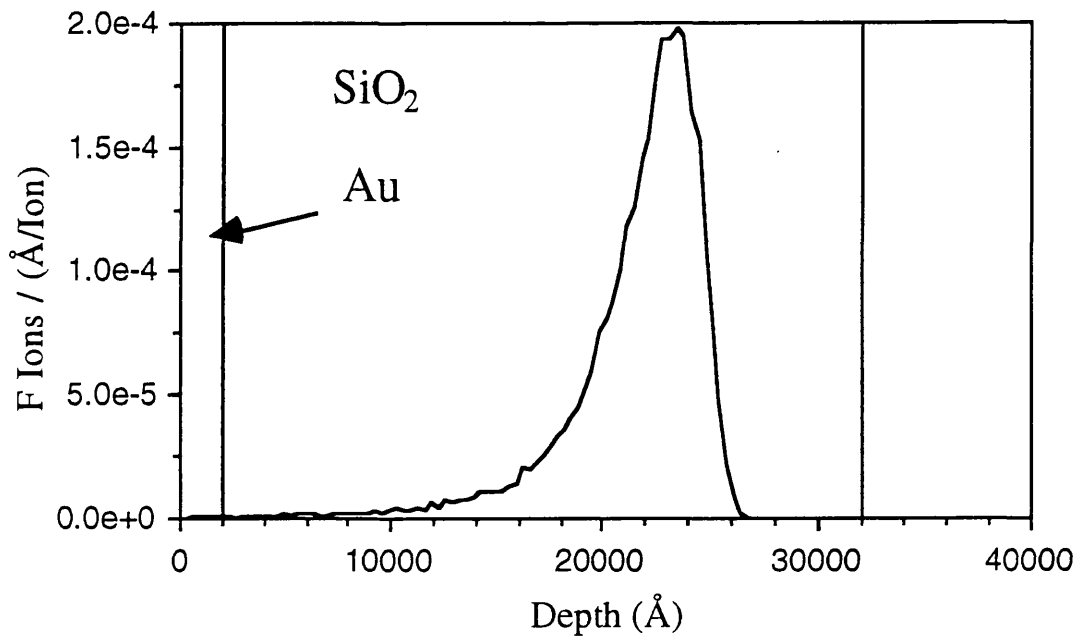


Figure 7.3 A TRIM plot 1.5 MeV Fluorine implantation into a 3 μm SiO_2 and 0.2 μm Gold implant mask.

2. The samples were then patterned with photoresist and baked at 120°C for 15 minutes before being etched; gold etch (KI:I_2) was used to remove the gold layer, and buffered HF to remove the silica. This stage thus creates the implant mask, the exposed areas being the regions where disordering is required. The Tally step was used to ensure that the SiO_2 was completely etched away. The InGaAs contact layer was also etched off at this point from the passive areas, nitric acid being used to etch the InGaAs since it is selective and does not etch InP. Figure 7.4 shows the layers present after this stage in the processing. During the first attempt at the fabrication procedure, the InGaAs layer was etched after the implant, but this procedure was not very successful. During the implant, damage is induced in the crystal structure which appears to affect the etching properties of the nitric acid. A very uneven etch was observed, leaving a rough surface. Processing of these samples was abandoned.
3. The sample was then implanted with fluorine ions at an energy of 1.5 MeV and dose of 1.4×10^{13} nuclei cm^{-2} to give an estimated fluorine concentration of 10^{18} cm^{-3} in the quantum well region.

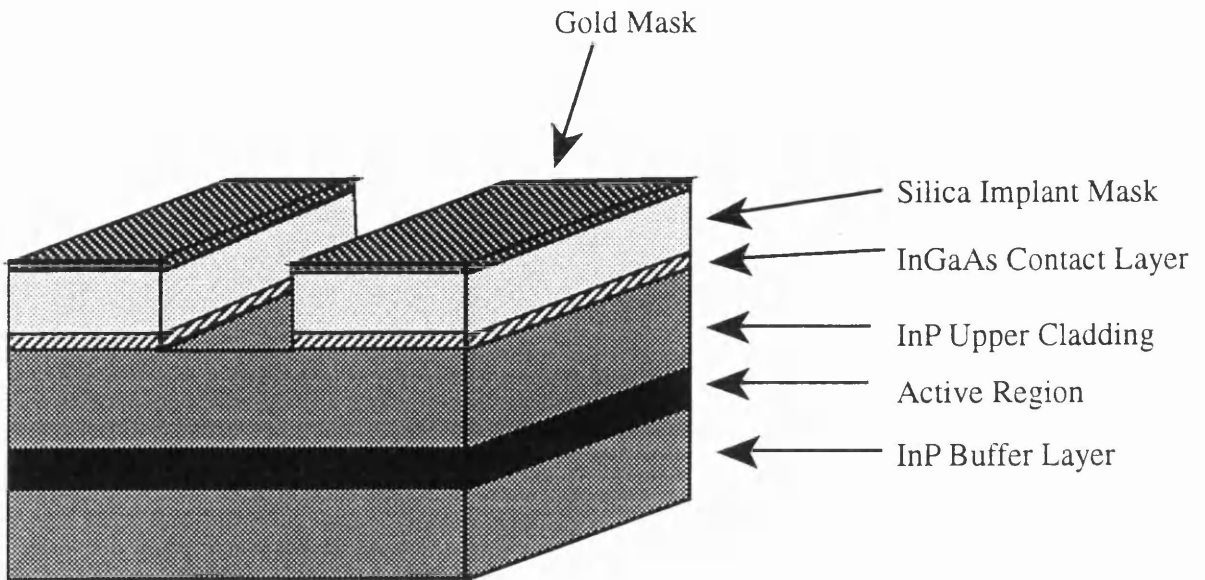


Figure 7.4 A schematic of the sample ready to be implanted. The active area is protected by a $3 \mu\text{m SiO}_2$ and $0.2 \mu\text{m Au}$.

- 5 After implantation the implant mask was removed and a new 1000\AA layer of SiO_2 was sputtered, to form a protective layer against evaporation of phosphorous during annealing.
- 6 The sample was annealed at 700°C for 30 seconds in the Rapid Thermal Processor.
- 7 The protective oxide cap was removed and another new 1000\AA layer of SiO_2 deposited. After annealing, the protective oxide cap becomes very difficult to remove by chemical etching, suggesting some change is occurring during the annealing process. For this reason a new layer was deposited to form the oxide stripes.

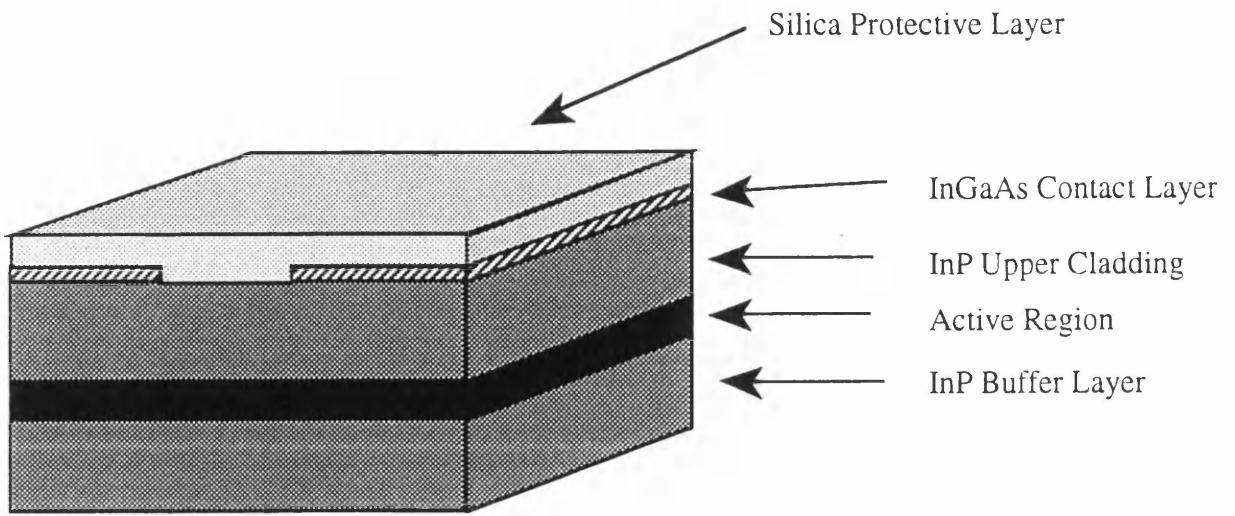


Fig. 7.5 The implanted areas are visible because the InGaAs has been removed over the disordered regions, the surface is protected with a layer of SiO₂ and then annealed in the RTP.

8. The negative of the original implant mask was used to pattern the sample again so that windows can be opened up over the contact regions (active regions)..
9. The sample was etched in SiO₂ etch. This left the sample with oxide over the entire surface except over the active region of the laser

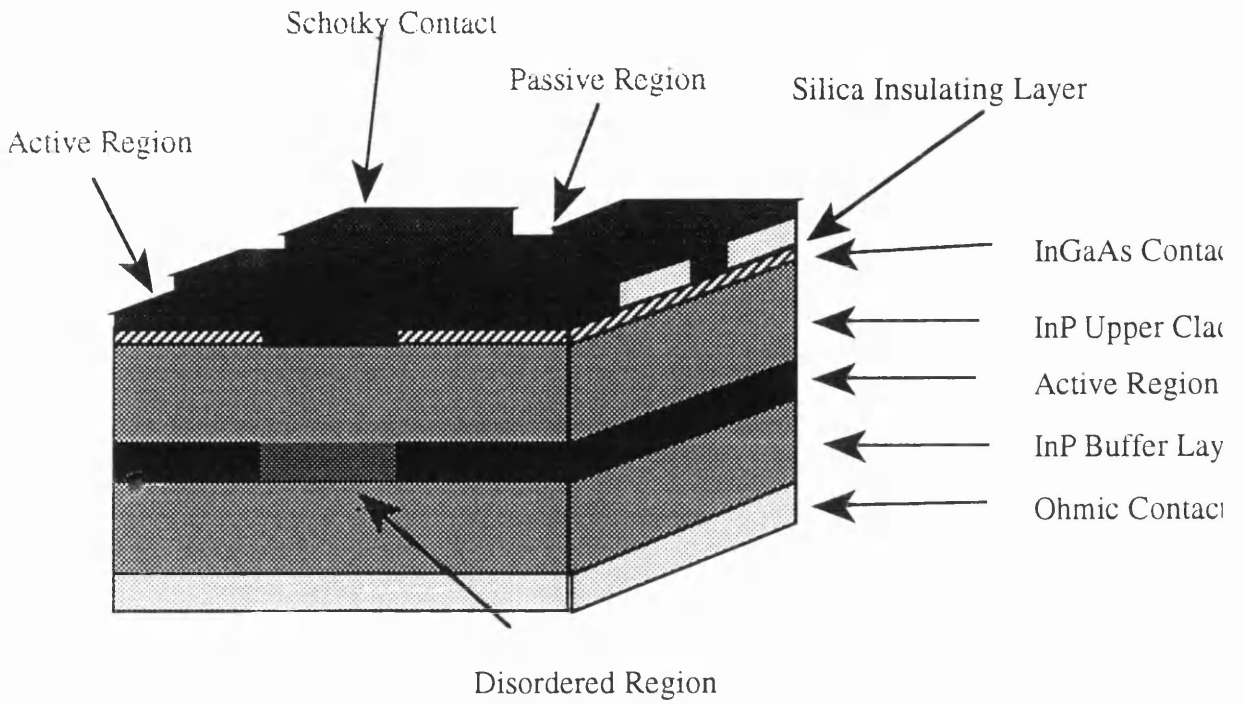


Figure 7.6 The oxide stripes are etched over the active region before the sample is thinned and the contacts evaporated.

10 The sample was then thinned and had contacts evaporated on as described in Section 7.2.2, the resulting wafer containing the devices as in Figure 7.6. The devices are then cleaved before being tested.

7.4.3 Test

The threshold currents were measured using the technique described in Section 7.3, with 80 ns pulses at a 1 kHz repetition rate.

7.4.4 Results

Active Length (μm)	Passive Length (μm)	Threshold Current (mA)	Threshold Current Density (kA cm^{-2})
400	N/A	550	1.8
400	N/A	650	2.2
750	N/A	700	1.3
400	250	1200	4
400	250	700	2.3
400	250	750	2.5
770	185	750	1.3
770	185	800	1.4

Table 7.4. Threshold currents of lasers with and without extended cavities as indicated

The set of devices tested in Table 7.4 show an increase in threshold current between lasers with and without extended cavities of about 0.1 - 0.2 A. The threshold current densities are calculated using the active area of the extended cavities. This change in threshold current can be used to calculate the loss of the disordered region of the lasers and was looked at in Chapter 8.

Oxide stripe lasers were also fabricated from sections of the wafer that had been implanted with fluorine, to see whether the disordered region was capable of producing gain. None of the devices fabricated showed any sign of producing luminescence up to injection currents of 3 A: around this current the devices broke down catastrophically.

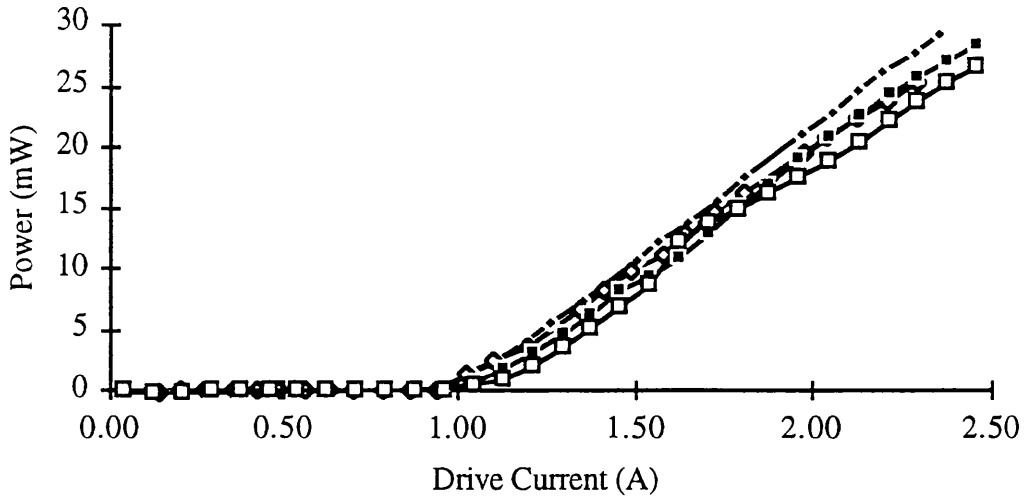


Figure 7.7 Output power vs. drive current, 80 ns pulse at 1 kHz repetition. 375 μm active region, 270 μm passive.

Spectra of the broad area lasers are shown in Figures 7.8–7.11. The change in the laser spectrum can clearly be seen as the injection current increased from 0.62 A (Figure 7.8), which as can be seen from Figure 7.7 is below threshold, to threshold at ~ 0.95 A (Figure 7.9), and beyond at 1.3 A (Figure 7.10) and 1.9 A (Figure 7.11).

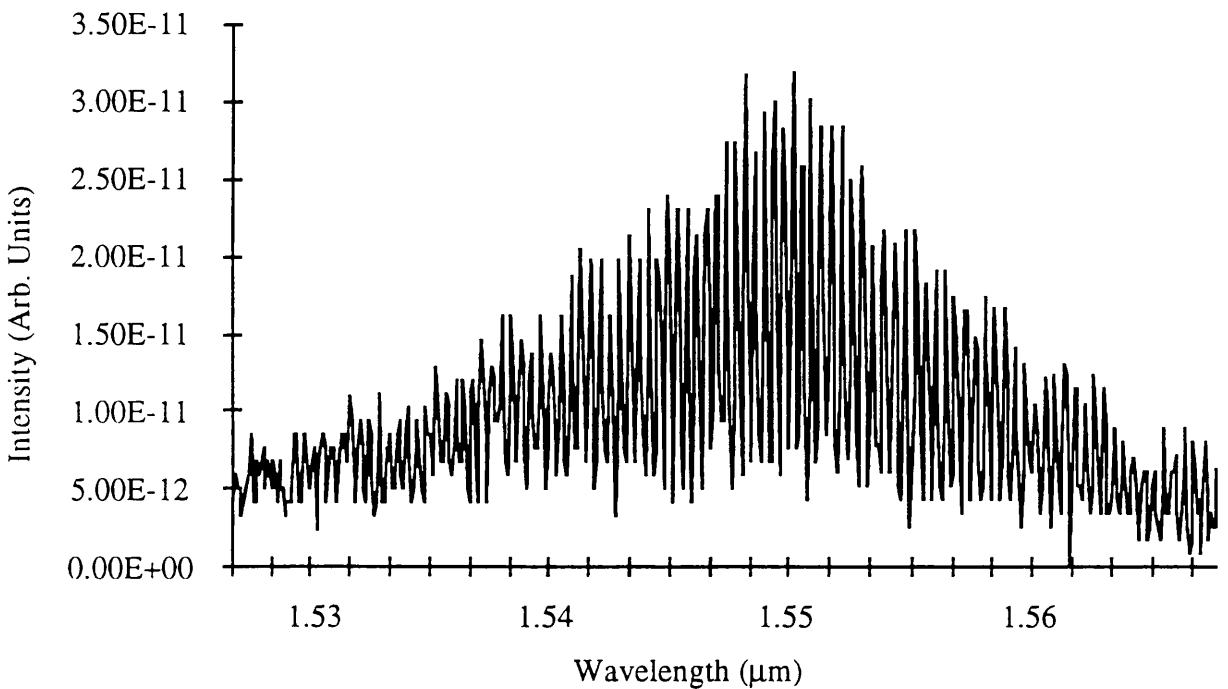


Figure 7.8 Spectrum of extended cavity oxide stripe laser at 0.63 A

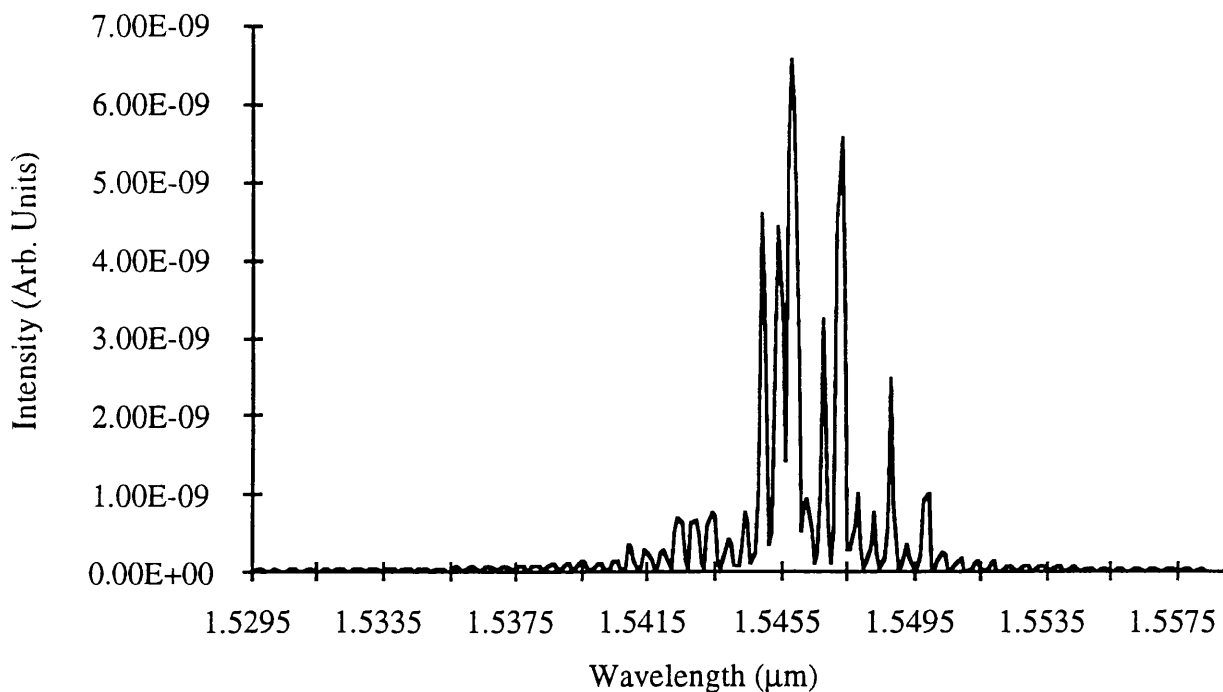


Figure 7.9 Spectrum of extended cavity oxide stripe laser at 0.93 A . The laser is operating well above the lasing threshold.

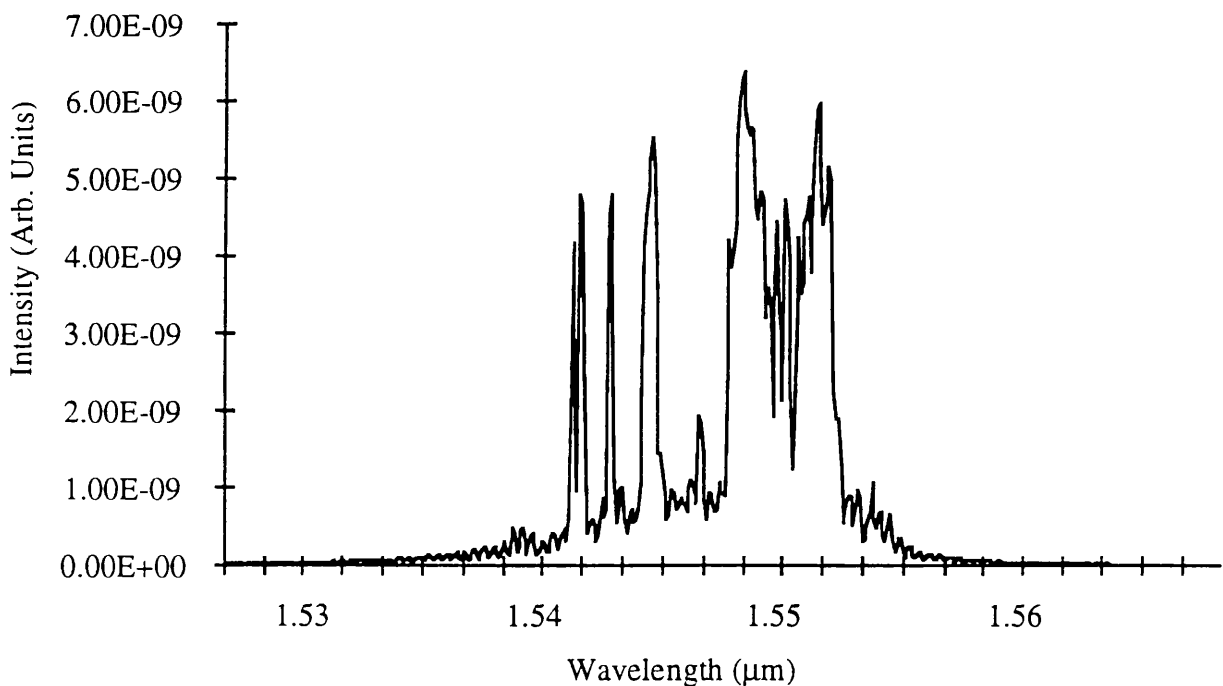


Figure 7.10 Spectrum of extended cavity oxide stripe laser at 1.3 A. As the injection current is increased the number of modes supported in the laser increases.

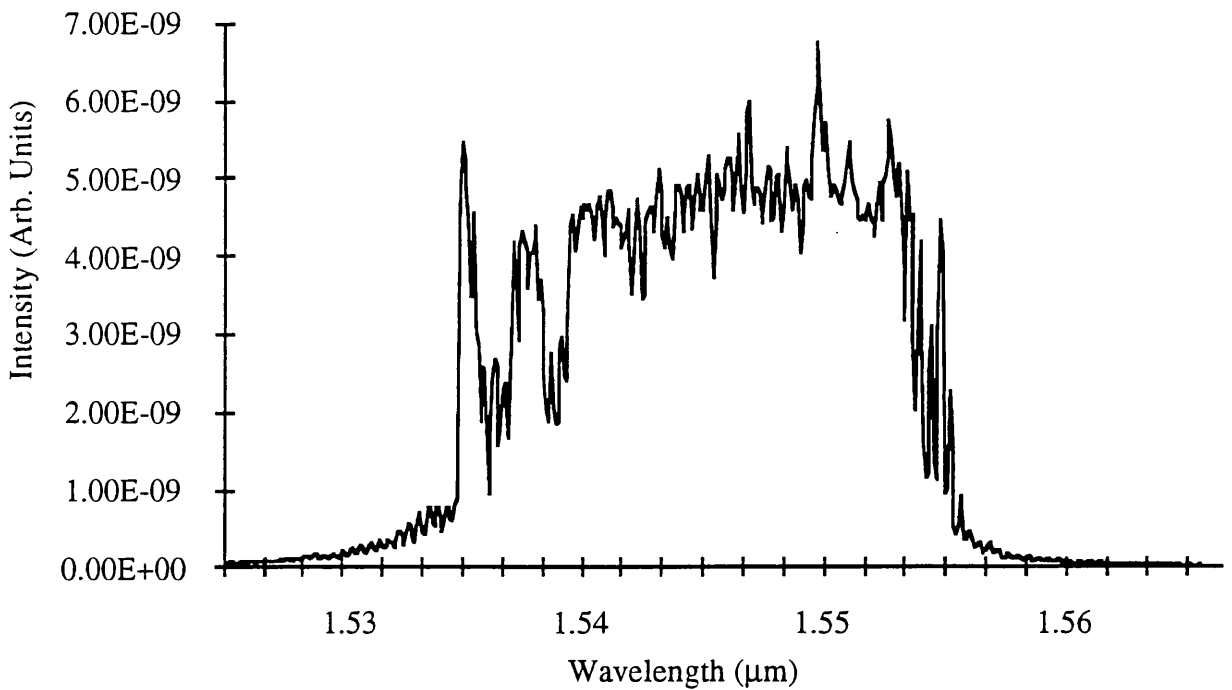


Figure 7.11 Spectrum of extended cavity oxide stripe laser at 1.9 A . At such high injection currents a broad linewidth is observed.

7.4 Conclusions

F IID has been used to fabricate extended cavity lasers. The lasers produced seem to have a higher threshold current than devices without extended cavities, which is probably due to residual absorption loss in the extended section. The increase in threshold current does not appear to be dramatic, this is encouraging since it indicates that the residual losses are small. Loss measurements are reported in Chapter 8 for the structures fabricated in this Chapter. The disordered sections seemed to become optically inactive after implantation with fluorine, lasers fabricated from F IID wafers showing no signs of producing luminescence.

References

- ¹J.H. Marsh, S.R. Andrew, S.G. Ayling, J. Beauvais, S.A. Bradshaw, R.M. De La Rue, and R.W. Glew, Mat. Res. Soc. Symp. Proc. Vol 240, pp679-690, 1992
- ²'DFB Lasers with Monolithically Integrated Passive Waveguide', T. Tanbun-Ek, P.A. Andrekson, R.A. Logan, S.N.G. Chu, D.L. Coblentz, A.M. Sergent, and K.W. Wecht, IEEE Photon. Tech. Lett. Vol. 4, No. 7, pp685-688, July 1992
- ³S.A. Bradshaw, 2 nd year Ph.D. Progress Report, 1991.

Chapter 8

Loss Measurement from Laser Characteristic

8.1 Introduction

It is important in the design of future devices containing quantum wells disordered with fluorine to know the absorption characteristics of optical waveguides, especially for photons around around the bandgap energy of the undisordered structure. The following Chapter discusses two techniques used to measure the absorption loss in the disordered region of the extended cavity lasers that were fabricated in Chapter 7.

In Section 8.2 the spontaneous emission from both the active and passive facets is monitored and recorded for the same injection current. Assuming that the disordered waveguide section does not produce any light, and that no gain occurs in the active section (below the lasing threshold), a comparison of the light levels at both facets gives an approximate value of the loss in the extended cavity.

Section 8.3 describes an alternative technique for measuring waveguide losses of extended cavity lasers. The loss induced by the extended cavity is deduced from the change in threshold current between a laser with an extended cavity and one without an extended cavity. The optical confinement factor and gain coefficients of the laser are also calculated in this section since they are required for the loss calculation.

8.2 Loss Measured by Luminescence

At injection current densities below those required to maintain population inversion, spontaneous emission occurs. Compared to the lineshape produced by stimulated emission the spontaneous lineshape is broad. The technique described below takes advantage of the broad spontaneous emission lineshape to produce a loss spectrum of the extended section of an extended cavity laser around its operating wavelength. The

broad spontaneous lineshape is therefore basically used as a source to probe the absorption characteristics of the disordered section.

8.2.1 Measurement Technique

At low excitation, there is no amplification by stimulated emission, and the same amount of light can therefore be assumed¹ to be emitted from the active region in all directions. If the intensity of light emitted from the active part of the device is given by $I(\lambda_0)$, then the intensity of luminescence escaping from the active facet is given by,

$$I_{act}(\lambda_0) = I(\lambda_0)(1 - R_0) \quad (8.1)$$

where R_0 is the reflection coefficient of the active facet. If we now include a passive waveguide section of length L_{pass} , then the intensity of light escaping from the passive facet, $I_{pass}(\lambda_0)$, can be expressed similarly as,

$$I_{pass}(\lambda_0) = I(\lambda_0)(1 - R_0)\exp[-\alpha(\lambda_0)L_{pass}] \quad (8.2)$$

where $\alpha(\lambda_0)$ is the absorption coefficient of the passive waveguide.

Equation 8.2 neglects losses due to divergence from the active region into the disordered section; in practice not all the light emitted from the active region would be emitted from the passive facet. However, a comparison of the two outputs will give a good approximation to the absorption loss of the disordered section. The absorption spectrum, $\alpha(\lambda_0)$, is therefore given by,

$$\alpha(\lambda_0) = -\frac{1}{L_{pass}} \ln\left(\frac{I_{pass}(\lambda_0)}{I_{act}(\lambda_0)}\right) \quad (8.3)$$

where $I_{pass}(\lambda_0)$ is the luminescence from the passive side of the waveguide and $I_{act}(\lambda_0)$ the luminescence from the active side of the waveguide.

Losses measured by this technique give an upper limit to the actual loss of the disordered waveguide section around the bandgap of the undisordered structure, as long

as there is no gain occurring in the disordered region of the waveguide. The technique gives an upper limit to the loss of the waveguide since it does not take into account any light that may be lost from the cavity, other than that being emitted from the passive facet.

8.2.2 Experimental Technique

The extended cavity lasers, as fabricated in Chapter 7, were used for the loss measurements discussed in this Chapter. A pulsed source is used to drive the lasers, as described in Section 6.3 of Chapter 6, and the output from the devices is monitored with a spectrum analyser as indicated in Figure 8.1. The drive current is adjusted so that the laser is producing a clear luminescence peak from both facets but the device is not lasing. In practice this means setting the drive current at approximately 75% of the device's threshold current.

In order to maximise coupling of the luminescence into the optical fibre, the internal slits of the spectrum analyser are set to the widest position (minimum resolution) to ensure maximum sensitivity to incident light. The trace on the spectrum analyser is then maximised by adjusting the position of the laser with respect to the fibre to get optimum coupling into the fibre. It is very important to take particular care with the alignment at this stage since the result depends on comparing the power levels between two separate readings. Once maximum coupling has been achieved, the slits are narrowed and the required spectrum is taken (Figure 8.2) and stored in the spectrum analyser as the reference signal. The sample is then rotated through 180° so that light from the passive facet is now coupled into the optical fibre, the coupling is then maximised by the same procedure as that described above.

The spectra are recorded in dB so that subtraction of the two stored spectra gives the ratio of optical power emitted from the facet in dB, as shown in Figure 8.3 and Figure 8.4. This ratio is the overall optical waveguide loss for the device, the loss in dB cm^{-1} being obtained by dividing the overall loss by the length of the extended cavity section

in cm. The spectra of interest are then downloaded onto a computer for future reference, using a simple LabVIEW programme and the IEEE interface between the spectrum analyser and a computer.

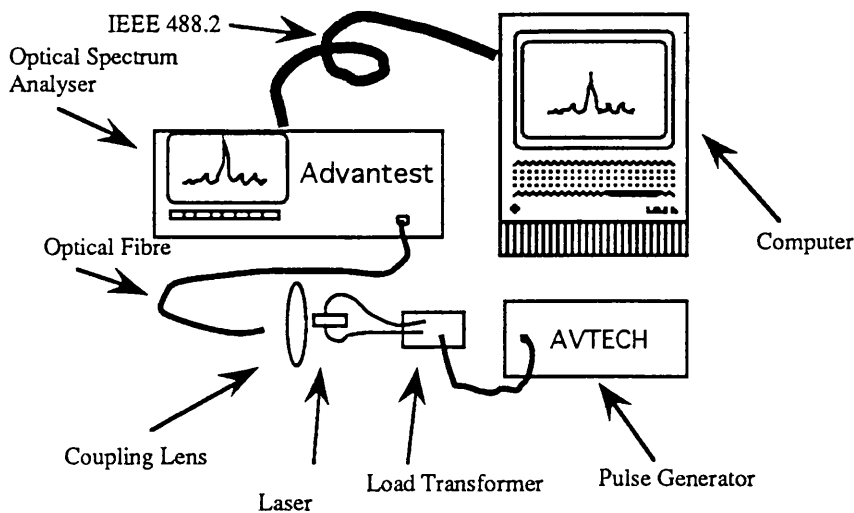


Figure 8.1 Experimental set-up used to measure the sub-threshold luminescence from the oxide stripe extended cavity lasers.

8.2.3 Results

Figure 8.2 shows the luminescence from the active and passive facets of an oxide stripe extended cavity laser. The stripe width is $75 \mu\text{m}$ with an active cavity length of $600 \mu\text{m}$, and a passive section of $400 \mu\text{m}$. The sample was implanted with F with a dose of $1.4 \times 10^{13} \text{ nuclei cm}^{-2}$ with an energy of 1.5 MeV giving a concentration of $\sim 10^{18} \text{ nuclei cm}^{-3}$ in the centre of the QW region. The sample was then annealed at 700°C for 30 s in the RTP with a 1000 \AA coating of silica. If the bandgap shift of the disordered section after annealing is estimated to be around 40 meV (Figure 3.10), then the absorption edge of the extended cavity will be at $1.47 \mu\text{m}$.

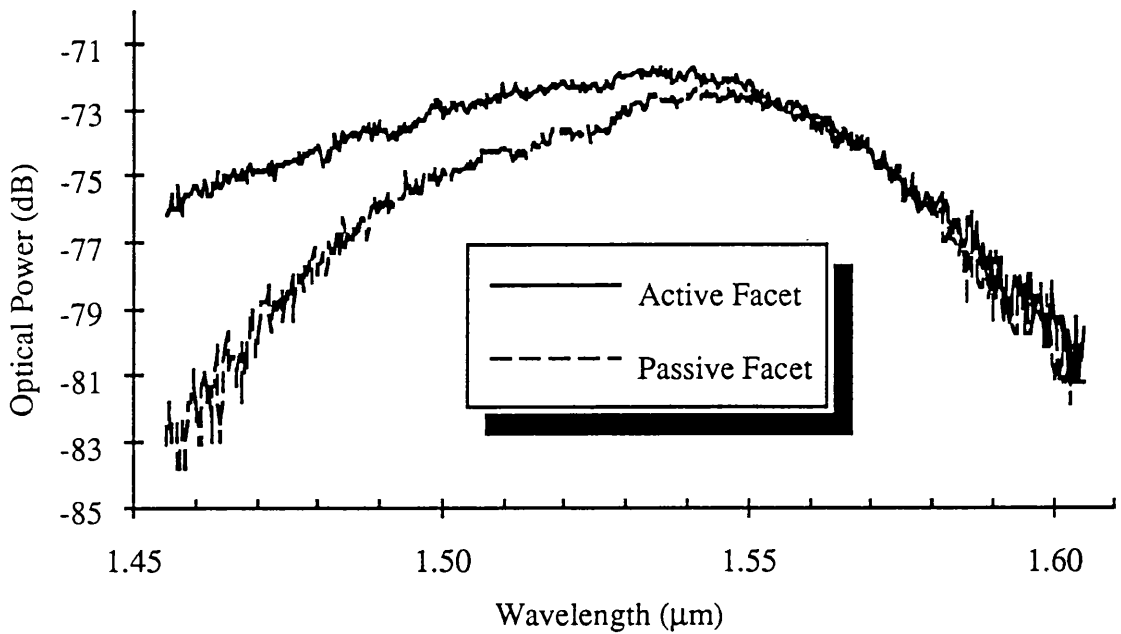


Figure 8.2 Luminescence Measurements.

Figure 8.3 shows the loss spectrum in dB calculated by the Advantest spectrum analyser. The wavelength about which lasing occurs in this particular structure is around 1.55 μm , indicating a loss of around 0.5 dB in the passive waveguide section. The passive region in this sample is 400 μm which gives an overall loss in the extended cavity as 12.5 dB cm^{-1} . Figure 8.4 shows the loss spectrum of another sample showing a higher loss of around 1 dB (20 dB cm^{-1}).

To investigate the accuracy of the technique, dummy measurements were taken, Figure 8.5. The procedure for measuring the loss as described above was carried out by using the active facet in both stages of measurement. The error was of the order of 0.05 dB at 1.55 μm , or 10 % of the measurement in Figure 8.3.

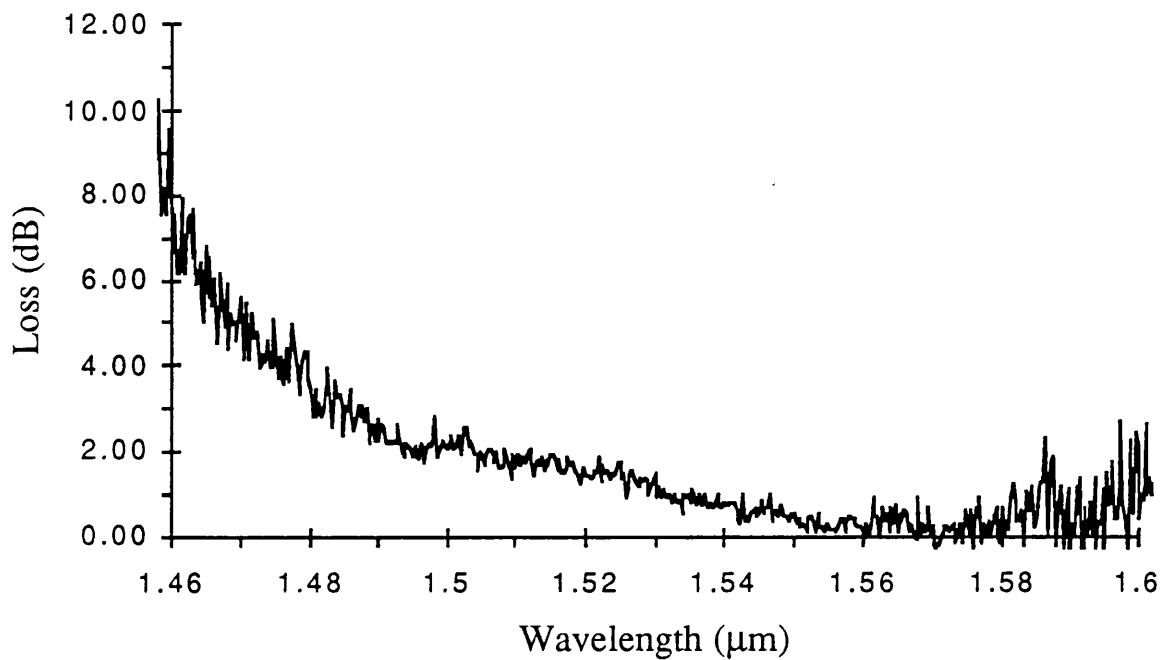


Figure 8.3 Loss measurement of a laser with an extended cavity of 400 μm.

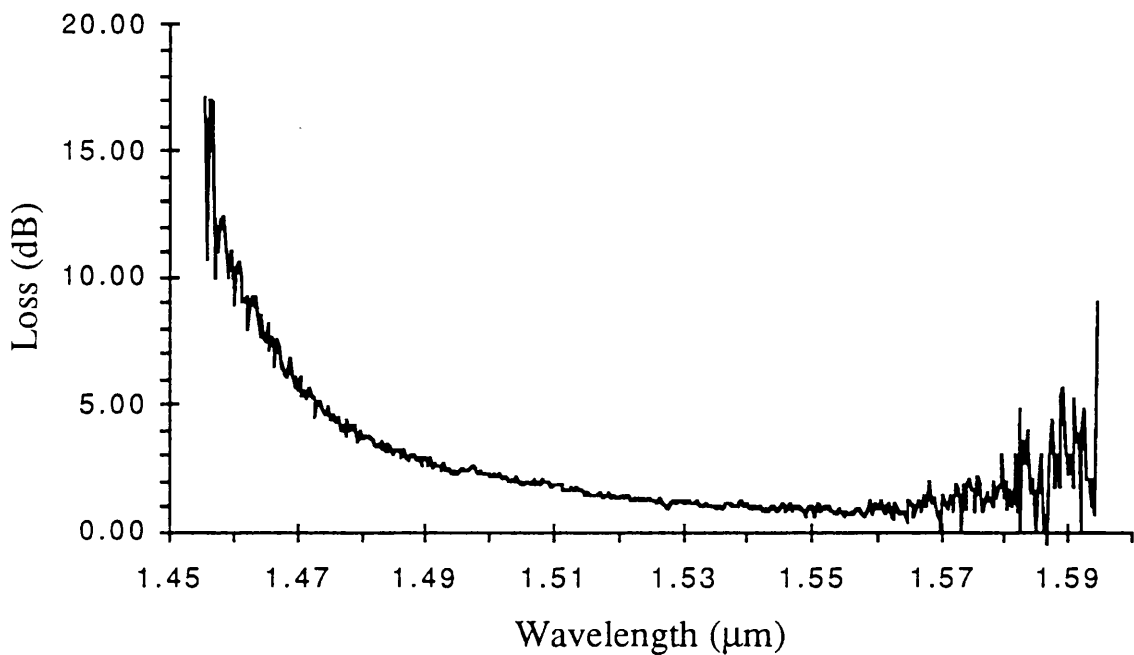


Figure 8.4 Loss measurement of a laser with an extended cavity of 500 μm.

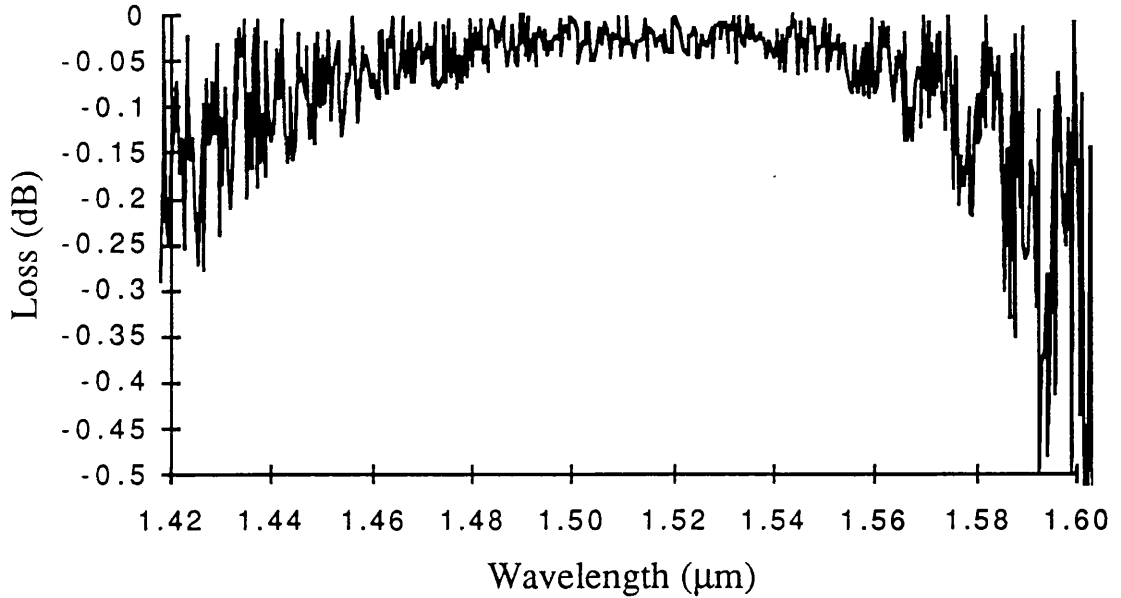


Figure 8.5 Test curve showing the result of taking the luminescence from the same facet.

8.3 Calculation of Loss From the Change in Threshold Current

By finding the change in threshold current between a laser with an extended cavity and one without an extended cavity, and assuming that all other parameters remain constant, it is possible to get an estimate of the loss introduced by the extended section.

The ratio of the threshold current of an extended cavity laser to that of normal laser can be found by considering the gain required for laser action (Equation 8.9), this is dealt with in greater detail in Section 8.3.2. The threshold current density for a normal laser cavity (J_{norm}) is given by Equation 8.4,

$$\ln(J_{norm}) = \ln\left(\frac{n}{\eta}\right) + \ln(J_o) + \frac{\alpha_a}{n\Gamma_w g_o} + \frac{\ln(1/R)}{n\Gamma_w g_o l_a} \quad (8.4)$$

where R is the reflection coefficient of the facets, n is the number of quantum wells in the active region, η is the internal quantum efficiency, g_o is the QW gain parameter, Γ_w is the optical overlap with a single well, l_a is the length of the active region and α_a is the loss of the active region. The threshold current density for a laser with an extended cavity (J_{ex}) of length l_p and loss α_p is

$$\ln(J_{ex}) = \ln\left(\frac{n}{\eta}\right) + \ln(J_o) + \frac{\alpha_a}{n\Gamma_w g_o} + \frac{\ln(1/R)}{n\Gamma_w g_o l_a} + \frac{\alpha_p l_p}{n\Gamma_w g_o l_a} \quad (8.5)$$

Subtracting Equations 8.4 and 8.5, a ratio of the threshold currents J_{ex} and J_{norm} can be found,

$$\ln(J_{ex}) - \ln(J_{norm}) = \ln\left(\frac{J_{ex}}{J_{norm}}\right) = \ln\left(\frac{I_{ex}}{I_{norm}}\right) = \frac{\alpha_p l_p}{n\Gamma_w g_o l_a} \quad (8.6)$$

so the loss of the passive section can be found with Equation 8.7.

$$\alpha_p = \ln\left(\frac{I_{ex}}{I_{norm}}\right) \left(n\Gamma_w g_o l_a / l_p\right) \quad (8.7)$$

where I_{ex} and I_{norm} are the threshold currents for the extended cavity and normal devices respectfully, α_p is the loss of the extended cavity section. In order to calculate α_p from Equation 8.4 we first need to calculate the optical overlap of each QW, Γ_w , and measure the gain coefficient, g_o .

8.3.1 Calculation of the Optical Confinement Factor (Γ_w)

The optical confinement factor represents the percentage of the optical field overlapping the quantum well. A program written by Dr. Ayling of this Department was used to calculate Γ_w for the structure used in the experiment. The program calculates the intensity distribution across three layered structure consisting of a lower cladding layer, an active region and an upper cladding layer. The percentage of light confined within the quantum well is then calculated by integrating the field at the centre of the well across the width of the well. This is then divided by the total integrated field to yield the optical confinement factor in the form of a percentage. The air layer above the upper cladding is ignored since the structure has been designed so that the field intensity at the top of the upper cladding is very small.

In order to calculate the optical confinement factor of the quantum wells within the laser structure a simplified structure is used. Figure 8.6 shows the simplification used in the

calculation. The upper cladding layer is assumed to be InP, the effects of the contact layer of InGaAs are ignored since very little of the optical field overlaps this region. The region labelled *Guide* in Figure 8.6 comprises the quantum well structure of the gain medium as well as the SCH structures above and below the QW region; the refractive index of this section is a weighted average of all the composite layers. Finally the *Lower Cladding* region is as on the actual wafer.

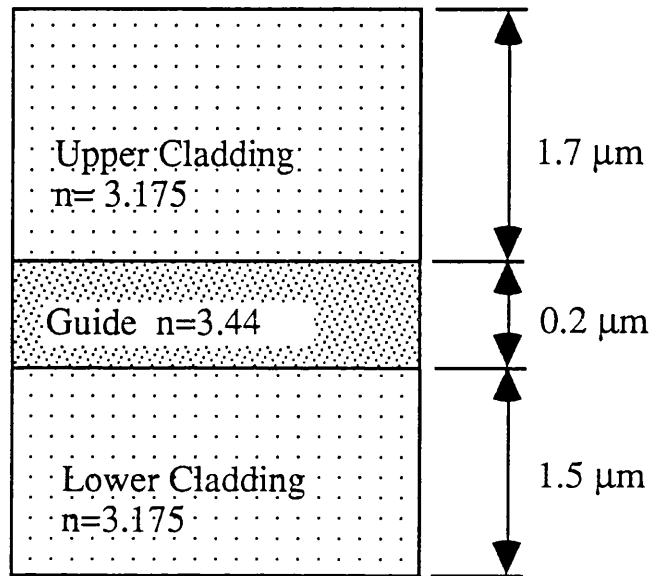


Figure 8.6. Simplified Structure used to calculate the confinement factor for loss calculations.

The results shown in Figure 8.7 are for 100 \AA wells in the structure represented in Figure 8.6. It is interesting to see here that the optical confinement is approximately constant at the centre of the structure, including the active region. This property is used when calculating the gain parameter in Section 8.3.2. Here the optical confinement was calculated to be $\sim 1.9 \%$.

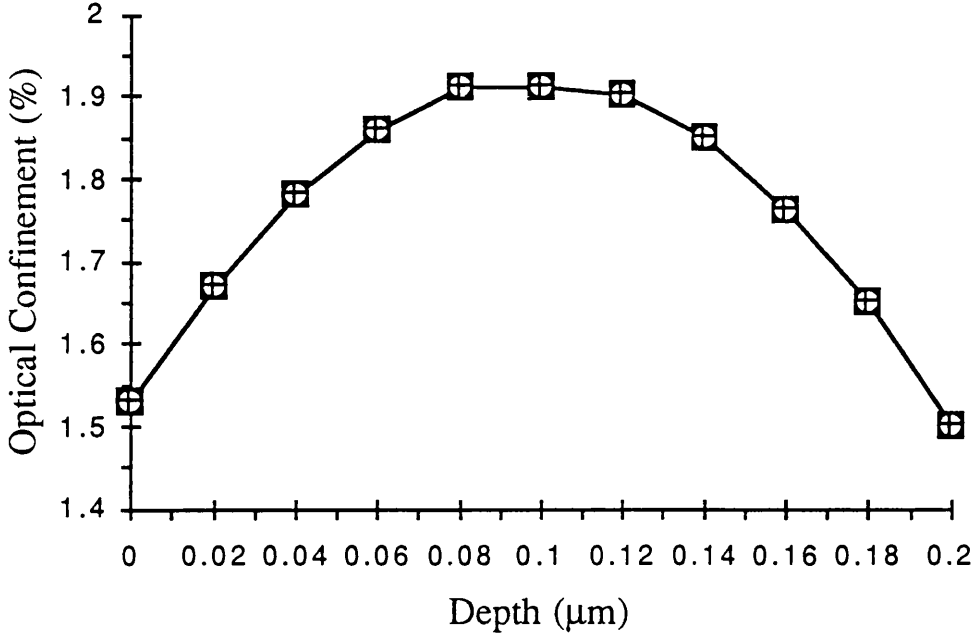


Figure 8.7 Optical Confinement for the simplified E288 Laser Structure as a function of depth below the cladding layer. The QWs are 100 Å.

8.3.2 Calculation of the Gain Parameter (g_o)

The gain coefficient g_o of a quantum well is proportional to the integral of available transitions between the conduction and valence bands and can be written in the form²,

$$g(h) = \frac{Z_o m_r}{\mu \pi \hbar^2 L_z} \sum_{n, n'} \int_{E_{cn} + E_{vn} + E_s}^{\infty} \langle R_{ch}^2 \rangle \frac{(f_c - f_v) \Delta E}{(E_{ch} - \hbar\omega)^2 + \Delta E^2} dE_{ch} \quad (8.8)$$

where $Z_o = (\mu_o / \epsilon_o)^{1/2}$ is the impedance of free space, $E_{ch} = E_c - E_v$ is the transition energy, E_{cn} and E_{vn} are the n th and n' th energy levels of the electron and hole quantum wells respectively, and f_c and f_v are the corresponding Fermi levels. R_{ch} is the intraband matrix element which is set to zero for $n \neq n'$. L_z is the quantum well width, and μ the effective index of the well.

If the total active width is less than ~ 1000 Å then the optical overlap with QWs positioned in the centre of the active region (Γ_w) is approximately proportional to the total number of wells² as can be seen in Figure 8.7. From this approximation it follows

that if one well produces a modal gain $\Gamma_w g$ with a current density J/η then, n wells will produce a modal gain of $n\Gamma_w g$ with current density nJ/η . The required gain at threshold now becomes

$$G = n\Gamma_w g = \alpha + \ln(1/R)/L \quad (8.9)$$

For small quantum wells the gain curves can be approximated to a logarithm function as a function of current. The gain curves can be simplified to

$$g = g_o \ln\left(\frac{J}{J_t}\right), \quad (8.10)$$

where g_o is the quantum well gain parameter, and J_t is the transparency current density.

The gain at threshold (G_{th}),

$$G_{th} = n\Gamma_w g_{th} = \alpha_a + \frac{1}{L} \ln\left(\frac{1}{R}\right) \quad (8.11)$$

where g_{th} is the gain parameter at threshold and,

$$n\Gamma_w g_o \ln\left(\frac{J_{th}\eta}{nJ_t}\right) = \alpha_a + \frac{1}{L} \ln\left(\frac{1}{R}\right), \quad (8.12)$$

where J_{th} is the threshold current density.

Rearranging Equation 8.12,

$$\ln(J_{th}) = J_\infty + \frac{\ln(1/R)}{n\Gamma_w} \frac{1}{g_o L}. \quad (8.13)$$

Where J_∞ is the threshold current density for a device with an infinite cavity length, and is given as,

$$J_\infty = \ln\left(\frac{n}{\eta}\right) + \ln(J_t) + \frac{\alpha}{n\Gamma_w g_o} \quad (8.14)$$

From Equation 8.13 it can be seen that the gradient of a plot of $\ln(J_{th})$ vs. $1/L$ will yield the required value of g_o for the loss calculation.

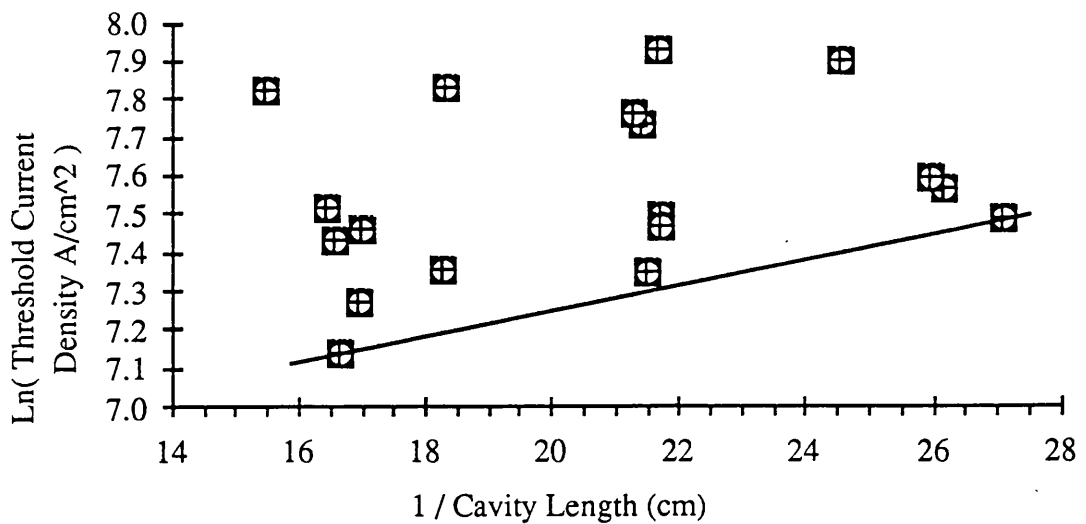


Figure 8.8. $\ln(\text{Threshold current density})$ vs. $1/\text{Cavity Length}$ for oxide stripe lasers used to estimate the gain coefficient (g_o) –required to calculate the loss in extended cavity lasers.

From the results in Figure 8.7 it is possible to estimate the gain coefficient. Equation 8.13 is simplified as discussed above and used in the form,

$$\ln(J_{th}) \cong J_{\infty} + \frac{B}{g_o} \cdot \frac{1}{L}, \quad (8.14)$$

where the constant B is given by,

$$B = \frac{\ln(1/R)}{n\Gamma_w}. \quad (8.15)$$

For the purpose of this calculation R (the reflection coefficient) is 30 %, n (the number of quantum wells) is 5, and Γ_w (the optical confinement) is 1.9 % as calculated in Section 8.3.1, B is therefore 3.75. The gradient (B/g_o) obtained from Figure 8.8 is 0.077, so substituting these values into Equation 8.14 we get a value of g_o of 165 cm^{-1} .

There is a large variation in threshold currents observed in Figure 8.7. This spread in results is a serious limitation in the estimation of g_o , and subsequently calculating the loss of the extend cavity by this technique. Large variations in the threshold current can be explained by;

1. Poor metallic contacts - leading to current spreading in the device.
2. Damaged optical facets - leading to a degradation in the optical feedback within the laser cavity.

Waveguide losses measured using the above technique will not be very accurate unless the measured threshold current densities show good consistency.

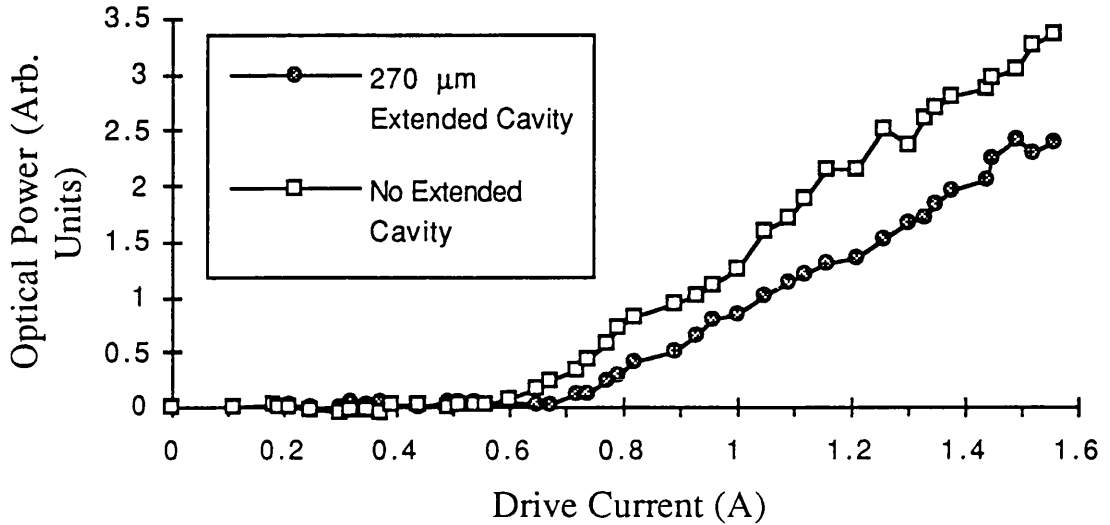


Figure 8.9 Typical output characteristics of a device with and without an extended waveguide. The closed circles represent a device with an extended cavity section of 270 μm produced by using F IID.

Figure 8.9 shows a typical drive current vs. output power curve obtained as described in Section 7.3. The curve is from a device having a 775 μm active section and a 270 μm passive section. Substituting the cavity lengths and change of threshold current back into Equation 8.4 we get a loss of 6.9 cm^{-1} (30 dB cm^{-1}).

8.4 Conclusions

Two methods have been used to calculate the waveguide losses for F IID extended cavity lasers. It was found that low loss optical cavities have been fabricated with an optical waveguide loss of between 30 dB cm^{-1} , found by comparing threshold currents, and a loss of 12.5 dB cm^{-1} , found by comparing sub-threshold luminescence. The loss

figure of 30 dB cm^{-1} , is not expected to be accurate due to the spread of threshold current densities measured, Figure 8.8.

The electrical isolation produced by disordering has not been measured here, this will require further investigation in order to advance the process towards producing a device containing several isolated active devices.

References

- ¹'Absorption of light in GaAs-Al_xGa_{1-x}As film waveguides and its influence on the threshold characteristics of heterojunction lasers with Bragg reflectors', S.A. Gurevich, E.L. Portnoi, and M.E.Raikh, *Sov. Phys. Semicond.* 12(6), pp. 688-694, 1978.
- ²'Analysis and Application of Theoretical Gain Curves to the Design of Multi-Quantum-Well Lasers', W.A. Paul, M.C. McIlroy, A. Kurobe, and Y. Uematsu, *IEEE J. of Quant. Electron.* **QE-21** (12), pp. 1958-1963, 1985.

Chapter 9

Near- and Far-Field Patterns

9.1 Introduction

The aim of this Chapter is to show that a useful device can be made using the technique developed in this thesis for creating low loss waveguides by fluorine implantation followed by thermal processing. The device that has been chosen to demonstrate the technique is an oxide stripe multiple quantum well laser with an integrated low-loss waveguide. The following sections describe the supermode behaviour of multiple stripe lasers, and show the type of near- and far-field patterns that can be expected. Experimental results are compared to theoretical calculations to explain the far-field patterns observed when an extended cavity is integrated with an oxide stripe laser.

It is well known that wide stripe, or broad-area, semiconductor lasers can generate high power optical pulses by virtue of their large emitting area¹. However, they do have problems; the beam tends to break up into either one containing high order lateral modes or into independent lateral filaments. In the former case the beam divergence is found to be greater than theory indicates and in the second case the light exhibits little or no spatial coherence. Filamentation has been studied extensively in high power solid-state lasers, where a positive change in refractive index is observed with increased optical intensity². The idea of integrating a low loss waveguide section onto the oxide stripe is to try to force the laser to operate in the fundamental supermode, i.e. make all the laser filaments lase in-phase, or to remove the filaments altogether. The required effect is to have maximum power output in the direction parallel to the waveguide and perpendicular to the laser facet.

The near- and far-field patterns of oxide stripe lasers with and without an extended cavity are investigated. The near-field patterns are measured using a camera, far-field patterns are measured by two techniques: the first using a camera, the second, and more geometrically correct, using a rotary stage and a Ge photodiode.

9.2 Near- and Far-Field Patterns

Laser light is emitted from the laser facet only near the active region in a pattern called the laser *near-field*. The near-field pattern is the distribution of the optical field in the laser cavity at the facet, which can be observed using a camera and an objective lens or microscope. Diffraction broadens the beam into the laser *far-field* pattern. The far-field pattern contains information concerning the phase relationship between adjacent lasers in laser arrays, or the filaments in broad area and oxide stripe lasers. Interference between the individual laser beams, or filaments, produces a pattern containing maxima and minima that can be easily detected.

The far-field pattern not only shows the phase relationship of the beam but also the angular distribution of the laser modes and is therefore important in determining the coupling efficiency between a laser and optical fibre. For high coupling efficiency the beam divergence should be small, this being due to the limited acceptance angles of modern communications fibres. For example, typical graded index glass multi-mode fibre will have a numerical aperture (NA) of between 0.2 and 0.3, the relationship of the NA to the acceptance angle (θ_a) of the fibre is,

$$\theta_a = \sin^{-1} NA \quad (9.1)$$

which gives an acceptance angle of between 17.5° and 11.5° .

For single moded fibres, the mode overlap between the guided mode in the fibre and the input laser mode is more important than the NA . A single lobed source will have a greater coupling efficiency into a fibre than one containing several lobes, even if all the lobes are within the acceptance cone of the fibre.

9.3 The Far Field Pattern

Mathematically the far-field pattern is the Fourier transform of the near-field pattern and, as its name suggests, is the distribution of light a long way from the laser facet (long compared to the laser dimensions).

According to diffraction theory, the angular separation of the lobes produced by *point radiators* is³,

$$\phi = 57.3^\circ \frac{\lambda_0}{S} \quad (9.2)$$

where S is the interval between the point source and λ_0 the emitting wavelength and the constant term is the conversion factor for radians to degrees. Experimental results do not agree exactly with Equation 9.2 for the case of broad area lasers, due to several factors including; extended sources (the filaments do not approximate to point sources, being of the order of a few microns), non-planar wavefronts, and the phase differences between the sources. If the wavefronts of each filament were exactly in-phase then the far-field pattern would be symmetric about 0° . On the other hand if adjacent filaments were exactly 180° out of phase, the far-field would consist of two identical lobes symmetric about the axis⁴.

From Equation 9.2, a laser array operating at $1.5 \mu\text{m}$ with filaments separated by $10 \mu\text{m}$ would have lobes at $\pm 8.6^\circ$.

The near- and far-field patterns of broad area lasers can be modelled by using coupled mode theory as detailed in Section 9.1. The filaments observed in the broad area devices are assumed to behave in a similar manner to an array of identical lasers.

9.4 Theory of Field Patterns in Laser Arrays

The following section contains the theory necessary to produce a simple model for the near- and far-field behaviour of semiconductor laser arrays. At the end of this section, the field patterns are calculated for a laser containing 10 stripes separated by $7.5 \mu\text{m}$

9.4.1 The Equations

For the case of a laser array containing N adjacent waveguides each of which can support a single mode, the m^{th} normalised electric field can be expressed as,

$$A_m(z)E_m(x, y)e^{-i\beta_m z}, \quad (9.3)$$

the total field at some arbitrary point can then be expressed as the sum of the individual fields,

$$E(z) = \sum_m A_m(z) E_m(x, y) e^{-i\beta_m z}, \quad (9.4)$$

where A_m represents the amplitude and phase of the individual modes, β_m is the propagation constant in the z direction and $E_m(x, y)$ the mode profile of the m^{th} element. In the simplest case all the A_m 's are independent of each other, and the spacing between the array elements is big enough so that the coupling between the electric fields in adjacent stripes is so small that there is no correlation between adjacent stripe modes. By definition the total power in the m^{th} guide is $|A_m|^2$, so that the total field at a distance z from the source can be expressed as,

$$E(z) \equiv \begin{pmatrix} A_1 e^{-i\beta_1 z} \\ A_2 e^{-i\beta_2 z} \\ \bullet \\ \bullet \\ \bullet \\ A_N e^{-i\beta_N z} \end{pmatrix} \equiv \begin{pmatrix} E_1(z) \\ E_2(z) \\ \bullet \\ \bullet \\ \bullet \\ E_N(z) \end{pmatrix}. \quad (9.5)$$

We are interested in the coupled case, since we would expect the filaments in broad area lasers to be close together.

Coupled mode theory gives the relationship between adjacent modes as,

$$\frac{dA_m}{dz} = \kappa_{m,m+1} A_{m+1} e^{i(\beta_m - \beta_{m+1})z} + \kappa_{m,m-1} A_{m-1} e^{i(\beta_m - \beta_{m-1})z} \quad (9.6)$$

assuming that coupling is only significant between adjacent modes. $\kappa_{m,m+1}$ represents the coupling between the m^{th} and $(m+1)^{\text{th}}$ guides and is equal and opposite to the coupling between the m^{th} and $(m-1)^{\text{th}}$ guides. By using the differential of a product rule, it follows that the component $E_m(z)$ of the vector $E(z)$ obeys the relationship,

$$\begin{aligned}
\frac{dE_m(z)}{dz} &= -i\beta_m A_m(z)e^{-i\beta_m z} + \frac{dA_m}{dz} e^{-i\beta_m z} \\
&= -i\beta_m A_m(z)e^{-i\beta_m z} + \kappa_{m,m+1} A_{m+1} e^{i\beta_{m+1} z} \\
&\quad + \kappa_{m,m-1} A_{m-1} e^{i\beta_{m-1} z}
\end{aligned} \tag{9.7}$$

which now forms a set of coupled equations. In vector terms, Equation 9.7 is written as,

$$\frac{d\mathbf{E}}{dz} = \tilde{\mathbf{C}} \mathbf{E} \tag{9.8}$$

where $\tilde{\mathbf{C}}$ is the matrix in Equation 9.8 and has the form,

$$\tilde{\mathbf{C}} = \begin{pmatrix} -i\beta_1 & \kappa_{1,2} & 0 & 0 & \bullet & \bullet & \bullet & 0 & 0 \\ \kappa_{2,1} & -i\beta_2 & \kappa_{2,3} & 0 & \bullet & \bullet & \bullet & 0 & 0 \\ 0 & \kappa_{3,2} & -i\beta_3 & \kappa_{3,4} & \bullet & \bullet & \bullet & 0 & 0 \\ \bullet & \bullet \\ \bullet & \bullet \\ \bullet & \bullet \\ 0 & 0 & 0 & 0 & \bullet & \bullet & \bullet & \kappa_{N,N-1} & -i\beta_N \end{pmatrix}. \tag{9.8}$$

The solutions to equation 9.7 are the propagating supermodes of the laser array, which are independent of z except for the phase factor expressed simply by,

$$\mathbf{E}(z) = \mathbf{E}(0)e^{i\gamma z}, \tag{9.9}$$

and differentiating with respect to z , results in Equation 9.10,

$$\frac{d\mathbf{E}(z)}{dz} = i\gamma\mathbf{E}(z). \tag{9.10}$$

When rearranged and combined with Equation 9.8 this becomes,

$$(\tilde{\mathbf{C}} - i\gamma\tilde{\mathbf{I}})\mathbf{E} = 0. \tag{9.11}$$

The solutions of Equation 9.11 are referred to as *supermodes* and represent the modes of the coupled array, not of the individual waveguides which we assumed previously to be single moded. $\tilde{\mathbf{I}}$ in Equation 9.11 is the $N \times N$ identity matrix. Equation 9.11, is in effect

a series of N equations with N unknowns which in general will result in N eigenvalues ($i\gamma_N$) with N corresponding eigenvectors, E^v .

The v^{th} supermode thus consists of a unique linear superposition of the individual waveguide modes $E_m(x, y)$ with a fixed relative phase between any two of them. The total field of the v^{th} supermode is written as,

$$E^v(x, y, z) = \left[\sum_m E_m^v E_m(x, y) \right] e^{i\gamma_v z} \quad (9.12)$$

Fortunately, in the case where the waveguides are equally spaced and the waveguides are identical, there is a simple solution to Equation 9.12. From experimental observation this appears to be the case for broad area lasers, i.e. the filaments appear to be equally spaced. The solution for this special case gives,

$$E_l^v = \sin\left(\frac{l\pi v}{N+1}\right) \quad \text{where} \quad \begin{array}{l} l = 1, 2, \dots, N \\ v = 1, 2, \dots, N' \end{array} \quad (9.13)$$

for the field amplitude of each modal element (l) in each supermode (v), and for the propagation constant,

$$\gamma_v = -\beta - 2\kappa \cos\left(\frac{\pi v}{N+1}\right). \quad (9.14)$$

The propagation constant has been left in the calculation for the sake of completeness, it will be used no further here.

The far-field pattern can be found in a similar way, by summing the component of the far-field from each individual emitter and then multiplying by a term which takes into account the coupling between emitters. The far-field pattern, $E(\theta)$, of a single emitter is the Fourier transform of the near-field⁵,

$$E(\theta) \propto \cos\theta \int_{-\infty}^{\infty} E(y) \exp(ik_y y \sin\theta) dy, \quad (9.15)$$

where θ is the observation angle, $E(y)$ is the field pattern across the emitter in the same plane as the observer, and D is the width of the near-field pattern. By superposition, the far-field pattern is expressed as,

$$F^v(\theta) = \sum_{l=1}^N E_l^v E_l(\theta) \quad (9.16)$$

where E_l^v is the amplitude of the field in the l^{th} guide (or emitter) in the v^{th} supermode, and $E_l(\theta)$ is the far-field pattern of the l^{th} emitter.

For the case of identical emitters, the far-field intensity of any of the individual emitters is equal to that of one multiplied by a phase factor. Figure 9.1 shows the case for two adjacent emitters. The path difference of light coming from the emitter at point A compared to that a distance S away at point B as seen by an observer at point O is given by simple geometry,

$$\text{Path Difference} = (S \sin(\theta) + OC \cos(\delta)) - OC. \quad (9.17)$$

If it is assumed that the observer is along way off, compared to the distance between the emitters (S), the δ becomes very small and $\cos(\delta) \rightarrow 1$. The path difference is now equal to $S \sin(\theta)$.

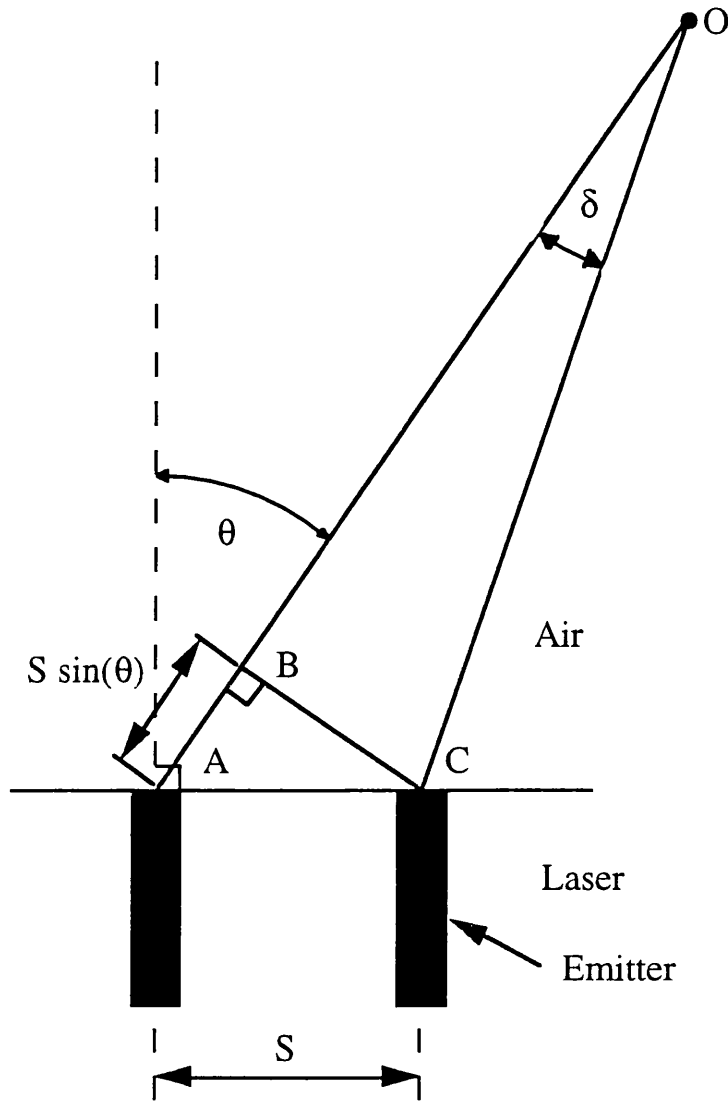


Figure 9.1. The path difference between two adjacent emitters at positions A and C is approximately $S \sin(\theta)$, if δ small.

The phase difference, which is what we actually interested in, is therefore $e^{ik_o S \sin \theta}$. If we now have l emitters all spaced a distance S from each other the phase difference between the first element and the l^{th} is $e^{ik_o l S \sin \theta}$, since the distance between them is lS . In the case of identical emitters spaced at an equal distance, equation 9.16 becomes,

$$F^v(\theta) = E_o(\theta) \sum_{l=0}^{N-1} E_l^v e^{ik_o l S \sin(\theta)}. \quad (9.18)$$

The far-field intensity pattern is,

$$|F^v(\theta)|^2 = |E_o^{(\theta)}|^2 G^v(\theta) \quad (9.19)$$

where $G^v(\theta)$ is the grating function,

$$G^v(\theta) = \left| \sum_{l=0}^{N-1} E_l^v e^{ik_o l S \sin(\theta)} \right|^2.$$

The grating function corresponds to the radiation pattern of N point radiators spaced a distance S apart and with relative amplitude equal to the function E_l^v .

9.4.2 Theoretical Calculations

A MATLAB computer program was written to calculate the expected near- and far-field patterns of the oxide stripe laser. A print-out of the computer programme is included in Appendix B. In order to evaluate the integral for the Fourier transform, a simple algorithm was written to sum the area under the field distribution curve, i.e.

$$\int_{y_1}^{y_2} F(y) dy = \sum_{n=0}^{n=N} F_n (y_n + y_{n+1}) \quad (9.20)$$

where $F(y)$ is the field distribution in the y direction, F_n is the value of the field at the n th point across the profile, y_n is the position of the n th point across the profile. The smaller the step size the more accurate the evaluation of the integral is.

9.4.3 Theoretical Calculation Results

The first stage in the calculation is to find the mode profile in an individual emitter. In the case of the laser array it is unclear as to the exact nature of the filaments so it is difficult to model. A slab waveguide mode is therefore calculated to find an approximate mode profile based on experimental observation. The following parameters were set in the MATLAB *m-file* 'data.m', and used in the routine 'mdfnd.m';

n1=3.540

n2=3.545

d=2.0e-6 m

$$\lambda = 1.55 \times 10^{-6} \text{ m}$$

Here n_1 and n_2 are the refractive indices in the cladding and core respectively, d is the half width of the core and λ the free space wavelength of the laser.

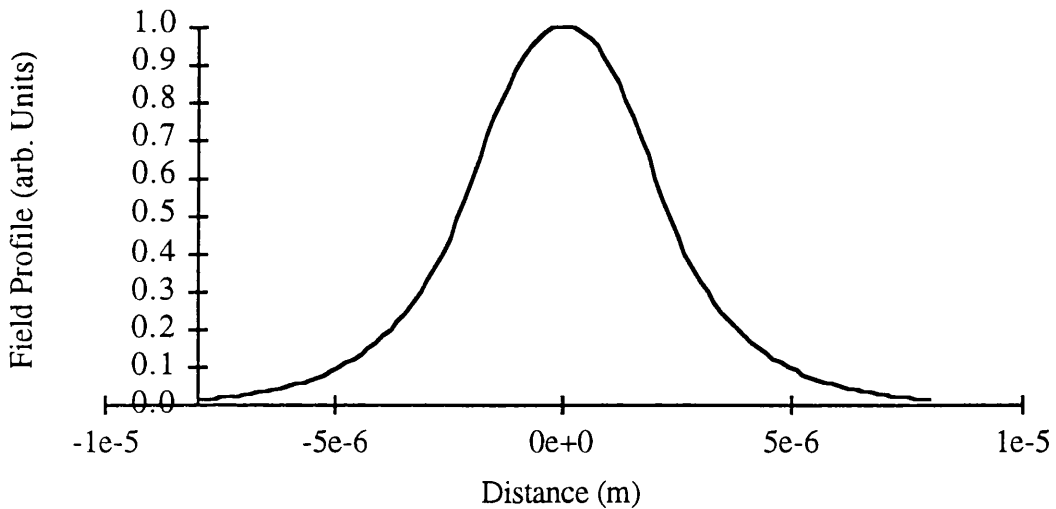


Figure 9.2. Waveguide mode for the slab waveguide calculated by the MATLAB routine 'mdfnd.m'

'mdfnd.m' calculates all the supported modes for the parameters set in 'data.m'. For the above case only a single mode is found, with the output as shown in Figure 9.2. The method used to find supported slab waveguide modes was discussed in Section 5.2.

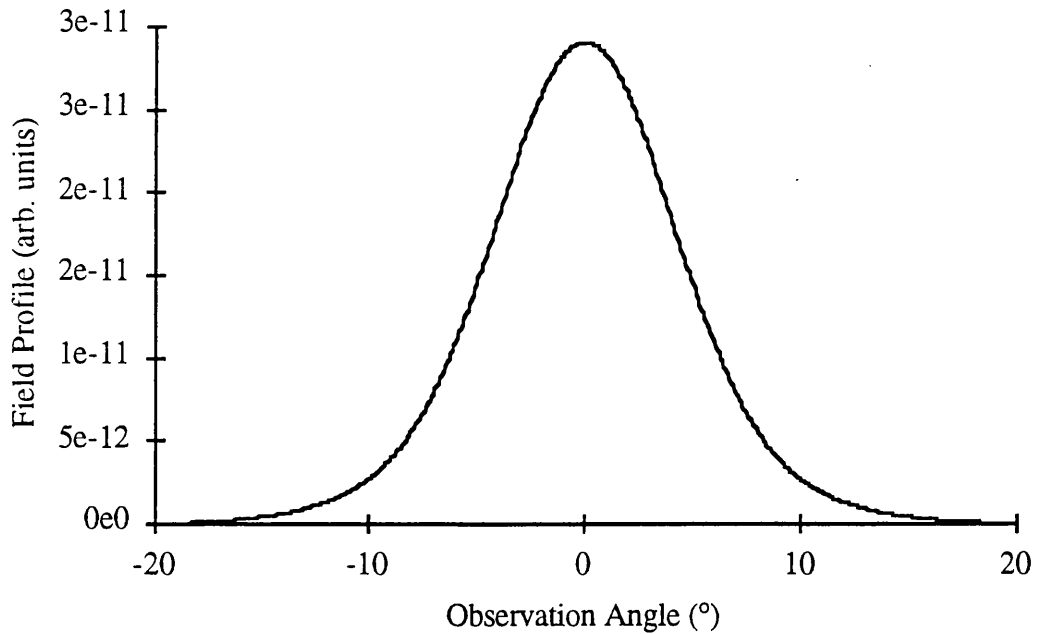


Figure 9.3 Far-Field pattern of the waveguide profile shown in Figure 9.2 calculated with the MATLAB routine 'ftnear.m'

In order to calculate the far-field patterns the Fourier Transform of a single guide's near-field must be calculated, as seen in Equation 9.20. In 'ftnear.m' the integral is carried out using trapezia to calculate the area under the curve. The far-field pattern has a similar overall shape to the near-field for a single stripe laser.

Sections 9.12a to 9.12d give outputs for some of the supermodes than can be supported in a ten element array.

9.4.3a Supermode $v=10$

The $v=10$ supermode is the highest order mode available for an $N=10$ element laser. It is also the mode in which we would expect the laser to oscillate.

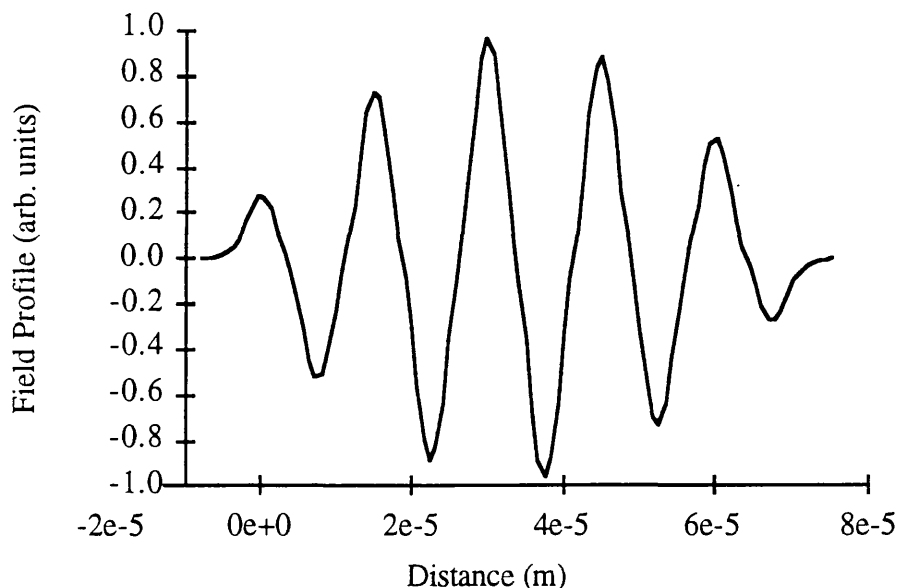


Figure 9.4 The near-field pattern of the $v=10$ supermode of a 10 channel array calculated with the MATLAB routine 'arrayfnd.m'.

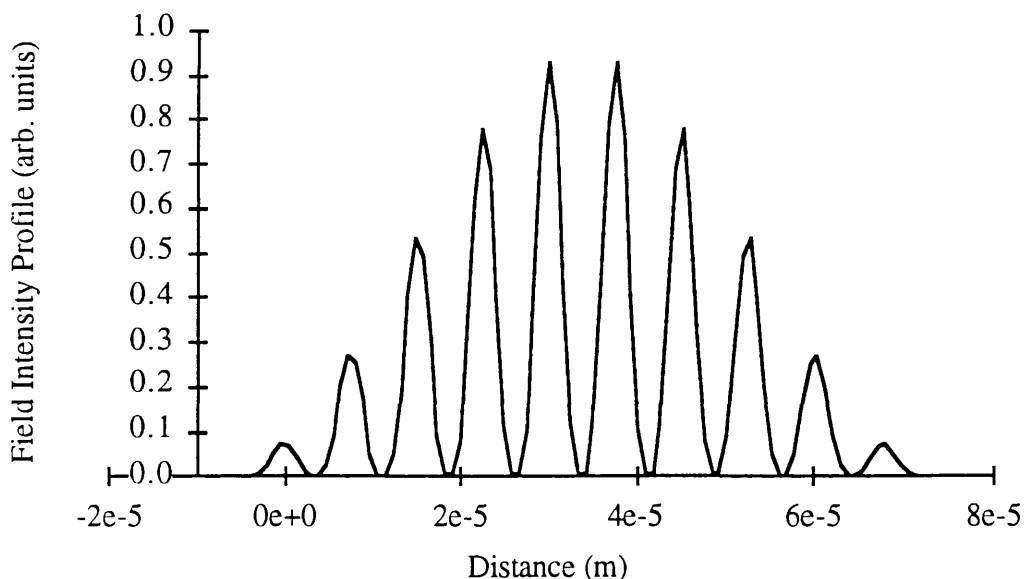


Figure 9.5 The near-field intensity pattern of the $v=10$ supermode of a 10 channel array calculated with the MATLAB routine 'arrayfnd.m'.

Each filament in the array is operating 180° out of phase with its nearest neighbours, as is seen in the near-field profile of Figure 9.4. Figure 9.5 shows the corresponding near-field intensity profile. An interesting point to note here is that, between each element in the

near-field, the intensity profile reduces to zero, which is due to interference between adjacent elements.

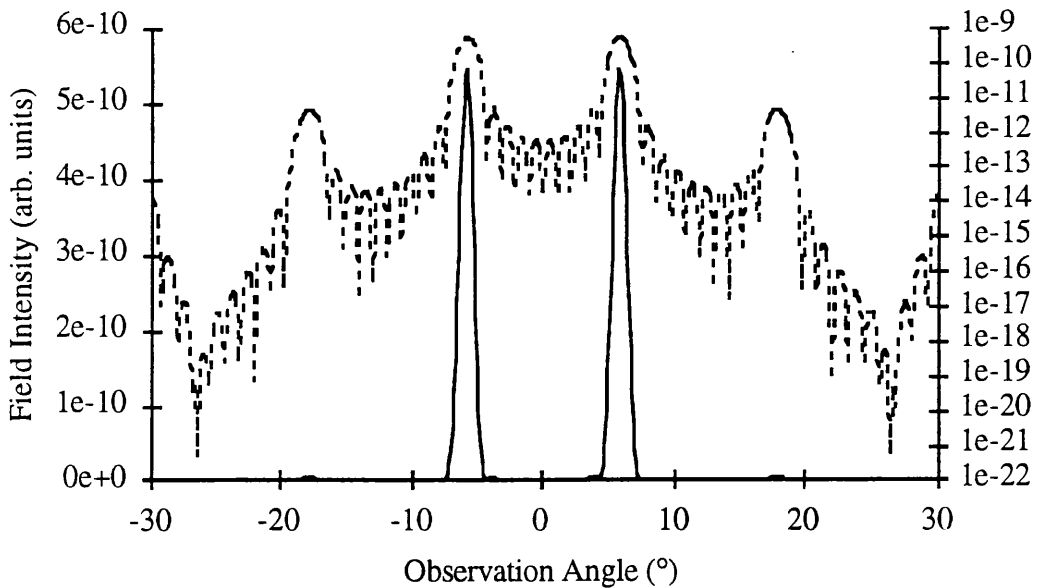


Figure 9.6 The far-field intensity pattern of the $v=10$ supermode of a 10 channel array calculated with the MATLAB routine 'fgtheta.m'. The dashed curve is a \log_{10} plot of the far-field intensity patten, the solid curve is the linear plot.

The far-field pattern is characterised by two prominent lobes at $\pm 6.5^\circ$. Figure 9.6 shows the far-field intensity profile on both a linear (left hand side) and a \log_{10} (right hand side) scale. Although there are two major lobes, it can be seen from the \log_{10} plot that there is much finer detail to the pattern at low intensity levels..

9.4.3b Supermode $v=9$

The $v=9$ supermode has the near-field pattern as shown in Figure 9.7. Here the filaments are 180° out of phase with their neighbours, except for the centre of the pattern where they are in-phase. Coupling effects create a minimum in the centre of this pattern, as can be clearly seen from the near-field intensity profile shown in Figure 9.7.

The far-field intensity profile shown in Figure 9.8 shows two twin lobed profiles either side of the normal. Again with the \log_{10} scale more detail can be observed between the central

lobes and at a wider observation angle from the main lobes. Also, as with the $\nu=10$ case, there is very little light emitted on axis.

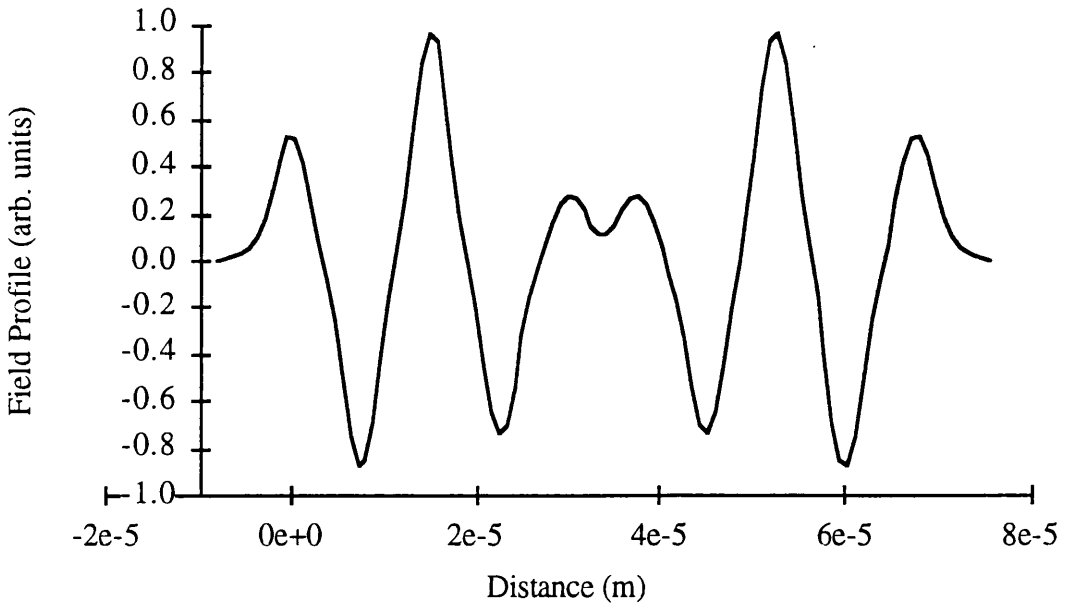


Figure 9.7 The near-field pattern of the $\nu=9$ supermode of a 10 channel array calculated with the MATLAB routine 'arrayfnd.m'.

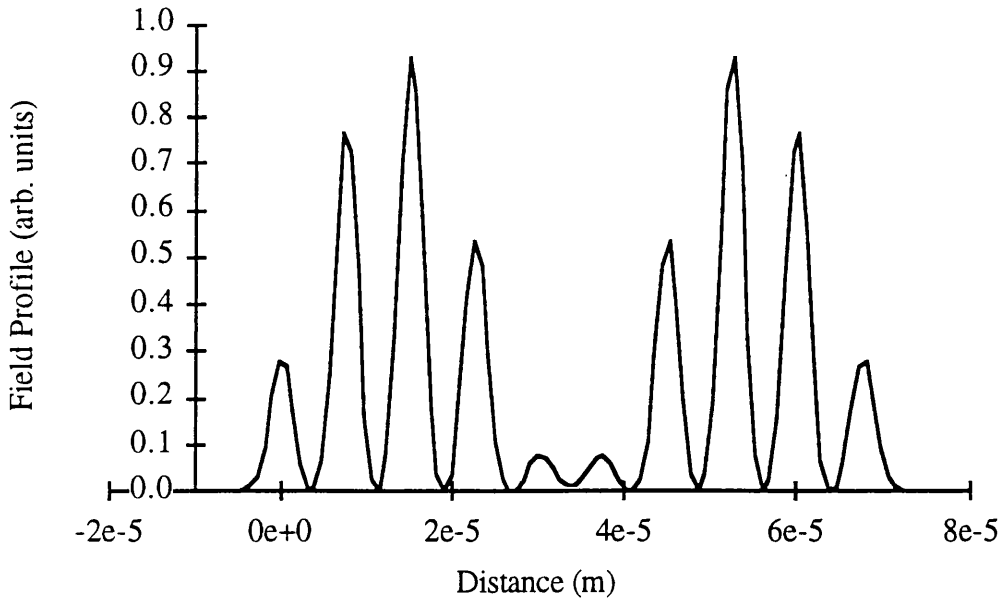


Figure 9.8 The near-field intensity pattern of the $v=9$ supermode of a 10 channel array calculated with the MATLAB routine 'arrayfnd.m'.

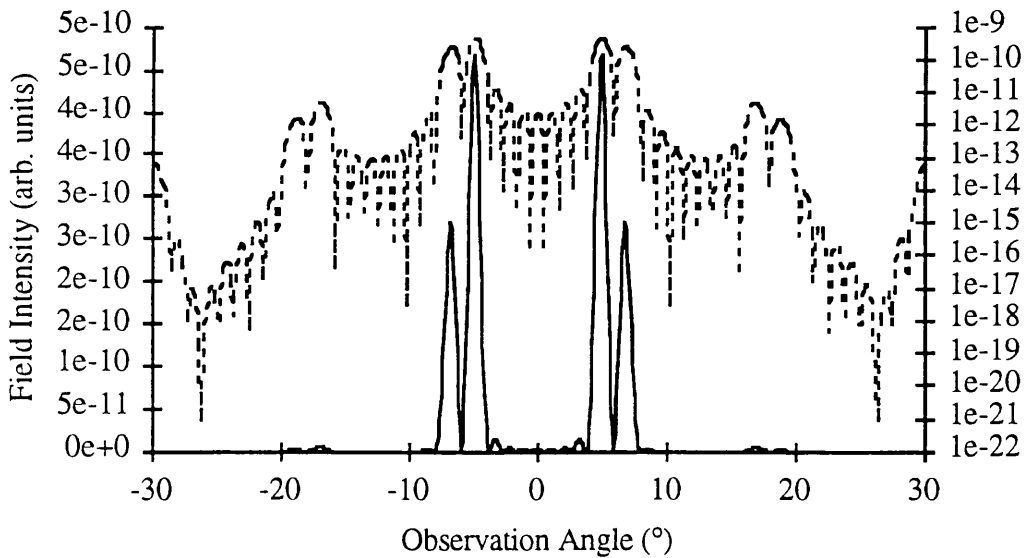


Figure 9.9 The far-field intensity pattern of the $v=9$ supermode of a 10 channel array calculated with the MATLAB routine 'fgtheta.m'. The dashed curve is a \log_{10} plot of the far-field intensity pattern, the solid curve is the linear plot.

9.4.3c Supermode $\nu=1$

The near-field pattern for the first order supermode ($\nu=1$) is shown in Figure 9.10, here all the elements are now in phase with each other. The intensity profile of the near-field looks very similar to that in Figure 9.5 for the $\nu=10$ supermode. There is one clear difference however: the intensity in the $\nu=1$ case between the peaks in the near-field does not drop to zero. This is because there is now constructive interference between the filaments instead of destructive interference.

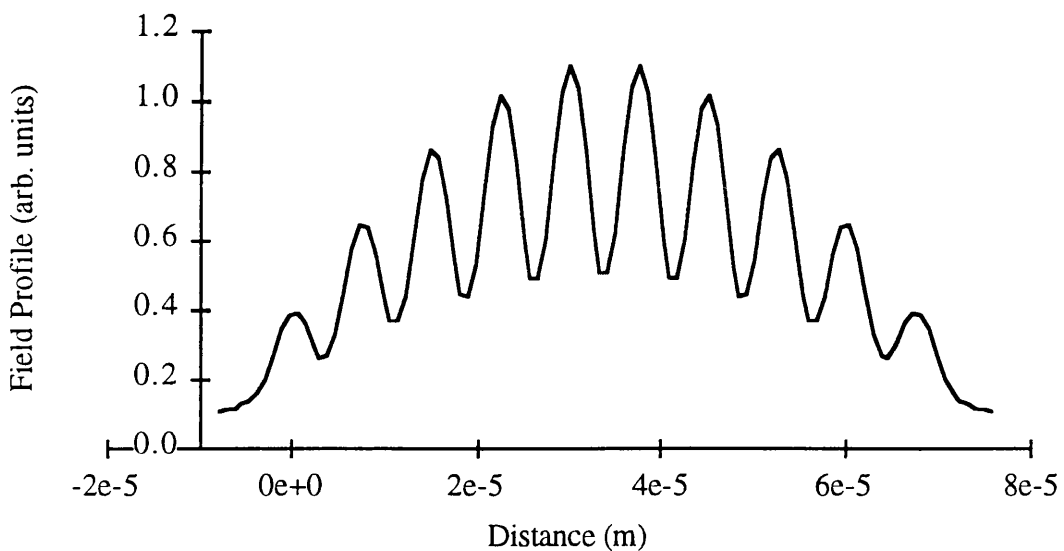


Figure 9.10 The near-field pattern of the $\nu=1$ supermode of a 10 channel array calculated with the MATLAB routine 'arrayfnd.m'.

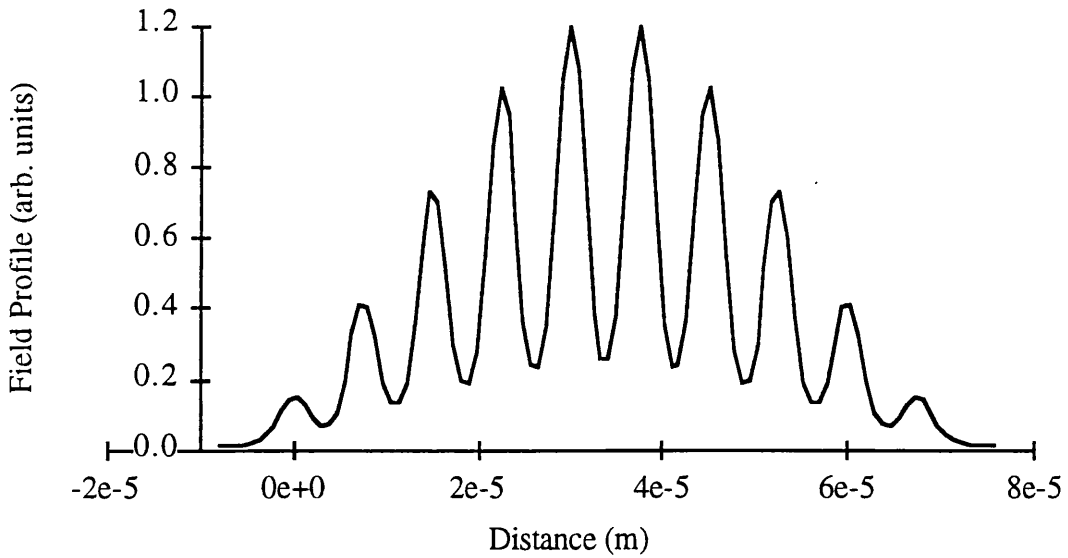


Figure 9.11 The near-field intensity pattern of the $v=1$ supermode of a 10 channel array calculated with the MATLAB routine 'arrayfnd.m'.

The far-field profile, shown in Figure 9.12, shows a very important difference to all other modes. In this case there is a peak directly on axis, with greatly reduced side lobes. The consequence of this is that virtually all the power emitted from the device is on-axis and therefore more easily coupled into an optical fibre or other photonic device. This is the supermode that we are looking for in the devices fabricated in this thesis.

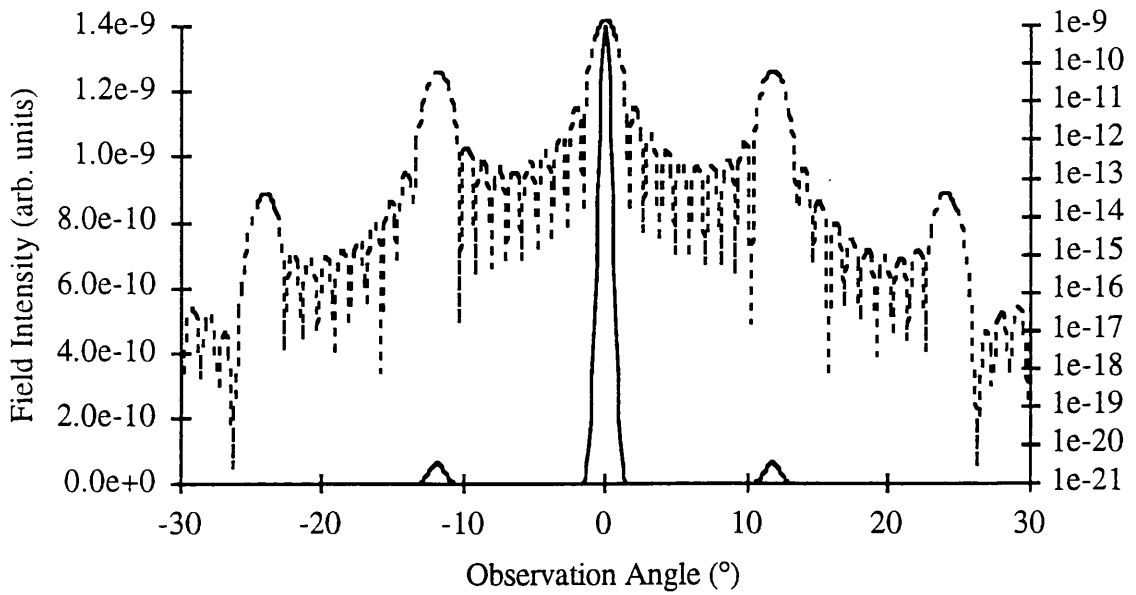


Figure 9.12 The far-field intensity pattern of the $v=1$ supermode of a 10 channel array calculated with the MATLAB routine 'fgtheta.m'. The dashed curve is a \log_{10} plot of the far-field intensity pattern, the solid curve is the linear plot.

Figure 9.13 shows a close up of the important $v=1$ case, this is used to estimate the FWHM of the supermode, in this case it is approximately 1.5°

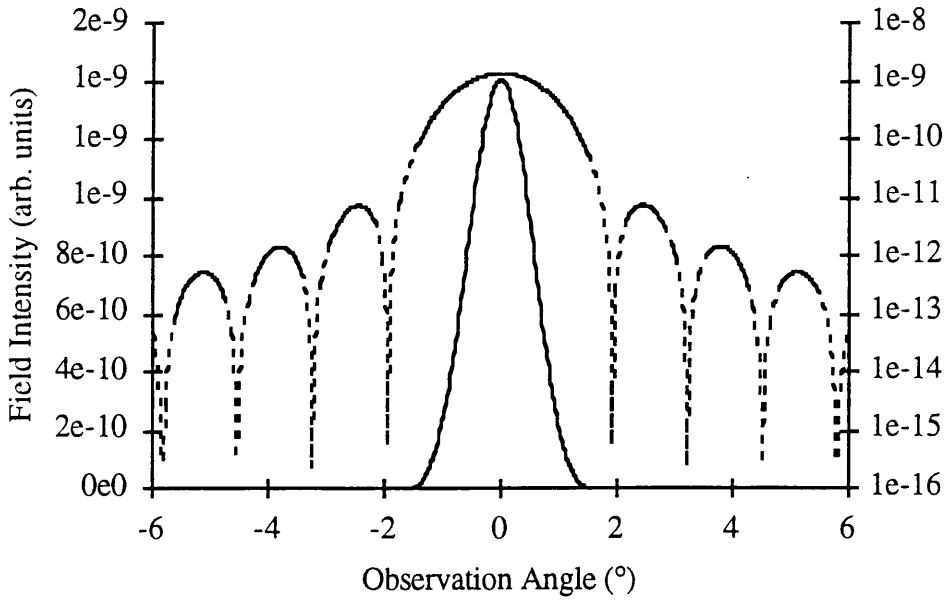


Figure 9.13. A close up of the $v=1$, $N=10$ far-field pattern used to estimate the mode lobe FWHM ($\sim 1.5^\circ$).

9.4.3c Supermode $v=2$

To show how easily the on-axis lobe is lost, the next supermode to the above is shown. Here the $v=2$ supermode shows a clear zero in the far-field of Figure 8.16. The near-field in this case also has a zero in the centre as shown in Figures 9.14 and 9.15. This mode, as well as all subsequent modes, is undesirable.

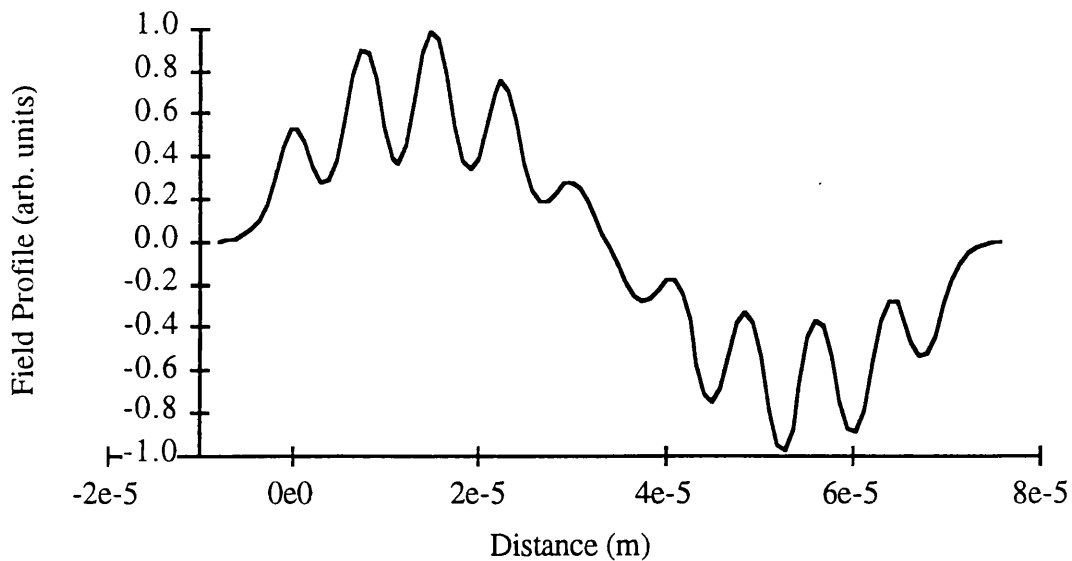


Figure 9.14 The near-field pattern of the $v=2$ supermode of a 10 channel array calculated with the MATLAB routine 'arrayfnd.m'.

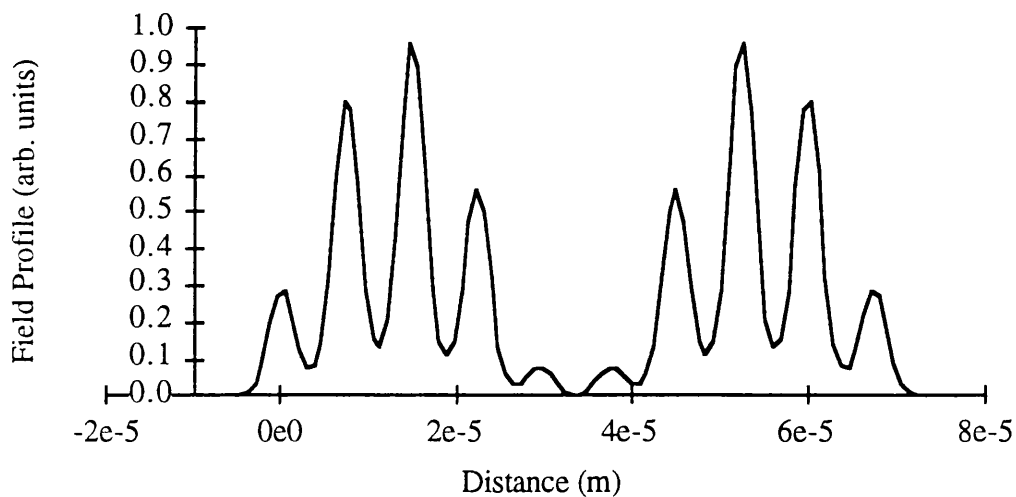


Figure 9.15 The near-field intensity pattern of the $v=2$ supermode of a 10 channel array calculated with the MATLAB routine 'arrayfnd.m'.

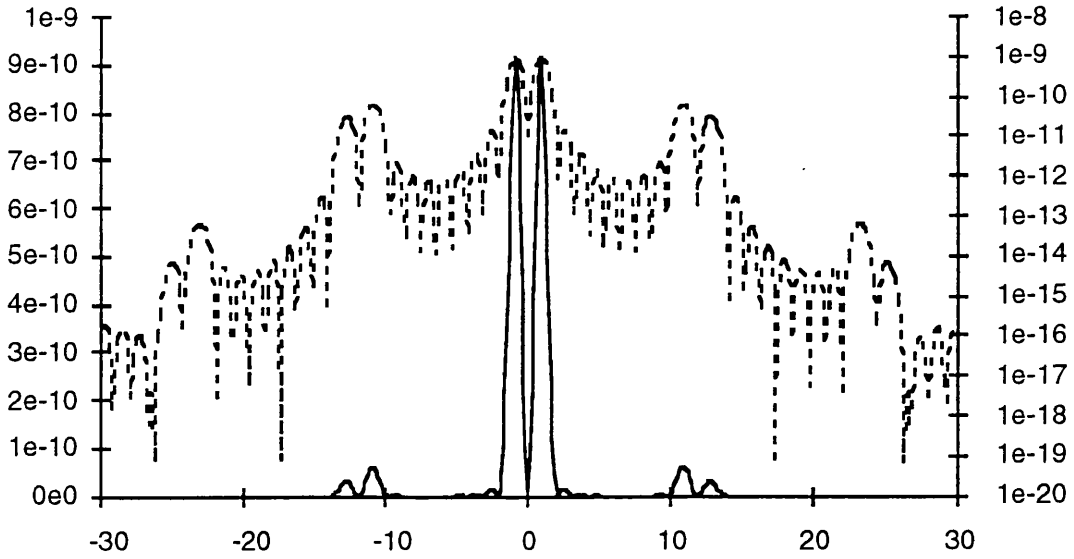


Figure 9.16 A close up of the $v=2$, $N=10$ far-field pattern used to estimate the mode lobe FWHM ($\sim 1.5^\circ$).

9.4.4 Summary

From the above calculations it is clear that only one supermode exists in any laser array that has a single lobe on-axis, that is the fundamental, or $v=1$ supermode. As the order of the mode increases to $v=N$, the lobes become more separated as the phase of the filaments changes. The highest order mode has filaments which are 180° out of phase with its nearest neighbours.

The above profiles and the associated MATLAB programme are to be used to identify equivalent slab waveguides for filamented laser arrays in the following sections. Filaments from broad stripe lasers have been observed to be stable in time, and are parallel with each other along the length of the laser, filaments will therefore act as if they were a gain or index guided laser array. The above model of a laser array can be used to describe the far-fields observed experimentally.

9.5 Measuring the Near-Field Pattern

The near-field pattern was recorded by collimating the beam at the laser facet with a '×50' objective and monitoring the output with a Hamamatsu Vidicon. The sample was mounted in a gold plated clip and powered by the same technique used in Section 7.2. The output of the camera (CCIR format) was fed into a Neotech frame grabbing board inside the Macintosh computer. This enabled picture to be recorded and enable image processing to be carried out. A simple LabVIEW programme was written to enable the intensity profile in the near-field pattern to be recorded. Three dimensional and two dimensional profiles of the image were also recorded via the same LabVIEW programme.

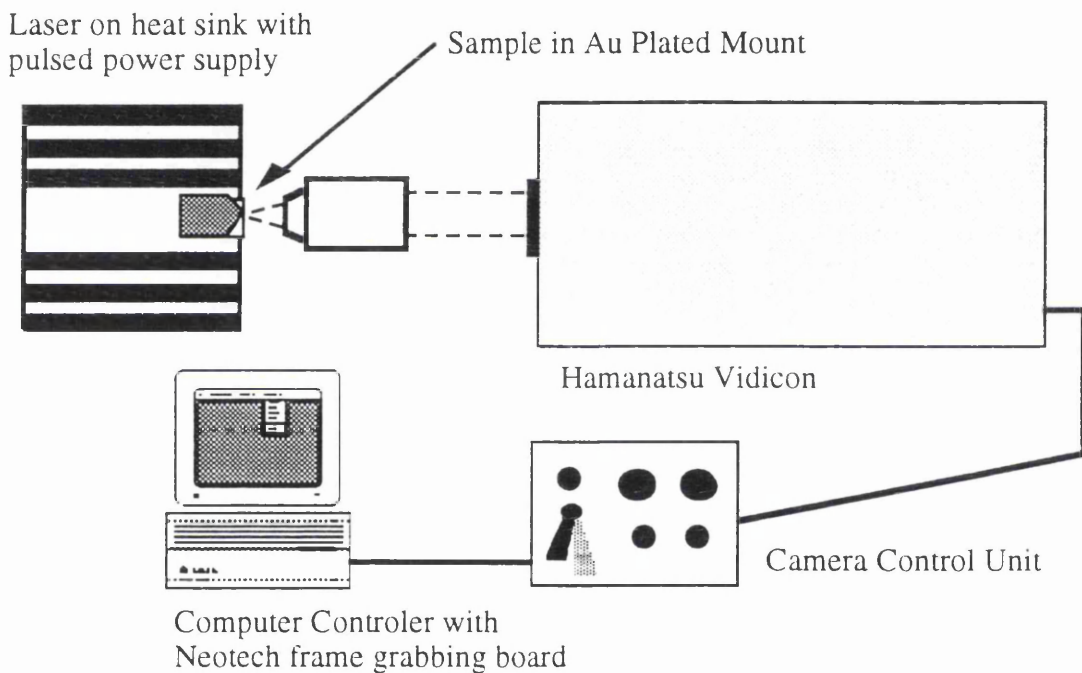


Figure 9.17. Apparatus used to measure the near-field patterns of the lasers using a Hamamatsu Camera and an objective lens. Pictures of the facet are loaded directly into the computer for fuse at a later stage.

9.6 Measuring the Far-Field Pattern

Two methods were employed to measure the far-field pattern:

1. The sample is placed onto a rotary stage and the field intensity monitored from a fixed point as the stage is rotated - this is referred to as the 'Rotary Stage Method'

in Section 9.6.1 and subsequent sections. This method is time consuming but, since the field is always measured at the same distance from the facet, a good representation of the far-field should be obtained. The disadvantages of this method are that it is slow and only one slice of the far-field pattern is measured at a time (although with an array of detectors this could be changed).

2. A camera is used to monitor the output of the laser. This method is very quick and provides a clear picture of the field distribution and the uniformity of any stripes.

9.6.1 Rotary Stage Method

The laser sample is mounted in a similar fashion to that described in Section 7.3.1 for the measurement of the IVL laser characteristics. In this case, however, the laser, mounted onto the heatsink, is secured on top of a rotary stage. The heatsink is put onto the rotary stage in such a position that the facet of the laser under test is in the centre of the rotary stage as indicated in Figure 9.18. The rotary stage is rotated by using a stepper motor controlled by a Macintosh computer via a Digiplan IEEE controller.

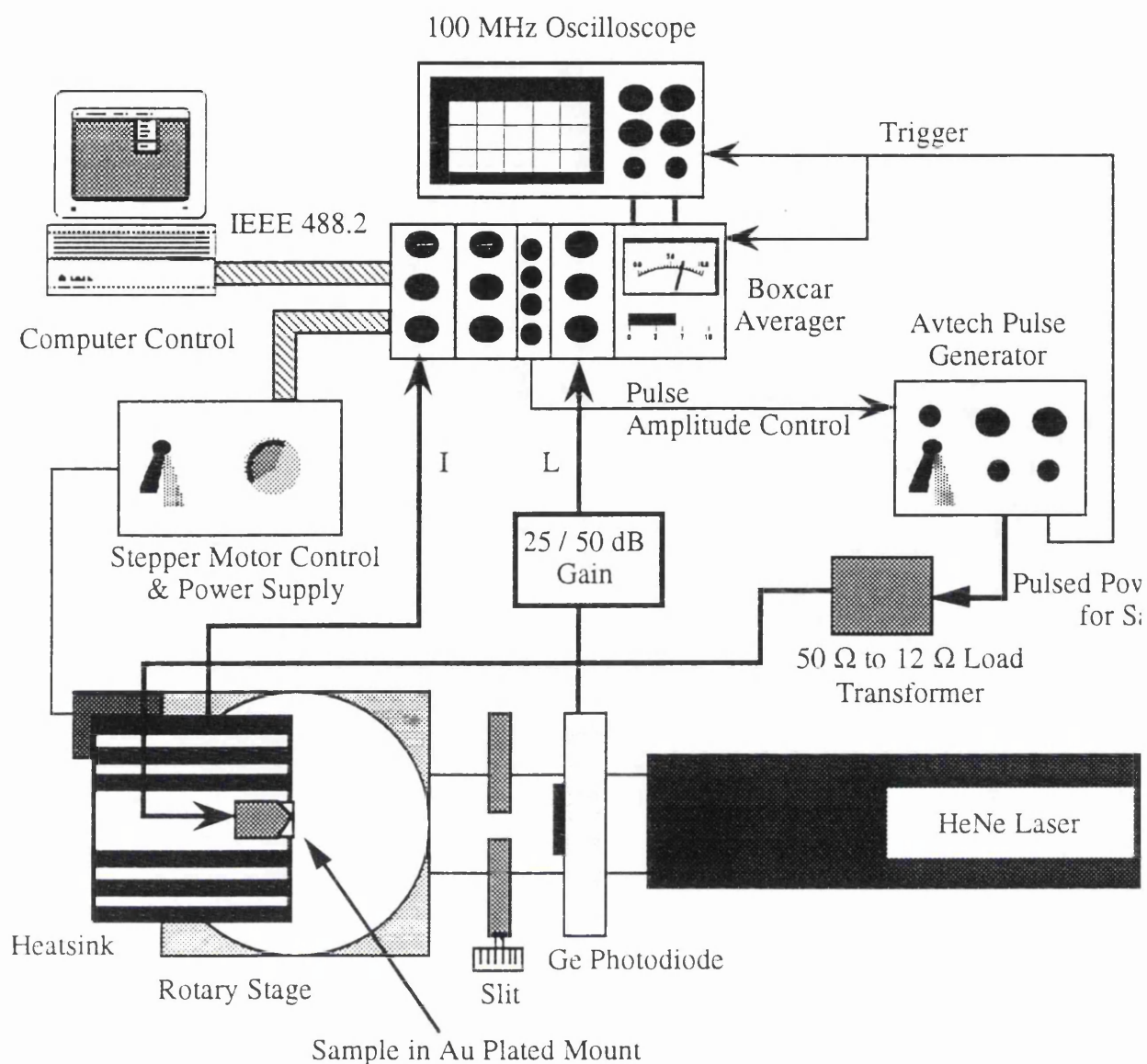


Figure 9.18 Experimental apparatus used to measure far-field patterns. The apparatus incorporates a rotary stage to enable the intensity of light emitted from the laser facet to be measured at different angles to the facet whilst maintaining a constant distance from the facet.

A LabVIEW programme was written to enable different measuring conditions to be used, and to enable data to be saved in a spreadsheet format for future retrieval. Via the programme, the time interval between measurements could be altered, as well as the step between measurements, and the total angle for measurements. Several safety features were also built-in including a power down facility in the case of the door to the laboratory being

opened (the programme also controlled the power supply to the laser), and a halt if the rotary stage was asked to rotate more than 180° in either direction.

The laser must be centred properly before a measurement is taken, to ensure that the 0° point is always perpendicular to the laser facet. To centre the laser a HeNe laser is reflected off of the laser under test, as shown in Figure 9.18. The rotary stage is then moved using a stepper button on the front panel of the LabVIEW programme, and once the reflected laser's spot is lined up with the incident beam the facet is perpendicular to the beam, the ZERO button is then pressed on the LabVIEW front panel. This now forms the 0° reference point. A slit is inserted into the beam and a reverse biased Ge detector is placed in behind the slit. Once the step conditions (including required input power to the laser) are set on the front panel the experiment is ready to run.

As a modification to the original experimental apparatus a box-car averager was used to measure the output from the Ge detector, and to monitor the power supply to the laser. The box-car averager enabled very fast averaging of the output pulses from the detector, giving a much smoother and more accurate far-field pattern. An external 50/25 dB amplifier was also used to amplify the signal before it entered the averager.

9.6.2 Camera Method

The far-field pattern can also be measured by the same procedure as that described in Section 9.2 to measure the near-field. The main difference being that the objective lens is not used. Results obtained by this method are valuable only to obtain a quick picture of the far-field, they should not be used for analytical purposes for two reasons:

1. The camera is non-linear - the resulting picture will be exaggerated in areas of low light intensity.
2. The field front of the far-field pattern is circular, but the camera has a flat detecting area: as a result of this the far-field pattern will appear distorted.

9.7 Results

The following section contains a mixture of graphs and pictures of near- and far-field patterns. The devices are $75\ \mu\text{m}$ oxide stripe lasers operating around $1.55\ \mu\text{m}$ with and without extended cavities that were fabricated as described in Chapter 8. All devices have an active cavity of $800\ \mu\text{m}$ unless otherwise stated.

The aim of the measurements, as stated in the introduction to this Chapter, is to establish whether or not the addition of an extended cavity onto an oxide stripe laser will improve its far-field characteristics. If the far-field can be improved to produce a single on-axis lobe, this could have important implications in the fabrication of cheap, but high powered semiconductor lasers operating around $1.55\ \mu\text{m}$.

9.7.1 No Extended Cavity

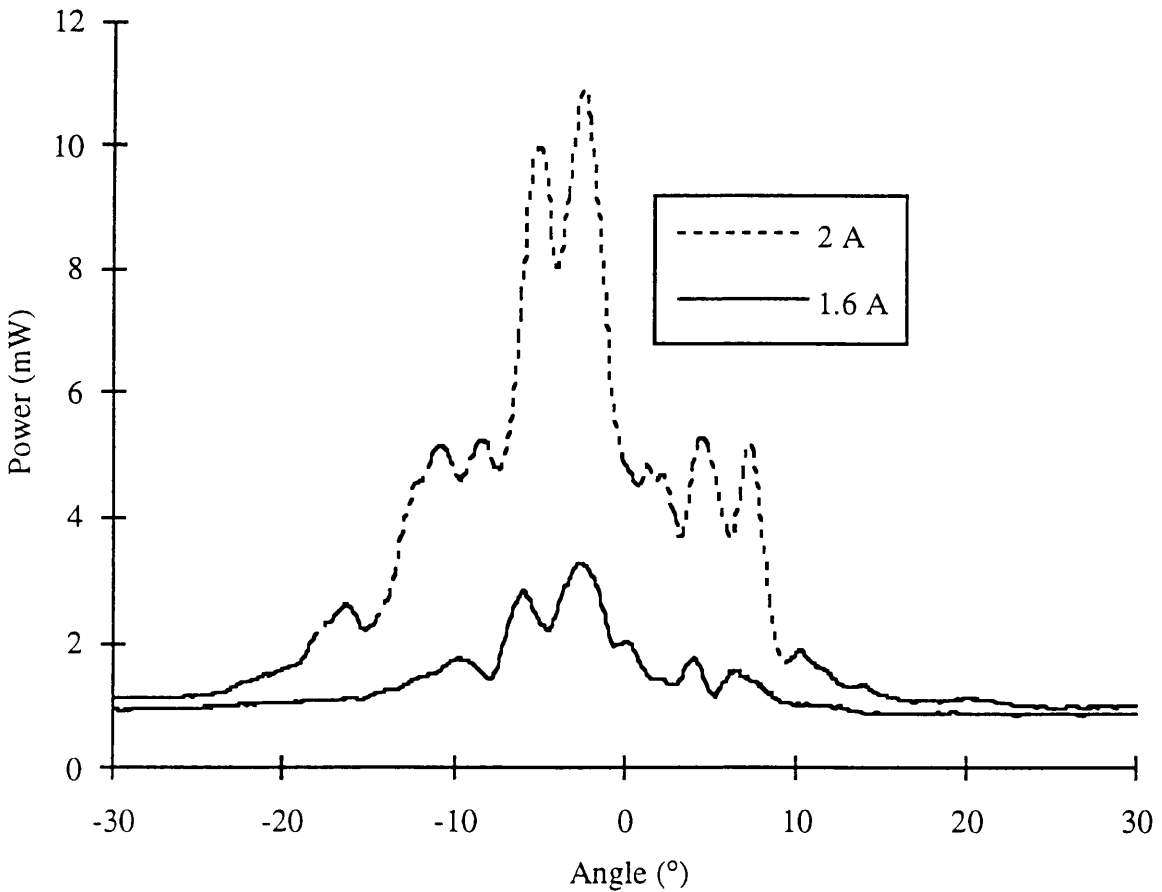


Figure 9.19a. Far-Field Pattern measured by the 'Rotary Stage' method.

Figures 9.19a to d are taken from an oxide stripe laser with a threshold current of 0.8 A. Figure 9.19a shows the far-field pattern measured using the rotary stage technique, as discussed above. The main feature of the far-field pattern is a minimum in the centre, with lobes contained within a 30° arc. Referring to the theoretical calculations in Section 9.4.3, this far-field profile can be explained in terms of a ten stripe laser array ($N=10$). The on-axis zero in the far-field profile indicates that the laser is not operating in the fundamental mode where all the filaments are in phase. The device is operating with adjacent filaments out of phase with each other, as characterised by a higher order supermode. Figure 9.19b shows a three dimensional picture of the far field as recorded with the camera, the central zero on-axis can clearly be seen in this pictures, and a good feel of the shape of the far-field can be gained from this type of image.

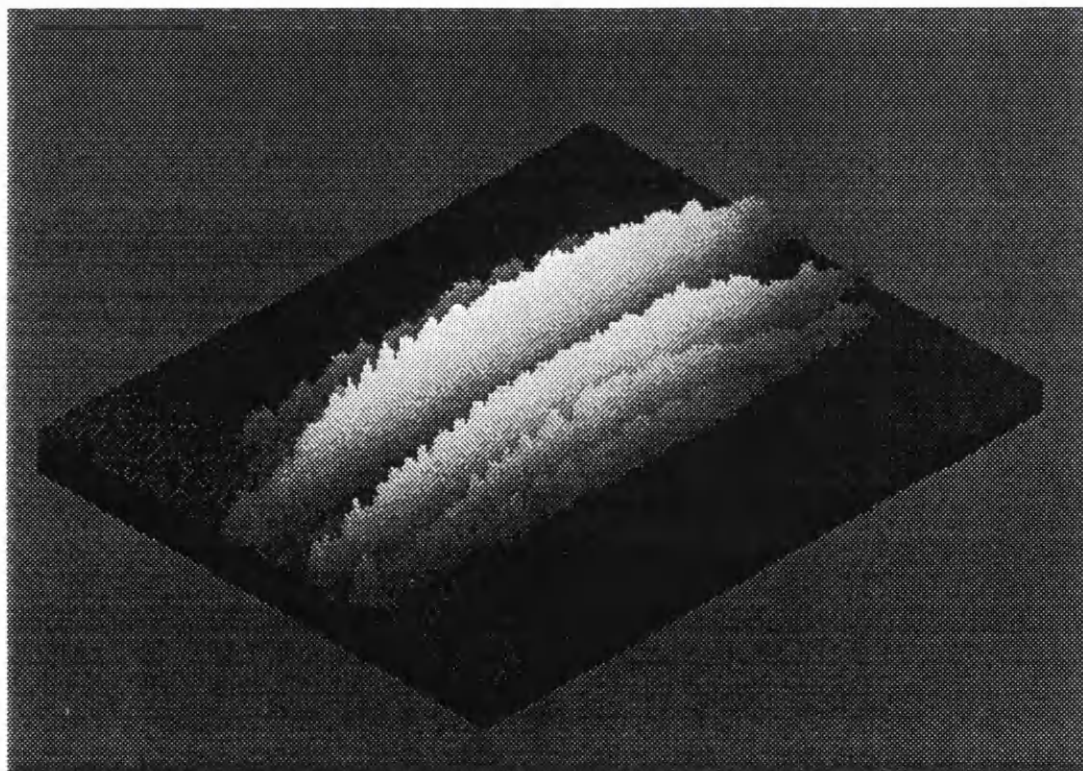


Figure 9.19b. 3D image of the far-field pattern of an $75\ \mu\text{m}$ oxide stripe laser, operating at 2 A.

The near-field pattern as shown in the Vidicon output of Figures 9.19c and d resembles the $v=10$ supermode, i.e. a maximum in the centre of the profile with clear definition between the spots. Increasing the theoretical separation of the guides to around $15\ \mu\text{m}$ would

produce a far-field intensity pattern that matches the experimentally recorded results more closely for the $\nu=1$ supermode, predicting the side lobes seen experimentally.

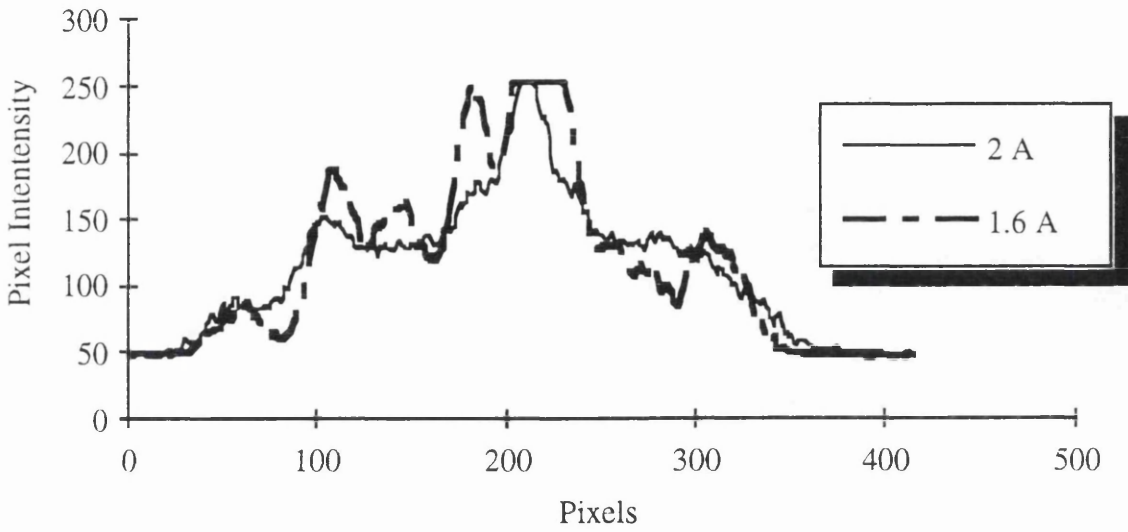


Figure 9.19c. Near-field pattern measured by taking intensity profile across Vidicon image. 400 pixels represents approximately $75 \mu\text{m}$.

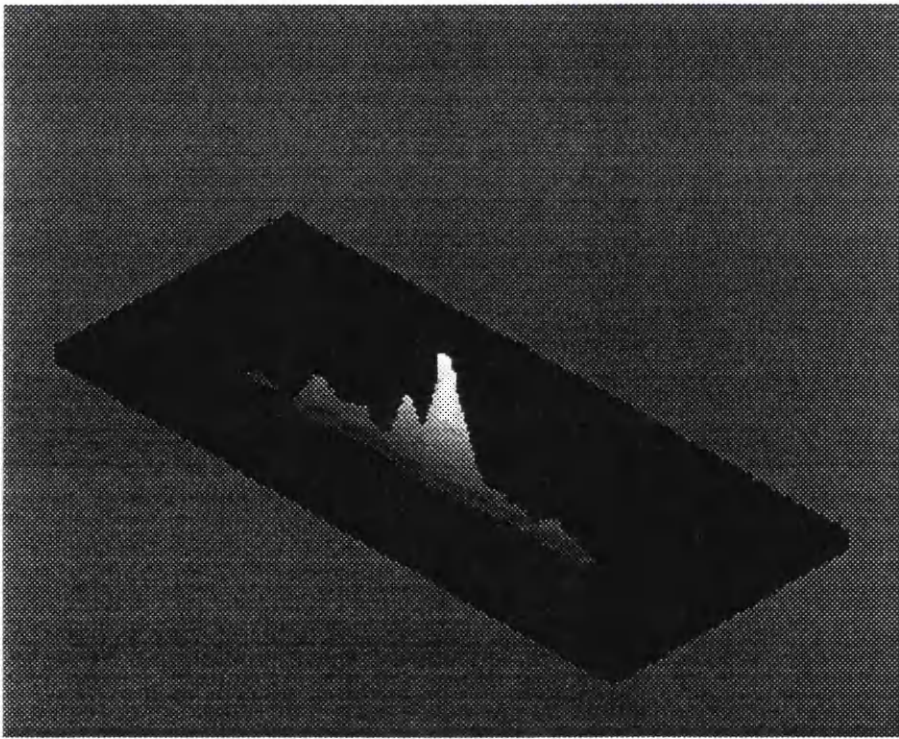


Figure 9.19d. Near-field pattern of a $75 \mu\text{m}$ oxide stripe laser at 2 A.

Figures 9.20a and 9.20b show a set of near and far-field patterns for another oxide stripe device operating at twice threshold (1.69 A). The near-field pattern (Figure 9.20a) for this device is particularly clear, and closely resembles the $\nu=10$ supermode; since the filaments

are operating out of phase in the $\nu=10$ case, the spots become well defined due to interference between adjacent filaments. Side lobes are easily observed using the camera but are greater than theoretical calculations predict. The enlarged side lobes could be due to the non-uniform nature of the near-field intensity profile which results from imperfections in the laser facet and the weak forces that create the filaments in the first place. An array of index guided lasers would have more strongly defined filaments which would lead to results closer to theory.

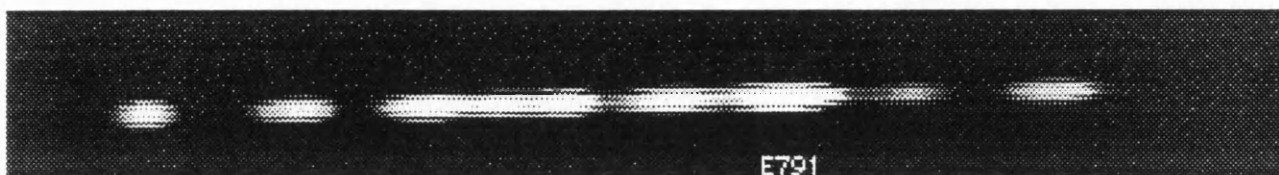


Figure 9.20a Near-field pattern of a 75 μm oxide stripe laser.

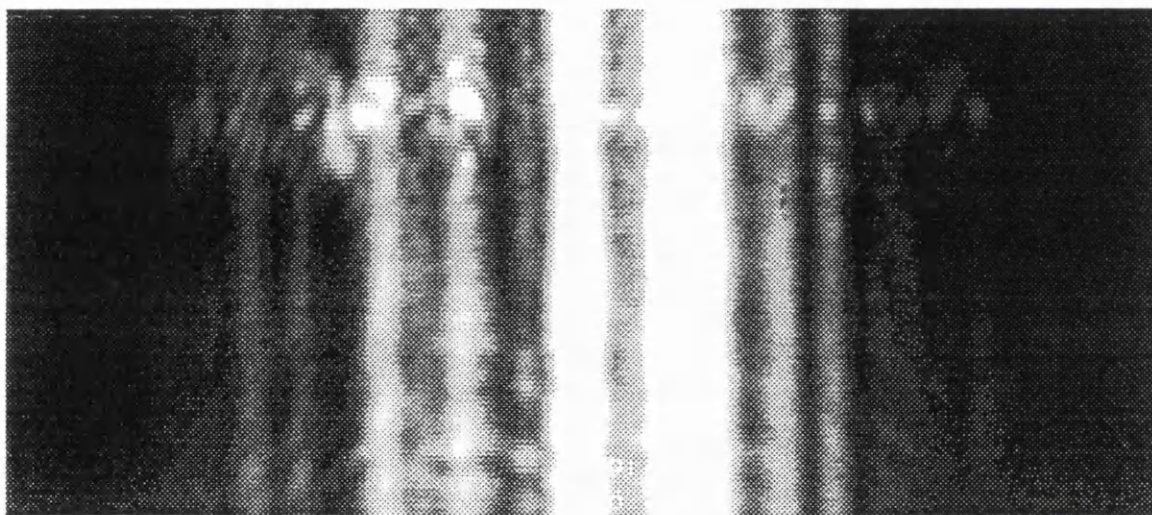


Figure 9.20b Vidicon picture of the far-field pattern for a device with a 800 μm active cavity.

9.7.2 Oxide Stripes with Extended Cavity

The results in Figures 9.21 to 9.23 are very similar to those predicted by theoretical calculations for the first supermode, where all of the filaments are operating in-phase. The near-field pattern in Figure 9.21a shows the filaments clearly, with an underlying field intensity as shown theoretically in Figure 9.11. The far-field pattern in Figure 9.21b shows a central lobe at low injection currents, at higher injection currents two side lobes appear. The proportions are not the same as those predicted in Section 9.4.3c, however the

approximations made in the calculations may explain the discrepancy. No other supermode has a peak on axis.

The central lobe is seen to be wider than that predicted; 2° FWHM experimentally compared to 1.5° for the theoretical calculation. Even taking the approximations into account a broader than theoretically expected central lobe has been observed previously⁶, in this reference the observed central lobe was twice as broad as that calculated.

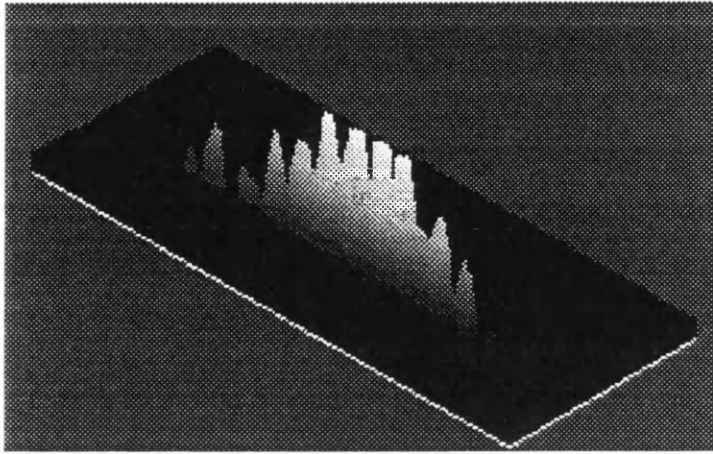


Figure 9.21a. Near-field pattern of the laser in Figure 9.23 operating at 2.3 times the threshold current.

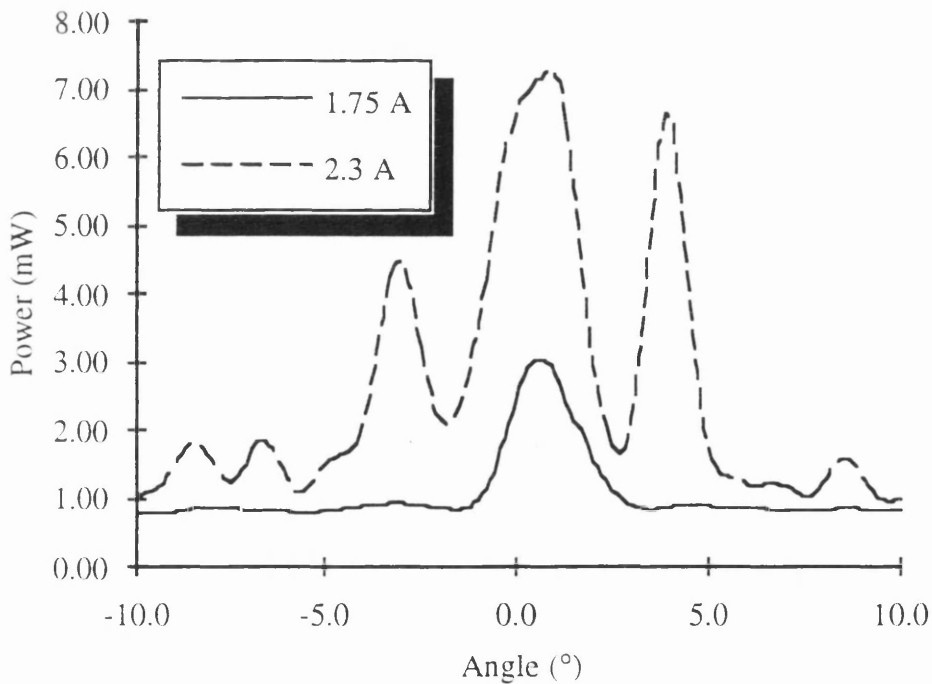


Figure 9.21b. Far-field intensity pattern of a laser containing a $800 \mu\text{m}$ active and a $1000 \mu\text{m}$ passive waveguide operating at 2.3 and 3 times the threshold current.

The threshold current for the device, whose characteristics are as shown in Figures 9.21 was 0.74 A. The curves shown in Figure 9.21 are therefore at 2.3 and 3 times the threshold current. The near-field image in Figure 9.21a was taken with a drive current of 1.75 A. The active cavity was 800 μm long with an extended cavity of 1000 μm .

In the following sample, Figure 9.22a to 9.22e the near-field is almost uniform and the far-field contains a strong on-axis peak in a manner similar to the theoretical calculations for the first order supermode. The active cavity length was 800 μm long and the passive cavity is 1000 μm and the laser had a threshold current of 0.8 A. The three dimensional image of the far-field shows a strong on-axis peak with side lobes very much reduced, the operating current was 2.1 A for this image (2.6 times threshold).

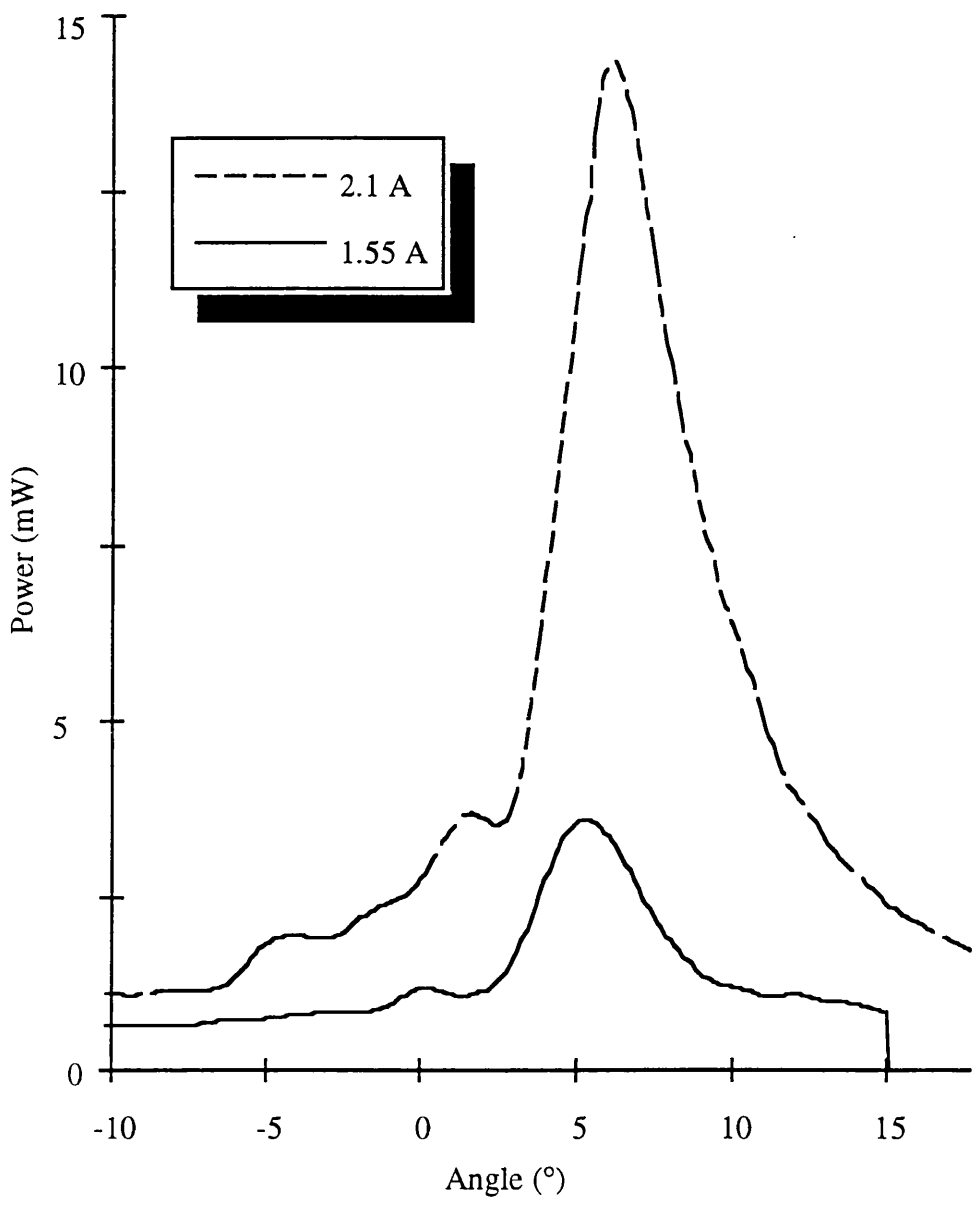


Figure 9.22a. Far-field pattern of the device with a drive current of 2.1 A.

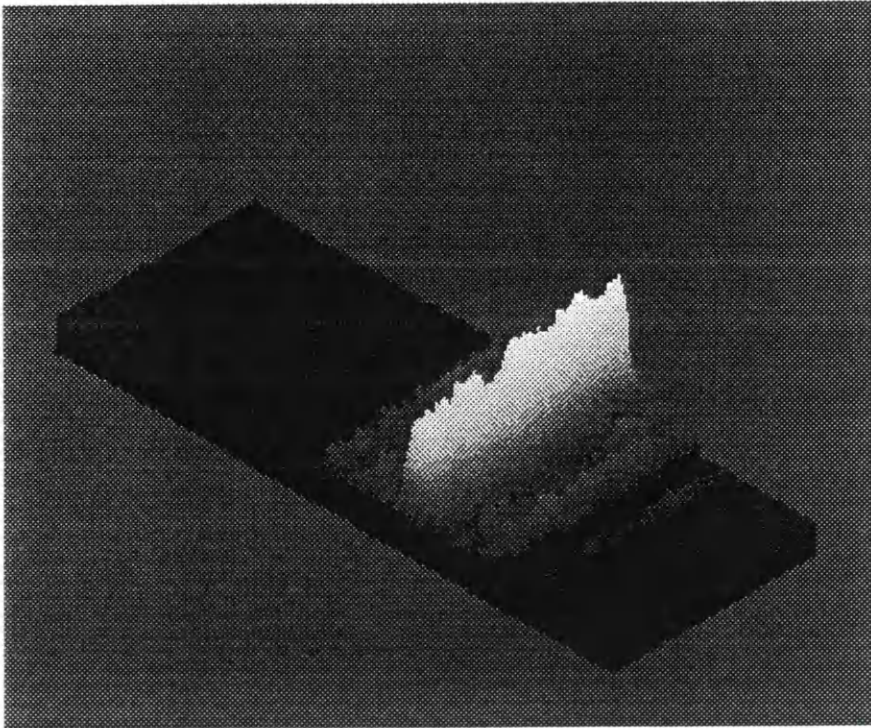


Figure 9.22b. Far-field pattern of the device with a drive current of 2.1 A.

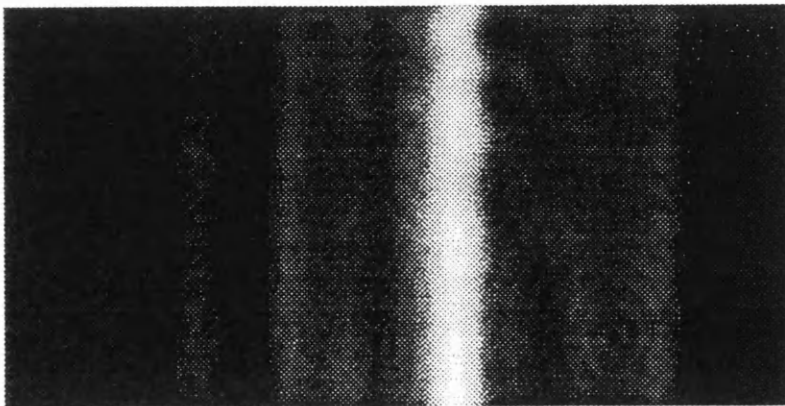


Figure 9.22c. Far-field pattern of the device with a drive current of 2.1 A.

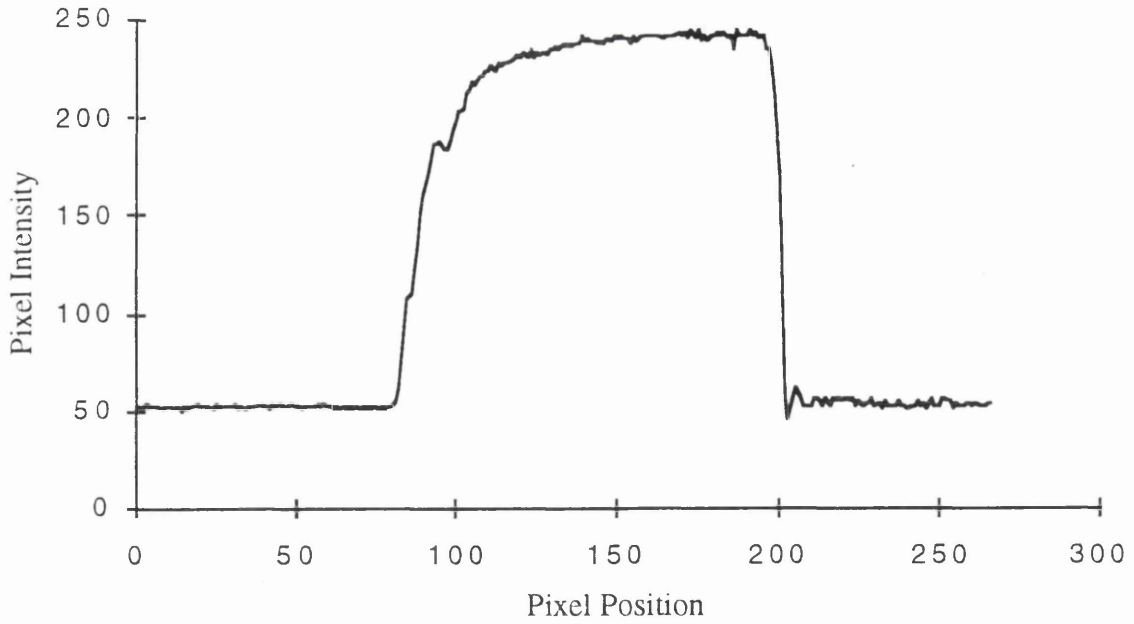


Figure 9.22d. Near-field pattern of the device in Figure 9.22 with a drive current of 2.1 A.

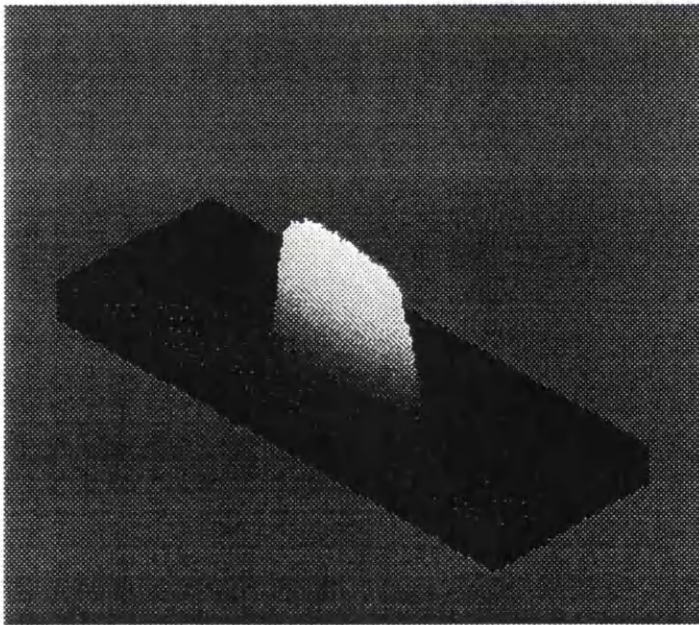


Figure 9.22e. Near-field pattern of the device with a drive current of 2.1 A.

The samples with outputs indicated in Figures 9.23a and b are taken from an oxide stripe extended cavity laser operating at three times threshold, 2.1 A. The near-field pattern is almost uniform, indicating first order mode behaviour, this is backed up by the far-field

pattern having a strong central lobe, on-axis. This device has a smaller active region (500 μm) than the devices reported above and has an extended cavity of 400 μm .

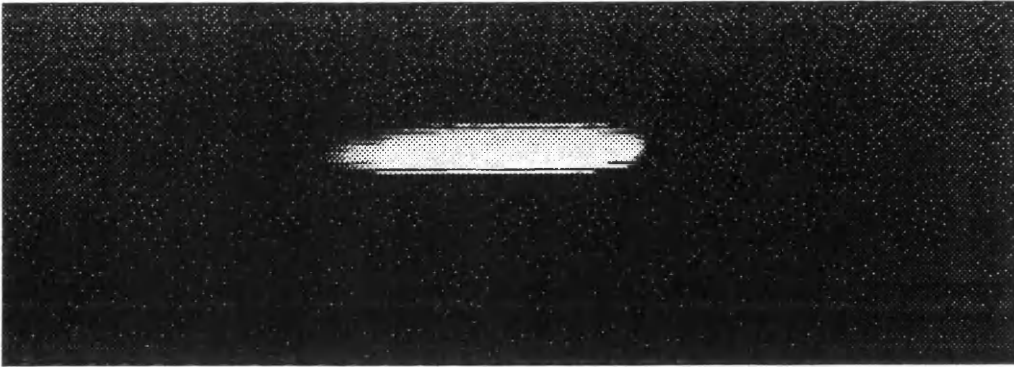


Figure 9.23a. Near-field of oxide stripe extended cavity laser at 2.3 A.

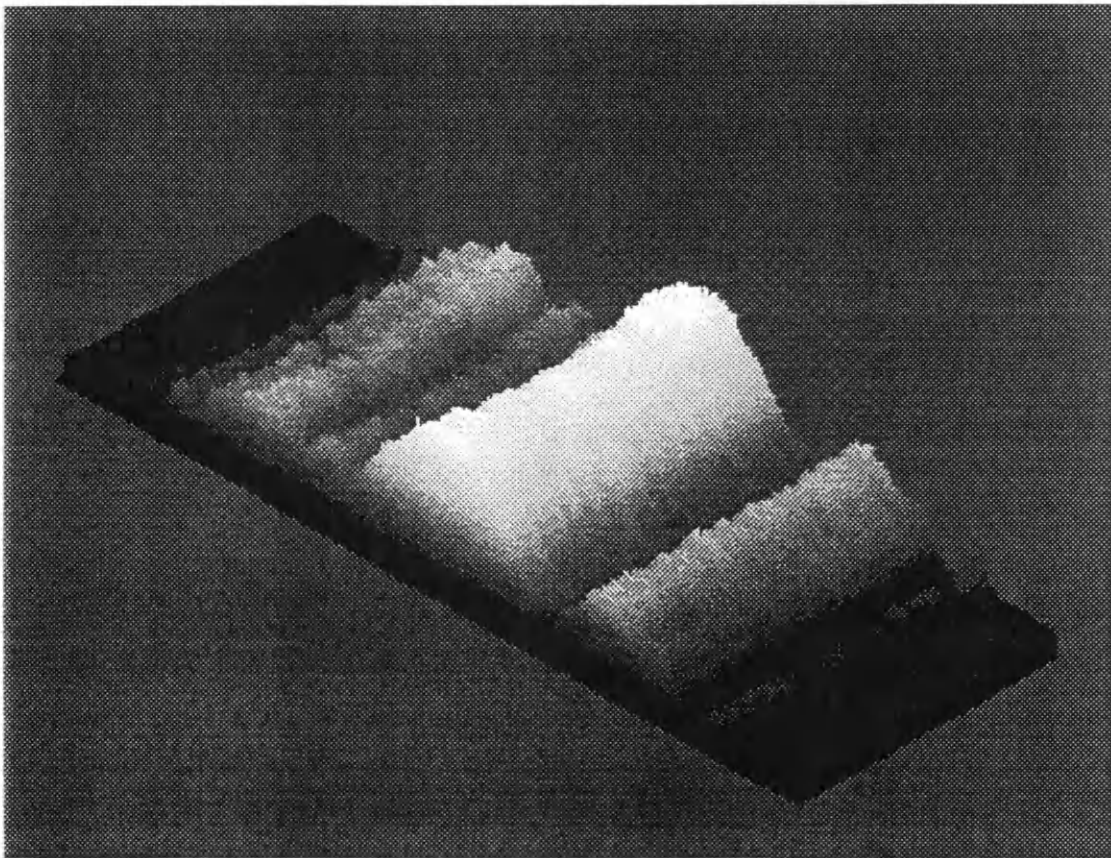


Figure 9.23b. Far-field pattern of an extended cavity oxide stripe laser with a drive current of 2.3 A.

9.8 Conclusions

The work carried out in this Chapter shows that, by the addition of an extended cavity, the far-field pattern of InGaAsP/InGaAs multiple quantum well lasers can be significantly

improved. It shows that the impurity induced disordering technique described in Chapter 6 can be employed to produce a device with improved far-field characteristics.

Whilst the experimental results do not agree perfectly with the measured field patterns, they do indicate that the different patterns observed are as a result of supermodes forming within the array of filaments in the oxide stripe lasers. With the addition of the extended cavity, the laser is forced to operate in the fundamental supermode, i.e. all the filaments are in phase, the result being a strong on-axis beam that can be easily coupled into a fibre, or controlled with relatively simple optics.

The power output of the oxide stripe lasers with or without the extended cavity is not very high. A peak value of 11 mW was measured for a normal oxide stripe device operating at 2 A, with an on-axis power of less than 8 mW, as measured using the rotary stage technique. The best extended cavity device, operating at 2.1A has a power of 14 mW on-axis with a FWHM of around 2.5° . Most oxide stripe extended cavity devices were only producing around 8 mW on axis at around 2 A injection current. Antiguide arrays are currently being investigated that can produce 200 - 300 mW of power in a lobe of less than 2° on axis.

Further work will be required on these devices to refine the process and to optimise the cavity lengths for optimum mode control, whilst reducing the threshold current of the devices, and increasing the output power. A structure containing more quantum wells may, for instance, produce an extended cavity with lower losses. On the other hand, the thermal processing required may cause the active layers to diffuse an unacceptable amount, changing drastically the operating wavelength of the device. The work presented here is, however, important in showing that it is possible to use the fluorine IID process to produce integrated passive cavities without having to go through expensive, and low yield regrowth steps.

-
- ¹'High power coupled multiple stripe phase locked injection laser', D.R. Scifres, W. Streifer, and R.D. Burnham, *Appl. Phys. Lett.*, **34** (4), pp.259-261, 1979.
- ²'Spontaneous Filamentation in Broad-Area Diode Laser Amplifiers', R.J. Lang, D..F. Welsh, and L. Goldberg, *IEEE J. of Quantum Electron.*, **30**(3), pp.687–693, 1994.
- ³M. Normm and E. Wolf, *Principles of Optics* p. 392ff Paragamon, New York, 1959.
- ⁴'High power coupled multiple stripe phase locked injection laser', D.R. Scifres, W. Streifer, and R.D. Burnham, *Appl. Phys. Lett.*, **34** (4), pp.259-261, 1979.
- ⁵'Experimental and Analytical Studies of Coupled Mode Stripe Diode Lasers', D.R. Scifres, W. Streifer, and R.D. Burnham, *IEEE Journal of Quant, Electron.*, **QE-15**(9), pp. 917-921, 1979.
- ⁶'Supermode Anaylsis of Phase-Lokcked Arrays of Semiconductor Lasers', E. Kapon, J. Katz, and A Yariv, *Optics Letters*, **10** (4), pp 125–127, 1984.

Chapter 10

Summary and Conclusions

The initial objectives of this thesis have been accomplished;

1. Fluorine, implanted at a concentration of 10^{18} cm^{-3} and followed by a 30 s anneal at 700°C , has been shown to intermix InGaAs/InGaAsP quantum well structures by 40 meV. Disordering occurs selectively, unimplanted areas retaining the quantum well structure of the as-grown material.

The thermal stability problems observed when annealing in conventional furnace have to a large degree been solved by thermally processing in an RTA. Potentially, shifts of over 100 meV can be expected for anneals at temperatures over 750°C in the RTA, however these shifts cannot be achieved selectively due to the thermal instability of the InGaAs/InGaAsP quantum wells.

2. Losses down to 0.57 dB cm^{-1} were measured by the Fabry-Perot technique for samples without a doped upper cladding region. By comparing the results of bandgap shifted waveguides with and without the fluorine implant, it was found that the fluorine implant does not add to the absorption loss of the waveguides. If fluorine existed as an ion at room temperature, a greater loss figure would be expected due to free carrier absorption.
3. As a demonstration device, an oxide stripe extended cavity laser was fabricated, the extended cavity formed using fluorine IID. The device was used to measure the loss of the passive waveguide sections. The losses were measured to be of the order of 8 dB cm^{-1} for a device annealed at 700°C for 30 seconds in the RTA.

The extended cavity lasers were shown to improve the far-field characteristics of the $75 \mu\text{m}$ oxide stripe device. A main central lobe, having a power of approximately 14 mW with a FWHM of 2° , was observed from the extended

device, compared a multi-lobed output spread over 30° with a minima on-axis from a conventional device.

The disordering process is very complicated, and it was not the intention of this thesis to model it. Evidence has come to light however that is worth noting;

1. Unlike GaAs/AlGaAs structures, InGaAs/InGaAsP QWs are not disordered using silica caps. Silica capping has been found to be useful since it helps to maintain good surface morphology during the annealing process, and will also protect the surface from accidental damage during manipulation.
2. Very short anneals with silicon nitride caps can be used to intermix InGaAs/InGaAsP QWs. Optimum conditions, for selective disordering, have been found to be 750°C for 5 seconds.
3. For low temperature anneals, and for short times, it is possible to produce a red shift in the QW bandgap. This can be explained by preferential group III disordering which causes a lowering of the well layer's bandgap, but will introduce strain into the wells. Conditions under which this has been observed are for thermal anneals at 650°C between 10 and 90 seconds where red shifts of up to 20 meV have been observed. The red shift is more pronounced the thinner the wells in a QW structure. The same effect is also observed with boron implants, annealed between 550°C and 750°C for 30 minutes in the conventional anneal furnace and for between 20 and 50 seconds at 700°C in the RTA.
4. Disordering is due to the combined effects of implantation damage as well as enhanced intermixing rates due to the change in Fermi level associated with a charged impurity.
5. Rapid thermal processing has been found to be the preferred thermal processing technique. This is because fluorine has a high diffusion coefficient in the QW

structure: F IID only occurs for a few seconds before the fluorine concentration falls below that required for intermixing. In a conventional annealing furnace after an initial disordering due to fluorine, thermal intermixing becomes the main disordering process.

Also, silicon nitride has been used to produce wavelength modified lasers by intermixing the QW structure. A 56 nm shift in lasing wavelength was observed after a 5 second anneal at 750°C with a 1000 Å coating of silicon nitride. The good lasing characteristics of the devices produced indicate that the electrical properties of the bandgap shifted sections remain intact. Silica capping was shown to be useful for maintaining good surface morphology in areas that were exposed to the N₂ atmosphere during annealing. Strontium fluoride was shown to have little effect on the intermixing process.

Diffusion coefficients of the fluorine IID process have been modelled by comparing the observed bandgap shift with a theoretical shift calculated by assuming that diffusion in the quantum well region follows Fick's laws, and the shape of the partially intermixed quantum well is that of the error function. Using this technique it has been estimated that for fluorine implanted samples, the diffusion coefficient is around 10¹⁵ cm² s⁻¹, compared to the thermal diffusion coefficient of between 10¹⁶ cm² s⁻¹ and 10¹⁷ cm² s⁻¹. The diffusion coefficients of both intermixing processes decay with increased anneal time, for constant anneal temperature—this indicates that the actual diffusion coefficients are concentration dependent and do not therefore follow Fick's simple laws of diffusion. Further, the Arrhenius plot of the diffusion coefficients show that whereas the F IID process is relatively linear, the thermal process appears to have two activation energies.

It would be of use in the future to investigate, in greater detail, the disordering processes which have been observed here. Techniques such as SIMS, X-ray diffraction, and Auger analysis can be employed to determine the interdiffusion species under different annealing conditions, and to assess quantitatively the degree of strain that is built up in a sample after red shifts have been observed.

Further, the oxide extended cavity lasers should be investigated in more detail to determine whether larger powers will be possible from this type of device. It may be necessary to use an array of single moded waveguides, with a disordered section at one end, to make the process more efficient and reproducible. The single moded waveguides should be designed so that the resulting near-field has the same spot separation and mode width as the filaments observed in the oxide stripe deices.

To conclude, a potentially useful process has been developed for use in the integration of InGaAs/InGaAsP optoelectronic devices operating in the 1.55 μm regime.

Appendix A

Wafer Structures

The following wafer structures were used in the work in this thesis. Figure A.1 shows the general structure with the layers that make-up the waveguides.

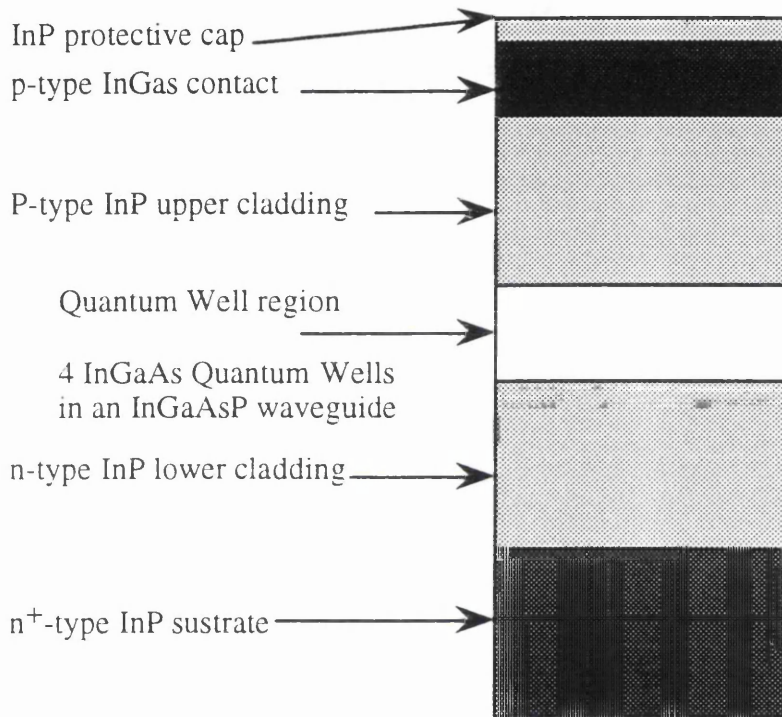


Figure A.1 Typical waveguide structures used for F IID tests and the fabrication of devices.

The following table indicates the exact structures of the wafers used. The substrates were

doped with selenium with a concentration of 10^{18} cm^{-3} . The wafers were grown at BNR Europe Ltd¹.

Wafer Ref.	Upper Contact	Upper Cladding	Quantum Well Region	Lower Cladding	Laser Strct Y/N
E 288	0.21 μm $\text{In}_{0.53}\text{Ga}_{0.47}\text{As}$	1.5 μm InP	4 \times 100 \AA $\text{In}_{0.53}\text{Ga}_{0.47}\text{As}$ wells 0.26 μm GaInAsP waveguide.	1.0 μm InP	Y
E242	not present	1.1 μm InP (undoped)	4 \times 100 \AA $\text{In}_{0.53}\text{Ga}_{0.47}\text{As}$ wells 0.28 μm InGaAsP	1.0 μm InP	N
E269	not present	1.2 μm InP (undoped)	4 \times 100 \AA $\text{In}_{0.53}\text{Ga}_{0.47}\text{As}$ wells 0.29 μm InGaAsP	1.0 μm InP	N
E791	0.1 μm $\text{In}_{0.53}\text{Ga}_{0.47}\text{As}$ + 300 \AA $\text{In}_{0.79}\text{Ga}_{0.21}\text{As}_{0.45}\text{P}_{0.55}$	1.5 μm InP	5 \times 90 \AA $\text{In}_{0.53}\text{Ga}_{0.47}\text{As}$ wells 180 \AA $\text{In}_{0.79}\text{Ga}_{0.21}\text{As}_{0.45}\text{P}_{0.55}$ barriers In 0.2 μm $\text{In}_{0.79}\text{Ga}_{0.21}\text{As}_{0.45}\text{P}_{0.55}$	1.0 μm InP	Y

E795	0.1 μm In _{0.53} Ga _{0.47} As + 300 Å In _{0.79} Ga _{0.21} As _{0.45} P _{0.55}	1.5 μm InP	5×30 Å In _{0.39} Ga _{0.61} As 170 Å In _{0.75} Ga _{0.25} As _{0.54} P 0.46 barriers In 0.2 μm In _{0.75} Ga _{0.25} As _{0.54} P 0.46 1% compressive strain in the wells.	1.0 μm InP	Y
E799	0.1 μm In _{0.53} Ga _{0.47} As + 300 Å In _{0.79} Ga _{0.21} As _{0.45} P _{0.55}	1.5 μm InP	5×30 Å In _{0.53} Ga _{0.47} As wells 180 Å In _{0.79} Ga _{0.21} As _{0.45} P 0.55 barriers In 0.2 μm In _{0.79} Ga _{0.21} As _{0.45} P 0.55	1.0 μm InP	Y
A2262	not present	1 μm InP	4×100 Å In _{0.53} Ga _{0.47} As wells 120 Å In _{0.81} Ga _{0.19} As _{0.37} P 0.63 barriers In 0.2 μm In _{0.81} Ga _{0.19} As _{0.37} P 0.63	1.0 μm InP	N

A2409	not present	1 μm InP	$4 \times 100 \text{ \AA}$ $\text{In}_{0.53}\text{Ga}_{0.47}\text{As}$ wells 120 \AA $\text{In}_{0.81}\text{Ga}_{0.19}\text{As}_{0.37}\text{P}$ 0.63 barriers In 0.2 μm $\text{In}_{0.81}\text{Ga}_{0.19}\text{As}_{0.37}\text{P}$ 0.63	1.0 μm InP	N
-------	-------------	---------------------	---	-----------------------	---

Figure A.1 Table containing the detailed structures of the wafers used in the thesis.

¹BNR Europe Ltd., London Road, Harlow, Essex CM17 9NA.

Appendix B

Computer Programme to Calculate the Near and Far-Field Patterns

The following listings are for a *Matlab 4.00*¹ computer programme for Windows. The series of routines calculates the field profile in a slab waveguide, and then goes on to calculate the near-field intensity and far-field intensity profiles.

Data for the programmes, i.e. the refractive indices, dimensions, wavelength etc are entered in *data.m*. The data in *data.m* file is accessible to all the other programmes. Figure B.1 shows the relationship between the following routines. All the routines are run independently except *data.m* which does not need to be executed independently.

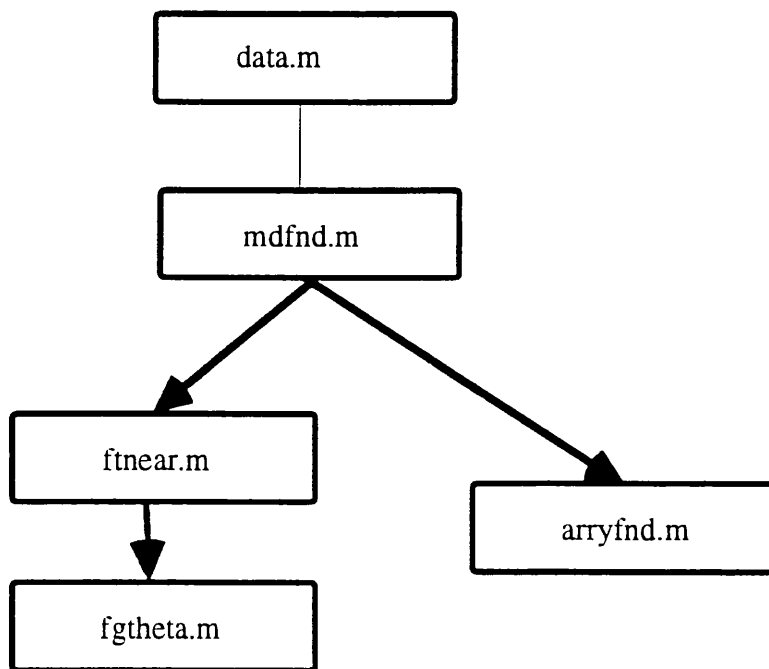


Figure B.1. Diagram to explain the sequence of Matlab routine to run in order to produce the graphs in Chapter 8.

The following sections contain the listing of the above mentioned routines, together with a summary of the routines.

B.1.1 data.m

```
%This file contains all of the variables required to calculate
%the near and far field patterns of an array of identical
% waveguides.
%
%      n1 = cladding refractive index
%      n2 = core refractive index
%      d      = half core thickness
%      lambda = wavelength of light generated
%      Steps = number of steps
%
%For use with;
%      mdfnd.m  Finds the modes in a slab waveguide.
%      arryfnd.m Finds the near field patter of the slab waveguide
%                defined in mdfnd.m
%                NOTE: mdfnd MUST BE EXECUTED FIRST!
%
n1=3.540; n2=3.545; d=2.0e-6; lambda=1.55e-6;
steps=100;

fundmode = 1;
numguides = 10;
space = 7.5e-6;
supermode =2;

%'angle' is halh the angle over which the far field pattern is calculated. angle
= 40;

%'numpoints' is the number of points cacluated in the near
%field pattern.
numpoints = 100;
anglinc = 500;
```

```

k=2*pi/lambda;
deg2rad = pi/180;

save data

```

B.2 mdfnd.m

```

%Find the modes of a symmetric slab waveguide
% with the following parameters,
%
% n1 = cladding refractive index
% n2 = core refractive index
% d = half core thickness
% lambda = wavelength of light generated
% Steps = number of steps
%
%The resultant curves are saved as the file modes.mat.
%routine data.m sets up the current waveguide parameters data

load data
global R
R=sqrt((n2^2-n1^2)*(2*pi/lambda)^2*d^2);
hd = linspace(0,R,steps);
pd1 = sqrt(R^2-hd.^2);
pd2 = hd.*tan(hd);
pd3 = -hd.*cot(hd);
pd2 = clip(pd2,0,R);
pd3 = clip(pd3,0,R);
clf
subplot(221),plot(hd,pd1,hd,pd2,hd,pd3)
xlabel('hd')
ylabel('pd')
hda=pi/4:pi/2:R+pi/4;
%'m' is the number of modes supported in the waveguide
m=length(hda)
%The following two FOR loops calculate the propagation constants

```

```

%and mode profiles for all of the proogating modes.
%EVEN modes
for i=1:2:m
    hroot(i)=fzero('pdeven',hda(i));
    h=hroot(i)/d;
    p=(hroot(i)*tan(hroot(i)))/d;
    x = linspace(-4*d,4*d,steps);
e = cos(h.*x).*[abs(x)<=d]+cos(h*d)*exp(-p.*(abs(x)-d)).*[abs(x)>d];
emat(i,:) = e;
    subplot(2,2,4),plot(x,e)
xlabel('y'); ylabel('E(y)- Even Modes');
hold on
end
%ODD modes
for i=2:2:m
    hroot(i)=fzero('pdodd',hda(i)); h=hroot(i)/d; p=(hroot(i)*(cot(hroot(i))))/d;
    x = linspace(-4*d,4*d,steps);
e = sin(h.*x).*[abs(x)<=d]+... sin(h*d)*(exp(-p.*(x-d)).*[x>d]-exp(p.*(x+d)).*[x<(-
d)]);
    emat(i,:) = e;
    subplot(2,2,3),plot(x,e)
xlabel('y'); ylabel('E(y)- Odd Modes');
hold on
end
%The ASCII file 'modes.dat' contains all the field profiles %propogating in the slab
waveguide.

profile = emat(fundmode,:);
dist = x';
save modes.dat 'profile' profile 'dist' dist /ascii; save modes.mat emat x R;

%subplot(1,1,1)

```

B.2.2 clip.m

```
function y = clip( x, lo, hi)
```

```

%clip.m
%function to 'clip' a curve between limits, 'lo' is the lower limit, 'hi' the upper
%limit

y = (x.*[x<=hi]) + (hi.*[x>hi]);
y = (y.*[x>=lo]) + (lo.*[x<lo]);

```

B.2.3 pdeven.m

```

%Function to find the even modes in 'mdfnd.m'
function y = pdeven(hd)

global R
y = sqrt(R^2-hd.^2)-hd.*tan(hd);

```

B.2.4 pdodd.m

```

%Function to find the odd modes in 'mdfnd.m'
function y = pdodd(hd)

global R
y = sqrt(R^2-hd.^2)+hd.*cot(hd);

```

B.3.1 arryfnd.m

```

%Sets an array of waveguides with mode profile read in from
%'modes.mat', and calculated using 'mdfnd.m'
% numguides      = number of waveguides / filaments
% fundmode       = fundametal waveguide mode (mode number in
%                  single guide)
% space          = guide separation
data
load data
load modes
esum=[]
E=emat(fundmode,:);

```

```

maxx = x(length(x))+(numguides-1)*space;
minx = x(1);
xarray = linspace(minx, maxx, numpoints);
for i= 1:numpoints
    esum(i)=0;
    for l= 1:numguides
multiplier = sin((l*pi*supermode)/(numguides+1)); xi = xarray(i)-(l-1)*space;
xi = clip(xi, x(1), x(length(x)));
Ei=spline(x,E,xi)*multiplier;
        esum(i) = esum(i)+Ei;
    end
end
end

```

```

length(xarray)
length(esum)
subplot(121)
xlabel('y/metres');ylabel('E(y)')
plot(xarray,esum)
subplot(122)
xlabel('y/metres');ylabel('E(y)')
intensum = real(esum).^2 + imag(esum).^2;
plot(xarray, intensum)
dist = xarray';
prof = esum';
intenprof = intensum';
save nrfield xarray esum;
save nrfield.dat dist prof intenprof /ascii;

```

B.4.1 fgtheta.m

%A routine to calculate the grating function for the laser array described in data.m
 %and to finally calculate the far-fielf pattern by multiplying the grating function
 %by the far-field of a single emitter.

```

subplot(1,1,1);
data

```

```

load data;
supermode
expand=1;
supermode
clear gprof kss thetadeg theta ittheta
thetadeg = linspace(-angle,angle,expand*anglinc);
theta = thetadeg.*deg2rad;
gprof=[];

for l=1:(numguides) elv=sin(l*pi*supermode/(numguides+1));
    for i=1:length(theta)
        thetai=theta(i);
        kss(i)=k*space*sin(thetai);
        ittheta(i)=elv*exp(sqrt(-1)*l*kss(i));
        end
        gprof=ittheta+gprof;
    end

gprof= real(gprof).^2 + imag(gprof).^2;
for i=1:length(ffprof)
    ffpatern(i)=ffprof(i)*gprof(i*expand);
end
subplot(211)
plot(thetadeg,gprof)
length(fthetadeg)
length(ffpatern)
subplot(212)
semilogy(fthetadeg,ffpatern)
save ff.dat thetadeg ffpatern /ascii

```

¹The Mathworks, Inc.

